



HAL
open science

Damage induced by crystallisation in confined reservoir conditions

Bruno Leclere

► **To cite this version:**

Bruno Leclere. Damage induced by crystallisation in confined reservoir conditions. Earth Sciences. Université de Pau et des Pays de l'Adour, 2021. English. NNT : 2021PAUU3004 . tel-03194127

HAL Id: tel-03194127

<https://theses.hal.science/tel-03194127>

Submitted on 9 Apr 2021

HAL is a multi-disciplinary open access archive for the deposit and dissemination of scientific research documents, whether they are published or not. The documents may come from teaching and research institutions in France or abroad, or from public or private research centers.

L'archive ouverte pluridisciplinaire **HAL**, est destinée au dépôt et à la diffusion de documents scientifiques de niveau recherche, publiés ou non, émanant des établissements d'enseignement et de recherche français ou étrangers, des laboratoires publics ou privés.

École doctorale 211 : Sciences Exactes et leurs Applications

THÈSE

pour obtenir le grade de docteur délivré par

l'Université de Pau et des Pays de l'Adour

Spécialité doctorale "Sciences de la Terre"

présentée et soutenue publiquement par

Bruno LECLERE

le 18 février 2021

Endommagement induit par cristallisation dans les conditions de réservoirs géologiques

Directeur de thèse : **David GREGOIRE**

Co-Directeur de thèse : **Jean-Paul CALLOT**

Co-encadrant de thèse : **Hannelore DERLUYN**

Jury

M. Jean-Paul Callot,	Professeur des universités	co-Directeur de thèse
Mme. Hannelore Derluyn,	Chargée de recherche CNRS	Examineur
M. Eric Gaucher,	Docteur	Examineur
M. David Gregoire,	Professeur des universités	Directeur de thèse
Mme Catherine Noiriel,	Maître de conférences HDR	Rapporteur
M. Leo Pel,	Associate Professor	Rapporteur
M. Alexandre Schubnel,	Directeur de recherche CNRS	President
M. Michael Steiger,	Full Professor	Examineur

UPPA

Laboratoire des Fluides Complexes et leurs Réservoirs

UMR 5150, F-64600 Anglet, France

«Il est souvent nécessaire d'entreprendre pour espérer et de persévérer pour réussir.»
Gilbert Cesbron

Remerciements

Le cheminement menant à la soumission de ce manuscrit de thèse fut une expérience qui laissera une trace indélébile tant dans ma vie professionnelle que personnelle. Il n'aurait pas été possible sans un certain nombre de personnes que je tiens à remercier en préambule de ce travail. Merci aux membres de mon encadrement, David et Jean-Paul mes directeurs de thèse et Hannelore qui a co-encadré ce travail. Merci de m'avoir fait bénéficier de vos connaissances sur la pression de cristallisation et d'avoir orienté patiemment mes tribulations de thésard. Merci Éric et Sylvain de nous avoir apporté le soutien financier de TOTAL et pour votre contribution scientifique. Je souhaite remercier les membres du jury pour leur participation à l'évaluation de ce travail et en particulier mes rapporteurs Catherine Noiriél et Leo Pel pour leur relecture et leurs commentaires constructifs.

Une grosse pensée pour Jérôme F. et Alexandre qui m'ont accueilli au laboratoire de Géologie de l'École normale supérieure et m'ont fait bénéficier de leur expérience du suivi acoustique des tests sous confinement. Merci Joseph et Olivier du LFCR ainsi que Jan et Jérôme A. de l'ENS pour votre disponibilité et votre aide pour la mise en place des expériences.

Merci aux doctorants que j'ai rencontrés à Pau, Anglet et chez Total, tout particulièrement Youssef, Dyhia, Kodi, Alex, Delphine, Rafik, Nicolas, Samuel. Notre soutien mutuel et les bons moments passés ont été précieux.

Merci à mes parents, frères et sœur ainsi que mes amis qui m'ont accompagnés sur ce chemin: Benoit, Vlad, Pierre, Bastoun, Féfé, Riton, Philou, Louis-Marie, Antoine, Valère, Anne Charlotte. Le meilleur reste à venir...

Résumé

La cristallisation dans les réservoirs géologiques est un problème complexe étudié dans le domaine des sciences de la terre. En conditions de laboratoire, les conditions réactionnelles sont bien définies ce qui n'est pas le cas dans les réservoirs géologiques où des objets géologiques déconcertants sont parfois générés et interrogent les concepts de cristallisation actuels. Les géologues les abordent selon deux approches : la première s'appuie sur les observations de terrains et l'échantillonnage pour retracer les séquences structurale, sédimentaire et diagénétique de la formation étudiée. La finalité de cette approche est aussi de formuler des hypothèses cohérentes avec le terrain, là où l'état de la connaissance est insuffisant. La deuxième approche, qu'on peut qualifier de géologie de laboratoire confronte les hypothèses des premiers à des expériences bien définies et dans le meilleur des cas bénéficiant d'un suivi in situ. Cette approche, faisant le lien avec des expériences plus fondamentales, apporte des pierres à l'édifice et remet au goût du jour l'état de la connaissance. Dans ce travail de thèse, nous empruntons la deuxième approche, afin d'éclaircir la formation des objets dont la genèse est expliquée par le concept de pression de cristallisation. C'est une pression qui peut s'exercer lorsqu'un cristal confiné dans un pore et baignant dans une solution sursaturée atteint les limites de l'espace disponible et s'il subsiste un film de solution sursaturée à l'interface entre le cristal et le pore. La pression dépend de la sursaturation de la solution par rapport au cristal précipité, de la température et du volume molaire du cristal précipité. Théoriquement cette pression peut être très grande et causer la rupture de n'importe quelle roche poreuse en pression de confinement de réservoir géologique. De plus, cette pression de cristallisation est très étudiée dans le domaine du génie civil car elle est responsable de l'altération rapide par les sels de monuments historiques aussi bien que de bâtiments plus récents. Il est important de noter que les sels précipitent fréquemment sous forme fibreuse ce qui n'est pas leur habitus cristallin classique. De même qu'en génie civil, les veines géologiques fibreuses sont régulièrement associées avec la pression de cristallisation. On les identifie en conditions de réservoir sous la forme de veines fibreuses de calcite, de quartz, de barite ou encore de serpentine, un phyllosilicate parfois fibreux et dans ce seul cas désigné sous le terme d'amiante. De même que pour les sels précipités en génie civil, la forme fibreuse n'est pas l'habitus cristallin classique des espèces minérales citées ci-dessus.

Suivant la méthode de travail expliquée plus haut nous avons proposé une série d'expériences visant à reproduire ce type d'objets. La contrainte que l'on s'est imposé est de parvenir à obtenir de l'endommagement par la cristallisation à des pressions de réservoirs géologiques. Pour le suivi des expériences, des dispositifs non destructifs comme l'acoustique ou la micro tomographie rayon X ont permis de s'assurer de l'état interne des échantillons avant de procéder à la confection de sections polis pour investiguer par microscopie électronique à balayage, la cristallisation, l'endommagement et la composition chimiques élémentaire.

L'étude bibliographique a très vite fait apparaitre que le maintien de la sursatura-

tion est primordial. Cela nécessite de minimiser l'énergie dans le transport et exclut de fait le transport advectif. Un avantage est apporté par la structure même des roches réservoirs constituée d'un réseau poreux où chaque pore est une chambre de cristallisation indépendante ce qui est un avantage certain pour limiter la nucléation dans la solution remplissant le milieu poreux. L'autre versant du problème est de générer une sursaturation suffisamment importante telle que le milieu poreux soit endommagé. Pour répondre à ces exigences, nous avons reproduit dans un calcaire de Lavoux et un grès d'Adamswiller, l'expérience de contre-diffusion de Prieto qui a précipité dans du gel de la barite à partir de deux solutions préparées l'une avec du chlorure de barium dissous l'autre avec du sulfate de sodium dissous. Une forte sursaturation avait été mesurée et reportée dans la littérature. Dans notre cas, aucun endommagement n'a été mesuré, mais nous avons observé des figures de précipitation qui montrent l'effet du milieu poreux et de sa minéralogie sur la précipitation d'espèces allochtones : dans le calcaire de Lavoux, les cristaux précipitent selon un front qui suit une logique bien particulière. Il suit un chemin qui favorise la précipitation au contact de la micrite des grains d'oolite microporeux, avec un seuil de nucléation plus bas. Lorsque le front de sursaturation rencontre un pore de grande taille, soit la barite précipite sous forme de cristaux de grande taille et court-circuite la propagation par les oolites, soit elle va contourner le pore par les grains d'oolite micritique. On explique cette compétition par la nucléation de la forme amorphe de la barite en amont de celle de la barite qui retarde la nucléation de la barite à l'endroit le plus favorable. Une discussion fructueuse avec Dr. Nikolaos Prasianakis (PSI) sur la précipitation de sulfate de strontium déformant un milieu artificiel constitué d'illite recompressée, a fait naître l'idée de précipiter la barite dans un milieu poreux riche en argiles. C'est avec surprise que l'on a observé la barite précipiter entre les feuillets de complexes argileux smectite-chlorite. Il semble que le barium remplaçant d'autres cations dans l'espace basale entre les feuillets TOT des smectites puisse être désorbé par le sulfate et que la barite précipite dans ce même espace ou alors que la brucite des chlorites se dissolvent et que l'espace soit occupé par la barite. Le gonflement de l'argile pourrait accompagner la précipitation de barite : cette question reste en suspens mais semble prometteuse car de nombreuses veines fibreuses précipitent en domaine argileux dans la nature. En parallèle de cette expérience, nous avons mis en place une collaboration avec Dr. Alexandre Schubnel, Dr. Jerome Fortin et Dr. Jan Borgomano de l'école Normale Supérieure à Paris (Ulm) qui utilisent une cellule expérimentale instrumentée pour suivre sous confinement, l'endommagement d'un échantillon grâce à un dispositif acoustique et des jauges collées sur l'échantillon. Pour exploiter au mieux ces possibilités, nous avons dû mettre au point un protocole expérimental qui garantisse un endommagement de l'échantillon dans un temps raisonnable. La mirabilite, la phase décahydratée du sulfate de sodium, est l'espèce chimique idoine puisque d'après la littérature sur le sujet, l'endommagement induit par sa précipitation intervient rapidement par transition de phase depuis la phase anhydre du sulfate de sodium, la thenardite, ou par des cycles de refroidissement d'une solution sursaturée. En contrepartie, ce sel ne peut exercer une pression de cristallisation supérieure à ~ 13 MPa à 20°C . Nous avons reproduit les expériences de la littérature qui furent riches d'enseignement et nous avons finalement trouvé un protocole pour précipiter un dôme de thenardite au milieu d'un échantillon de roche cylindrique poreux. A l'E.N.S., nous avons suivi la reimplémentation par de l'eau pure de l'échantillon imprégné de thenardite d'abord sans pression de confinement puis à une pression isotrope de 10 MPa correspondant à un enfouissement de ~ 300 mètres. D'une part, le suivi de la propagation des ondes P dans le milieu a montré une saturation progressive de la porosité par l'eau

sous le dôme qui constitue dans un premier temps une barrière de perméabilité à l'eau et à l'humidité. D'autre part, au travers du dôme de sel, initialement la vitesse des ondes est plus rapide que dans l'échantillon sec. Lorsque le front d'imbibition atteint le dôme de thenardite, la transformation de la thenardite en mirabilite donne lieu à la base du dôme à une augmentation de la vitesse des ondes P qui se transforme rapidement, sans pression de confinement, en une chute brutale de celle-ci suite à la dispersion des ondes conséquence de la fissuration induite par la cristallisation de la mirabilite. Dans l'échantillon confiné à 10 MPa, la vitesse ne cesse d'augmenter tout au long de l'expérience ce qui traduit une fissuration moins importante et contrebalancée par le gain de vitesse lié à la précipitation de mirabilite. La fissuration est enregistrée par les émissions acoustiques, à la hauteur de 170 événements sans pression de confinement et seulement 54 événements dans l'échantillon confiné à 10 MPa. La fissuration du dôme le rend perméable au fluide. Dans le but d'augmenter la pression de confinement à des valeurs flirtant avec les 1000 mètres d'enfouissement (~ 30 MPa), le même protocole a été testé avec le sulfate de magnésium et la transition de phase kieserite/epsomite. Les premières expériences montrent que la réaction est plus lente probablement dû à la conjonction d'une nucléation inhibée et d'une cinétique de dissolution/cristallisation divisée par deux vis-à-vis de celle du couple thenardite/mirabilite. Cela a pour conséquence la remobilisation du sulfate de magnésium qui est transporté et reprécipite en formant un nouveau dôme. La séquence d'endommagement par pression de cristallisation intervient d'abord par la fragilisation du squelette du grès traversé de fissures inter granulaires qui sont visibles à toute pression de confinement et qui ne donne pas lieu à l'enregistrement d'émissions acoustiques. Sans pression de confinement pendant une expérience plus longue, l'epsomite s'accumule et forme des veines millimétriques qui sont ensuite dissoutes et transportées par pression de capillarité plus haut dans l'échantillon où un autre cycle d'endommagement a lieu. Pour clôturer cette étude, nous avons reproduit par des modèles analytiques simples la transition de phase thenardite/mirabilite dans un grès d'Adamswiller sans pression de confinement. Ces modèles mettent en exergue la compétition entre l'effet de cimentation par la cristallisation du sulfate de sodium sous la forme anhydre puis hydratée et la dispersion des ondes par la fissuration induite par la pression de cristallisation de la mirabilite. En conclusion, nous avons montré au premier ordre que la pression de cristallisation est un mécanisme d'endommagement valable en conditions de réservoirs géologiques. Au second ordre, nous avons validé une méthode acoustique de suivi du changement de phase intervenant dans le milieu poreux en considérant l'endommagement induit par la pression de cristallisation. Enfin, sur le versant de la nucléation des espèces chimiques dans les réservoirs géologiques, la précipitation de barite a permis d'entrevoir le rôle joué par la forme amorphe de la barite et les interactions avec les argiles. En guise de perspective, il y a d'autre réaction d'hydratation qui semble procéder par pression de cristallisation comme la serpentinsation qui a un réel intérêt économique à cause de l'hydrogène natif coproduit. Il serait donc judicieux d'instrumenter une expérience de serpentinsation avec un dispositif acoustique pour mesurer le niveau d'émissions et l'endommagement en direct. Cependant cela se heurte à des contraintes techniques tant en termes de temps d'expérience qu'en terme de résistance des capteurs piézoélectriques dans les conditions expérimentales. Mais si comme on le pense une telle réaction donne lieu à des séismes de faible énergie, le suivi de cette sismicité peut renseigner sur la réactivité du réservoir de roche ultramafique, du potentiel de production d'hydrogène natif et donc de la valeur économique de la réserve. Le deuxième point de perspective rejoint les observations de (Maliva and Siever, 1988a) qui voyait comme moteur dans

le remplacement diagénétique la pression induite par le minéral remplaçant qui faisait augmenter le seuil de saturation de la roche remplacée. C'est une autre manière de voir la pression de cristallisation car au lieu de fissurer elle dissout la roche hôte: pression solution. Le protocole expérimental défini dans cette thèse permet de tester cette hypothèse car si on fixe une pression de confinement qui dépasse la pression maximum pouvant être exercée par la phase qui cristallise, la pression de cristallisation ne va pas se dissiper par pression de cristallisation mais pourrait dissoudre la phase hôte. Ce serait tout particulièrement intéressant de faire cela avec un calcaire comme phase hôte et du sulfate de magnésium comme phase précipitée. La présence de carbonate et de magnésium en solution pourrait aboutir à la précipitation de dolomie.

Abstract

Veins in geological reservoir settings are mineral-filled fractures that are being associated with the model of ‘crack-seal’ by structural geologists. However, some veins exhibit features that do not match with the model of ‘crack seal’ but would better fit with a ‘seal-crack’ model driven by the concept of crystallisation pressure. From this, two main experimental tests are conducted. We start with an experiment of counter diffusion to precipitate a barite front in an oolite limestone, the Lavoux limestone, and a sandstone with a clay fraction, the Adamswiller sandstone. The reacted samples are analysed via 3D X-ray microtomography, microscopy and SEM-EDS microanalysis. Although we do not observe damage, we show that barite nucleation and crystallisation is linked to the pore distribution and the matrix mineral. In particular, barium interacts with clay minerals like the smectite-chlorite complex. Ultimately, this interaction may expand the complex basal space when barite precipitates. Then salt studies for the understanding of damage induced on cultural heritage are the starting point of a new protocol with Na_2SO_4 and $MgSO_4$ to be tested under isotropic confining pressure inside a triaxial cell (ENS Paris). It consists of precipitating an anhydrous salt layer in an Adamswiller sandstone. Later the anhydrous salt layer is rewetted to precipitate a more hydrated salt phase. The damage is monitored at a confining pressure up to 27 MPa with acoustic emission, elastic wave propagation, strain gauges and 3D X-ray microtomography. These experiments emphasize the competition between salt cementation of the porous medium and salt crystallisation induced damage. The last point is confirmed by the effective modeling of the elastic properties of a porous medium impregnated with sodium sulphate when it is rewetted without confining pressure.

Contents

Remerciements	iii
Résumé	v
Abstract	ix
General introduction	1
1 State of the art	5
1.1 Crystallisation in porous media	8
1.2 Experimental examples of crystallisation induced damage on porous rock	22
1.3 Geological veins and objects related to crystallisation pressure	24
1.4 Poromechanic's of variably saturated porous rock	35
1.5 Modeling of the effective elastic properties of porous medium with cracks	41
1.6 Conclusion	44
2 Materials and Methods	45
2.1 Materials	48
2.2 Methods	65
3 Unclassical crystallisation of barite during diffusion driven barite precipitation in sedimentary rock	73
3.1 Introduction	76
3.2 Materials and methods	76
3.3 Results	79
3.4 Discussion	84
3.5 Conclusion	89
4 Damage induced by mirabilite precipitation in confined reservoir conditions	91
4.1 Sample preparation	94
4.2 Acoustic monitoring of damage induced by mirabilite precipitation in confined shallow reservoir conditions	100
5 Damage induced by epsomite precipitation in confined reservoir conditions	117
5.1 Sample preparation	120
5.2 Damage induced during rewetting of an Adamswiller sandstone impregnated with kieserite	122
5.3 Damage induced by epsomite crystallisation in a uni-axially confined sample at 10 MPa	127

5.4	Mechanical stiffening driven by crystallisation of epsomite in confined reservoir conditions	134
5.5	General conclusion	143
6	Effective modeling of crystallisation in a porous sandstone	145
6.1	Introduction	148
6.2	Material	148
6.3	Modeling of water capillary uptake in the thenardite rich Adamswiller sandstone	149
6.4	General conclusion	156
	Conclusion and perspectives	157
6.5	Conclusion	158
6.6	Perspectives	159
A		I
A.1	Geodesign triaxial cell	I
A.2	Shots picking methods	II
A.3	P-wave propagation spectogram in ENS experiments	III
A.4	Adamswiller sample description	VII
A.5	Supplementary material	VIII
B	Glossary	IX

General introduction

Precipitation of minerals in geological reservoirs is a complex problem studied in geosciences for mining, oil and gas production, gas storage, nuclear waste management, geothermal energy, and the emerging native H_2 production. In the mining industry, ore deposits are precipitated by hydrothermal-related diagenesis processes like zebra textures in carbonate and dolomitic host rock (Wallace and Hood, 2018). In the oil and gas industry, the properties of oil and gas reservoirs are key questions during exploration because they determine reservoir productivity and its economic value. Then, the operator may have recourse to secondary recovery methods as the injection of seawater to drain the trapped fluid and stimulate the oil production. This method modifies the chemical equilibrium and may lead to precipitation of foreign aqueous species (Collins, 2005; Poonosamy et al., 2020). Similarly, in the field of nuclear waste storage, crystallisation may happen over the long term via exchanges between the confining shale formation and the stored materials (Chagneau et al., 2015a).

Green energies are booming nowadays, and some solutions deal with the exploitation of geothermal energy or the trapping of undesirable gas. They are not exempted by crystallisation issues: the trapping of CO_2 in saline aquifers is exposed to injection problems that arise when salt crystallisation occurs, leading to injection reduction (Miri and Hellevang, 2016; Peysson et al., 2011). During geothermal energy production, the dragged warm brine cools down, which may induce crystallisation that reduces the production well efficiency (Regenspurg et al., 2015). More problematic, geothermal drilling through hundred meters deep anhydrite bearing formation leads to the dramatic hydration of anhydrite in gypsum and the swelling of the whole anhydrite formation into gypsum (Ramon and Alonso, 2018). On the surface, the historical town of Staufen in Breisgau (Germany) suffers irremediable damages (Sass and Burbaum, 2010). Finally, crystallisation pressure may have favorable outcomes like reactive surface generation related to serpentine precipitation during serpentinisation reaction (Kelemen and Hirth, 2012; Malvoisin, Brantut, and Kaczmarek, 2017). It fosters native H_2 generation, a decarbonated gas naturally expelled during serpentinisation of mafic rocks (Gaucher, 2020; Marcaillou, 2011; McCollom and Donaldson, 2016).

As illustrated above, crystallisation has wide applications from the permeability reduction in geological reservoirs to the potential onset of crystallisation induced damage like in saline aquifer, the zebra textures, or the serpentinisation reaction. Geoscientists often dismissed this point of view on crystallisation-induced alteration in geological settings. Nonetheless, the theoretical background and observations in the field show that this happens probably at a broad range in geological features. Likewise, the prediction of damage in the industrial applications exposed above is of great importance. In parallel, damages induced by salt crystallization are famous for building stone, concrete, or brick (Caruso, Wangler, and Flatt, 2018; Filho et al., 2019; Scherer, 2004). Figure 1 is a photography taken in Santander cloister that illustrates marine salt alteration on cultural heritage. Salt crystallisation accelerates soil and cliff weathering as

studied in the ongoing Ezponda project (quantification of Basque coast cliffs erosion induced by salt weathering ¹).



Figure 1: Detail of a pilar in the Santander Cathedral cloister weathered by salt crystallisation.

Large progress has already been made on this issue since the 90's, in civil engineering and cultural heritage preservation. A broad literature exists that describes the damages induced by precipitation of chemical species in porous building materials. The theoretical background is well defined and the modeling of chemo-mechanical interactions between the precipitated aqueous species and the porous rock is on track (Coussy, 2006; Derluyn, 2012).

The motivation of this thesis is to introduce the problem of crystallisation-induced damage under geological reservoir conditions. Experimental proof of crystallisation-induced damage on porous rock confined in geological settings is the main objective. To proceed, we plan different crystallisation experiments to study crystallisation in porous rock. Several monitoring technics are employed including 3D X-ray microtomography, acoustic monitoring and SEM-EDS microanalysis.

The thesis is organized as follows: at first in chapter 1, we will review the theoretical knowledge concerning crystallisation and the concept of crystallisation pressure. Alongside this, we will report experiments and geological occurrences that are our source of inspiration. Next in chapter 2, we describe the properties of the aqueous chemical species and the porous rock and we address the methods employed. In chapter 3, we comment on unclassical barite precipitates obtained through the mean of a contra-diffusive setup. Meanwhile, we adopt a salt crystallisation protocol in confined conditions and in a reasonable time. The sample preparation protocol is described at the beginning of chapter 4. Next, in chapter 4, mirabilite crystallisation-induced

¹www.get.omp.eu/recherche/projets-scientifiques/projet-feder-nouvelle-aquitaine-ezponda/

damage in an Adamswiller sandstone is described up to a 10 MPa isotropic confining pressure. In chapter 5, the damage of epsomite crystallisation in an Adamswiller sandstone are presented up to 27 MPa isotropic confining pressure. Finally, in chapter 6, based on the theory of Eshelby, the modeling of the effective elastic properties of a porous rock homogenised with salt inclusion and cracks is compared with experimental data.

Chapter 1

State of the art

Contents

1.1	Crystallisation in porous media	8
1.1.1	Definitions	8
1.1.2	Crystal nucleation	9
1.1.3	Crystal growth/dissolution	12
1.1.4	Theoretical approach on crystallisation pressure	14
1.2	Experimental examples of crystallisation induced damage on porous rock	22
1.2.1	Damages induced by precipitation of a fibrous salt front	22
1.2.2	Damages induced by rewetting thenardite impregnated porous rock	23
1.2.3	Temperature cycling provoking mirabilite crystallisation induced damage	23
1.3	Geological veins and objects related to crystallisation pressure	24
1.3.1	Fibrous veins	25
1.3.2	Zebra structure	28
1.3.3	Diagenetic replacement	30
1.3.4	Asbestiform veins	31
1.4	Poromechanic's of variably saturated porous rock	35
1.4.1	Elastic properties of homogeneous isotropic material	35
1.4.2	Propagation of P-wave in fluid-saturated porous medium	36
1.4.3	P-wave propagation in a partially fluid-saturated porous medium	38
1.4.4	P-wave velocity propagation in a porous medium submitted to an increasing confining pressure	39
1.5	Modeling of the effective elastic properties of porous medium with cracks	41
1.5.1	Modeling of the effective elastic of a homogeneous isotropic material with spherical inclusions	41
1.5.2	Modeling of the effective elastic properties of a cracked material	41
1.6	Conclusion	44

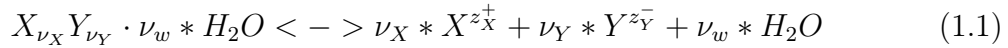
Abstract

In the chapter state of the art, we aim to recall the information necessary to grasp the problem of crystallisation pressure in confined reservoir conditions and its experimental monitoring. The first part deals with the chemical considerations on crystal nucleation, crystallisation and crystal growth in bulk and more disturbed conditions that may lead to nucleation inhibition and the building of a saturated solution with respect to the precipitating mineral. This is of first importance for crystallisation pressure that depends on the solution saturation. We will give the equations to determine the crystallisation pressure and we will take advantage of the opportunity to develop the concept of crystallisation pressure to contextualize the level of crystallisation pressure with the size and connectivity of the pores, the transport mode, the presence of precipitation inhibitors and of course the chemical properties of the precipitating mineral. In the second section, we will describe crystallisation pressure experiments. These experiments have been reproduced as sources of inspiration to our protocol in confined conditions. To successfully adapt these protocols, it is important to contextualize crystallisation pressure in reservoir conditions, because it will give the type of minerals, chemical reactions and porous mediums that are concerned. Thus, we will recall the geological veins and objects related to crystallisation pressure in the literature. We will describe their morphology and provide the formation hypothesis given in the literature. In particular, we will see that those hydration reactions like serpentinization are prominent in geological settings. The next section is related to the laboratory techniques chosen to monitor the experiments in-situ: ultrasonic wave. They imply the propagation of elastic P-wave across a porous medium in changing water saturation conditions. Depending on the frequency of the elastic waves and the water saturation, dispersion and attenuation effects are caused by wave-induced fluid flow. Thus, we will review poromechanics basics and the different frequency-dependent regimes, namely the drained or undrained regime otherly called the low-frequency or high-frequency regime involved during our experiments. Numerical applications based on the initial material properties will be calculated. The cases of humidity, partial saturation and free water imbibition in a porous rock will be reviewed and summarized in a recap figure. Finally, for modeling sake, the equation to homogenize a porous rock with inclusions of different nature and fluid-saturated cracks are given. They will be used later for the effective modeling of the free water imbibition in a porous rock containing salt.

1.1 Crystallisation in porous media

1.1.1 Definitions

Crystallisation is the operation by which a solid forms. The atoms or molecules are highly organized into a lattice known as a crystal. Within this work, we will deal with chemical species dissolving and precipitating out of an aqueous solution. The reaction of dissolution/crystallisation of crystal with ν_w molecules of hydration water is then written as:



The activity of the ions in solution, a_i is expressed as a function of the concentration of the chemical species (X or Y), C_i , the reference concentration C_0 equal to 1 mol.L^{-1} and the activity coefficient γ_i :

$$a_i = \frac{C_i}{C_0} * \gamma_i \quad (1.2)$$

the **Ion Activity Product (IAP)** is expressed as $IAP = a_X^{\nu_X} * a_Y^{\nu_Y} * a_w^{\nu_w}$ and K_{sp} is the solubility product, i.e., the IAP at equilibrium for a solute dissolved in an aqueous solution. Finally, we define the **Saturation (S)** in equation 1.3:

$$S = \frac{IAP}{K_{sp}} \quad (1.3)$$

Within this work, we will also mention the **Saturation index (SI)** written as:

$$SI = \log_{10} S \quad (1.4)$$

- if $SI < 0$, the solution is undersaturated with respect to the given crystal and no crystal precipitates or if there is a crystal in solution it will dissolve.
- if $SI = 0$, the solution is at saturation, the crystal is at equilibrium with the solution.
- finally, if $SI > 0$, the solution is supersaturated with respect to the given crystal and a crystal may precipitate.

To supersaturate a solution with respect to a given crystal, one can increase the concentration of the aqueous species in solution by adding reagents or evaporating the solvent. On the other hand, because the solubility product is changing with temperature and pressure, varying these parameters might create a supersaturated solution. Supersaturation is an unstable state where more solute is dissolved in the aqueous solution than the equilibrium concentration of the solute in the solution. This unstable state remains as long as nucleation has not happened and may increase to a limit named supersaturation threshold where spontaneous nucleation happens in any case (Putnis and Fernandez-Diaz, 1990). This unstable state can be understood as a chemical potential held in a solution. In certain circumstances, this energy can be released as crystallisation stress when the solute precipitates in a pore, which can subsequently damage the surrounding skeleton.

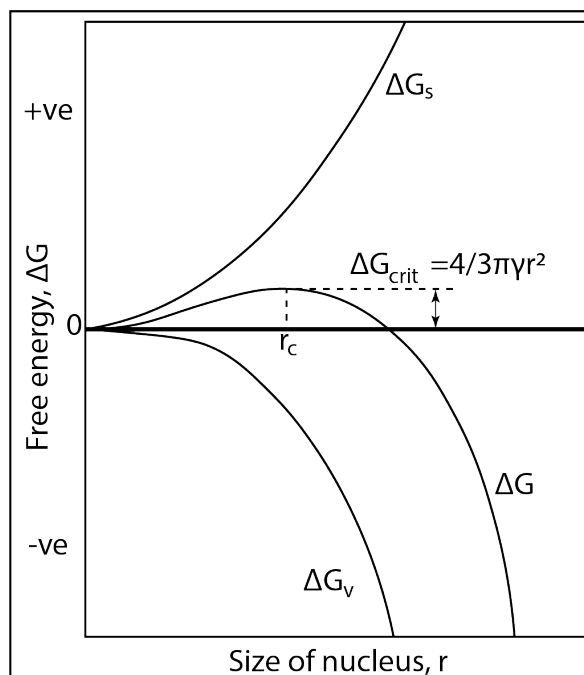


Figure 1.1: Free energy diagram explaining the existence of a critical nucleus. Figure and caption reproduced from (Mullin, 2001). ΔG is the excess free energy between a small solid particle of solute and the solute in solution and is equal to the sum of the surface excess free energy ΔG_s (positive quantity depending on the interfacial tension between the crystal and the supersaturated solution) and the volume excess free energy ΔG_v (negative quantity). ΔG_{crit} corresponds to the maximum of ΔG and gives the radius of the critical nucleus for a stable newly created crystalline lattice.

1.1.2 Crystal nucleation

In this subsection, we describe in detail the theoretical considerations on crystal nucleation in an aqueous solution. Nucleation defines the onset of crystallisation in a system that has become supersaturated. It determines the supersaturation threshold, which is the level of supersaturation at nucleation, and the nucleation rate. These concepts are of first importance because they constrain the potential level of [Crystallisation Pressure \(CP\)](#) exerted during aqueous species precipitation.

1.1.2.1 Basics on nucleation

To start crystallisation, nuclei or seeds will act as a center of crystallisation. Their existence can be spontaneous or induced artificially by external stimuli like agitation, mechanical shock, pressure increase, cavity collapse in under-cooled liquid, electric or magnetic fields, ultraviolet light, X-rays, sonic and ultrasonic irradiation (Mullin, 2001). One should distinguish primary nucleation when there is no seed preexisting in solution, and secondary nucleation, when there are crystals already precipitated. In the first case, homogeneous nucleation is used for spontaneous nucleation while heterogeneous nucleation applies for nucleation cases fostered by external causes (Mullin, 2001).

1.1.2.2 Homogeneous nucleation

The formation of a critical nucleus is a difficult process. The molecules have to coagulate, become oriented in a fixed lattice without the nuclei redissolving under the

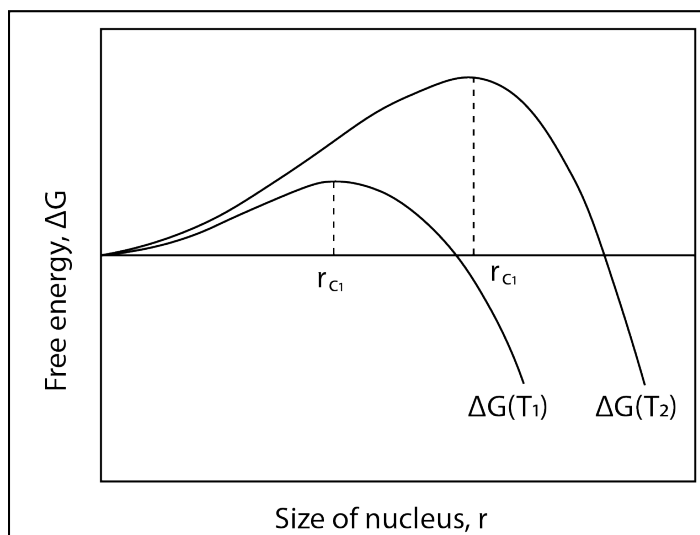


Figure 1.2: Effect of temperature on the size and free energy of formation of a critical nucleus ($T_1 < T_2$). Figure and caption reproduced from Mullin (2001).

conditions of supersaturation in solution. In Prieto (2014), in the frame of the **Classical Nucleation Theory (CNT)**, a time-dependent threshold predicts the first critical nucleus and the nucleation rate. An oversimplification assume that the interfacial tension between the solution and the crystal is the same for a macroscopic crystal and the smallest nucleus: this is the capillary assumption. Because the total bulk and surface energies of the nascent particle scale with the cube and the square of the radius of the nucleus respectively, the bulk energy begins to balance the energetic costs due to the generation of a phase interface at the so-called critical size. Smaller nuclei than the critical size are thermodynamically unstable and redissolve (figure 1.1) (Gebauer and Cölfen, 2011; Mullin, 2001). According to the thermodynamic approach of Gibbs given in Mullin (2001), as soon as a nucleus reaches its critical size, it reaches equilibrium energy. The size of a critical crystal depends on the temperature (figure 1.2), it appears that at a lower temperature, the critical radius will be smaller. The laws of probability predict that for every saturation higher than 1, a critical nucleus will agglomerate if sufficient time is given.

However, the **CNT** is criticized because there is no agreement on whether the critical nucleus size is dependant on the supersaturation (Gebauer et al., 2018). The capillary assumption which states the same interfacial tension for a large crystal and a nucleus is challenged as well because clusters of a few elements behave differently than bulk substances. Moreover, even if an improvement in **CNT** does consider the size dependence of interfacial tension, it would still focus on thermodynamic barriers and neglect additional kinetic factors like internal molecular rearrangement and de/hydration. In conclusion, the **CNT** prediction often leads to a difference by several orders of magnitude in estimating the nucleation duration compared to experimentally measured values, according to Gebauer et al. (2018).

The **Pre-nucleation Cluster (PNC)** pathway developed in Gebauer and Cölfen (2011) and Gebauer et al. (2014, 2018) brings a novel understanding of the nucleation pathways based on the onset of a prenucleation cluster.

The **PNC** are thermodynamically stable and precede the nucleation of stable crystal nuclei. Experimental proof of their existence has been reported for numerous chemical species like calcite, hydroxide (Gebauer and Cölfen, 2011; Gebauer et al., 2014), and

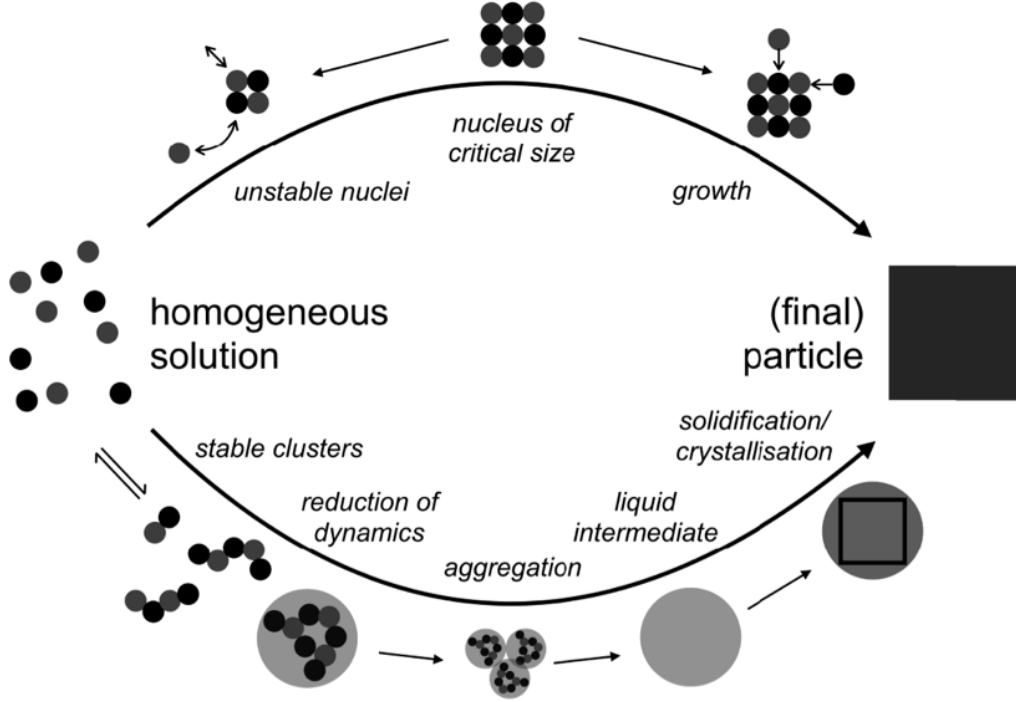


Figure 1.3: Schematic illustration of the mechanism of nucleation according to classical nucleation theory (CNT, top) and the pre-nucleation cluster (PNC) pathway (bottom). Figure and caption reproduced from Gebauer et al. (2018).

barite (Ruiz-Agudo et al., 2020). The first nucleation step is the agglomeration of molecules forming a prenucleation cluster that can be interpreted as a meso-crystal. A secondary nucleation step refers to the organization of this meso-crystal in a building block of the final crystal structure (figure 1.3).

1.1.2.3 Heterogeneous nucleation

The rate of nucleation is affected by the presence of impurities or already nucleated crystals in solution on which a crystal can seed. In the presence of a three-phase system, crystal-foreign solid-liquid, one should consider the interfacial tension between crystal-foreign solid (γ_{cs}), crystal – liquid (γ_{cl}), foreign solid-liquid (γ_{sl}). θ indicates the contact angle between the crystalline deposit and the foreign solid surface (figure 1.4) and γ_{sl} is expressed in equation 1.5 (Mullin, 2001).

$$\gamma_{sl} = \gamma_{cs} + \gamma_{cl} * \cos\theta \quad (1.5)$$

Volmer (1939) defined the factor ϕ in 1.6

$$\phi = \frac{(2 + \cos\theta) * (1 - \cos\theta)^2}{4} \quad (1.6)$$

Three cases are then distinguished:

1. $\theta = 180^\circ$, and $\phi = 1$: non-affinity between the crystal and the foreign solid. It is the case described in the section 1.1.2.2 for homogeneous nucleation of crystal. It applies to a bulk solution or poral solution in an inert porous medium.
2. $0 < \theta < 180^\circ$ and $\phi < 1$: partial affinity between the crystal and the foreign solid. This case applies to impurities in solution and favors an easier crystal nucleation.

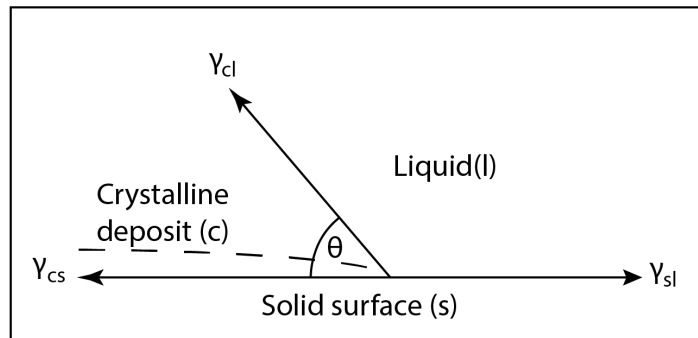


Figure 1.4: Interfacial tension at the boundary between the solid-crystal and liquid phases. Figure and caption reproduced from Mullin (2001).

In particular, it covers the case of a foreign solid at various rugosity: a crystal will preferably nucleate on its rough surface than its slick one.

3. $\theta = 0^\circ$ and $\phi = 0$: complete affinity between the crystal and the foreign solid. It is called secondary nucleation which describes the case of a supersaturated solution seeded with the crystal expected to precipitate. Shahidzadeh-Bonn et al. (2010) cite the case of thenardite (Na_2SO_4) rewetting and dissolving. The remaining thenardite crystals act like seeds for mirabilite ($Na_2SO_4 \cdot 10H_2O$) secondary nucleation.

1.1.2.4 Nucleation of hydrated crystals

Ostwald's rule of stages describes the behavior that an unstable system does not necessarily transform directly into the most stable state, but into another transient state whose formation from the original is accompanied by the smallest loss of energy. Ostwald's rule of stages can be applied to the phase transition between hydrated crystals. For example, when acting in the stability domain of mirabilite, precipitation of the metastable heptahydrate ($Na_2SO_4 \cdot 7H_2O$) might occur instead of direct mirabilite precipitation (Derluyn et al., 2011; Hamilton, Hall, and Pel, 2008; Rijniers et al., 2005).

1.1.3 Crystal growth/dissolution

In this section, crystal growth and dissolution are addressed. As pointed out by Naillon, Joseph, and Prat (2018), the growth kinetics of a crystal is a key factor in the generation of stress by salt crystallisation.

1.1.3.1 Crystal growth/dissolution kinetics

Gibbs-Volmer theory assesses that when ions arrive at the crystal face, they are not immediately adsorbed but they migrate by surface diffusion over the crystal lattice, regardless of the ions transport mode to the crystal face (Mullin, 2001). The surface diffusion happens in a thin layer, the diffusion zone, at the interface between bulk solution and crystal. Additionally, the growth of a dedicated face is proportional to its respective surface free energies, giving the equilibrium shape to the crystal. This leads to variations in crystal face growth rate and often to the disappearance of the smaller by the faster-growing face, called overlapping growth. The availability of ions to grow crystal faces can also lead to variations in the standard crystal habitus. Other factors affect the growth rate, like the presence of impurities adsorbed in the crystal

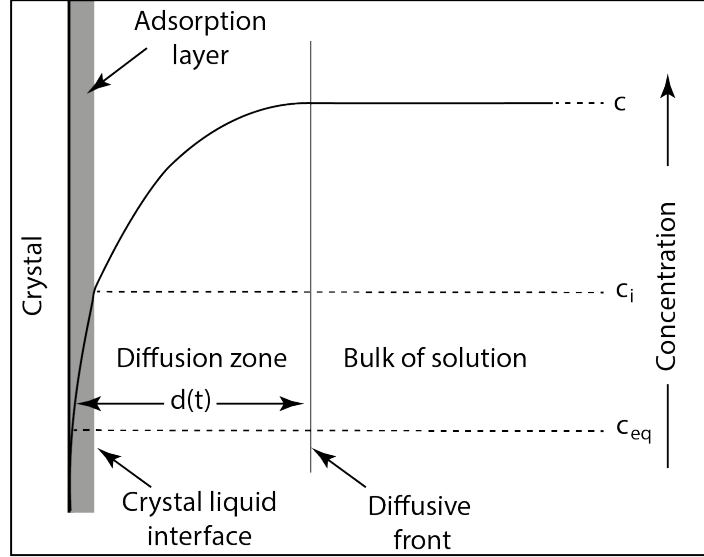


Figure 1.5: Model of crystal unit transport in crystal face based on Gibbs-Volmer theory. Caption and figure adapted from Mullin (2001).

lattice (Godinho and Stack, 2015; Mullin, 2001), the transport mode of the ions in the bulk to the diffusion zone and the variation of parameters like the pore pressure (Wiltshko and Morse, 2001), the temperature or the [Hydrogen Potential \(pH\)](#) of the solution (Ruiz-Agudo et al., 2015).

Derluyn (2012) quotes the growth rate $G_{r,cr}$ of a single crystal of radius r according to the saturation S , the temperature dependent growth rate parameter expressed with the Arrhenius law $K_{r,cr}$ and the exponent of the rate law g_{cr} :

$$G_{r,cr} = \frac{dr}{dt} = K_{r,cr} * (S - 1)^{g_{cr}} \quad (1.7)$$

The Arrhenius law is expressed with the growth rate constant $C_{r,cr}$, the Activation energy of the specific process E_a , the universal gas constant R , and the temperature T .

$$K_{r,cr} = C_{r,cr} * \exp \frac{-E_a}{R * T} \quad (1.8)$$

Conversely to the growth rate, the dissolution rate is expressed as $D_{r,cr} = \frac{dr}{dt} = K_{r,dis} * (1 - S)^{g_{dis}}$

1.1.4 Theoretical approach on crystallisation pressure

This section leans on equations developed in Steiger (2005a,b). The ideal case of pressure induced by crystallisation is induced by a crystal growing from a supersaturated solution under anisotropic stress in a cylindrical pore (figure 1.6). In between the crystal and the pore wall, there is an interstitial film of the solution. The interstitial film is fundamental because the pressure is building from the film. Espinosa-Marzal and Scherer (2010) explains that the formation of the thin liquid film between the growing crystal and the pore surface comes from the action of repulsive force. The origin of the force may be electrostatic interactions and structural forces like hydration forces. The van der Waals force at the salt-mineral interface is another explanation.

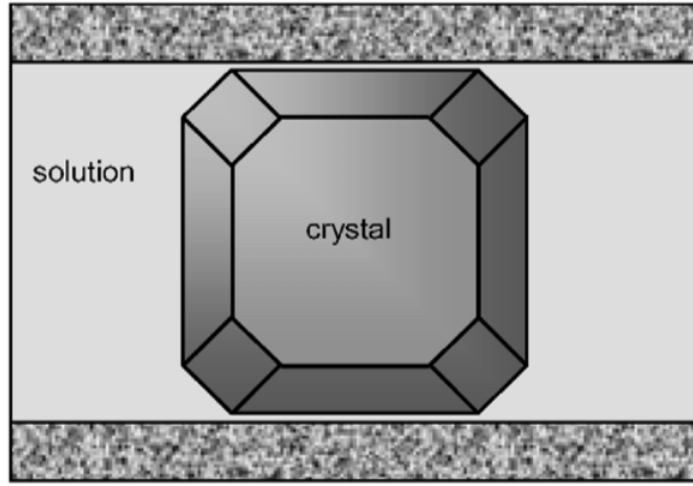


Figure 1.6: Illustration of a crystal confined between in a cylindrical pore; note that loaded surfaces of the crystal are in contact with the pore solution. Figure and caption reproduced from Steiger (2005a).

According to Gibbs, the expression of the chemical potential of the crystal dissolved in solution is written as Eq. 1.9.

$$\mu_l = \mu_{l0} + R * T * \ln(a) \quad (1.9)$$

with:

a , the activity of the ions in solution;

T , the temperature in Kelvin;

R , the gas constant;

μ_l , the chemical potential of the crystal dissolved in solution;

μ_{l0} , the chemical potential of the crystal dissolved in solution in the standard state.

In this case, the chemical potential of the unstressed face is equal to the chemical potential of the crystal in solution, Eq. 1.10.

$$\mu_p = \mu_0 + w + p * \bar{V}_m \quad (1.10)$$

with,

w , the molecular strain energy

\bar{V}_m , the molar volume of the crystal

μ_0 , the mean chemical potential of the crystal faces in the unstressed state.

The chemical potential of each face of the crystal under anisotropic stress may be calculated using:

$$p = p_c \text{ the pressure of the stressed face,}$$

$$p = p_l \text{ the pressure of the unstressed face.}$$

Considering the equilibrium in-between the crystal face and the solution in a pore, the chemical potential of the solute in solution should equal the chemical potential of the different faces of the crystal, Eq. 1.11.

$$\mu_{l0} + R * T * \ln(a) = \mu_0 + w + p * \bar{V}_m \quad (1.11)$$

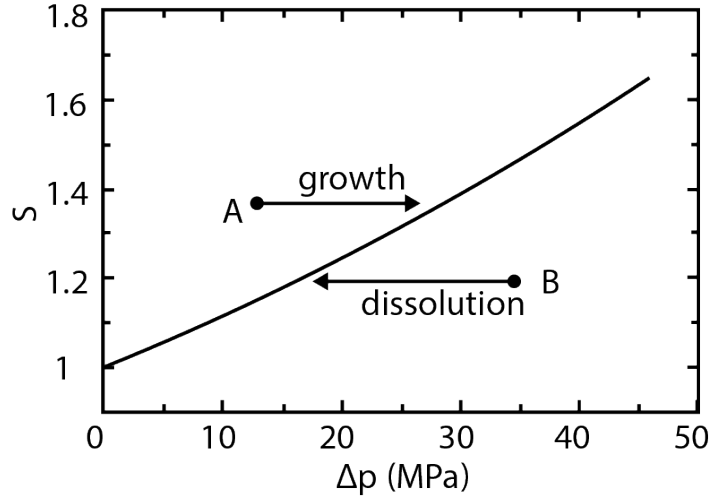


Figure 1.7: Solubility increase of a loaded surface of a NaCl crystal (\bar{V}_m 27.02 $cm^3.mol^{-2}$) at 298.15 K against pressure. Figure and caption reproduced from Steiger (2005a).

Logically, the solubility of the stressed faces is higher than the solubility of the unstressed faces. If the reference state is defined as an unstressed crystal face under hydrostatic pressure, p_l , with a_0 the activity of the unstressed crystal face, the stressed face expression of the solubility increase is expressed in 1.12

$$\ln\left(\frac{a}{a_0}\right) = \frac{(p_c - p_l) * \bar{V}_m + \Delta w}{R * T} \quad (1.12)$$

In the studied case, the molar volume difference of the reference state and the stressed state is minor. For a pressure difference of less than 100 MPa, the molar strain energy of a deformed crystal is also very low. In fact, the molar volume difference and the molar strain energy can be neglected and the expression of the pressure difference, Δp , is:

$$\Delta p = \frac{R * T}{\bar{V}_m} \ln\left(\frac{a}{a_0}\right) \quad (1.13)$$

In the end, the crystallisation pressure of a solute depends on the activity of the solute in solution, its molar volume and the temperature. When a crystal grows in a pore smaller than 100 nm, we shall add a term related to the crystal curvature (Espinosa-Marzal and Scherer, 2010).

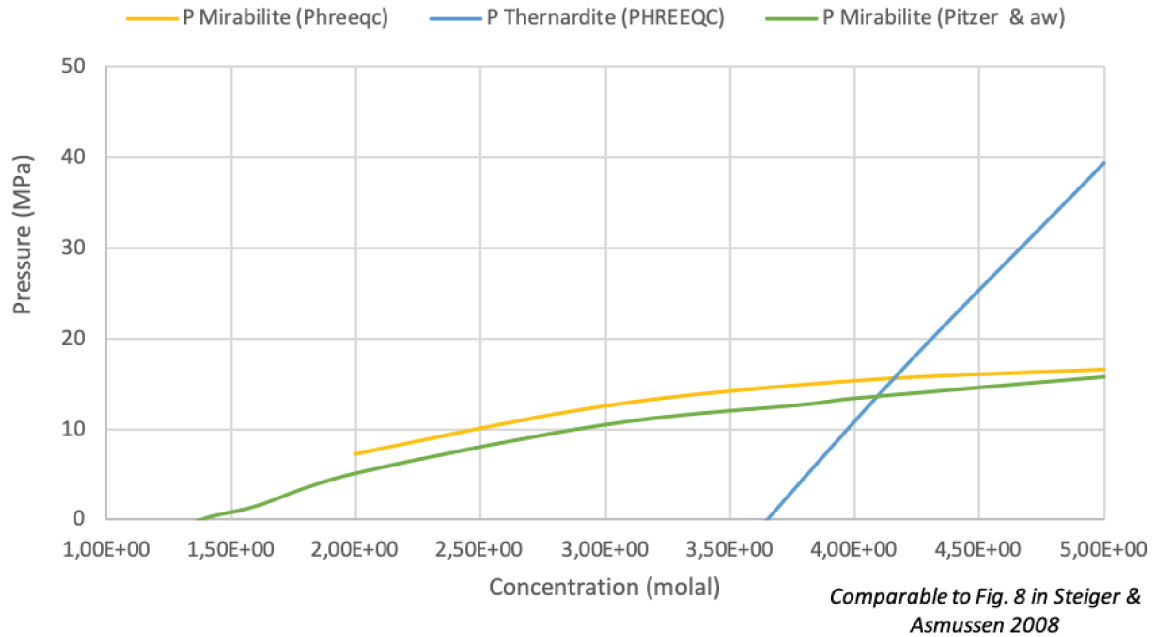


Figure 1.8: Sodium sulfate phase stability dependence at 20°C with respect to the pressure exerted on crystal faces comparable to Fig.8 in Steiger and Asmussen (2008). Our data are calculated with PhreeqC using database phreeqc.dat (Parkhurst and Appelo, 2013) and plotted with Microsoft Excel.

1.1.4.1 Pressure dependence of phase stability

Previously, the phase stability is not considered according to the hydrostatic pressure exerted by the solution on the crystal face and it sounds like every mineral species can reach an infinite crystallisation pressure if S tends to infinity. This is not the case at least for hydrated form according to Steiger (2005a) and Steiger and Asmussen (2008). They provide an example of the pressure dependence of sodium sulfate phases showing that if submitted to hydrostatic stress higher than 13.9 MPa, mirabilite would not precipitate. We reproduce the calculation with PhreeqC in figure 1.8, for sodium sulphate and found a limiting hydrostatic pressure at 13.7 MPa for mirabilite precipitating at 20°C.

1.1.4.2 Factors influencing the level of crystallisation pressure

1.1.4.2.1 Crystal growth kinetics

Crystal growth kinetic is a key factor because it determines the rate at which crystal growth will consume the ions and reduce the supersaturation before the crystal face reach the pore wall. If the crystal growth is low, the ions have time to diffuse through the thin film of the solution to feeding the growth of not confined walls which are still in disequilibrium with the solution. Then, the solution between the confined face and the wall is not building a sufficient crystallisation pressure to deform and damage the pore wall (Mullin, 2001; Naillon, Joseph, and Prat, 2018).

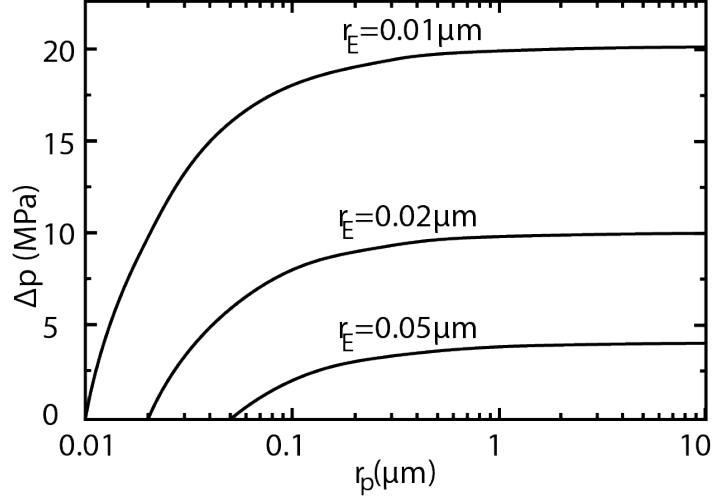


Figure 1.9: Crystallisation pressure of cubic *NaCl* crystal precipitating in a pore of radius r_p in equilibrium with a pore of radius r_E at 298.15 K. Figure and caption reproduced from Steiger (2005b).

1.1.4.2.2 Pore size and connectivity

In a porous medium with dual pore size distribution when the mean radius of the family of smaller pores is inferior to 100 nm, the crystal will precipitate in the larger pore (Putnis and Mauthe, 2001). Knowing this, the crystallisation pressure may be the result of an equilibrium situation where the growing unstressed faces present the same solubility increase as the stressed faces due to the curvature of the faces in a large spherical pore with a small cylindrical pore entrance. In that case, the growth of a crystal in the small pore entrance requires a larger supersaturation than the crystal in the large pore. In fact, the large crystal is under strengthened pressure (figure 1.9). The expression of the crystallisation pressure in this situation involved the difference between the free surface tension.

$$\ln \frac{a_E}{a_{\text{inf}}} = \gamma_{cl} * \frac{V_m}{R * T} * \frac{2}{r_E} \quad (1.14)$$

with, a_{inf} is the activity of the solute in solution with regards to the crystal of reference, a_E is the activity of the solute in solution in equilibrium with a spherical crystal of radius r_p ,

r_E is the radius of the tiny cylindrical pore entrance,

γ_{cl} is the free surface energy averaged on all crystal faces.

The pressure necessary to maintain the equilibrium between the spherical crystal of radius r_p and the solution whose solute activity is a_E , is calculated with the following expression of Everett written in Steiger (2005b):

$$\Delta P = \frac{R * T}{V_m} * \ln \frac{a_E}{a_{\text{inf}}} - \frac{2 * \gamma_{cl}}{r_p} \quad (1.15)$$

1.14 is introduced in 1.15

$$\Delta P = 2 * \gamma_{cl} * \left(\frac{1}{r_E} - \frac{1}{r_p} \right) \quad (1.16)$$

The expression of Everett given in equation 1.16, emphasizes the influence of the crystal size with the limit of pore entrance of a radius smaller than 100 nm (figure 1.9). The maximum value of crystallisation pressure is $\Delta P = 2 * \frac{\gamma_{cl}}{r_E}$.

1.1.4.2.3 Crystal molar volume

Crystallisation pressure is often observed during the hydration of an anhydrous mineral (Espinosa Marzal and Scherer, 2008; Keulen, Brok, and Spiers, 2001; Wolterbeek, Noort, and Spiers, 2018). Indeed the hydrated phase is less soluble in the condition of the experiment, $K_{sp\text{anhydrous}} > K_{sp\text{Hydrate}}$ and the supersaturation of the hydrated phase expresses as $S = \frac{K_{sp\text{anhydrous}}}{K_{sp\text{Hydrate}}}$ is higher than 1. Additionally, because the molar volume of a hydrate is often higher than an anhydrous phase, the phase transformation is accompanied by a volume increase: the study of the impact of volume change during precipitation of mirabilite in porous medium shows that the volume change can not explain the damage observed unless considering the crystallisation pressure exerted by the hydrated phase (Flatt, 2002). Another geological example is the serpentinization of ultramafic mantle rock that is known to be fostered by reaction induced cracking (Kelemen and Hirth, 2012; Lafay et al., 2018; Malvoisin, Brantut, and Kaczmarek, 2017). In other words, a consequence of the reaction is the fracturing of the reacting rocks. A substantial volume increase between the reactant and the product (Lafay et al., 2018) leads to desiccation like fracture out of the area of reaction (Xing et al., 2018; Zhu et al., 2016). Especially for the serpentinization reaction, the fluid flow is inhibited because the products precipitate in situ (Lafay et al., 2018) and then crystallisation is then supposed to crack the reacting rocks, increase the porosity and provide free volume for precipitation (Malvoisin, Brantut, and Kaczmarek, 2017).

1.1.4.2.4 Nucleation inhibitor

By acting on the nucleation of crystal, it is possible to reach a higher supersaturation. The succession of crystal precipitation and dissolution upon temperature cycling leads to a purification process and then a more homogeneous nucleation (Desarnaud and Shahidzadeh-Bonn, 2011; Espinosa Marzal and Scherer, 2008). Natural precipitation inhibitors like Al for quartz or Mg for calcite helps the solution to reach higher supersaturation. Naturally, the mineral species of clay rock adsorbed Al and Mg (Wiltshko and Morse, 2001), which may explain the abundance of fibrous veins in shales. An artificial inhibitor is sometimes used to maintain solid species like barite in solution (Prieto, Putnis, and Fernandez-Diaz, 1993) because barite is renowned to clog tubing of oil and gas installation (Collins, 2005). (Putnis, Prieto, and Fernandez-Diaz, 1995) showed that it can naturally reach very high supersaturation, which makes it also a good candidate for exerting crystallisation pressure in geological settings. It tells us as well that higher supersaturation will be attained by the least soluble chemical species like barite. Conversely, the number of ions in solution will be low even at high S .

1.1.4.2.5 Transport mode

Transport by advection is energetic and would lead to homogeneous nucleation. In porous rock, we can consider that the pore network limits the transport. Nonetheless higher supersaturation is obtained with homogeneous nucleation and the time taken to build the saturation is related to the level of supersaturation (Prieto, 2014). That is why, to obtain high supersaturation, the transport of chemical species is by diffusion as suggested in Elburg et al. (2002). Combined with a porous rock, the saturation has an extensive time to increase in the pore acting as small crystallisation chamber (Prieto, 2014).

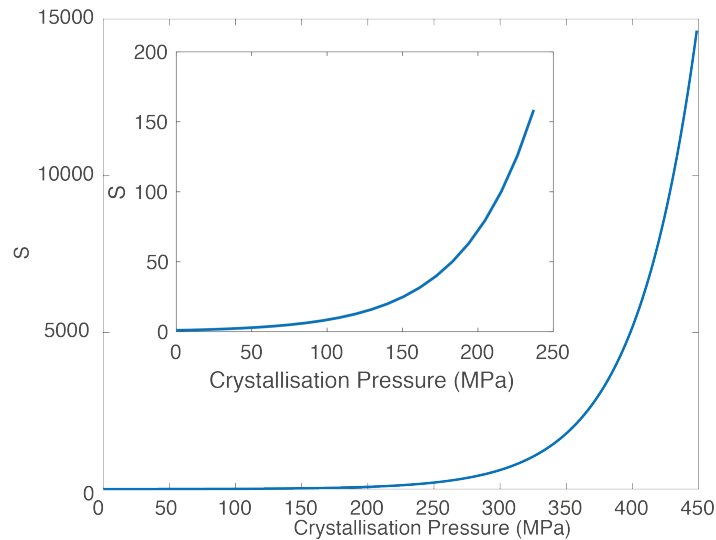


Figure 1.10: Crystallisation pressure at 293.15 K in function of aqueous solution supersaturation with respect to $BaSO_4$.

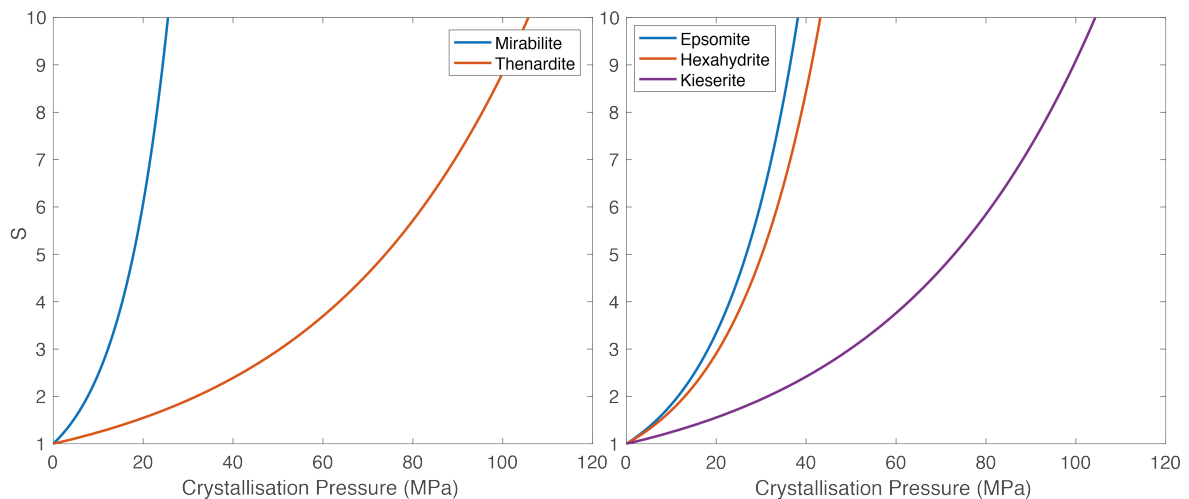


Figure 1.11: Crystallisation pressure at 293.15 K in function of aqueous solution supersaturation with respect to Na_2SO_4 and $MgSO_4$.

1.1.4.2.6 Studied aqueous species crystallisation pressure profiles

In this paragraph, we provide the value of crystallisation pressure as a function of the saturation, for barite (figure 1.10) and for sodium sulphate (figure 1.11). These estimations should be taken with precaution for the following reasons:

1. The function represented is a logarithm of an increasing S . Thus theoretically, the crystallisation pressure tends to infinite but in fact, the supersaturation will rarely exceed a few degree.
2. The second reason is that as soon as a critical nucleus will nucleate, the supersaturation will collapse.
3. The last reason is discussed previously when a chemical species has several hydrated phases, the higher hydrate will become less stable in increasing confining pressure.

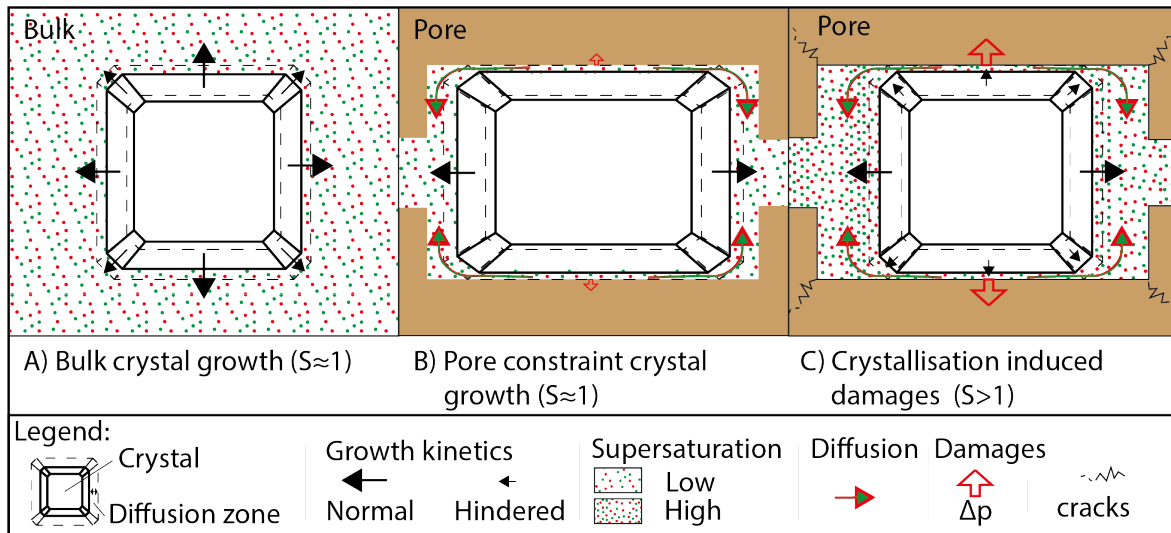


Figure 1.12: Summary diagram on crystallisation in porous medium A) Crystallisation in the bulk. The ions in the bulk solution diffuse in the diffusion zone and adsorbed on the crystal faces. In absence of confined crystal faces, the crystal faces grow at the same growth rate depending on the saturation. B) A crystal is confined in a cylindrical pore. The supersaturation in the thin supersaturated film between the confined crystal faces and the pore walls is too low to exert a crystallisation pressure sufficiently high to deform and damage the pore. Meanwhile, a concentration gradient exists between the thin film and the solution in the vicinity of the growing unconfined faces. Consequently, the ions are transported by diffusion to the unconfined crystal faces. C) A crystal is confined in a cylindrical pore. The saturation in the thin film is high enough to damages the pore by crystallisation pressure despite the diffusion of ions to the solution in the vicinity of the unconfined crystal faces induced by the concentration gradient between the growth hindered and confined crystal faces and the unconfined faces solution. After a while, if the supersaturation is not maintained by an external mean, the growth will consume the supersaturation.

In the literature, some values of supersaturation are experimentally measured: for barite, Putnis, Prieto, and Fernandez-Diaz (1995) measured a supersaturation threshold equal to 14632 that corresponds to a crystallisation pressure equal to approximately 450 MPa. Recently Ruiz-Agudo et al. (2020) measured the IAP at barite nucleation and the corresponding crystallisation pressure is 18.7 MPa. Finally, in Espinosa Marzal and Scherer (2008), a S close to 7 is measured below 0 °C for mirabilite with cooling cycle on a highly saturated solution of sodium sulfate. It corresponds to a crystallisation pressure equal to 21.6 MPa. Even if a potentially high supersaturation can be reached in a solution, crystallisation induced damage is rarely observed. Mirabilite is one of the least interesting minerals in terms of supersaturation threshold but is one of the most damaging salt on cultural heritage and in experimental work. On the contrary, no literature work reports damages induced by barite precipitation. Then the problem does not consist only in getting the highest supersaturation possible but also the retention of the supersaturation at a certain level. The volume change that is sometimes high in hydration reaction like thenardite to mirabilite intervenes in the crystallisation pressure because the limited volume available to precipitate the hydrate crystal phase from the a least hydrate crystal phase is not augmented and prevent the precipitation of the hydrate crystal phase. Consequently the saturation of the solution with respect to mirabilite will increase and augments the crystallisation pressure. On the contrary, the molar volume of thenardite is lower than mirabilite. Then for a

same supersaturation, the crystallisation pressure produced in the interstitial film at the interface between the pore wall and the crystal will be higher with thenardite than mirabilite. Figure 1.12 recaps with our own interpretation of the issue of crystallisation pressure in a pore. It points to the need to combine several conditions (chemical species transport, crystal growth rate, supersaturation level, etc) in order to maintain a sufficient supersaturation in the vicinity of the crystallising mineral and induce damage by crystallisation.

1.2 Experimental examples of crystallisation induced damage on porous rock

Salt crystallisation induced damages by the mean of crystallisation pressure exerted in the thin liquid film between the salt crystal and the pore wall. Numerous experiments regarding salt crystallisation induced damages on rock sample are described in the literature and are a source of inspiration.

1.2.1 Damages induced by precipitation of a fibrous salt front

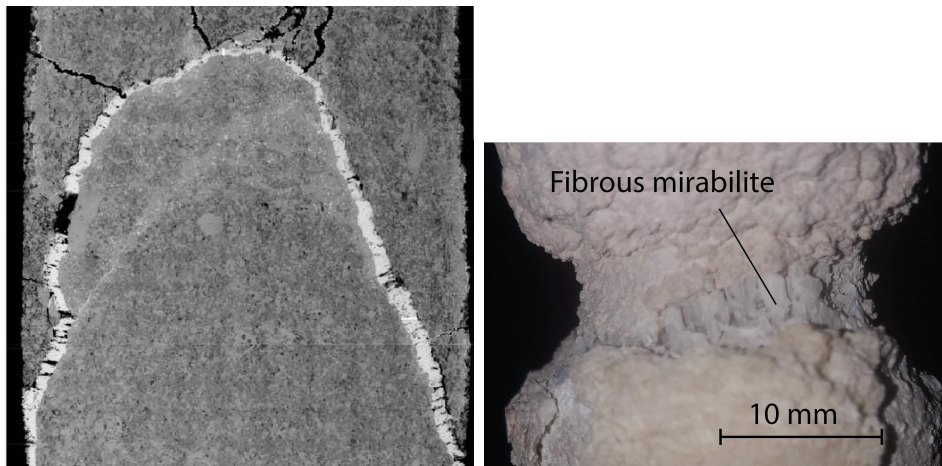


Figure 1.13: Left: Frontal cross-section made of an assemblage of 200 SEM images depicting a Lavoux limestone sample damaged by a fibrous halite vein after 80 days of a sodium chloride rich solution capillary uptake, pictures and caption adapted from Noiriél et al. (2010). Right: Fibrous mirabilite front precipitated in a Tervoux limestone sample cylinder at an height of ~ 30 mm after 3 days. A hot sodium sulphate rich solution (28.5% (W/W) at 32°C) uptakes from the bottom and by capillarity in a sample placed in a covered plastic dish containing the solution maintained at constant temperature.

Several authors obtained a well-defined salt precipitating front through a porous medium, with a free salty solution imbibition (Espinosa-Marzal and Scherer, 2010; Flatt et al., 2014; Noiriél et al., 2010; Scherer, 2004; Steiger, Kiekbusch, and Nicolai, 2008). They found that the salt precipitated at a certain level in the rock depending on the humidity, the temperature, the concentration of the original brine and the type of salt. In particular, Noiriél et al. (2010) observed, after several weeks, well-defined cracks filled with fibrous halite, NaCl . Atop the front, the surrounding porous rock was damaged and tensile vertical cracks branched on the halite front. Conversely, below the front, no damages were reported, only some efflorescence on the sample surface occurred (figure 1.13, left).

A similar capillary uptake experiment in a Tervoux limestone with a warm solution rich in sodium sulphate (28.5 % (W/W) at 32°C) results after 3 days in fibrous mirabilite veins precipitation (figure 1.13, right).

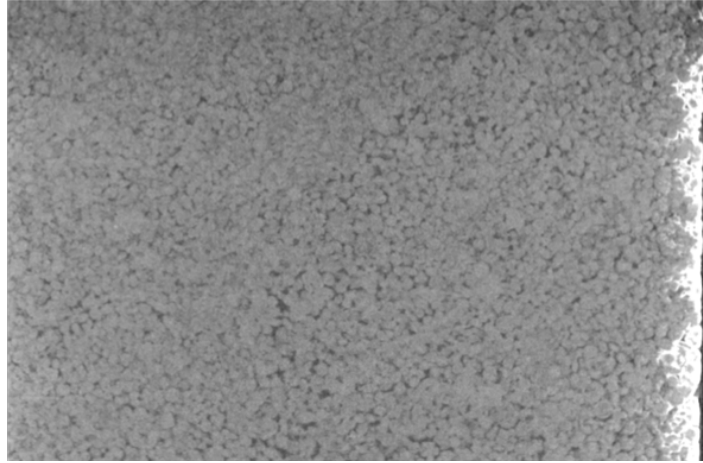


Figure 1.14: Vertical cross section of X-ray tomographic datasets at $9.92\mu m$ resolution. One cycle of imbibition – drying with $BaCl_2$ solution on a Lavoux limestone. The whitish mineral on the right is the subflorescent barium chloride. (1 cm wide)

1.2.2 Damages induced by rewetting thenardite impregnated porous rock

Another experiment consists of impregnating a sample by cycles of imbibition - drying with an aqueous solution highly concentrated with respect to a specific salt. The salt has several stable hydrated phases like Na_2SO_4 or $MgSO_4$ (Caruso, Wangler, and Flatt, 2018; Espinosa-Marzal et al., 2011). At the end of the preparation, the sample is dried to precipitate the least hydrated phase without noticeable damages on the sample. As we can see in figure 1.14, after one cycle, the salt naturally precipitates during drying as efflorescence on the surface or as subflorescence just below the surface. This explains peeling often observed on cultural heritage. With the multiplication of salt impregnation cycles, the sample contains more salt precipitated at the heart of the rock sample. The salt impregnated sample is finally immersed in pure water and the least hydrated form dissolves and recrystallizes in a higher hydrated form. Crystallisation of the hydrated phase induces important damages in the sample in only a few hours (figure 1.15, top). We reproduce this experimental protocol with a Lavoux limestone impregnated multiple times with a sodium sulphate rich solution (28.5 % (W/W) (figure 1.15, bottom).

1.2.3 Temperature cycling provoking mirabilite crystallisation induced damage

The solubilities of chemical species like salts vary with temperature. Espinosa Marzal and Scherer (2008) published an experimental protocol where a porous rock is imbibed with a hot solution supersaturated with respect to mirabilite at ambient temperature. The saturated sample is submitted to cooling-heating cycles between $-10^\circ C$ and $50^\circ C$ to crystallize and dissolve mirabilite. It resulted in dilatation and heat of crystallisation attributed to mirabilite crystallisation in the porous rock.

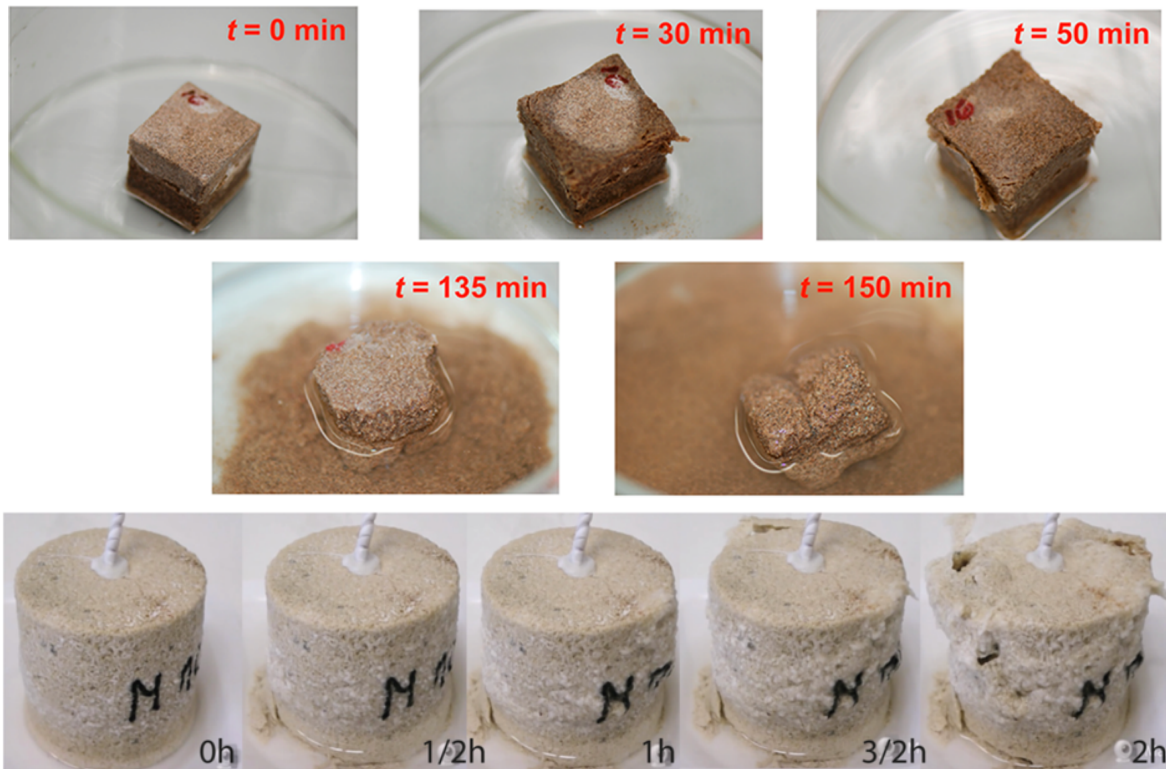


Figure 1.15: Experimental re-wetting of a porous rock impregnated with a fraction of thenardite according to the protocol described in Caruso, Wangler, and Flatt (2018). Top, dramatic effect over time of a 20% (W/W) solution of sodium sulfate entering into a sandstone cube previously impregnated with thenardite. (sample is a $3 \times 3 \times 3 \text{ cm}^3$ cube) Pictures and caption reproduced from Caruso, Wangler, and Flatt (2018). Bottom, time lapse between 0 and 2 hours of re-wetting in pure water of a Lavoux limestone cylinder impregnated with thenardite at 20°C . (sample is a $2.5 \times 2.5 \times 2.5 \text{ cm}^3$ cylinder)

1.3 Geological veins and objects related to crystallisation pressure

Veins define the cemented fractures examined on the outcrop to unravel the deformation, the diagenetic and metamorphic history of their host rock. They are paleostrain indicators via the orientation and disposition of the fracture plane. They also give the paleo-conditions of crystallisation and the origin of the fluid precipitated via their mineral composition and the trapped fluid and gaseous inclusion (Bons and Montenari, 2005). Among the veins, the fibrous veins raised concern among structural geologists on their conditions of formation because they exhibit a fibrous habitus that may not be interpreted solely by the crack-seal mechanism (Hilgers and Urai, 2005; Wiltschko and Morse, 2001). Other authors use the crystallisation pressure to explain the formation of asbestiform veins (Kelemen and Hirth, 2012; Malvoisin, Brantut, and Kaczmarek, 2017; Taber, 1916), fibrous antitaxial veins (Bons, Elburg, and Gomez-Rivas, 2012; Elburg et al., 2002; Hilgers and Urai, 2005; Ukar et al., 2017), diagenetic replacement in sedimentary rocks (Maliva and Siever, 1988b), self organized zebra texture (Merino, Canals, and Fletcher, 2006; Wallace and Hood, 2018) and the travertine lifting horizontal calcite veins (Gratier et al., 2012). To illustrate their point of view, we will review some of the most marking occurrences of crystallisation pressure-related objects in geological settings.

1.3.1 Fibrous veins

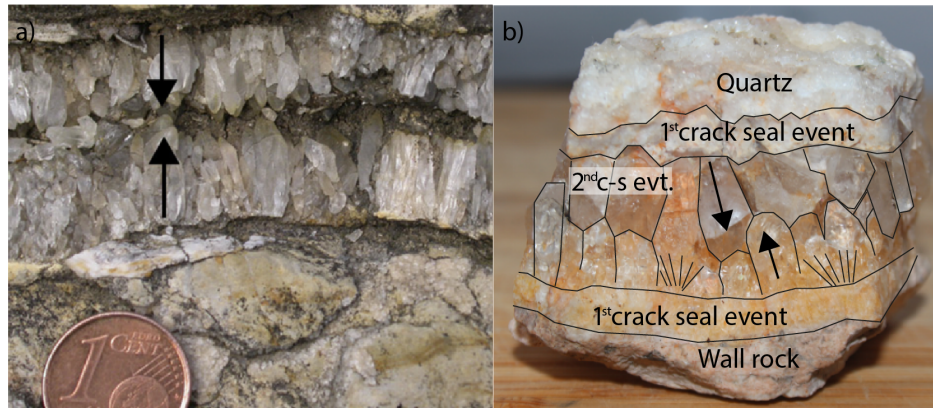


Figure 1.16: a) Syntaxial calcite vein, where crystals grow from the wall rock into the vein (Biure, Spain). Picture and caption reproduced from Bons, Elburg, and Gomez-Rivas (2012). b) Picture of a syntaxial quartz vein in pink quartzite. (30x30x30 mm). Unknown origin, personal collection.

1.3.1.1 Type and occurrences of fibrous veins

Fibrous veins refer to fibrous minerals precipitated with the fiber oriented perpendicular to the fracture wall (Cobbold et al., 2013). In the fibrous veins one can distinguish, the syntaxial veins (figure 1.16) the antitaxial veins (figure 1.18) and the stretching veins by comparing the fibers growth mechanism and growth direction. Fibrous veins are encountered worldwide in sedimentary basins. Cobbold et al. (2013) published a catalog of bedding parallel fibrous veins occurrence. It appears that the most common host rock for calcite fibrous veins are organic-rich shale, mudstone and claystone. Some gypsum beef precipitated as well in mud rich rock but are mostly found in evaporitic formations and lacustrine deposit (Hilgers and Urai, 2005). Ore deposits contain quartz bedding parallel fibrous veins along with other minerals like sulfides (Wallace and Hood, 2018). Note that barite fibrous veins are found in marine shale (Cobbold et al., 2013).

1.3.1.2 Distinction between antitaxial, syntaxial and stretched fibrous veins

The supposed growth mechanism for stretched and syntaxial veins is the filling of an open space fractured by over-pressurized fluid in the so-called crack-sealing mechanism (Bons, Elburg, and Gomez-Rivas, 2012; Cobbold et al., 2013; Mourgues, 2004; Ramsay, 1980; Zanella, Cobbold, and Boassen, 2015).

The syntaxial veins will grow from both sides of the wall inwards the fracture or from one side to the other with strong growth competition between the crystals. The gap created by over-pressurized fluids is filled by the extension of the existing crystal. The distinction between syntaxial and stretched veins lay on the position of the crack surface: in the syntaxial vein, the crack surface lays in the growth front where the growing crystal converge, whereas, in stretched veins, the crack surface can cut through precipitated material and even the wall rock. Disks of the same materials fill the gap by epitaxial growth.

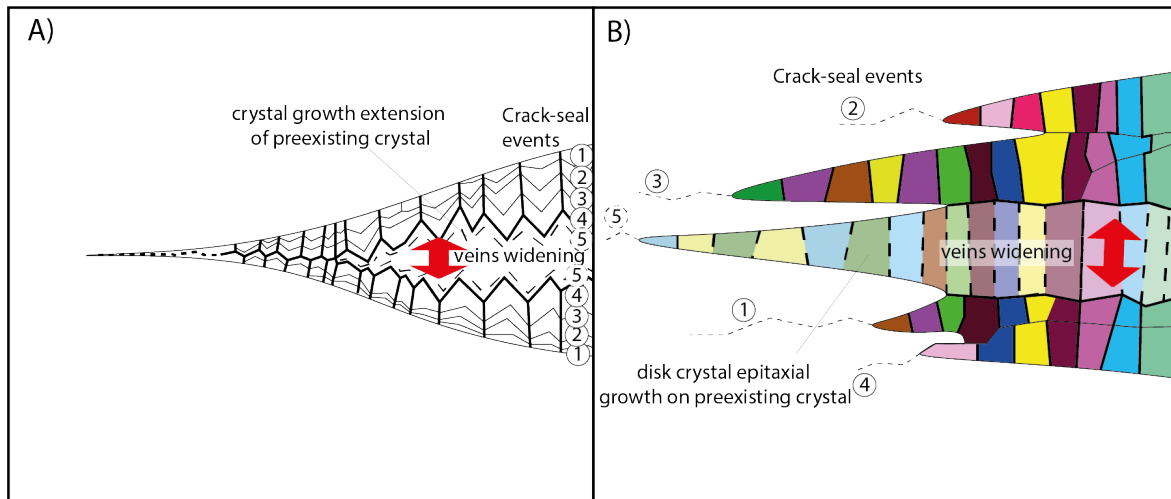


Figure 1.17: Basic scheme of 'fibrous' veins formed after crack-seal events inspired by Bons, Elburg, and Gomez-Rivas (2012) : A) syntaxial veins B) stretched veins. At each crack-seal event provoked by drop on the effective pressure, crystals seeds on the preexisting crystal and fill the gap.

The repetition of the crack sealing mechanism elongates the stretched grains and gives the fibrous aspect. Even if visually the syntaxial and stretched veins appear fibrous, micrograph observations assess the non-continuity in the precipitated crystals (figure 1.17).

Contrary to the syntaxial veins that grow from one growth surface, antitaxial veins grow from two outer surfaces at the same time in the direction of a median zone. Curiously, the median zone contains small blocky minerals (Bons, Elburg, and Gomez-Rivas, 2012). The veins width is millimetric to pluri-centimetric and they spread out up to tens of square meters (Cobbold et al., 2013; Ukar et al., 2017; Zanella, Cobbold, and Boassen, 2015). Crystals in the veins are real thin fibrous crystal while the precipitated mineral, often calcite or quartz, does not exhibit such habitus in bulk solution. The crystal fibers keep the width of the seed crystal on which they branch (Bons, Elburg, and Gomez-Rivas, 2012) and the growing competition between the fibers growing in the same direction is absent or only minor. Bons, Elburg, and Gomez-Rivas (2012) and Elburg et al. (2002) report stylolites in the vicinity of fibrous antitaxial veins that are probably the dissolved source of nutrients for the fibrous veins.

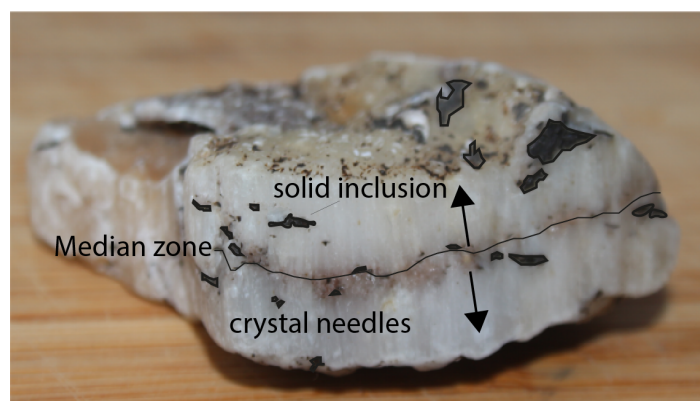


Figure 1.18: Antitaxial calcite fibrous vein with black shale solid inclusion 50x50x10 mm. Unknown origin, personal collection.

1.3.1.3 Model for antitaxial vein formation

Besides the crack-sealing mechanism to explain the formation of antitaxial veins (Zanella, Cobbold, and Boassen, 2015), an alternative scenario involving crystallisation pressure has been brought up to date in the early 2000s by Bons and Jessell (1997) and Wiltschko and Morse (2001) after the early assumptions of Taber (1916) one century before. The proposed models are discussed below:

1. Rejected crack – seal model: Antitaxial vein form by crack-sealing as asserted by Cobbold et al. (2013), Cox and Etheridge (1983), Ramsay (1980), and Zanella, Cobbold, and Boassen (2015). It implies crack-seal cycling to form fibrous veins. The problem with such a scenario is that it could not justify the presence of two growth surfaces, the continuity of the crystal fibers and the disposal of solid inclusions band (Hilgers and Urai, 2005).

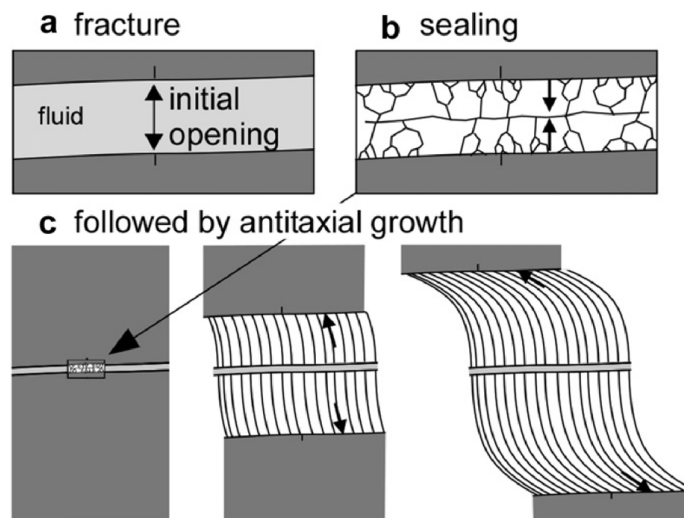


Figure 1.19: Stages in the formation of an antitaxial vein a) Fracturing by over-pressurized fluid b) blocky mineral precipitation in the void c) seeding on the blocky minerals and continuous growth of crystal fibers outward the median zone from a supersaturated solution provided by diffusion through the host rock to the fracture wall. Figure and caption reproduced from Bons, Elburg, and Gomez-Rivas (2012).

2. Proposed seal-crack model: Since Taber (1916) and numerous recent studies (Desarnaud, Bonn, and Shahidzadeh, 2016; Means and Li, 2001; Noiriél et al., 2010), we know that crystallisation can induced stress and is often growing with a fibrous habitus. Therefore, crystallisation pressure was proposed as a cracking mechanism because it explains the continuous vein opening (Bons and Jessell, 1997; Hilgers and Urai, 2005; Wiltschko and Morse, 2001). The stress is induced at the interface between the crystal tip and the vein wall where the fibers grow from a thin film of the supersaturated solution. Moreover, another element consolidates the model described above: it is reported that fibrous antitaxial veins grow in a large majority in shall host rock where the pores are nanoporous (Cobbold et al., 2013; Yuan and Rezaee, 2019). Thus high supersaturation level may be maintained in the host rock (Putnis and Mauthe, 2001). It is the situation described in the Everett model (Scherer, 1999; Steiger, 2005b) stating that high crystallisation pressure will be exerted by a crystal growing in large pores connected to a nanoporous host rock filled with a solution supersaturated with respect to the

precipitating mineral (Scherer, 1999; Steiger, 2005b). About the origin of the solution supersaturation, Elburg et al. (2002) assumes that dissolved materials in the stylolites are transported by diffusion through the porous host rock to the growing surface. To us, The fibrous habitus of the crystal is linked to the growth in an unique direction at the interface with fracture wall and the crystal fiber tip.

3. Proposed mix model: we mention that the median zone of an antitaxial vein is filled with blocky minerals. It indicates that the first episode of an antitaxial vein formation is induced by the crack-seal mechanism (Bons, Elburg, and Gomez-Rivas, 2012). It creates the room for precipitating the blocky median zone on which will seed the fibrous crystals (figure 1.19). In addition, high pore fluid pressure lower the effective pressure ($P_{effective} = P_{totalconfinement} - P_{pore}$) applied on the saturated porous host rock. According to the Terzaghi principle, it also lowers the crystallisation pressure necessary to outreach the failure envelope of the host rock (Bons, Elburg, and Gomez-Rivas, 2012).

1.3.2 Zebra structure

1.3.2.1 Description

Zebra textures are late diagenetic features precipitated within carbonate rock. They are commonly found in association with carbonated hosted ore deposit of economic significance and hydrothermal dolomite reservoir (Wallace and Hood, 2018). Zebra textures are rock fabric that consists of alternating light and dark band within sedimentary strata most of the time a host dolostone (figure 1.20). The banded structures are genetically-related. The main attributes are the alternation of light and dark band of an equal thickness generally at a millimeter scale. The bands are parallel or slightly inclined to the bedding plane. Finally, they are associated with diagenetic minerals that have replaced the host rock, dolomite or ore deposit (Merino, Canals, and Fletcher, 2006; Wallace and Hood, 2018). Open space is also common within the band and zebra texture is sometimes associated with evaporite deposits like the Cadjebut lead-zinc deposit in Australia, which is an ore deposit with zebra texture laterally equivalent to an adjacent bedded evaporite according to Wallace and Hood (2018).

1.3.2.2 Hypothesis for Zebra texture formation

1.3.2.2.1 Structural process

Tension gashes, parallel vein system and en-echelon vein array are structurally controlled features and resemble zebra texture. But the main characteristics of structural veins do not fit with the rhythmicity, the millimeter scale and the lateral continuity of zebra texture (Merino, Canals, and Fletcher, 2006; Wallace and Hood, 2018). It is admitted that the dark bands of zebra texture are caused by mineral replacement (Maliva and Siever, 1988a) and that the light band is a cement fill cavity. Consequently, a formation process involving crystallisation pressure is proposed to form zebra textures in Merino, Canals, and Fletcher (2006) and Wallace and Hood (2018).

1.3.2.2.2 Chemo-mechanical process

In zebra texture like in some breccia texture, stylolites are found in and out of the zebra pattern alongside small faults. The stylolites occur in-between the veins

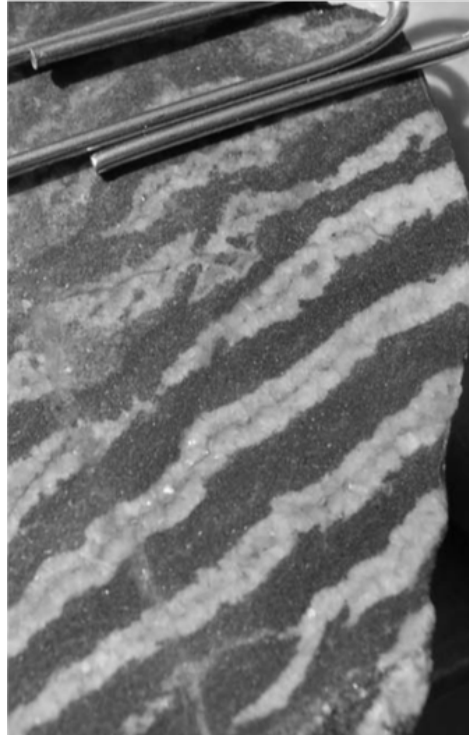


Figure 1.20: White bilateral dolomite veins in black host dolostone. (Spain) Image and caption reproduced from Merino, Canals, and Fletcher (2006). (3 x 5 cm²)

assessing that stress high enough to dissolve the host rock happened. The transform faults displace the host rock without going beyond the margins of the vein, proving that the stress happens locally (Merino, Canals, and Fletcher, 2006). Then in his model Merino, Canals, and Fletcher (2006), explains the zebra texture and simultaneously the stylolitisation of the host rock as the consequence of displacive stress induced by the vein growth. The direction of principal stresses may lead to the formation of breccia instead of zebra texture. If the principal stress direction is poorly defined, the original dolostone can rather develop into randomly oriented veins, nucleating and intersecting to create a breccia texture, instead of a zebra texture with veins growing normally perpendicularly to the least compressive stress (Merino, Canals, and Fletcher, 2006). However, this hypothesis has been overturned since many breccias are finally attributed to sedimentary processes followed by chemical replacement.

1.3.2.2.3 Compaction wave as the origin of the rhythmicity in zebra

Recently, a generic model based on a compaction band coupled with a reaction-diffusion model predicts the periodicity between stylolites and displacive veins (Kelka et al., 2017). This theoretical model catches up with the crack seal model. Our interpretation for the zebra formation issue is 1) localization of the veins where the fluid pore pressure peaks (low effective pressure), 2) stylolitisation where the fluid pore pressure is the lowest (high effective pressure) and 3) vein growth related to crystallisation pressure favored by the low effective pressure and feed by the nutrients coming from the stylolites. With this interpretation, crystallisation pressure is combined with the effective pressure and helps to locate structural discontinuities like veins or even faults for en-echelon veins.



Figure 1.21: Idiomorphic crystal of dolomite replaces botrioidal sphalerite at Galmoy, Ireland. The dolomite is idiomorphic in spite of the fact it did not grow in a void, as it preserves the morphology of the replaced sphalerite layers. Image and caption reproduced from Merino, Canals, and Fletcher (2006).

1.3.3 Diagenetic replacement

1.3.3.1 Description

Frequently observe in dolomitized rock chert or silicified fossils (Maliva and Siever, 1988a; Tada, Maliva, and Siever, 1987), the diagenetic replacement consists in the dissolution of the host phase replaced by an authigenic mineral preserving the morphology (figure 1.21). A graphic example of diagenetic replacement is the silicification of fossils in limestone as the calcite original fossil is silicified without losing the original fossil shape. From a petrographic examination of chertification thin sections (a type of silicification of limestone), Maliva and Siever (1988a) pointed that every mineral is replaced no matter if the grain is more or less stable. They report the presence of ghosts of host microstructure in the authigenic mineral and euhedral authigenic crystal face in planar contact with unreplaced host crystal.

1.3.3.2 Role of pressure solution

The process of mineral replacement involved two conditions for the replacement of the host phase by another: the host phase dissolving surface is soluble in the poral solution and the authigenic phase is supersaturated relatively to the poral solution. From textural evidence, Maliva and Siever (1988a) argues for a diagenetic replacement triggered by pressure solution in the thin film of solution between the authigenic and host minerals. In this case, the pressure exerted in the supersaturated solution does not crack the surrounding host rock but it increases the solubility of the host phase and dissolves it.

Metasomatism (atoms replacement in the lattice of the crystal with preservation of the crystal lattice) may also explained such object. We should mention for example the work of (Putnis and Putnis, 2007) that proves experimentally that the morphology and the crystallographic information can be transfer during an interface coupled dissolution - reprecipitation mechanism by epitaxial growth: the authigenic phase nucleate on the host phase and take the crystallographic parameter of the substrate.

1.3.4 Asbestiform veins

The first tectonics veins that were related to crystallisation pressure are the asbestiform veins. This term refers to the fibrous veins of the monoclinic amphiboles, the serpentinites, that occasionally reach 100 feet in the chrysotile deposits of southern Quebec, Canada (Taber, 1916). More recently, from field observation, experimental and theoretical work, crystallisation pressure was put in the spotlight to explain the reactive surface generation during serpentinization reaction (Hirth and Guillot, 2013; Iyer et al., 2008; Jamtveit, Putnis, and Malthe-Sørensen, 2009; Kelemen et al., 2018; Lafay et al., 2018; Malvoisin, Brantut, and Kaczmarek, 2017; Rudge, Kelemen, and Spiegelman, 2010).

1.3.4.1 Geological context

Serpentinites are found in two main domains, the old orogenic belt and the surface of the oceanic lithosphere where they result in the hydration of exhumed mantle peridotites. The exhumed mantle peridotite are termed ophiolite. the ophiolite log is constituted from top to bottom by basaltic pillows lavas, basaltic dikes, the gabbroic complex and finally the ultrabasic complex made of peridotite rock (hazburgite, lherzolite and dunite¹). The ophiolitic massif in orogenic belts may originate from subduction. The ophiolites are overheated because they are aggregated in the accretionary wedge during the subduction and uplifted at a later stage of the orogenesis. For example, in the Pyrenees, the Lherzolite and hazburgite massif originated with smaller bodies and lenses exhumed during the hyper-stretching of the passive margin. As the passive margin inverted, the lenses were aggregated to the accretionary wedge and dragged by inverse faulting (Corre et al., 2016; Jourdon et al., 2019). The convergence of two oceanic plates may also result in the obduction of the serpentinized oceanic lithosphere, like the Oman ophiolite (Guillot et al., 2015; Vacquand et al., 2018). serpentinization happens down to 7 km in oceanic crust, on ocean ridge hydrothermal field and potentially during subduction at the base of the mantle wedge according to seismic velocities in that location (Evans, Hattori, and Baronnet, 2013). The occurrence of H_2 and or CH_4 rich seeps expelled from ophiolite bodies like in Oman, New Caledonia (Vacquand et al., 2018), the Olympos mountain in Turkey (Hosgörmez, 2007) and maybe the first native H_2 field in production in Bourakébougou (Mali) (Prinzhofer, Tahara Cissé, and Diallo, 2018) are very interesting for potential economic native H_2 recovery e.g. (Gaucher, 2020).

1.3.4.2 Description

Macroscopically, the serpentinized mafic rock has a hierarchical fracture pattern (figure 1.22), induced by the volume change associated with the serpentinization of the original rock (Kelemen and Hirth, 2012; Malvoisin, Brantut, and Kaczmarek, 2017; Plümper et al., 2012). The fracture pattern has a polygonal shape and T-junction marking the fracture stopping at a right angle of the pre-existing pattern. Petrographic observation of millimetric hydrated olivine revealed that the crystals are fragmented by microcracks even at a low reaction rate. The grains are penetrated by dissolution wormhole alternatively named etch pits (Plümper et al., 2012) (figure 1.23). From these etch pits, microcracks extend and divide the domain and new etch pits are dug in the olivine. Serpentine is found precipitated in the microcracks. The process terms into a

¹source: <https://planet-terre.ens-lyon.fr/article/diversite-des-ophiolites.xml>

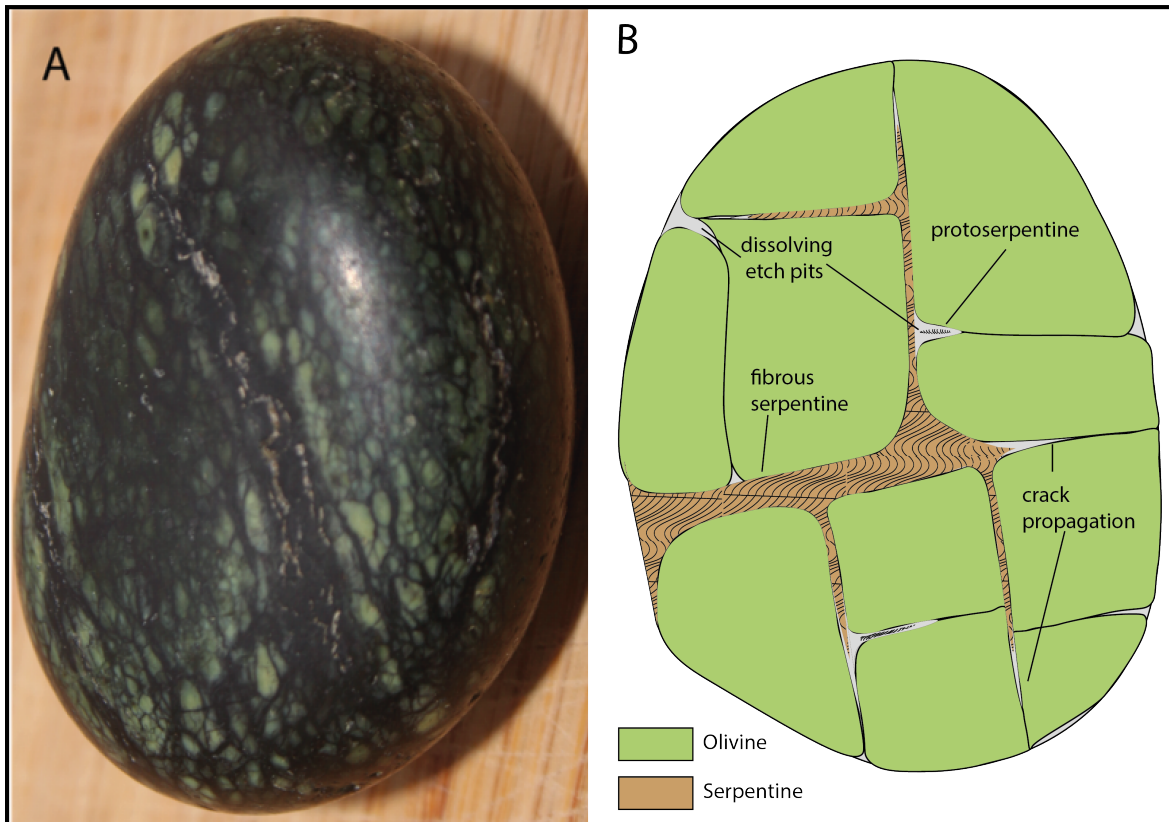


Figure 1.22: A) Hierarchical fracture pattern on serpentinized mafic rock pebble 50x30 mm. Unknown location, personal collection. B) Scheme revealing the relation between fibrous serpentine precipitated in dissolved etch pits and cracks propagation.

hierarchical fracturing (Kelemen and Hirth, 2012; Malvoisin, Brantut, and Kaczmarek, 2017; Plümper et al., 2012).

1.3.4.3 Reactive surface generation

We have seen in the previous paragraph that hierarchical fracturing is visible at macroscopic and microscopic scale adding more material susceptible to react in contact with water. According to Malvoisin, Brantut, and Kaczmarek (2017), dissolution and precipitation are fast compared to the ions transport. The risk to clog the fractures acting as the fluid pipe is high due to the volume increase. However, a residual porosity is measured in serpentinized rock. Several hypotheses exposed by Malvoisin, Brantut, and Kaczmarek (2017) try to explain the hierarchical fracturing at the grain scale: (1) thermal cracking during fast tectonic exhumation (2) preferential dissolution (figure 1.23) and (3) crystallisation induced damage. The first hypothesis is rejected since cracking happens during experimentation at the temperature and pressure of the reaction in a geological context. The second option is preferred by Peuble et al. (2018) and by Dr. Ph. Gouze (personal communication). It perhaps involved the phenomenon of subcritical crack growth in a rock under its failure stress (Olson, Laubach, and Lander, 2007).

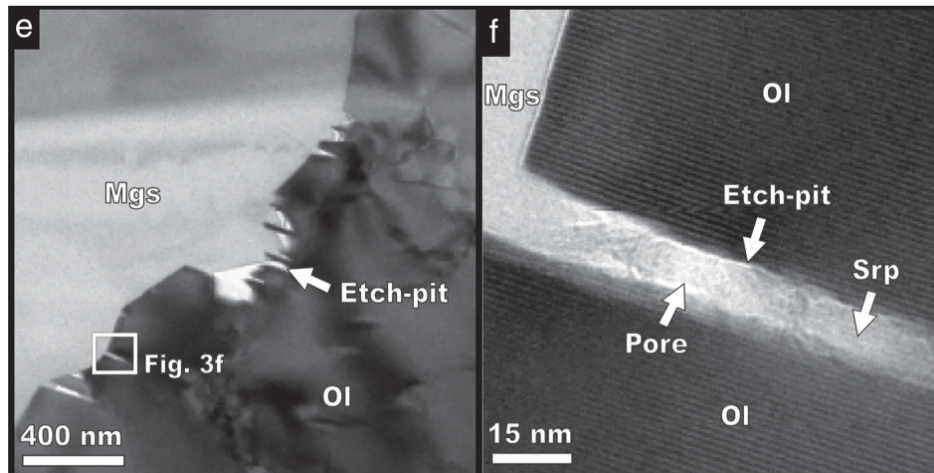


Figure 1.23: (e and f) Nano-pits (~ 15 nm) containing proto-serpentine on its internal tip and pores on its external border. Figure and caption reproduced from (Peuble et al., 2018).

The last option is crystallisation pressure exerted by serpentinite growing in the etch pits (Lafay et al., 2018; Malvoisin, Brantut, and Kaczmarek, 2017). Damage induced by crystallisation in the surrounding rock is experimentally proven for periclase hydration (Zheng et al., 2019, 2018), CaO hydration with a potential application for wellbore leakage mitigation (Wolterbeek, Noort, and Spiers, 2018) and olivine carbonatation (Kelemen and Hirth, 2012; Xing et al., 2018; Zhu et al., 2016).

From crystallisation pressure to poromechanical behavior

Plenty of geological objects like antitaxial veins, zebra textures or serpentized mafic rocks are related to crystallisation pressure exerted during mineral precipitation. The model developed in the literature involving the concept of crystallisation pressure is a mix of chemical reactions of dissolution/crystallisation coupled with transport and ultimately the generation of stress high enough to damage a confined porous rock. But the case gathering the right conditions is difficult to achieve: high poral solution supersaturation, low energy transport, extensive time, nano-porous medium... Furthermore, we reviewed that sometimes alternative scenarios explain the described geological objects without the concept of crystallisation pressure. Meanwhile, experimental work (Balboni et al., 2011; Caruso, Wangler, and Flatt, 2018; Derluyn, 2012; Espinosa Marzal and Scherer, 2008; Means and Li, 2001; Noiriél et al., 2010) and modeling (Coussy, 2006; Derluyn, 2012) proved and studied the relation between the chemical concept behind salt crystallisation in a porous medium and its mechanical interaction via the crystallisation pressure with the porous rock.

Similarly, we plan to monitor salt crystallisation reaction in a porous medium and measure the causes and effects of salt crystallisation in porous rock. To do that, we want to use acoustic monitoring techniques in the range of ultrasonic waves described in the chapter 2. Basically, it consists of emission and acquisition by piezoelectric sensors of elastic waves propagating through a porous medium that provides the elastic properties of the medium and the extent of the damage by the recording of acoustic emissions. However, the post-processing of the data recorded is not straightforward since frequency-dependent attenuation and dispersion affect the elastic wave during the propagation through the porous medium in changing pore saturation (David et al., 2017a,b; Müller, Gurevich, and Lebedev, 2010; Pimienta et al., 2019) and damage conditions (Fortin et al., 2006; Schubnel and Guéguen, 2003). Then, the poromechanical considerations about the propagation of the ultrasonic wave in porous rocks are provided in the following section. In the end, homogenization methods to determine analytically the effective medium properties are substantially presented to model the effective elastic properties of a porous rock after salt crystallisation and damage.

1.4 Poromechanic's of variably saturated porous rock

To write this section, we were inspired by the work of Borgomano (2019) and Fortin (2007). We give the basics to grasp the problem of wave propagation in a porous rock submitted to different fluid saturation from dry, partially to fully saturated. In this respect, we will introduce the theory of elasticity in a homogeneous medium and the theory of poroelasticity that applies specifically to the porous rock saturated with a fluid. As such, we define the different wave propagation regime and calculate their limits for the Adamswiller sandstone that we will use later in our experiment. Second, the case of partially saturated porous sandstone will be presented with examples and theoretical concepts. In the third part, we addressed the particular case of P-wave propagation during capillary uptake in porous sandstone.

1.4.1 Elastic properties of homogeneous isotropic material

The model of elasticity of homogeneous elastic material is a linear function stated by the Hooke law. The law is true for small deformation in the domain of elasticity. Deformation, ϵ , 1.17, and stress, σ , are expressed in the generalized form of the Hooke law, 1.18.

$$\epsilon = \frac{\Delta l}{l_0} \quad (1.17)$$

$$\sigma = \mathbb{C} * \epsilon \quad (1.18)$$

\mathbb{C} is the fourth-order invertible tensor of the elastic modulus. In the case of an isotropic medium, two coefficients are sufficient to express the tensor of elasticity \mathbb{C} , E the Young modulus (GPa) and ν the Poisson coefficient, 1.19.

$$\sigma = \frac{E}{1 + \nu} * (\epsilon + \frac{\nu}{1 - 2 * \nu} * tr(\epsilon) * I) \quad (1.19)$$

And with the index notations, 1.20

$$\sigma_{ij} = \frac{E}{1 + \nu} * (\epsilon_{ij} + \frac{\nu}{1 - 2 * \nu} * (\epsilon) * \delta_{ij}) \quad (1.20)$$

With δ_{ij} the Kronecker symbol ($\delta_{ij} = 1$ if $i = j$; $\delta_{ij} = 0$ if $i \neq j$). In the uniaxial loading (σ_{33}), the Young modulus relates directly to the axial stress to the axial strain and the Poisson ratio relates the radial strain to the axial strain.

Knowing the Young modulus and the Poisson ratio, one can express the elastic moduli of the homogeneous rock: the Bulk modulus, K , that express the resistance of the material to compression, 1.21 and the shear modulus, G that gives the material response to shear stress, 1.22.

$$K = \frac{E}{3 * (1 - 2 * \nu)} \quad (1.21)$$

$$G = \frac{E}{2 * (1 + \nu)} \quad (1.22)$$

The Poisson ratio, ν , express according to K and G :

$$\nu = \frac{3 * K - 2 * G}{2 * (3 * K + G)} \quad (1.23)$$

Across elastic material, the velocity of compressive P-wave and Shear S-wave is related to the elastic moduli and the material density. The expression of P-wave velocity is expressed in 1.24.

$$V_p = \sqrt{\frac{K + \frac{4}{3} * G}{\rho}} \quad (1.24)$$

The expression of S-wave velocity is expressed in equation 1.25.

$$V_s = \sqrt{\frac{G}{\rho}} \quad (1.25)$$

Conversely, the elastic properties can be inverted from the measurement of P and S wave velocity propagating in a material knowing its density. The expressions of elastic wave velocity are valid when the size of the heterogeneities is smaller than the wavelength due to potential scattering effect (Sarout, 2012). The ultrasonic wave in this study have a P-wave velocity distributed between 2000 to 4000 m/s and a central frequency calculated by taking the Fourier transform of the ultrasonic P-wave propagated through the Adamswiller sandstone. This frequency is $f=0.5$ MHz. The ultrasonic wavelength, λ is given in $\lambda = \frac{V}{f}$ giving λ between 400 and 800 μm . The mean grain size of the Adamswiller sandstone is 70 μm . The condition is then fulfilled.

1.4.2 Propagation of P-wave in fluid-saturated porous medium

Biot (1956a,b) proposed the theory of poroelasticity to extend elasticity to porous saturated rock. 'Drained' condition defines a regime where the fluid is free to go in or out of a fluid-saturated Representative Elementary Volume (REV). The contrary is called the 'Undrained' condition where the pore pressure builds up when a hydrostatic stress increment is applied on the REV like during the propagation of an ultrasonic P-wave. In the unrelaxed regime, the frequency of the propagating wave is so high that the fluid cannot flow through the pore throat to equilibrate the pressure.

1.4.2.1 Undrained and drained regime

In the drained regime (subscript $_d$), the compressibility and the shear moduli are equalized with the measured moduli on the dry rock. In the undrained regime (subscript $_u$), the fluid pore pressure increases during hydrostatic stress increment on the REV, then the undrained bulk modulus is given in Borgomano (2019), 1.26.

$$K_u = K_d + \frac{K_f * (1 - \frac{K_d}{K_m})}{\phi + ((1 - \frac{K_d}{K_m}) - \phi) * \frac{K_f}{K_m}} \quad (1.26)$$

With, K_m the skeleton bulk modulus, ϕ the porosity and K_f the fluid bulk modulus. The shear modulus of a fluid is null, then the undrained shear modulus does not change, 1.27.

$$G_u = G_d \quad (1.27)$$

In the next paragraph, we define the cut-off frequency to distinguish the two regimes.

1.4.2.2 Biot-Gassmann distinction of low (drained) and high frequency (undrained) regime in undamaged porous rock

Biot (1956a,b) theory aims to describe the interactions between fluid and solid during wave propagation in a porous medium. Under an oscillating stress field, the deformation-induced on the fully saturated porous medium may induce pore pressure oscillation. Biot defines the ‘characteristic’s Biot frequency’, f_b , to express the frequency dependence of the wave with respect to a porous medium, 1.28. Bellow f_b , the global flow defined in Mayr and Burkhardt (2006) as a coupled motion of fluid and matrix in large pores lower the wave velocity. At a higher frequency, the fluid has no time to diffuse in the porosity by global flow and because the fluid is immobile in the pore, the apparent stiffness of the porous saturated medium increases and consequently the wave velocities. Close to f_b , deformation induced by viscous fluid flow increases the attenuation of the wave.

$$f_b = \frac{\phi * \eta_f}{2 * \pi * \rho_f * \kappa} \quad (1.28)$$

In chapter 2 we provide ϕ , the porosity equal to 20%, κ , the intrinsic permeability (100 mD) in Adamswiller sandstone (Rimmelé, Barlet-Gouédard, and Renard, 2010; To and Chang, 2019), η_f the dynamic viscosity of the fluid ($18.5 * 10^{-6}$ Pa.s for air and $1 * 10^{-3}$ Pa.s for water) and ρ_f the fluid density (1.204 kg.m^{-3} for air and 1000 kg.m^{-3} for water). We recall that the ultrasonic wave frequency is close to 500 kHz. Then, the calculated Biot’s characteristics frequency for the dry Adamswiller is between 4.9 MHz and 49 MHz, thus the inertial effect is predominant. For the water-saturated Adamswiller the Biot’s characteristics frequency is above 322 kHz. A mix of viscous and inertial effect is awaited at full water saturation of the porous medium.

The frequency dependence on the microstructure of a cracked porous rock is treated with the squirt fluid flow cut-off frequency.

1.4.2.3 Squirt fluid flow cut-off frequency delimiting the relaxed and unrelaxed regime in micro-cracked porous rock

ζ is a shape factor for the penny shaped cracks ($w \ll c$) and the squirt flow cut-off frequency is expressed in equation 1.29 by Schubnel and Guéguen (2003). Above f_{sq} , Schubnel and Guéguen (2003) assume that the description of the interaction between the fluid and the crack corresponds to the case when the volume of fluid in the crack is constant which means that the fluid does not circulate. This inertial effect increases the wave velocities. On the contrary, bellow f_{sq} , the squirt fluid flow or local flow reduces the wave velocities

$$f_{sq} = \frac{\zeta^3 * E_m}{24 * \eta} \quad (1.29)$$

The squirt flow cut-off frequency is calculated according to the intact Adamswiller Young modulus (ch. 2), E_m , 10.38 GPa, and a crack aspect ratio equal to 10^{-3} common in similar material (Schubnel and Guéguen, 2003). The dynamic viscosity of water is $1 * 10^{-3} \text{ Pa.s}$ then the squirt flow cut-off frequency is ~ 409 kHz well below the experimental ultrasonic wave frequency obtained by calculating the acoustic signal [Fast Fourier Transform \(FFT\)](#), (~ 500 kHz). With this crack aspect ration, the fully saturated damaged rock is considered in the frame of the unrelaxed regime.

We next focus on water capillary uptake experiments in sandstone that are reported in the literature. Because partial saturation is prevailing in the porous medium, the effects awaited during ultrasonic P-wave propagation differ from the ultrasonic P-wave propagation in a fully saturated porous medium.

1.4.3 P-wave propagation in a partially fluid-saturated porous medium

1.4.3.1 Experimental description of partial saturation in porous sandstone

During saturation monitored by X-ray radio scans, it is experimentally observed that partial saturation is sometimes patchy in other words gas pocket in the porous sample surrounded by fully fluid-saturated porosity. (Mayr and Burkhardt, 2006; Müller, Gurevich, and Lebedev, 2010). The first approach to the problem is to calculate the properties of an effective medium considering the two fluids phases. The perturbation induced by an ultrasonic wave induces an interstitial pressure in the pores. Then the model of effective fluid works only when the fluid pressure is balanced to avoid potential scattering effect (Barrière, 2011; Sarout, 2012). The wavelength must be greater than the size of heterogeneities to balance the pore fluid pressure. Then, the condition is not always fulfilled for ultrasonic waves. Hopefully, the gas pocket may not be the norm as we do not observe it experimentally in the Adamswiller sandstone like David et al. (2017b) and Pimienta et al. (2019) in the Sherwood sandstone. Thus, we will circumvent the scattering effect in absence of gas pockets.

1.4.3.2 Competing mechanism during water imbibition

The evolution of amplitude and velocity during free imbibition raised some questions regarding the mechanism responsible for the evolution of the seismic properties of the porous rock. David et al. (2017b) observed thanks to a combination of X-ray radio-graphies and ultrasonic monitoring that energy loss on the ultrasonic wave happened well ahead to the waterfront reaching the detection volume (Fresnel clearance zone) of a couple of [lead-zirconate piezoceramic transducers \(PZT\)](#) (piezoceramic transducers). Pimienta et al. (2019) explored the moisture effect by putting an originally dry Sherwood sandstone in a chamber with controlled humidity. He reported a slight decrease in the velocity and the amplitude until a high [Relative Humidity \(RH\)](#) (80%) followed by an exponential decrease for both properties. The effect of moisture on the Sherwood sandstone is fully reversible. The same physical properties evolve differently in a water imbibition experiment of Sherwood sandstone (Pimienta et al., 2019). The exponential decay of the normalized amplitude comes before the exponential decay of normalized velocity. Besides, the minimum normalized velocity is 20% higher than the minimum velocity obtained during moisture adsorption. The final overall saturation of the porous medium is measured at 70%. (Pimienta et al., 2019) formulate that the effect observed is primarily linked to the physical adsorption of water molecules at the contact between grains which has a softening effect leading to amplitude and velocity drop. When the contact grain-grain is saturated, the P-wave velocity increase which is attributed by Pimienta et al. (2019) to the Gassmann effect intervening at the grain-grain contact.

Figure 1.24 recaps our understanding of the normalized velocity and amplitude evolution of ultrasonic P-wave during the saturation of sandstone similar to the Adamswiller

sandstone used in our experiments. The sandstone has a uni-modal porosity distribution meaning that alongside large pores, there are pore-throats and cracks. The recaps figure 1.24 relies on Pimienta et al. (2019) that reveals the evolution of P-wave velocity and attenuation at a low water-saturation level and Mayr and Burkhardt (2006) that deals with partial water saturation to full water saturation:

1. The initial normalized P-wave and amplitude are set for the dry porous medium.
2. Under moisture adsorption up to a very low partial saturation of the porous medium ($\sim 2\%$), the P-wave velocity and amplitude drop exponentially at a high level of relative humidity ($\sim 80\%$). It is explained by water molecule adsorption in the cracks and pore-throats leading to a softening effect revealed by the propagation of the ultrasonic P-wave. This stage is not observed completely or bypassed during free imbibition probably because the relative humidity does not reach such a high level before the detection of the imbibition front (Pimienta et al., 2019).
3. A stiffening effect via progressive saturation of the cracks and pore-throats and reduction of squirt fluid flow increases the compressive P-wave velocity via the Gassmann effect in pore-throats and cracks (Mayr and Burkhardt, 2006).
4. After the fluid saturation of the pore-throats and cracks, the partially saturated porous medium is best to describe as large pores partially saturated. The pressure gradient induces fluid flow in the saturated medium during the propagation of the ultrasonic wave. It dissipates energy and explains the reduced P-wave velocity. Close to pore saturation, the P-wave velocity abruptly increases via the Gassmann effect (Mayr and Burkhardt, 2006).
5. At full fluid saturation, the fully saturated porous medium is stiffened via the Gassmann effect: the fluid in the pore behaves like a solid which increases the P-wave velocity of the saturated material relative to the dry material.

1.4.4 P-wave velocity propagation in a porous medium submitted to an increasing confining pressure

At enhanced confining pressure and constant pore pressure, the velocity and the amplitude of the ultrasonic P-wave passing through a porous medium increase and tend to an asymptote that corresponds to a porous medium without cracks (Fortin et al., 2006).

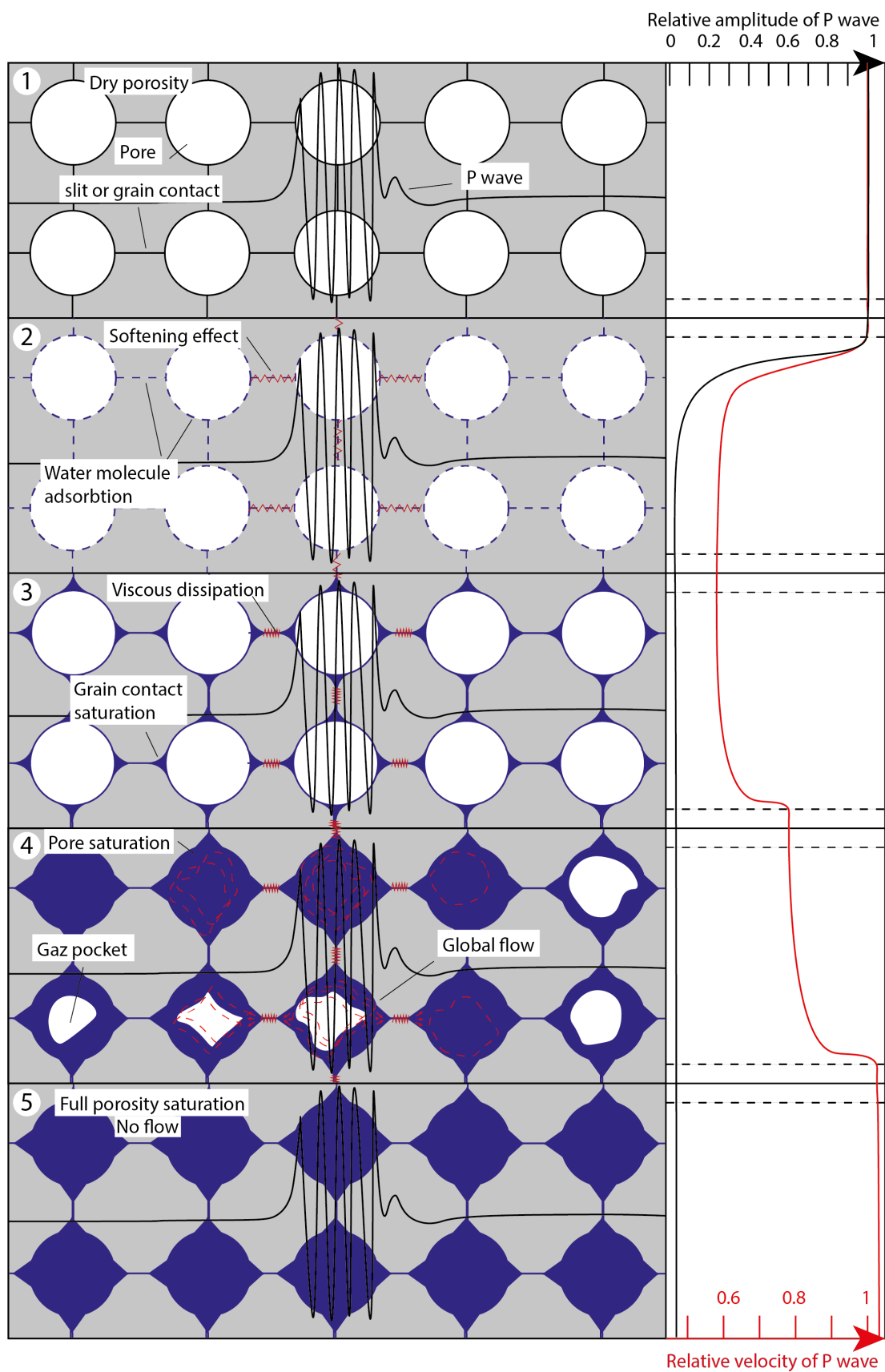


Figure 1.24: Evolution of normalized velocity and amplitude of ultrasonic P-wave propagating across a porous sandstone during capillary uptake: 1) dry stage, 2) water molecule adsorption at the grain-grain contact, 3) progressive saturation of grain-grain contact, small pores and cracks 4) Progressive saturation of large pores 5) fully saturated porous sandstone.

1.5 Modeling of the effective elastic properties of porous medium with cracks

In this section, we give the equation to determine effective moduli of porous rock containing inclusions of different nature and shape and cracks based on the model of Eshelby. We implement these equations in MATLAB (2010) to compute the elastic properties of assumed homogeneous isotropic materials with homogeneous isotropic inclusions. Then, it is a powerful tool to model analytically the effect of crystallisation in a porous medium and to estimate the damage induced by crystallisation. The theoretical consideration and the schema of Eshelby in the relaxed regime are extensively described in Fortin (2007) and Huynh (2007). In this review, we will recall the modeling based on the auto-coherent schema of spherical inclusions distributed randomly in a homogeneous isotropic material (Huynh, 2007). Also, we recall the case of penny-shaped cracks with different cracks distribution damaging a homogeneous isotropic material (Fortin et al., 2011; Schubnel and Guéguen, 2003).

1.5.1 Modeling of the effective elastic of a homogeneous isotropic material with spherical inclusions

1.5.1.1 Auto-coherent schema

Huynh (2007) introduce the **Auto-coherent (AC)** schema for a poly-crystal material with no limitation in inclusion volume fraction, f . We choose the auto-coherent schema to the Mori-Tanaka (Fortin et al., 2006; Huynh, 2007) because the inclusions volume fraction in the homogenised medium may exceed the limit of validity of the Mori-Tanaka schema fixed at 20%. By contrast, the auto-coherent schema is valid at a higher inclusion volume fraction. In fact, according to comparisons the results given by the Mori-Tanaka schema revealed to be closely comparable to the **AC** schema outcomes.

For a material modeled with spherical grains of two homogeneous and isotropic materials, 1 and 2, the homogenised bulk, K_{hom} and shear moduli, G_{hom} are the solutions of this system of two equation:

$$\begin{cases} f_1 * \frac{K_1 - K_{hom}}{K_{hom} + \alpha_{hom} * (K_1 - k_{hom})} + f_2 * \frac{K_2 - k_{hom}}{K_{hom} + \alpha_{hom} * (K_2 - k_{hom})} = 0 \\ f_1 * \frac{G_1 - \mu_{hom}}{G_{hom} + \beta_{hom} * (G_1 - G_{hom})} + f_2 * \frac{G_2 - G_{hom}}{G_{hom} + \beta_{hom} * (G_2 - G_{hom})} = 0 \end{cases} \quad (1.30)$$

with

$$\alpha_{hom} = \frac{3 * K_{hom}}{3 * K_{hom} + 4 * G_{hom}}$$

and

$$\beta_{hom} = \frac{6 * (K_{hom} + 2 * G_{hom})}{5 * (3 * K_{hom} + 4 * G_{hom})} f_1 \text{ the volume fraction of material 1 and } f_2 \text{ the volume fraction of material 2.}$$

1.5.2 Modeling of the effective elastic properties of a cracked material

We will rely on the approach presented in Sayers and Kachanov (1995), used in Fortin et al. (2011), Fortin (2007), and Schubnel and Guéguen (2003) to model the elastic properties of an homogeneous isotropic material damaged by cracks filled with fluid. The method rely on the non interacting cracks approximation assuming that

interactions between cracks compensate. A second assumption consists in considering penny shaped cracks with c , the crack radius and w the crack width. To calculate the effective elastic moduli of the cracked rock, the crack density tensor $\bar{\alpha}$ must be defined: $\bar{\alpha} = \frac{1}{V} * \sum^N (c^3 * \vec{n} \otimes \vec{n})_i$ in 3D or $\bar{\alpha} = \frac{1}{A} * \sum^N (c^2 * \vec{n} \otimes \vec{n})_i$ in 2D where N the total number of cracks embedded in the REV, V or **Representative Elementary Area (REA)**, A , c the crack radius, \vec{n} the normal unit vector to the crack and $\vec{n} \otimes \vec{n}$ the dyadic product. In case of a random orientation of cracks, the crack distribution is expressed by a crack density scalar, ρ equal to $tr(\bar{\alpha})$.

In the formulation of the elastic compliance of the material with cracks, a second crack density parameter, \mathbb{B} is a fourth rank tensor defined as $\mathbb{B} = \frac{1}{V} * \sum^N (c^3 * \vec{n} \otimes \vec{n} \otimes \vec{n} \otimes \vec{n})_i$.

The compliance of the cracked medium is expressed with \mathbb{S}^0 , the compliance tensor of the original medium for an isotropic medium (inverse of the elastic tensor calculated with equation 1.20) and $\Delta\mathbb{S}$ the additional compliance tensor brought by the crack distribution:

$$\mathbb{S} = \mathbb{S}^0 + \Delta\mathbb{S} \quad (1.31)$$

The variation of the additional effective elastic compliance for any kind of distribution of cracks filled with fluid is defined in equation 1.32:

$$\Delta S_{ijkl} = \frac{1}{h} * \left(\frac{1}{4} * (\delta_{ik} * \alpha_{jl} + \delta_{il} * \alpha_{jk} + \delta_{jk} * \alpha_{il} + \delta_{jl} * \alpha_{ik}) + C * B_{ijkl} \right) \quad (1.32)$$

and

$$C = \left(\left(1 - \frac{\nu_0}{2}\right) * \frac{\delta}{1 + \delta} - 1 \right) \quad (1.33)$$

$$h = \frac{9 * K_0 * (1 - 2 * \nu_0) * (2 - \nu_0)}{32 * (1 - \nu_0^2)} \quad (1.34)$$

With δ_{ij} is the Kronecker symbol (if $i \neq j$, $\delta_{ij} = 0$ else $\delta_{ij}=1$). δ characterizes the coupling between the stress and the fluid pressure. As such it gives the effect of fluid on the effective crack compliance (Schubnel and Guéguen, 2003):

$$\delta = \frac{9 * \pi * (1 - 2 * \nu_0)}{16 * (1 - \nu_0^2)} * \frac{K_0}{K_f} * \zeta \quad (1.35)$$

with K_0 and K_f the material and fluid bulk moduli. ν_0 the material Poisson ratio and ζ the crack aspect ratio defined as: $\zeta = \frac{w}{c}$.

The cracks patterns encountered within this thesis are inter and intra-granular cracks that are approximated by a random distribution of disk cracks. The other crack pattern represents cracks parallel to a paraboloid surface that we choose to model by parallel horizontal disk cracks. The random distribution of disk cracks is characterized by x_1 , x_2 and x_3 as axis of symmetry and it leads to $\alpha_{11} = \alpha_{22} = \alpha_{33} = \frac{\rho}{3}$, $B_{1111} = B_{2222} = B_{3333} = \frac{\rho}{5}$, $B_{1212} = B_{1313} = B_{2323} = B_{1122} = B_{1133} = B_{2233} = B_{1111}/3$ (Fortin et al., 2011; Sayers and Kachanov, 1995).

$$\left\{ \begin{array}{l} \Delta S_{1111} = \frac{1}{E_0} + \frac{1}{h} * (\alpha_{11} + C * B_{1111}) \\ \Delta S_{1111} = \Delta S_{2222} = \Delta S_{3333} \\ \Delta S_{1313} = \frac{1}{G_0} + \frac{1}{h} * (2 * \alpha_{11} + \frac{4}{3} * C * B_{1111}) \\ \Delta S_{1313} = \Delta S_{1212} = \Delta S_{2323} \\ \Delta S_{1122} = -\frac{\nu_0}{E_0} + \frac{1}{h} * \frac{1}{3} * C * B_{1111} \\ \Delta S_{1122} = \Delta S_{1133} = \Delta S_{2233} \end{array} \right. \quad (1.36)$$

In the case of a perfectly aligned cracks with normal along axis x_3 , the only non vanishing component are $\alpha_{33} = \rho$ and $B_{3333} = \rho$ (Sayers and Kachanov, 1995) and the only non zero value in the elastic compliance tensor is:

$$\Delta S_{3333} = \frac{1}{E_0} + \frac{1}{h} * (\alpha_{33} + C * B_{3333}) \quad (1.37)$$

Finally, the elastic stiffness tensor is obtained by inversion of the elastic compliance tensor.

The P-wave velocity in the material, defined with the elastic stiffness tensor, C , is different according to the angle, γ , between the wave vector and axis 3 if the material is anisotropic. We plot the P-wave velocity according to equation 1.38 (Fortin et al., 2011; Schubnel and Guéguen, 2003):

$$V_p = \sqrt{\frac{C_{1111} * \sin^2 \gamma + C_{3333} * \cos^2 \gamma + C_{2323} + \sqrt{M}}{2 * \rho}} \quad (1.38)$$

where:

$$M = ((C_{1111} - C_{2323}) * \sin^2 \gamma - (C_{3333} - C_{2323}) * \cos^2 \gamma)^2 + (C_{1133} + C_{2323}) * \sin 2 * \gamma^2 \quad (1.39)$$

In our study we consider the wave with a wave vector at 90° to axis 3. It simplifies the equation like 1.40:

$$V_p = \sqrt{\frac{C_{1111} + C_{2323} + \sqrt{M}}{2 * \rho}} \quad (1.40)$$

where:

$$M = (C_{1111} - C_{2323})^2 \quad (1.41)$$

1.5.2.1 Inverse problem

The homogenized or effective properties of a porous medium are often correctly estimated with the help of standard test and imaging technics that gives the pore and cracks shape. Conversely, estimating the elastic properties of the skeleton is difficult. These properties can be obtained with an iterative algorithm on the inversed Mori-Tanaka schema (Huynh, 2007). In this situation, one considers a well defined porous medium and pore shape but an unknown skeleton. The calculation can also be achieved with the auto-coherent schema: K_{hom} and G_{hom} corresponds to the dry porous medium elastic moduli, K_2 and G_2 the air elastic moduli and K_1 and G_1 the unknown skeleton bulk moduli. The problem consists of solving the system to get K_1 and G_1 . However,

with the autocohherent schema, no pore shape is assumed and it doesn't work at high inclusion volume fraction. It works as well to estimate the characteristics of cracks like in Fortin et al. (2011). He inverted from shots of P and S- wave through a cracked basalt the evolution of the porosity and the cracks aperture and density.

1.6 Conclusion

In the chapter state of the art, we have reviewed the theoretical pieces of knowledge necessary to grasp the problem of crystallisation in porous rock and the potential crystallisation pressure that may be exerted. Because we will use ultrasonic waves to evaluate the elastic properties of a porous medium during the crystallisation, we recalled the effects on the P-wave velocity and attenuation that may be encountered during the saturation and the crystallisation in the porous medium. Ultimately, a homogenisation method is described to model crystallisation pressure experiments.

In chapter 2, the experimental apparatus and the in-situ, post-mortem monitoring techniques will be described. Besides their advantages, we will see how they constraint the realisation of a crystallisation pressure experiment in confined geological settings.

Chapter 2

Materials and Methods

Contents

2.1	Materials	48
2.1.1	Basic properties of sodium sulfate, magnesium sulfate and barite	48
2.1.2	Experimental porous rock	61
2.2	Methods	65
2.2.1	3D X-ray micro tomography	65
2.2.2	Ultrasonic wave monitoring and acoustic emission	68
2.2.3	Strain gauges	72

Abstract

The chapter materials and methods is divided into two parts. Section 2.1 is dedicated to the description of the chemical species (barium sulphate, sodium sulphate and magnesium sulphate) and the porous rock (Lavoux limestone and Adamswiller sandstone) employed in experiments described in the next chapters. For the chemical species, attention will be paid to the solubility of the phases according to the temperature, the concentration of the solution and the RH. Aside, the morphology of crystals is given and for barium sulphate we insisted on the nucleation sequence. Section 2.2 aims to explain the main monitoring techniques namely the 3D X-ray micro-tomography and the acoustic monitoring systems. In parallel, the use of those techniques in our experimental work is developed: for 3D X-ray micro-tomography, we compare the X-ray absorption spectrum of the minerals to know if the different minerals can be segmented and for acoustic monitoring, we present two systems and the types of analytic data recorded. Aside, we describe the mounting of the sensors on the sample and picking methods to measure the P-wave velocity in the sample.

2.1 Materials

2.1.1 Basic properties of sodium sulfate, magnesium sulfate and barite

Aqueous species experimentally known for inducing stress by precipitation are in a large majority salt like Alum chrome and copper sulfate (Taber, 1916), sodium chloride (Desarnaud, Bonn, and Shahidzadeh, 2016; Noiriél et al., 2010), ammonium thiocyanate (Means and Li, 2001), sodium sulfate (Derluyn et al., 2014; Espinosa Marzal and Scherer, 2008; Flatt et al., 2014; Scherer, 2004) and magnesium sulfate (Balboni et al., 2011; Haynes, 2005; Ruiz-Agudo et al., 2007; Steiger et al., 2011). Under confining pressure, Taber (1916) supposed that the precipitation of asbestiform veins cracks the surrounding rocks and nowadays the damaging potential of the serpentinization reaction is experimentally observed (Kelemen and Hirth, 2012; Lafay et al., 2018; Malvoisin, Brantut, and Kaczmarek, 2017; Zhu et al., 2016). Recently, Li et al. (2017) provided experimental proof that calcite can induce stress under confining pressure. We choose to use the hydrating properties of Na_2SO_4 and $MgSO_4$ to circle the constraint inherent to the realisation of crystallisation pressure experiment in porous rocks under high confinement. The choice of $BaSO_4$ is driven by the potential high supersaturation reachable in a counter diffusion experiment (Putnis, Prieto, and Fernandez-Diaz, 1995).

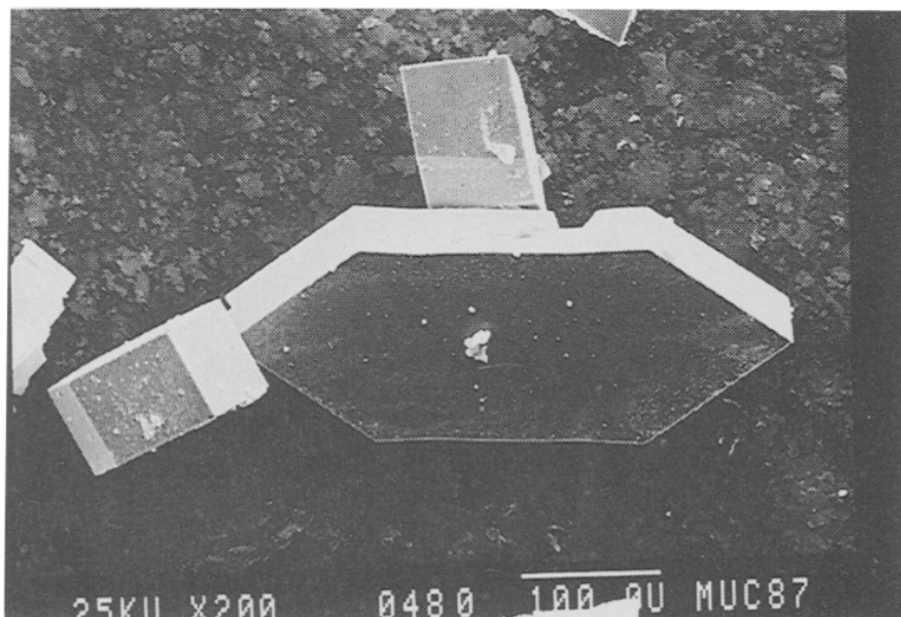


Figure 2.1: Final habit of a barite single crystals grown in silica gel (Prieto et al., 1992).

2.1.1.1 Barite ($BaSO_4$)

Barite precipitation has been extensively studied to better understand homogeneous nucleation of aqueous species (Putnis and Fernandez-Diaz, 1990; Putnis, Prieto, and Fernandez-Diaz, 1995), explore growth rate and ontogeny of barite crystal in porous medium (Godinho et al., 2016; Godinho and Stack, 2015; Prieto et al., 1992) (figure 2.1). Recently the need to study precipitation and dissolution mechanisms in porous medium comes up with the problem of nuclear waste long-term storage durability in a

deep geological repository. The research focuses on the interaction between the cementitious materials with the formation water from the surrounding host rock (Poonoosamy et al., 2016; Poonoosamy et al., 2020, 2015).

2.1.1.1.1 Crystallisation in geological settings

In nature, barite precipitates through various processes:

1. Mixing of a barium bearing hydrothermal fluid reacting with sulphate dissolved in seawater precipitate barite in shallow sediment or on the seabed (Castellini et al., 2006). Such deposits are called sedimentary exhalative deposits and barite is often found with sphalerite (ZnS) and galena (PbS). For example, the ore deposit of Arrens (Central Pyrenees, France) is a Devonian SEDEX (SEDimentary EXhalative) deposit consisting of a metric band of barite with PbS and ZnS mineralisation (Hoareau, 2009; Pouit and Bois, 1986).
2. Advection or diffusion of deep barium bearing fluid precipitate barite at the sulphate-methane transition zone. The barium may originate from a crustal source like granite or other metamorphic rock alteration or have a diagenetic origin. For example, the first generation of barite precipitated at la Montagne Noire (Lodève basin, France), comes from the alteration of interlayered volcanic ashes in a bituminous marl (Laurent, 2015). The mixing with a sulphate rich fluid or oxidation of H_2S from bacterial sulphate reduction results in precipitation of fibrous barite in a lithological interface and hydraulic breccia (Laurent, 2015; Torres et al., 1996).
3. Use of secondary oil recovery methods, in particular the injection of fresh seawater rich in sulphate in a geological reservoir, mix the sulphate rich seawater with the formation water carrying barium. It results in pipe and valves clogging with barite precipitate. Because the barite is sparingly soluble ($\log(K_{sp}) = -9.96$, 25°C) (Ruiz-Agudo et al., 2015) in common solvent it is a major concern for oil operator (Collins, 2005).

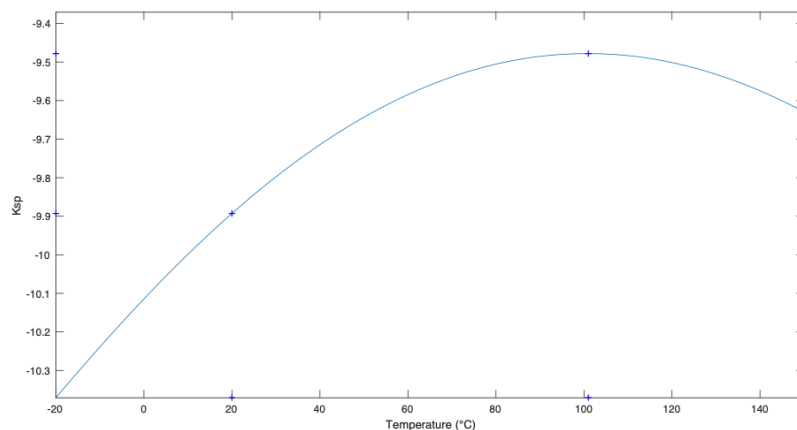
Barite is also renowned because it uses in drilling to adjust the mud density during the operations.

2.1.1.1.2 Chemical properties of barite ($BaSO_4$)

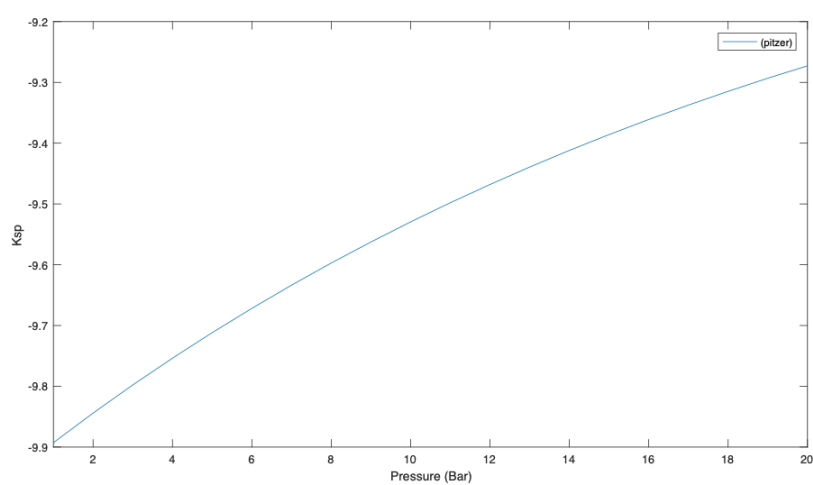
The basic properties of barium sulphate are displayed in table 2.1. The aqueous solubility product at 20°C is modeled in Phreeqc with the parameter file pitzer.dat for the hyper-saline environment (Parkhurst and Appelo, 2013).

Table 2.1: Basic properties of barite

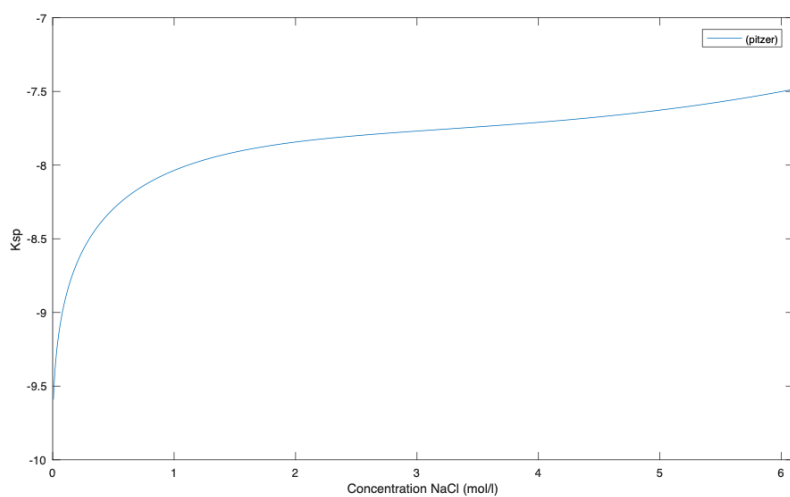
Unit	Molar mass $g.mol^{-1}$	Molar volume $m^3.mol^{-1}$	$K_{SP_{aq20^\circ C}}$
Barite	233.39	$5.21.10^{-5}$	$1.08.10^{-10}$ Ruiz-Agudo (2020)



(a) Barite solubility versus temperature.



(b) Barite solubility versus pressure.



(c) Barite solubility versus $[\text{NaCl}]$.

Figure 2.2: Barite solubility versus Temperature and Pressure, Phreeqc modelisation based on database Pitzer (Plummer and others, 1988).

2.1.1.1.3 Solubility of Barite

The mineral solubility product, K_{sp} of barite, depends on temperature, pressure and aqueous solution composition (Mullin, 2001). We calculate the $\log_{10}K_{sp}$ with Phreeqc considering the Pitzer database (Parkhurst and Appelo, 2013), plots in figure 2.2. $BaSO_4$ solubility at 1 bar and for temperature between -20 and 150°C is very low with a maximum solubility $\log_{10}K_{sp102^\circ C} = -9.48$ at 102°C. At 20°C, $\log_{10}K_{sp20^\circ C} = -9.85$ (figure 2.2a). Solubility is greater when submitted to a pressure increase. At 2 MPa, the $\log_{10}K_{sp2MPa} = -9.27$ (figure 2.2b). Barite solubility in an aqueous solution increases according to simulation with dissolved NaCl in solution. The solubility of NaCl in an aqueous solution is 6.1 molal in this case the $\log_{10}K_{spNaCl}$ of $BaSO_4$ is equal to -7.48 (figure 2.2c).

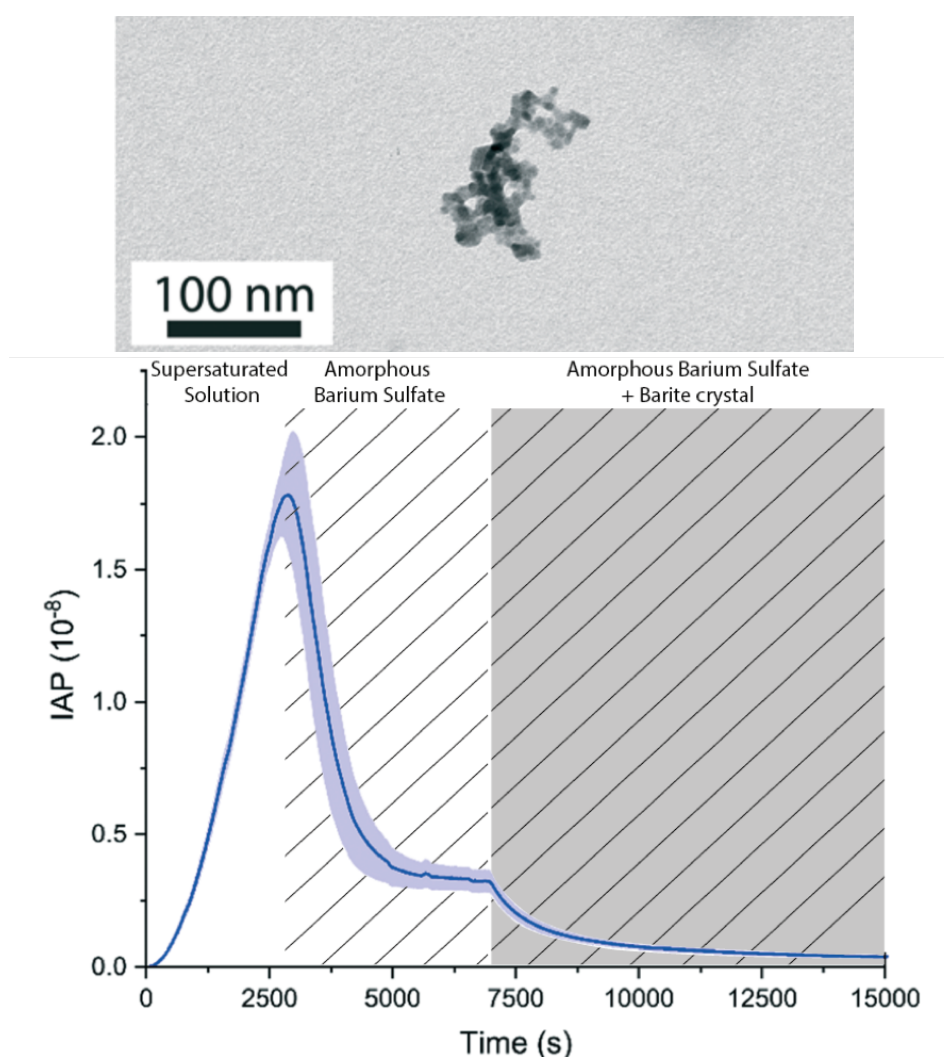


Figure 2.3: Top: TEM image of nanometric barite amorphous precursor (Ruiz-Agudo et al., 2020). Bottom, average evolution of ion activity product, showing nucleation onset. Blue area represents the standard deviation of IAP. Stripped domain corresponds to the Amorphous Barite Sulfate (ABS) domain. Grey domain is the domain of existence of barite crystal. Figure and caption adapted from Ruiz-Agudo et al. (2020).

2.1.1.1.4 Morphology of barite

The morphology dependence of crystals has been studied relatively to supersaturation (Prieto et al., 1992) and pH (Ruiz-Agudo et al., 2015). Prieto et al. (1992) concludes that barite crystal ontogeny depends on the supersaturation at which the crystal nucleates. They find that the grown crystal in silica gel at high supersaturation has the same morphology as crystals found in geological settings. They suggest that such high supersaturation might prevail naturally. Ruiz-Agudo et al. (2015) discover that pH influences barite growth: the barite crystal size tends to a reduce and more equidimensional crystal form when the alkalinity of the solution increases at equivalent supersaturation index. At low and high pH, the nucleation density is higher.

2.1.1.1.5 Barite nucleation

High supersaturation is obtained in silica gel column during double diffusion of dissolved $BaCl_2$ and Na_2SO_4 at various concentrations in pure water which means that the nucleation threshold is high for barite (Prieto, 2014; Putnis and Fernandez-Diaz, 1990; Putnis, Prieto, and Fernandez-Diaz, 1995). Recently, in the frame of non-classical nucleation theory (Gebauer and Cölfen, 2011; Ruiz-Agudo et al., 2020) observed the nucleation of a non-crystalline [Amorphous Barite Precursor \(ABS\)](#) prior to barite precipitation during a 4 hours long, additive-free, titration (figure 2.3, top). The supersaturation obtained at ABS first apparition was 2.24 ± 0.04 and 1.5 ± 0.05 , at barite nucleation (figure 2.3, bottom). Prieto et al. (1992) explained that the supersaturation threshold is a kinetic factor depending on the supersaturation rate. This explains partly the lower value of Ruiz-Agudo et al. (2020) since Prieto experiment lasted more than 15 days.

2.1.1.2 Sodium Sulfate ($Na_2SO_4 \cdot H_2O$)

2.1.1.2.1 Chemical properties of sodium sulphate (Na_2SO_4)

The basic properties of sodium sulphate are displayed in table 2.2 for the anhydrous phase, Na_2SO_4 named thenardite and the decahydrate phase, $Na_2SO_4 \cdot 10H_2O$ named mirabilite. The aqueous solubility product at 20°C is modelled in Phreeqc with the parameter files pitzer.dat (Parkhurst and Appelo, 2013).



Figure 2.4: Pluri-decimetric mirabilite wreath growing from a cave soil, (Arbailles Massif, Pyrenees, France) © Dimitri Laurent.

2.1.1.2.2 Natural occurrences of sodium sulphate

Depending on the condition of conservation, crystallized sodium sulphate is mostly encountered in nature under the decahydrate form of mirabilite or the anhydrous phase of thenardite. Sodium sulphate is present in the drilling cores through evaporitic deposits, redissolved by hot fluids, it precipitates in the subsurface for example in caves like in the Arbailles massif (Pyrenees) in figure 2.4 or surface like in the Salar de Uyuni. Finally, sodium sulphate is renowned to be one of the most damaging salt for cultural heritage and civil construction (Flatt et al., 2014).

Table 2.2: Basic properties of sodium sulphate

	Molar mass $g.mol^{-1}$	Molar volume $m^3.mol^{-1}$	$KSP_{aq20^{\circ}C}$
Mirabilite	322.19	$2.198.10^{-4}$	$3.39.10^{-2}$ Phreeqc (Pitzer)
Thenardite	142.04	$5.31.10^{-5}$	$5.2.10^{-1}$ Phreeqc (Pitzer)

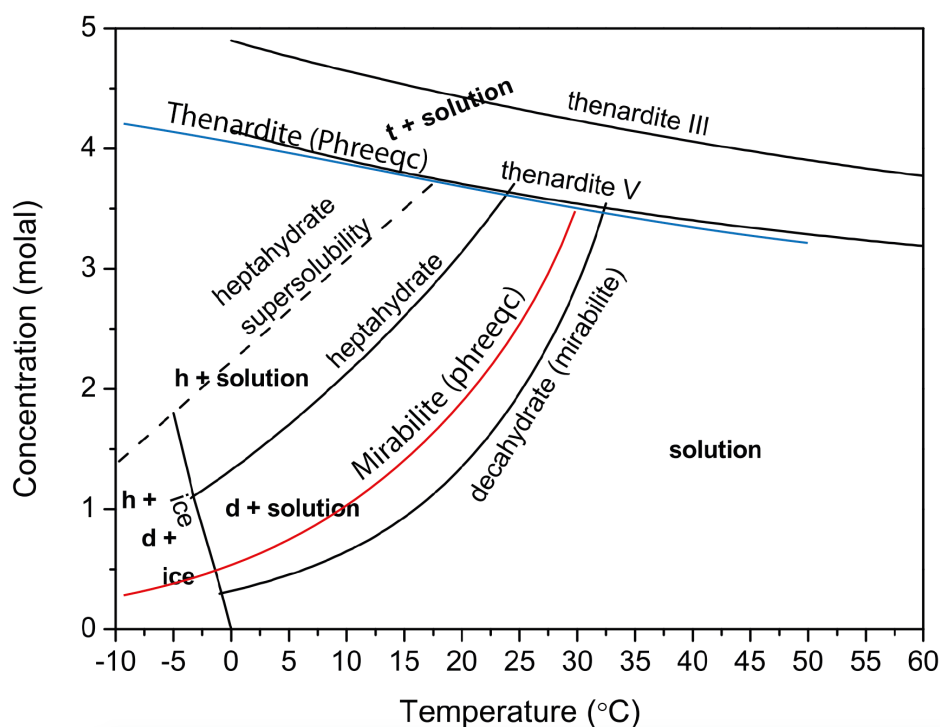


Figure 2.5: Solubility diagram of sodium sulfate (Derluyn, 2012): thenardite (t), Na_2SO_4 (V) (stable) or Na_2SO_4 (III) (metastable), anhydrous salt; mirabilite (d), $Na_2SO_4 \cdot 10H_2O$ (stable); and heptahydrate (h), $Na_2SO_4 \cdot 7H_2O$ (metastable), Mirabilite and Thenardite (Phreeqc) modelisation based on Pitzer database (Parkhurst and Appelo, 2013).

2.1.1.2.3 Sodium sulphate phases stability

In the literature on sodium sulfate crystallisation in porous rock, concentration is preferred to the solubility product. We will adopt this nomenclature. The solubility diagram expressed the equilibrium concentration of the different phases in the function of temperature. Sodium sulfate crystallises in two different phases in normal atmospheric conditions: mirabilite or Glauber salt, the decahydrate phase, $Na_2SO_4 \cdot 10H_2O$ and thenardite (V), the anhydrous phase, Na_2SO_4 . Thenardite solubility slowly decreases versus temperature increase. Mirabilite phase dissolves above 32°C and its solubility decreases rapidly versus a decreasing temperature. At 32°C, thenardite and mirabilite have the same solubility at about 3.5 molal (figure 2.5).

The molar volume of mirabilite is 314% higher than the molar volume of the thenardite. However, the volume of mirabilite shrinks by 5.6% compared to the volume of the same molal quantity of thenardite and the corresponding volume of water integrated into the mirabilite lattice (Flatt, 2002; Haynes, 2005). Mirabilite becomes less stable with decreasing humidity and a phase transition happens around 75% RH at 20°C. Transition in presence of water from thenardite to mirabilite is not a hydration reaction (water integration into the crystal lattice) because of the lattice mismatch between the two phases. Thenardite converts into mirabilite via dissolution of the anhydrous phase and reprecipitation of the decahydrate (Flatt, 2002). The metastable heptahydrate phase of sodium sulfate, $Na_2SO_4 \cdot 7H_2O$ is often precipitated before mirabilite during rapid cooling of a sulfate sodium solution supersaturated with respect to mirabilite (Derluyn, 2012; Derluyn et al., 2011; Espinosa Marzal and Scherer, 2008; Steiger, Kiekbusch, and Nicolai, 2008).

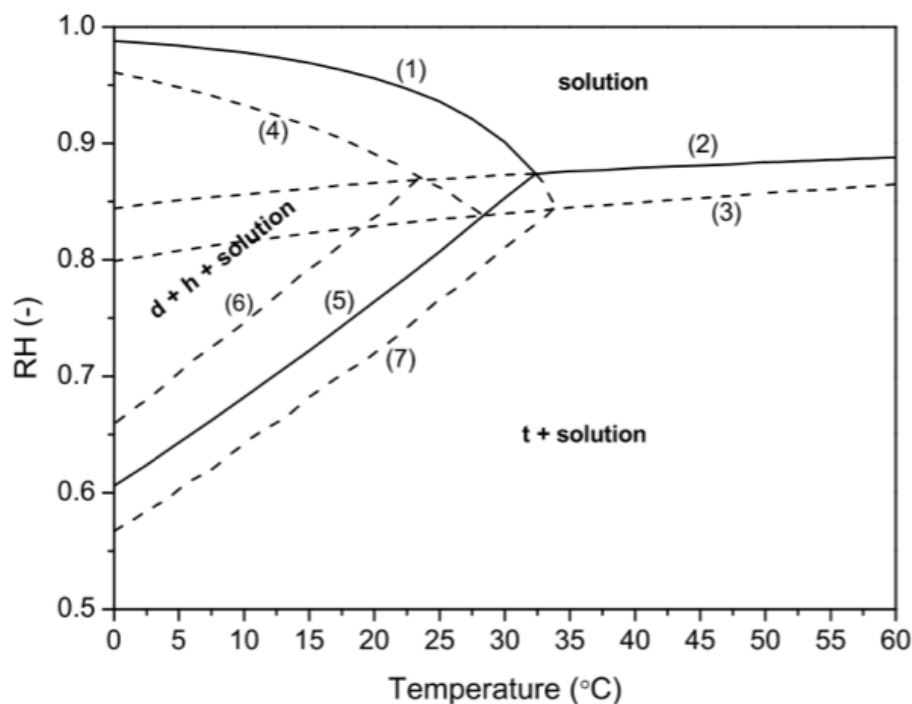


Figure 2.6: RH diagram of the system $Na_2SO_4 \cdot H_2O$ (Steiger, Kieckbusch, and Nicolai, 2008) stable (full line), metastable (dashed line). (1)-(5) solid solution equilibrium (5): $Na_2SO_4(V)-Na_2SO_4 \cdot 10H_2O$, (6): $Na_2SO_4(V)-Na_2SO_4 \cdot 7H_2O$ and (7): $Na_2SO_4O(III)-Na_2SO_4 \cdot 10H_2O$.

2.1.1.2.4 Morphology of sodium sulphate

Mirabilite crystals can crystallise with a needle-like structure, or with a prismatic shape (figure 2.7a). Heptahydrate has a pyramidal shape. Upon evaporation drying of a sodium sulfate solution or a hydrated phase of Na_2SO_4 , two phases precipitate, metastable thenardite III with a needle-like branches shape (figure 2.7d), and V with a prismatic structure (figure 2.7c) (Derluyn, 2012). Anhydrous phases are whitish. Thenardite III is more frequent when the drying temperature increase but turn into Thenardite V when RH is enhanced (Steiger, Kieckbusch, and Nicolai, 2008).

2.1.1.2.5 Crystallisation of Na_2SO_4 phases

Mirabilite and heptahydrate can be precipitated by cooling a sufficiently rich Na_2SO_4 solution or by evaporating a Na_2SO_4 rich solution below $32^\circ C$ and at RH above 93%. Above this temperature or RH, one would precipitate thenardite. The nucleation of $Na_2SO_4 \cdot 7H_2O$ is more favorable than $Na_2SO_4 \cdot 10H_2O$ and require a lower supersaturation threshold due to a smaller crystal liquid interfacial energy (Espinosa Marzal and Scherer, 2008). Some supersaturation thresholds are reported in Espinosa Marzal and Scherer (2008) for Na_2SO_4 hydrate precipitating in two limestones by cooling cycle: the supersaturation threshold of mirabilite is greater than 7 for a temperature below $0^\circ C$ and less than 2 in the case of heptahydrate for a temperature between 7 and $15^\circ C$. Thenardite partly dissolves and the remaining crystal may act as nucleation seed for mirabilite (Caruso, Wangler, and Flatt, 2018; Flatt, 2002).

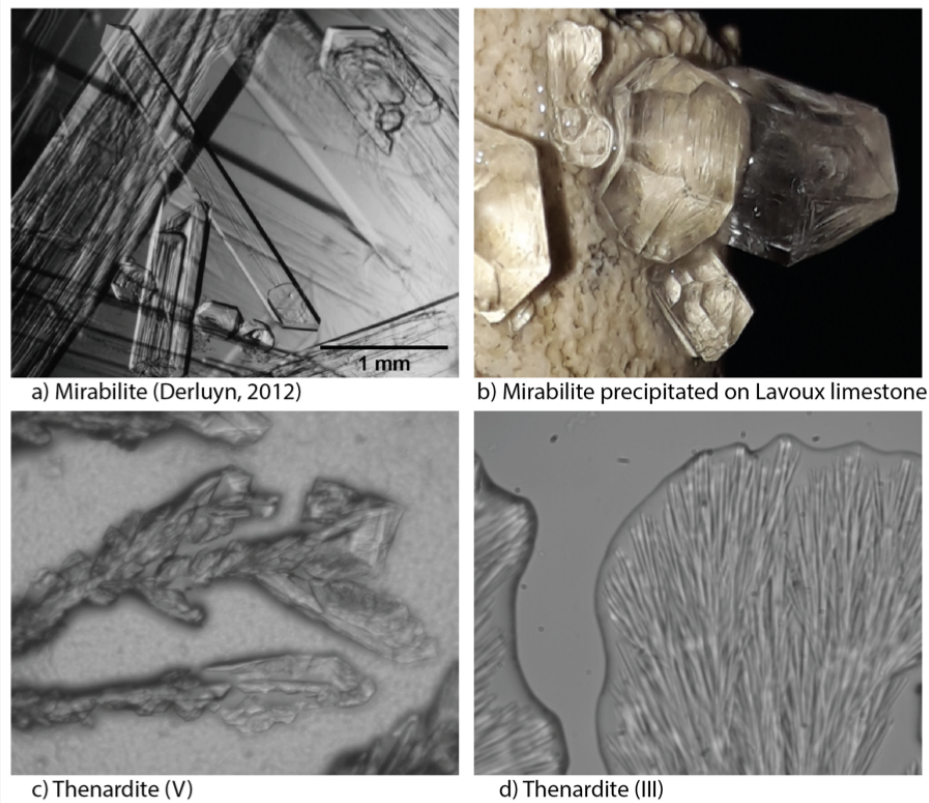


Figure 2.7: Pictures of Sodium Sulfate phases: a) Mirabilite (Derluyn, 2012), b) mirabilite grown on Lavoux limestone obtained during saturation under vacuum of a sodium sulphate rich solution in a Lavoux limestone ($1 \times 1 \text{ cm}^2$), c) micrograph of thenardite (V) captured while drying a sodium sulphate rich solution ($0.5 \times 0.5 \text{ mm}^2$), d) micrograph of thenardite (III) captured while drying a sodium sulphate rich solution ($0.5 \times 0.5 \text{ mm}^2$).

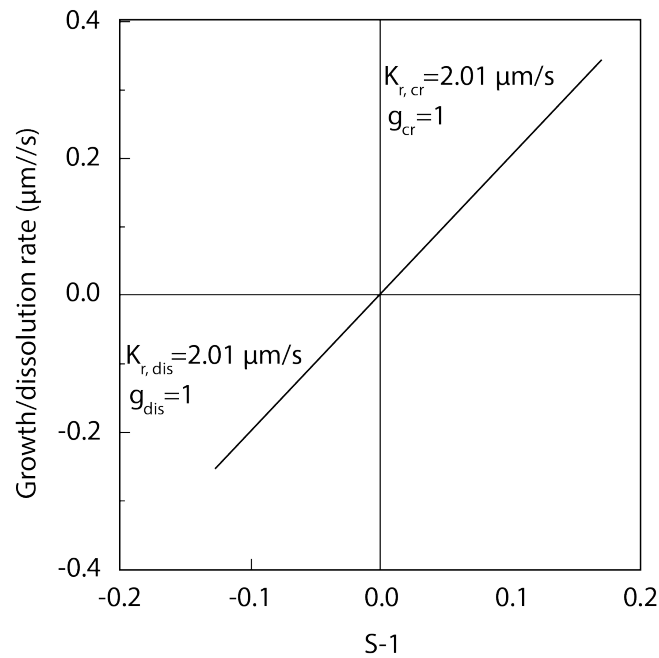


Figure 2.8: Growth rate of mirabilite at 26°C according to the supersaturation S , reproduced from Derluyn (2012).

2.1.1.2.6 Mirabilite growth rate at ambient temperature

The growth rate of mirabilite in function of the aqueous solution supersaturation with respect to mirabilite at 26°C is reproduced from (Derluyn, 2012). The growth rate slope is equal to $2.01 \mu\text{m}\cdot\text{s}^{-1}$ if g_{cr} is assumed equal to 1 (figure 2.8)

2.1.1.3 Magnesium Sulphate ($MgSO_4$)

Magnesium sulfate is precipitated in the sea or marine evaporite in geological settings and like sodium sulphate can be redissolved in hot hydrothermal fluid and enriched hot spring like the thermal bath of Epsom in England that gives its name to epsomite. Kieserite, Hexahydrate and epsomite are the stable magnesium sulphate phase on earth. Interestingly, chemical analysis detects magnesium sulphate in significant quantity in Mars soil and rocks Steiger et al. (2011). The hydrated phase precipitated is not clearly identify. Besides Kieserite, higher hydrates are present. Hydrates are thought to carry a significant amount of the water present on Mars (Peterson et al., 2007; Steiger et al., 2011). $MgSO_4$ may precipitate from a sulfuric acid attack on a magnesium-rich rock like basalt on Mars. On earth, $MgSO_4$ may come from magnesian limestone, dolomitic sandstone and dolomitic lime mortar (Steiger et al., 2011). Rapid decay happens by repeated cycles of deliquescence and crystallisation as well as hydration dehydration of magnesium sulfate (Espinosa-Marzal et al., 2011; Haynes, 2005; Ruiz-Agudo et al., 2007; Steiger, Kiekbusch, and Nicolai, 2008; Steiger et al., 2011) and magnesium sulfate mixture (Lindström et al., 2016). Finally, $MgSO_4$ is studied for energy storage application with the capture of energy during dehydration and energy release during hydration (Okhrimenko, 2018).

2.1.1.3.1 Chemical properties of magnesium sulfate ($MgSO_4$)

The basic properties of magnesium sulphate are displayed in table 2.3. The aqueous solubility product at 20°C is modeled in Phreeqc with the parameter files pitzer.dat (Parkhurst and Appelo, 2013).

Table 2.3: Basic properties of magnesium sulphate

	Molar mass $g\cdot mol^{-1}$	Molar volume $m^3\cdot mol^{-1}$	$KSP_{aq20^\circ C}$
Epsomite	246.48	$1.47\cdot 10^{-4}$	$1.3\cdot 10^{-2}$ Phreeqc (Pitzer)
Hexahydrate	228.46	$1.3\cdot 10^{-4}$	$2.79\cdot 10^{-2}$ Phreeqc (Pitzer)
Kieserite	138.38	$5.38\cdot 10^{-5}$	$6.54\cdot 10^{-1}$ Phreeqc (Pitzer)

2.1.1.3.2 Magnesium sulphate phases stability

At least six phases of hydrate magnesium sulfate exist. Phreeqc simulation based on the Pitzer database (Plummer and others, 1988) is in agreement with the solubility diagram determined by Steiger et al. (2011) for stable phase excepting the undecahydrate that is not represented in figure 2.9. The stable phases are: Meridianiite ($MgSO_4 \cdot 11H_2O$), Epsomite ($MgSO_4 \cdot 7H_2O$) and hexahydrate ($MgSO_4 \cdot 6H_2O$)

solubilities increase with temperature. Kieserite ($MgSO_4 \cdot H_2O$) solubility decrease with temperature and tends to 0. Two metastable phases can be encountered between 0°C and 100°C : starkeyite or leonhardtite ($MgSO_4 \cdot 4H_2O$) and pentahydrate ($MgSO_4 \cdot 5H_2O$).

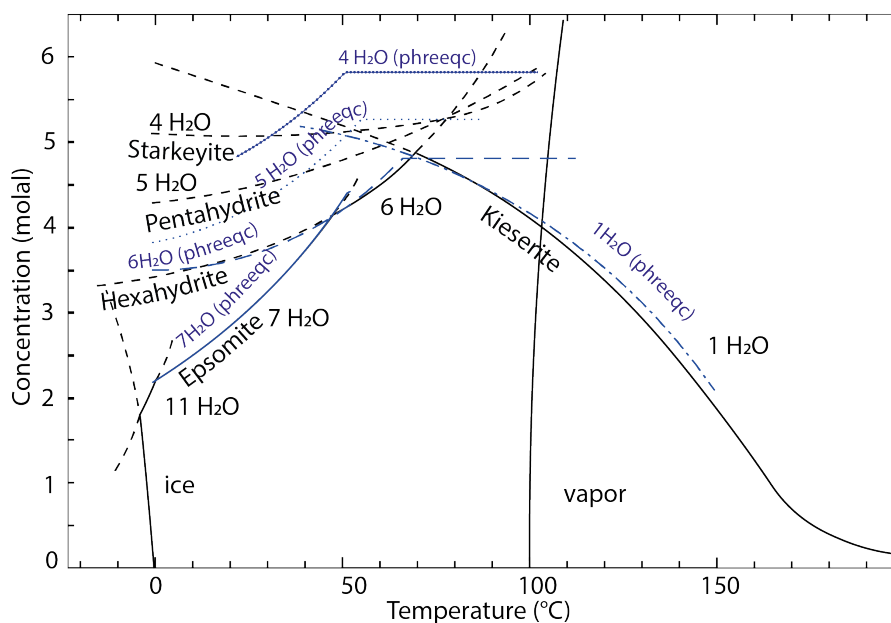


Figure 2.9: Solubility diagram of the system $MgSO_4 - H_2O$ according to Steiger et al. (2011). Solid and dashed curve represent stable and metastable equilibria for ice, vapor, $MgSO_4 \cdot H_2O$, $MgSO_4 \cdot 4H_2O$, $MgSO_4 \cdot 5H_2O$, $MgSO_4 \cdot 6H_2O$, $MgSO_4$, $MgSO_4 \cdot 4H_2O$, $MgSO_4 \cdot 5H_2O$, $MgSO_4 \cdot 6H_2O$, $MgSO_4 \cdot 7H_2O$ and $MgSO_4 \cdot 11H_2O$. Phreeqc calculated solubility with Pitzer database are shown for $MgSO_4 \cdot H_2O$, $MgSO_4 \cdot 4H_2O$, $MgSO_4 \cdot 5H_2O$, $MgSO_4 \cdot 6H_2O$ and $MgSO_4 \cdot 7H_2O$.

The phase diagram of the $MgSO_4 - H_2O$ gives at normal atmospheric conditions the deliquescence humidity of each hydrate phase (figure 2.10). At deliquescence humidity, Meridianiite ($MgSO_4 \cdot 11H_2O$) is the stable phase below 1.8°C (Haynes, 2005; Peterson et al., 2007; Steiger et al., 2011). Epsomite is stable between $1.8 - 48.3^\circ\text{C}$, then hexahydrate is stable until 68°C followed by kieserite stability until 180°C (Haynes, 2005)). By dehydration of a magnesium sulphate-rich solution in Steiger et al. (2011), four main phases precipitated, epsomite, hexahydrate, starkeyite and kieserite. They will precipitate in this order with an increased temperature and reduced RH. Steiger et al. (2011) detected other precipitate like $MgSO_4 \cdot 2H_2O$ and $MgSO_4 \cdot 1.25H_2O$ conjointly with other phases (figure 2.10).

2.1.1.3.3 Metastable phase persistence in the reaction product during dehydration

According to Steiger et al. (2011), kieserite formation is sluggish and metastable magnesium sulphate hydrate like the pentahydrate or starkeyite are major product of the dehydration reaction. Moreover, the persistence of hexahydrate and starkeyite in the reaction product of epsomite dehydration reaction to form kieserite is an issue to establish the final reaction product for energy storage cells and damages induced by $MgSO_4$ phases crystallisation in a porous medium. A study using the ASTM C 88 test on Soundness of Aggregate (Haynes, 2005) measured that during drying of epsomite in an oven, kieserite was precipitated at 112°C . Another study measured after 43 days

of drying at 105°C a partition between $\text{MgSO}_4 \cdot 1.25\text{H}_2\text{O}$ (15%) and kieserite (85%) (Balboni et al., 2011).

2.1.1.3.4 Metastable phase persistence in the reaction product during hydration of kieserite

After the dehydration of epsomite, Balboni et al. (2011) proceeded to the rewetting of the stone plate impregnated with a known mass of kieserite. The thermodynamically stable salt at the experiment temperature (22°C) is epsomite, but hexahydrate may have crystallised first.

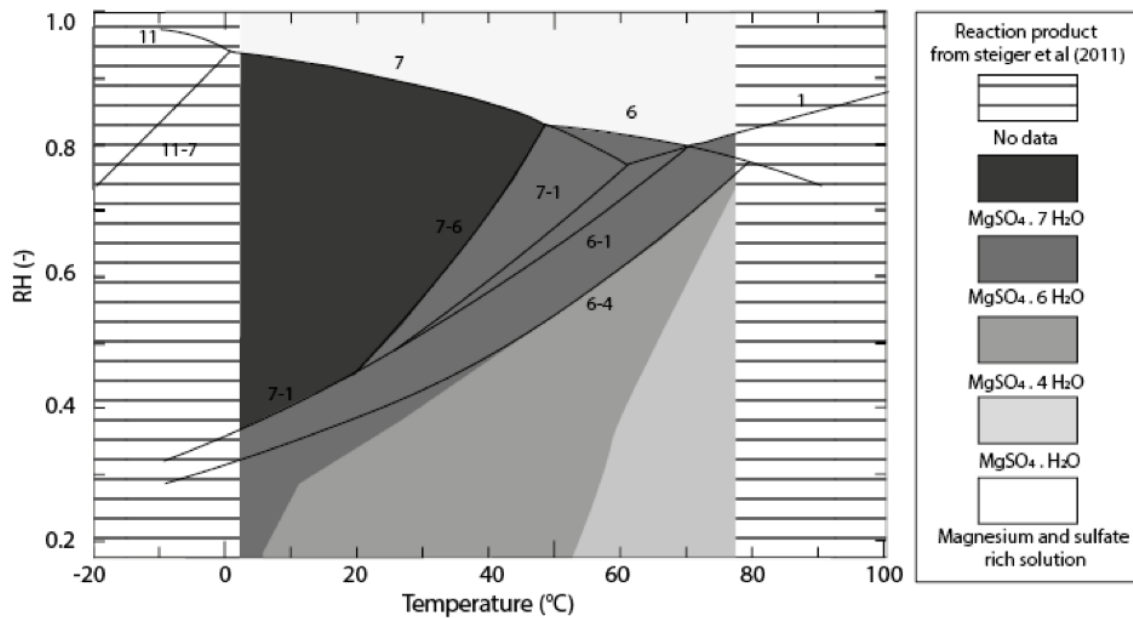


Figure 2.10: Phase diagram of the system $\text{MgSO}_4 - \text{H}_2\text{O}$ of Steiger et al. (2011): equilibrium humidities of (7-6), $\text{MgSO}_4 \cdot 7\text{H}_2\text{O} - \text{MgSO}_4 \cdot 6\text{H}_2\text{O}$; (7-1), $\text{MgSO}_4 \cdot 7\text{H}_2\text{O} - \text{MgSO}_4 \cdot \text{H}_2\text{O}$; (6-4), $\text{MgSO}_4 \cdot 6\text{H}_2\text{O} - \text{MgSO}_4 \cdot 4\text{H}_2\text{O}$; (6-1), $\text{MgSO}_4 \cdot 6\text{H}_2\text{O} - \text{MgSO}_4 \cdot \text{H}_2\text{O}$. Deliquescence humidities of (11) $\text{MgSO}_4 \cdot 11\text{H}_2\text{O}$; (7) $\text{MgSO}_4 \cdot 7\text{H}_2\text{O}$; (6) $\text{MgSO}_4 \cdot 6\text{H}_2\text{O}$; (1) $\text{MgSO}_4 \cdot \text{H}_2\text{O}$. The reaction product are delimited according to magnesium sulphate phase precipitated during dehydration reaction at various temperature done in Steiger et al. (2011).

2.1.1.3.5 Volume change during hydration-dehydration reaction

The hydration of MgSO_4 lower hydrate to higher hydrate, like kieserite to epsomite, increase the crystal volume by 159%. Similarly to Na_2SO_4 , the change in the total volume of water and kieserite combining to form epsomite is only decreasing by 10.9% (Haynes, 2005).

2.1.1.3.6 Epsomite growth rate at ambient temperature

The epsomite growth rate at 25°C is reproduced from Al-Jibbouri, Stregé, and Ulrich (2002) in the function of the aqueous solution supersaturation with respect to epsomite, S-1. The slope of the growth rate is equal to $0.5\mu\text{m}\cdot\text{s}^{-1}$ for $g_{cr} = 1$ (figure 2.11).

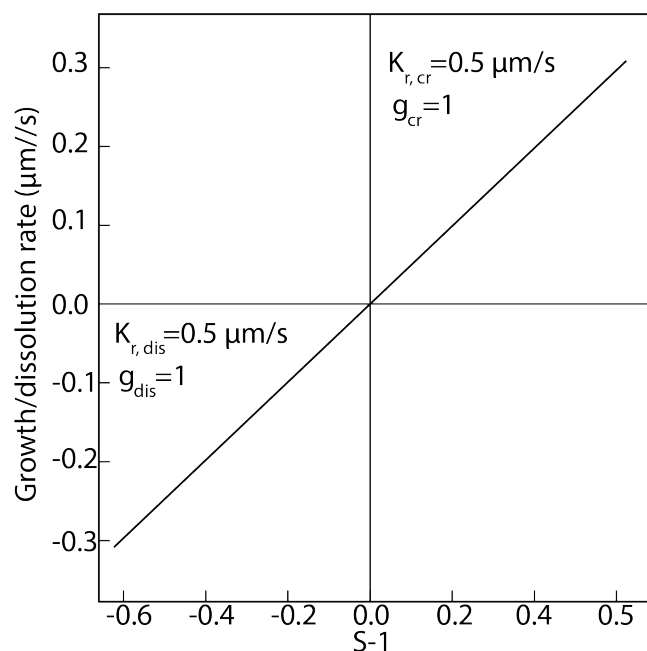


Figure 2.11: Growth rate of Epsomite at 25°C according to the supersaturation S , reproduced from (Al-Jibbouri, Stregé, and Ulrich, 2002).

2.1.1.3.7 Morphology of magnesium sulphate stable phase

Epsomite crystallise in the orthorhombic crystallisation shape and is usually found as fibrous to prismatic acicular fibers. Hexahydrate crystallise in the monoclinic crystal shape, it precipitates in acicular needles, tablet or crust. It often dehydrates in starkeyite. Kieserite crystallise in the monoclinic crystallisation system (figure 2.12).



Figure 2.12: a) Fibrous crystal of epsomite b) Hexahydrate crystal partly dehydrate in whitish starkeyite c) Crystal of kieserite. Kieserite is stored in a waterproof box to avoid hydration in atmospheric conditions.

2.1.2 Experimental porous rock

In this section, we will first describe the mineralogical composition and petrochemical characteristics of the Lavoux limestone and the Adamswiller sandstone based on our own analysis and compared with some literature measurements. Second, the measured mechanical properties of the porous rock will be discussed.

2.1.2.1 Mineralogical and petrochemical description of porous experimental rock

2.1.2.1.1 Lavoux limestone

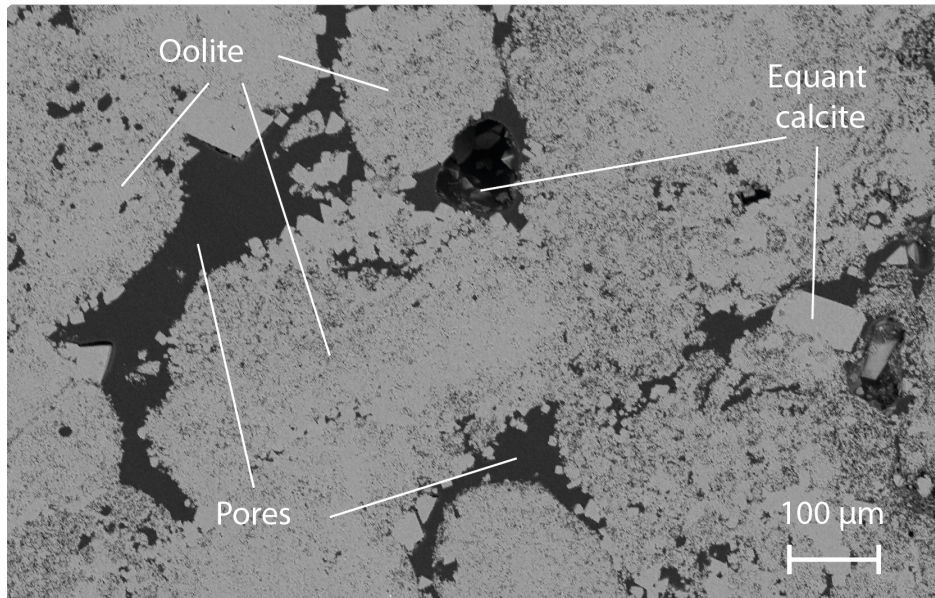


Figure 2.13: SEM observation of Lavoux limestone polish section.

The Lavoux limestone is an extensively studied limestone for CO₂ storage (Kalo et al., 2017; Radilla et al., 2010; Rimmelé, Barlet-Gouédard, and Renard, 2010). It is a Callovian age pelletal, oolitic and bioclastic grainstone originating from the south-west of the Paris basin. Our sample are extracted in the Carrière de la Vienne. It is composed of oolites (100 to 1000 μm size) and echinoderm fragments cemented by syntaxial sparitic cement (equant calcite) with traces of clay and dolomite (figure 2.13).

Mercury intrusion porosimetry (MIP) displays a bimodal pore size distribution with the first peak at 317 nm and a second peak at 20.7 μm (figure 2.14) corresponding to two kinds of pores: intra-oolitic pores with pore entrance radius between 30 nm to 3 μm and the inter-oolitic pore with pore entrance radius between 5 μm and 100 μm . The oolites have more or less a spherical shape. The interoolitic pores have an irregular shape. The porosity measured is equal to 19.2% and the mean oolite grain size is 190 μm .

2.1.2.1.2 Adamswiller sandstone

The Adamswiller sandstone is a Triassic detrital sandstone originating from Bas-Rhin, France (Rimmelé, Barlet-Gouédard, and Renard, 2010). Our sample are extracted in the Rauscher quarry. The red color comes from the ferric oxide that are

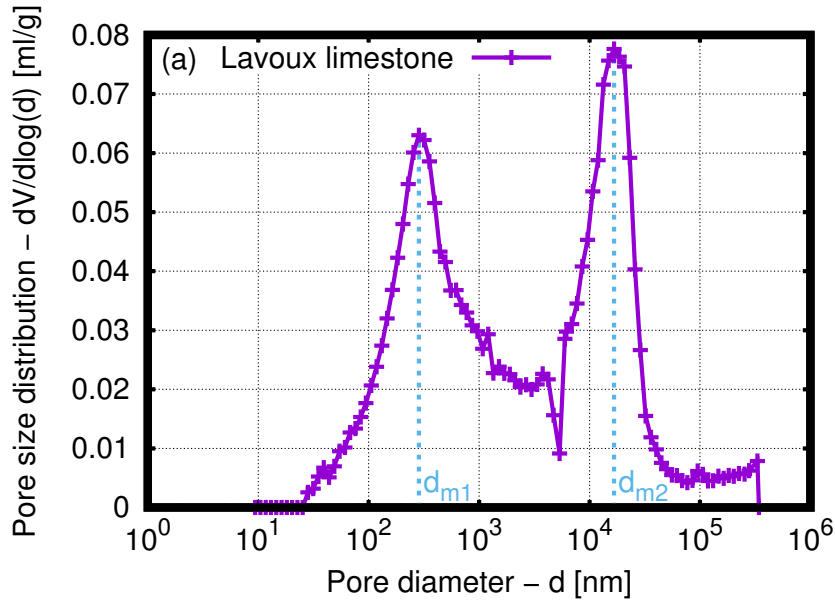


Figure 2.14: Pore distribution in a Lavoux limestone sample characterized with mercury intrusion porosimetry in the LFCR laboratory.

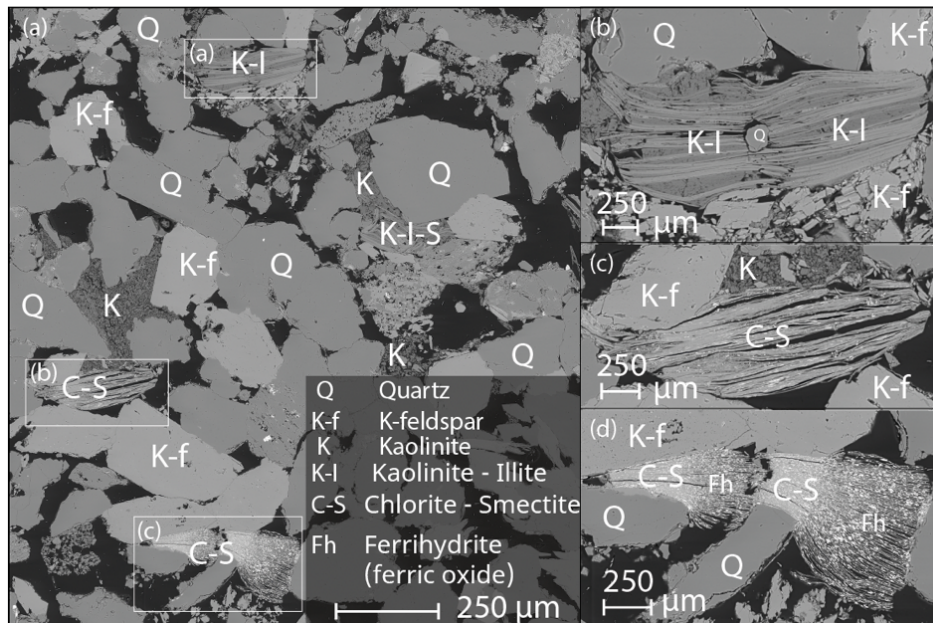


Figure 2.15: BSE 300 nm of a thin section of Vosges sandstone with details on clay particles (a) Representative overview of Vosges sandstone composition. Quartz and K-feldspar are the major elements followed by kaolinite, authigenic illite and chlorite — smectite complex (b) interstratified illite and kaolinite precipitated around a quartz grain. (c) interstratified chlorite — smectite (d) Peeled inter stratified chlorite — smectite filled with ferric oxide or ferrihydrite ([Energy Dispersive X-ray Spectroscopy \(EDS\)](#) interpreted over $3\mu\text{m}$ layer).

alteration product of the iron-rich minerals like magnetite or mica. A quantitative evaluation of the material by QEMSCAN provides the modal mineral distribution of the stone, 59% quartz, 27% feldspar, 6% illite/smectite, 1,5% kaolinite, 1% chlorite, muscovite and minor trace of oxide (titane, ferric) carbonate, sulfur (pyrite) (figure 2.15). Blaise et al. (2016) report, partly dissolved feldspar reprecipitated in illite alongside with Illite-smectite, I-S, and Chlorite- Smectite association, C-S. Pyrite is also precipitated with authigenic clay. K-I complex, as shown in figure 2.15a and b. Chlorite is

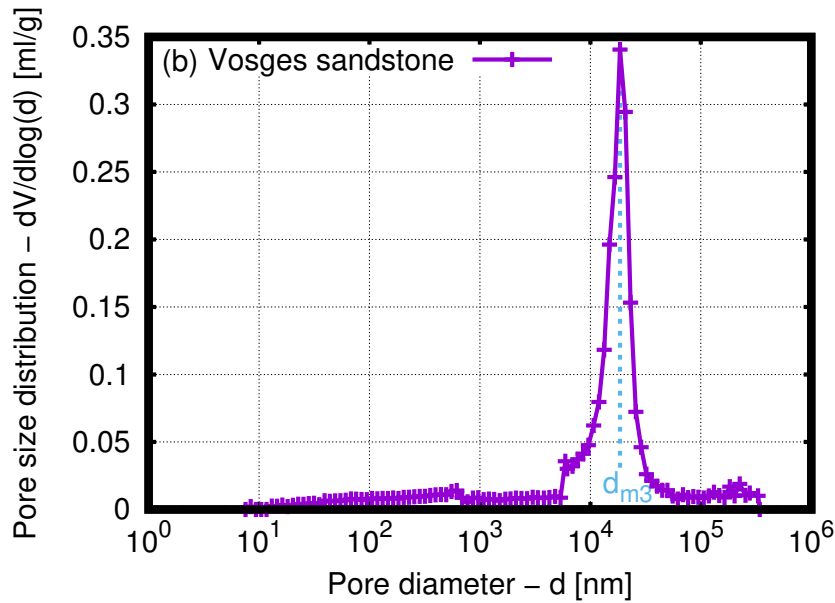


Figure 2.16: Pore distribution in a Lavoux limestone sample characterized with mercury intrusion porosimetry in the LFCR laboratory.

associated with smectite. A whitish mineral is precipitated in the void identified as a trace of ferric oxide or ferrihydrite (figure 2.15a and c). Chlorite — smectite complex, C-S, is torn apart by the swelling induced by the adsorption of hydrated cations, a transformation from smectite to chlorite by addition of a brucite layer and possibly the precipitation of a ferrihydrite (Brandt et al., 2012) (figure 2.15a and d). Considering the illite and kaolinite fraction in our sample of Vosges sandstone, a Cationic Exchange Capacity (CEC) is calculated and ranges between 1.3410^4 molc/kg and 0.0024 molc/kg for the total rock, by taking the theoretical CEC of illite between 10 – 40 molc/kg and kaolinite between 5-15 molc/kg (). Mercury intrusion porosimetry (MIP) displays a unimodal pore size distribution with a single peak at $18.5 \mu\text{m}$ (figure 2.16). The pore entrance radius is between $8 \mu\text{m}$ and $50 \mu\text{m}$. (Rimmelé, Barlet-Gouédard, and Renard, 2010) measure the average pore size at $90 \mu\text{m}$. The porosity measured is equal to 20.5% and the mean quartz and feldspar grain size is $70 \mu\text{m}$. The permeability for a similar stone given in Rimmelé, Barlet-Gouédard, and Renard (2010) is 11 mD.

2.1.2.2 Mechanical properties

2.1.2.2.1 Mechanical Testing procedure

The splitting tensile strength of intact dry core samples is measured according to the ASTM¹ standard. Additionally, the compressive strength and the Young modulus are obtained following the ASTM² standard. The core samples are perfect cylinders with a diameter equal to 25, 40 mm or 100 mm and the length to diameter ratio is between 2.0:1 and 2.0:5 for elastic moduli and compressive strength measurement. For the splitting tensile strength measurement, the diameter to length ratio is above 1:1. The measured mean value are reported in tables 2.4 and 2.5.

¹ASTM D3967-16

²ASTM D7012 – 14

Table 2.4: Mechanical rock properties

	Splitting tensile strength (MPa)	Young Moduli (GPa)	Uniaxial compressive strength (Mpa)
Lavoux	8.6	17 (Van Den Abeele, 2002)	25 (Van Den Abeele, 2002)
Adamswiller	4.9±0.5	9.8±0.4	24.1±4.1

2.1.2.2.2 Bulk moduli and Biot modulus estimation

Table 2.5: Elastic moduli of Adamswiller sandstone

	Poisson ratio 1.23	Bulk modulus (GPa)	Shear modulus (GPa)
Adamswiller	0.24	6.3±0.3	4.0±0.2

The modeling of an effective medium corresponding to the Adamswiller sandstone necessitates knowing the Bulk and Shear moduli of the dry rock. Ultrasonic P wave is propagated through different dry Adamswiller sandstones and acquired with the Richter mini system in the ENS Geosciences laboratory (UMR 8538). After Matlab postprocessing, the P wave velocity is averaged to 2300 m/s. The mean P wave velocity combined with the Young modulus gives a Poisson equal to 0.16. The calculated Poisson modulus is too low compared to the values of Adamswiller sandstone Poisson ratio reported in Mohamad-Hussein and Ni (2018), 0.24 and Rimmelé, Barlet-Gouédard, and Renard (2010), 0.25. We will keep the value of 0.24. The elastic moduli and Poisson ratio are reported in table 2.5.

Table 2.6: Biot coefficient and elastic moduli of the skeleton

	Biot coefficient	Skeleton bulk modulus (GPa)	Skeleton shear modulus (GPa)
Adamswiller	0.62	7.89	7.23

The elastic moduli of the skeleton, K_m and G_m are calculated by resolving the auto-coherent schema in the dry case, taking for the homogenised medium elastic properties the mean elastic moduli in table 2.5. It necessitates knowing the porosity, 20.5 %, and the elastic moduli provided in table 2.5 of the Adamswiller sandstone. The Biot coefficient, b , is related to the Bulk modulus of the Adamswiller sandstone skeleton and the bulk modulus of the drained Adamswiller sandstone $b = 1 - \frac{K}{K_m}$ (table 2.6).

2.2 Methods

In this section, we will introduce the monitoring methods used to analyse the chemical species precipitated, the deformation and the elastic properties of the porous medium. The two experimental techniques are the 3D X-ray microtomography and the ultrasonic wave active and passive monitoring. These techniques are advantageously non-destructive. In the first part, we give the relation between matter and X-ray. In the second part, we will describe the principle of ultrasonic monitoring and acoustic emission acquisition.

2.2.1 3D X-ray micro tomography

2.2.1.1 Definition

X-ray microtomography is a 3D imaging method that reveals the internal structure of the studied object. The chemical elements are attenuated according to their atomic number: the heavier their atomic nucleus, the more they will be attenuated. Beer-Lambert law expresses the attenuation of X-ray passing through matter. It uses the absorption coefficient, μ calculated with the absorption coefficients, $\mu_{species1}$ (depends on energy), of the mineral constituting the material and concentrations of the mineral, $C_{species_i}$ (we shall here consider the density of the different phase). We shall not forget the phase filling the pore: water or air.

$$\ln \frac{I}{I_0} = \mu_{species1} * C_{species1} + \mu_{species2} * C_{species2} \quad (2.1)$$

For a given mineral, the profile of the absorption coefficient globally decreases with a growing level of photonic energy and is characterized by a peak of absorption at a certain level of photonic energy. An optimum level of energy can be set to take advantage of the different X-ray absorption peaks between minerals. and fluids constituting a material and then differentiate them (Derluyn, 2012). However, the absorption peaks appear in majority at low photonic energy, necessitating a longer exposition so that a sufficient level of energy reach the X-ray detector. It is worth noting that to preserve the X-ray source, it is not recommended to proceed to an X-ray acquisition longer than 24 hours.

2.2.1.2 Use of X-ray tomography

Table 2.7: Technical characteristics of X-ray MicroCT Skyscan 1172 (Bruker)

Level of energy (keV)	Resolution μm	Sample max diameter (mm) Sample max height (mm)
30 to 100	3 to 27.26	50 x 100

We plot in figures 2.17 and 2.18 the evolution of the absorption coefficient of minerals and fluids involved in our experiments, between 1 keV and 100 keV in the energy range of the micro-CT skyscan described in table 2.7 (source NIST³). In figure 2.17, the X-ray absorption energies of the skeleton minerals (calcite for Lavoux limestone and quartz and K-feldspar for the Adamswiller sandstone) are compared with the X-ray

³<https://www.nist.gov/pml/x-ray-mass-attenuation-coefficients>

absorption of the precipitated mineral, barite and water and air that are absorbent at low photonic energy. Barite is very absorbing at every depicted energy level and as such the distinction is straightforward between barite, the skeleton of the Lavoux limestone or the Adamswiller sandstone and the fluids.

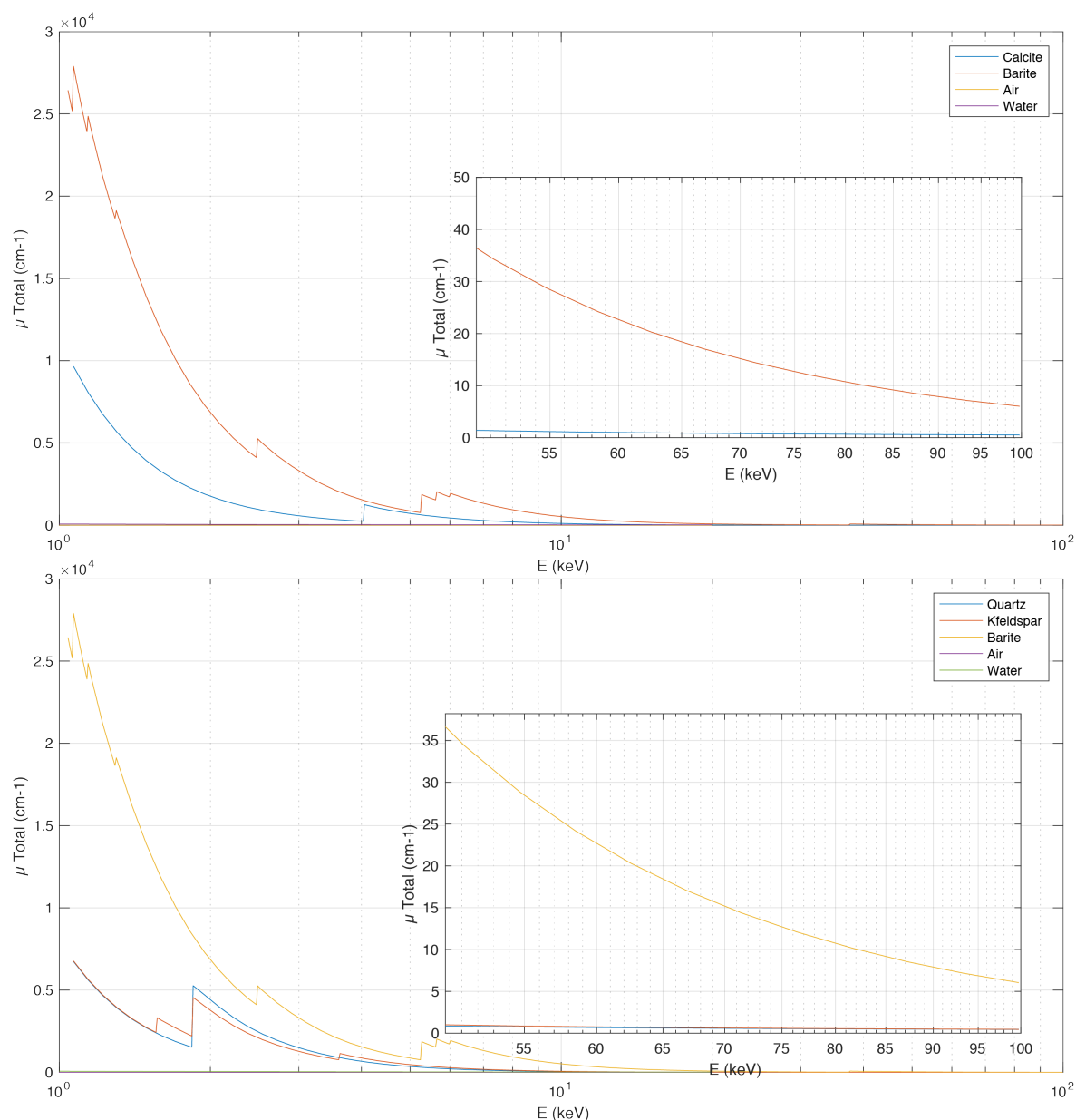


Figure 2.17: X-ray absorption comparison of chemical species present in the experiments with barite. Top: Xray absorption of barite, calcite, water and air between 1 and 100 keV and focus on 50 to 100 keV. Bottom: Xray absorption of barite, quartz, K-feldspar, water and air between 1 and 100 keV and focus on 50 to 100 keV.

In figure 2.18, top, the X-ray absorption of sodium sulphate stable phases (thenardite and mirabilite) are compared with the X-ray absorption of Quartz, K-feldspar and air, constituting the skeleton of Adamswiller sandstone. At a low energy level (< 3 keV), the peaks in X-ray absorption of thenardite and the skeleton can be exploited to distinguish them. By contrast, at 100 keV, the X-ray absorption diagrams are too similar to distinguish them. Mirabilite X-ray absorption is lower at every energy level than thenardite and the skeleton of the Adamswiller sandstone. In figure 2.18, bottom, the

X-ray absorption coefficient of magnesium sulphate phases (kieserite and epsomite) are compared with the skeleton of the Adamswiller sandstone and air. At low energy level (< 3 keV) the contrasting peaks in X-ray absorption can be exploited and at 100 keV, the precipitated salt is less X-ray absorbent than the skeleton. In both case, the fluid is the less absorbent phase.

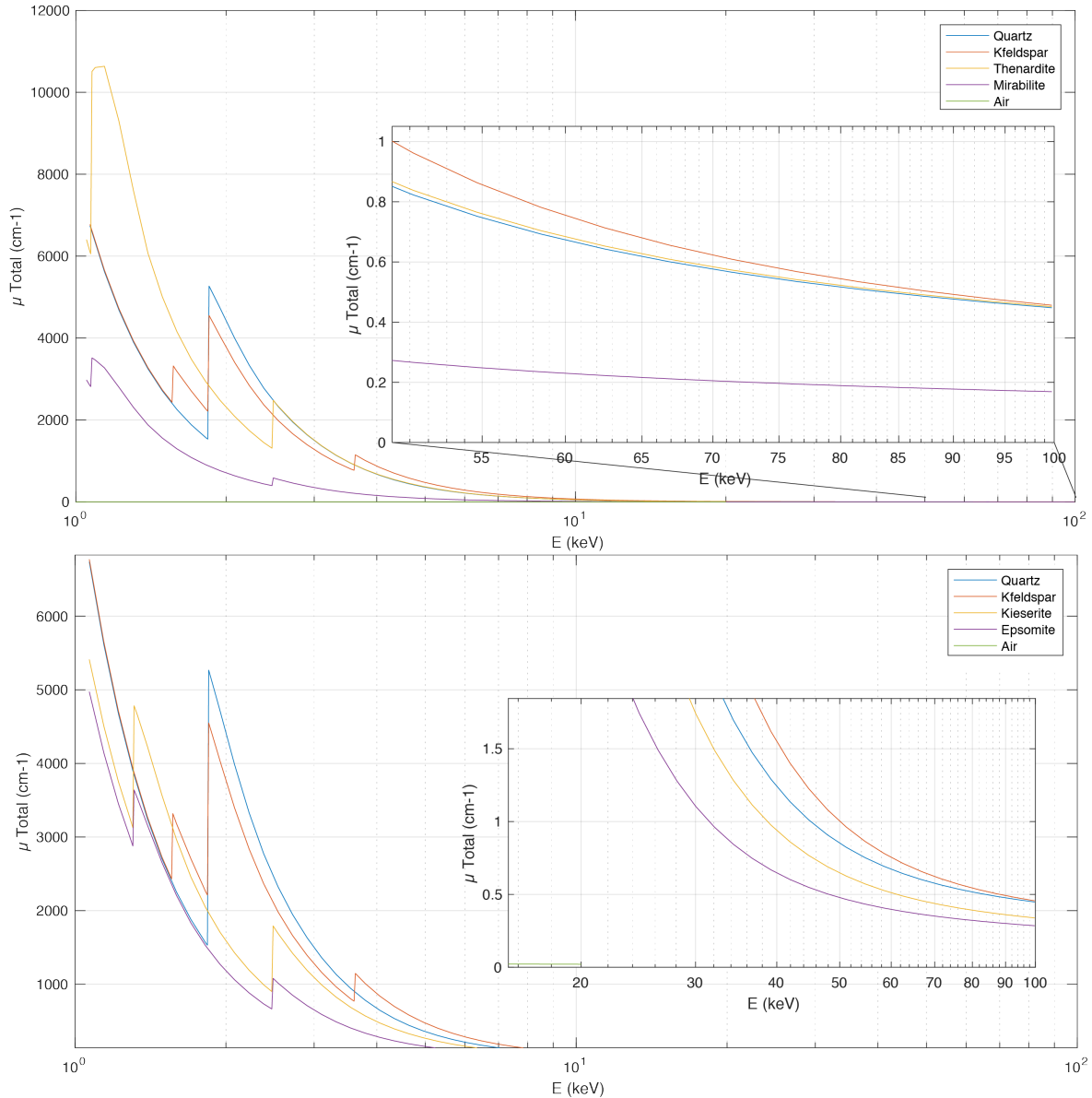


Figure 2.18: X-ray absorption comparison of chemical species present in the experiments with Sodium sulphate and magnesium sulphate. Top: Xray absorption of thenardite, mirabilite, quartz, K-feldspar and air between 1 and 100 keV and focus on 50 to 100 keV. Bottom: Xray absorption of kieserite, epsomite, quartz, K-feldspar and air between 1 and 100 keV and focus on 20 to 100 keV.

2.2.2 Ultrasonic wave monitoring and acoustic emission

The Lead zirconate piezoceramics have the interesting property to vibrate when submitted to an electric signal and to return an electric current when vibrating. This property of PZT make them a good tool to survey the conditions of various industrial buildings like dams, nuclear power plants, bridges or experimental sample (Fortin et al., 2006; Grégoire et al., 2015; Incel et al., 2019; Marty et al., 2019; Menéndez and David, 2013). Indeed, microcracking produces vibration in the ultrasonic frequency range that can be recorded by the PZT. Additionally, by monitoring ultrasonic wave propagation in the material, the 'shot', the time spectrogram of the wave lets evaluate the pore fluid saturation and the evolution of the damage (Barrière et al., 2012; David et al., 2017a,b; Fortin, 2007; Pimienta et al., 2019). Figure 2.19, right presents a sample instrumented with 8 P-PZT aligned vertically and positioned by pair on opposite side of the sample cylinder surface at different heights to evaluates the evolution of the material properties between these pairs of PZT.

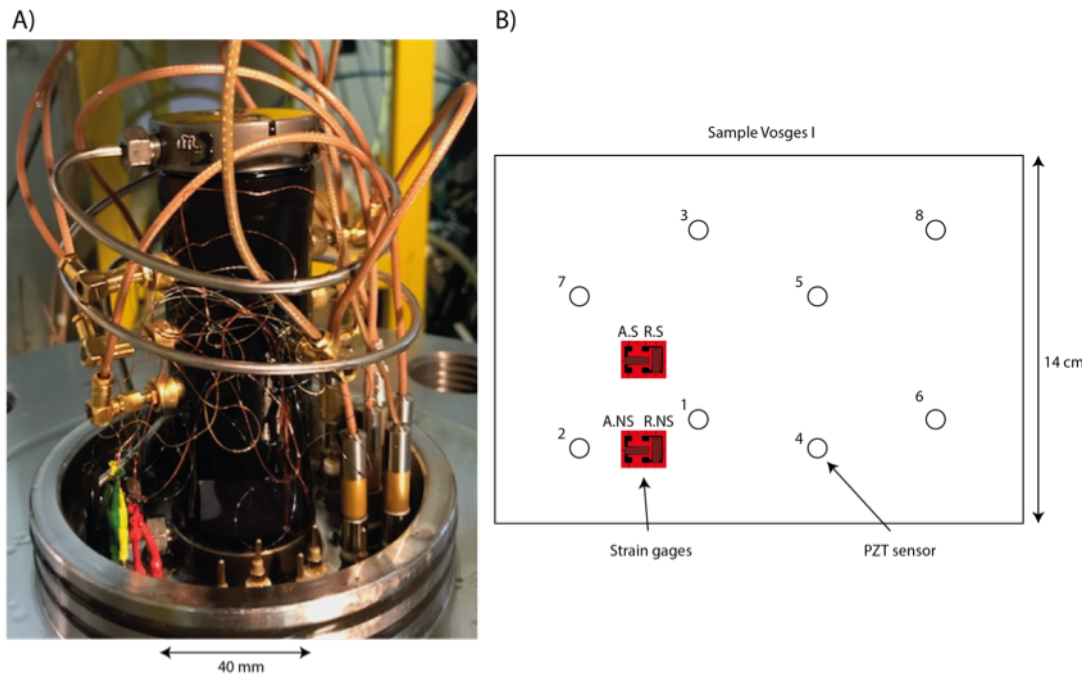


Figure 2.19: Right: Sample clamped in a neoprene jacket instrumented with eight piezoelectric transducers and four radial axial strain gauges and positioned in the 'Geodesign' cell designed and constructed by the company Geodesign figure A.1. Left: Cylindrical projection of the PZT and the strain gauges position on the hole pierced jacket.

2.2.2.1 Monitoring of Acoustic Emissions

2.2.2.1.1 Nature of Acoustic emission (AE)

An AE is a transitory elastic wave resulting from local micro displacement in a solid material. Plastic deformation, rupture mechanism, corrosion, friction, mechanical impact, micro-cracking are sources of acoustic emission. Two type of AE are distinguished:

- discrete AE or 'Hit', a sinusoid linked to high energy emission mechanism like crack propagation,

- continuous **AE**, a serie of discrete **AE** that cannot be distinguished from each other. Constantly active phenomenon like plastic deformation can induce such continuous **AE**.

2.2.2.1.2 Detection and recording

The detection of **AE** is as follows: a detection threshold is set for each channel with regards to the background noise to capture the **AE**. When the electrical signal transmitted by the preamplifier exceeds this value, the signal is recorded. The mechanical oscillation is transformed by the **PZT** into an electrical signal. The signal is reamplified (40 dB). Then a system board digitizes and transfers the **AE** data to a PC for data storage and analysis (figure 2.20). This record is denominated 'Hit'. The final objective is the determination of the **AE** hypocenter: if at least 4 **PZT** out of the 8 **PZT** detect the **AE**, the system will compare the 'Hit' with each other to gather them in an 'Event' and calculate the corresponding hypocenter. The major pieces of information extracted from the signal are:

- the first arrival time (s) to locate the 'Event' with at least four values,
- the amplitude (dB) is the maximum amplitude detected on the **AE** signal. It is calculated according to 2.2,
- absolute energy (attoJoule) which is derived from the integral of the squared voltage signal divided by the reference resistance over the duration of one second.

$$dB = 20 * \log\left(\frac{V_{max}}{1s} * \mu_{volt}\right) - PreamplifierGain(indB) \quad (2.2)$$

The amplitude and the absolute energy associated with the 'Event' hypocenter are relevant for differentiating a process zone (low energy) and a crack (high energy) (Grégoire et al., 2015).

2.2.2.2 Principle of ultrasonic wave monitoring technics

Basically, ultrasonic wave monitoring is the emission of a well-known short mechanical oscillation by a source **PZT** and the recording of the oscillation after a certain time by the receivers. Two types of **PZT** with different polarization are available to emit/receive shear (S) waves or compressional (P) waves. Each transducer will act alternatively as a source while the other will be set as receivers. The received signal is a 'shot'. Providing a sufficient number of **PZT**, the 3D velocity tomography or 3D inelastic strain distribution like in Zotz-Wilson et al. (2020) is achievable.

The analysis of the ultrasonic wave monitoring consists of the picking of the acoustic signal first arrival which gives the oscillation propagation time and lets us calculate the wave mean velocity along the wave path. If P and S waves are picked, the mechanical properties of the studied sample are accessible. The amplitude and velocity of the P-wave and S-wave are good indicators because they change with the fluid saturation in the porous medium (David et al., 2017a,b; Sarout, 2012).

2.2.2.3 First arrival picking method

For the 'shot' analysis, the data are extracted and post-processed in MATLAB (2010). Different picking routines of the acoustic signal first arrival were computed:

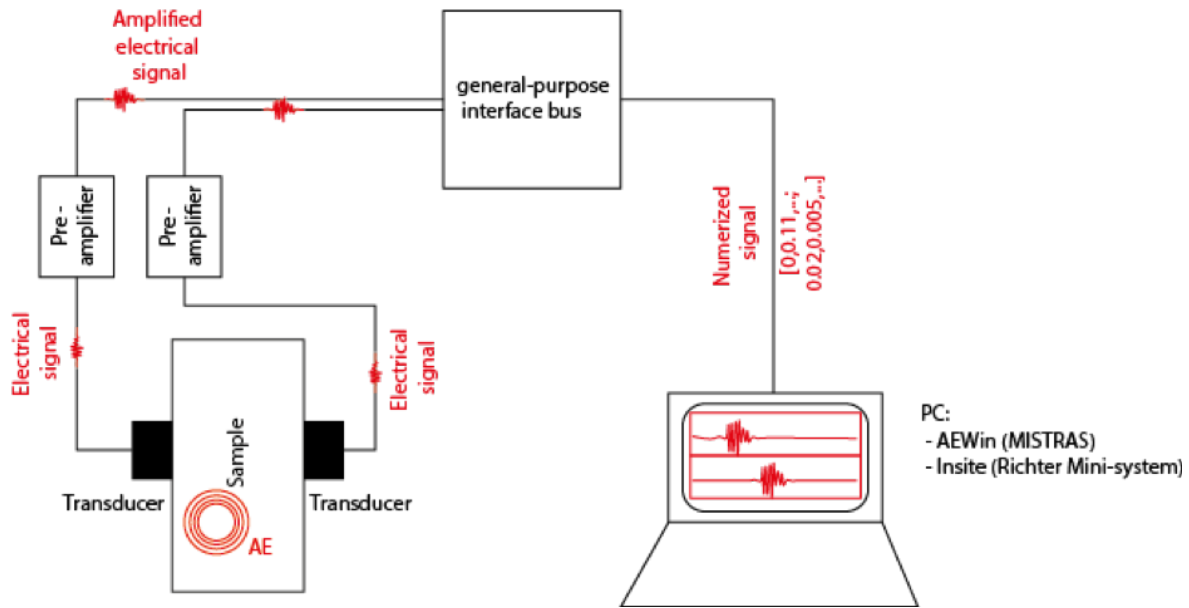


Figure 2.20: Schematic representation of system measuring ultrasonic wave propagation through a sample and the detection of acoustic emission.

automatic double picking, semi-automatic double picking and manual picking (appendix A.2). The automatic picking algorithm was computed based on the double picking algorithm proposed in Fortin (2007). The maximum frequency of the signal is determined and two sinusoids having the frequency equal to the maximum of the FFT of the signal are drawn, one passing by the maximum amplitude value of the signal and the other one by the minimum amplitude value of the signal. We enter a starting velocity and the algorithm will pick in a window centered on the starting velocity, the crossing point between sinusoids and the abscissa ax. The velocity is the median of the two crossing points. Next, the velocity becomes the reference velocity for the next shot and so on. Semi-automatic has the same principle excepting that the reference velocity is the velocity picked manually. By using these automatic and semi-automatic methods we faced the problem of transmitted wavelet frequency evolution pointed by David et al. (2017a) during transient saturation of the sample for example. For this reason, we concluded that manual picking remained the preferential method as may be observed on figure 2.21 where we see that the manual picking curve (blue curve) sticks to the signal first arrival while the automatic double picking of the first arrival (red curve) overvalues the velocity increase due to the wavelet frequency evolution. The drawback to the manual picking methods is that it is difficult to give a better estimation of the manual picking accuracy than roughly $\pm 25\text{-}50 \text{ m}\cdot\text{s}^{-1}$. The picked diagram of the shot transmitted between the pairs of PZT is visible in appendix A.3. For a matter of clarity, they are represented with the function imagesc available in MATLAB (2010) but in fact, we manually picked the signal plotted on the same graph with the ordinate corresponding to the shot emission time (every 2 or 5 minutes depending on the experiment duration) and the abscissa to the signal time in μs or the velocity in $\text{m}\cdot\text{s}^{-1}$.

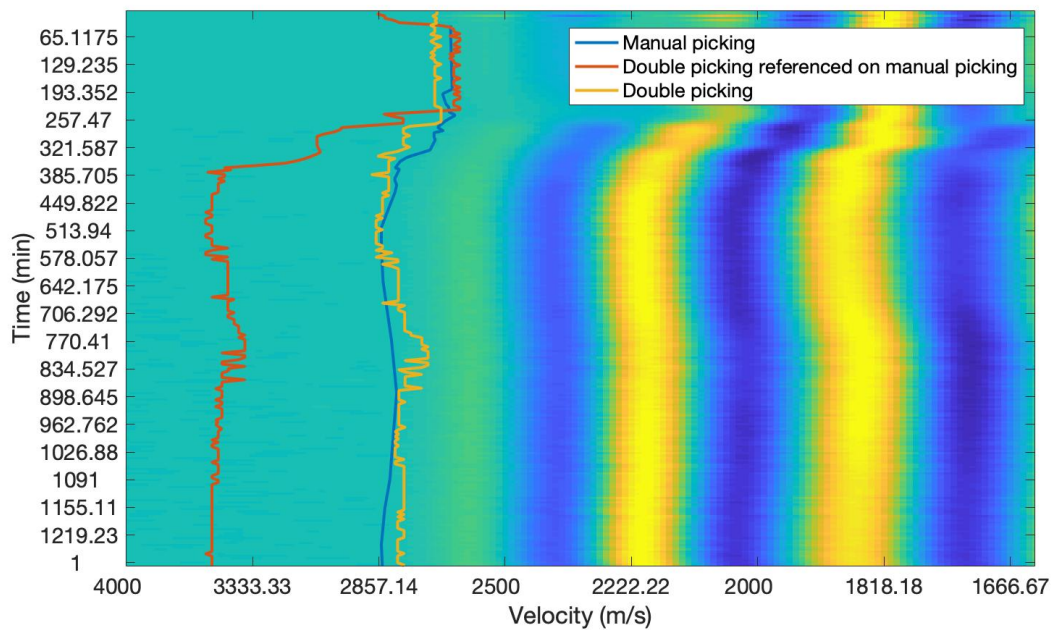


Figure 2.21: Example of spectrum of P wave propagated horizontally through a sandstone cylinder during water capillary uptake and overprinting of manual and automatic double picking profiles.

2.2.2.4 Description of “Richter Mini-system”

The acoustic monitoring system owns to the geological laboratory of Ecole Normale Supérieure (UMR 8538)⁴. It adapted to a wide range of experiment from the study of compaction band (Fortin, 2007; Fortin et al., 2009) to high energetical laboratory earthquakes (Aubry et al., 2018; Marty et al., 2019). It is an 16 channels system with transducer resonant frequency at 1 MHz. The wave propagation through the porous sample filter the signal at 500 kHz. The sensor diameter is 5 mm and the sensor are fitted in holes pierced in a neoprene jacket and bonded on the sample with epoxy or superglue, figure 2.19. This system is integrated in the ‘geodesign cell’, a triaxial cell with a hydrostatic pressure up to 300 MPa and a deviatoric pressure up to 700 MPa, figure A.1. Prior to an experiment, the correct coupling between the sensor and the sample is checked by evaluating the transducer response on the oscilloscope during shot survey (similar to AST). The visualisation and analysis software InSite Seismic processor made by ITASCA Ltd⁵ streams the data stored and displays the ‘Shot’ and the ‘Event’ signals.

InSite provide two options to pick the wave packet first arrival: automatic or manual. An autopicking tool can be trained by the user to improve the picking. To localise the AE, the user can choose an isotropic velocity model or with an upgraded license more model are open which may better fit the reality of the sample. Several localisation algorithms are proposed using the first P-wave arrival and the first S-wave arrival when available.

Another acoustic monitoring system, the MISTRAS system, is used in chapter 5. It locates the acoustic emission hypocentres, records the hits, and logs the absolute acoustic energy but the shots picking is not available.

⁴<http://www.geologie.ens.fr/recherche/plateformes/plateforme-experimentale/>

⁵<https://www.itascainternational.com/software/InSite-Lite>

2.2.3 Strain gauges

Together with the acoustic monitoring by the Richter Mini System, four FCB-6-350 (Tokyo Measuring Instruments Laboratory Co., Ltd) metal-foil strain gauges with axial and radial orientations are glued at the bottom of the sample lateral surface and the surface of the salt impregnated sample lateral surface. A detailed description of typical sample preparation is provided in Borgomano (2019). The strain gauges implemented in the geodesign cell have connectivity issues. This is why the strain gauges profiles are not plotted in every experiment.

Chapter 3

Unclassical crystallisation of barite during diffusion driven barite precipitation in sedimentary rock

Contents

3.1	Introduction	76
3.2	Materials and methods	76
3.2.1	Materials	76
3.2.2	Experimental protocol	76
3.2.3	Characterization methods	78
3.3	Results	79
3.3.1	Barite front precipitation in Lavoux limestone	79
3.3.2	Barite front precipitation in Adamswiller sandstone	80
3.4	Discussion	84
3.4.1	Preliminary discussion on minerals of barite group precipitation in sedimentary porous rock	84
3.4.2	Discussion on barite crystallisation in sedimentary rock	86
3.5	Conclusion	89

*CHAPTER 3. UNCLASSICAL CRYSTALLISATION OF BARITE DURING
DIFFUSION DRIVEN BARITE PRECIPITATION IN SEDIMENTARY ROCK*

Abstract

The need to investigate mineral precipitation in natural sedimentary rock with complex pore network and mineral composition arise with problems like pore clogging by barite precipitation during sulfate-rich water injection in geological reservoirs or crystallisation pressure induced by precipitating crystals in the porous medium. At the LFCR (Laboratory of Complex Fluids and their Reservoirs, Pau, France), we aim to reproduce geological objects in laboratory conditions. In this frame, we built a contra-diffusive set up to precipitate a barite front in two sedimentary rock samples, a Lavoux oolitic limestone and a Vosges Sandstone with a fraction of clay. Two opposite reservoirs are filled with BaCl_2 and Na_2SO_4 dissolved in milli-Q water to ensure precipitation of barite. In the end, the sample is scanned with X-ray microtomography and set into a polish section for further MEB/EDS microanalysis. A connected barite front is witnessed in the Lavoux limestone. Fine Barite aggregates preferentially precipitate in small rough micritic intra-oolitic pores of the in the Lavoux sample, whilst the large crystals precipitated in large pores have often an orientation perpendicular to the pore wall. In the Vosges sandstone, the barite front is scattered with well-crystallised barite precipitated in large pores and a more striking thin layer of barite precipitated in the interfoliar space of chlorite - smectite complex. Finally, theoretical values of crystallisation pressure exerted during barite precipitation are a first step toward the experimental generation of barite crystallisation induced damages in a confined porous rock.

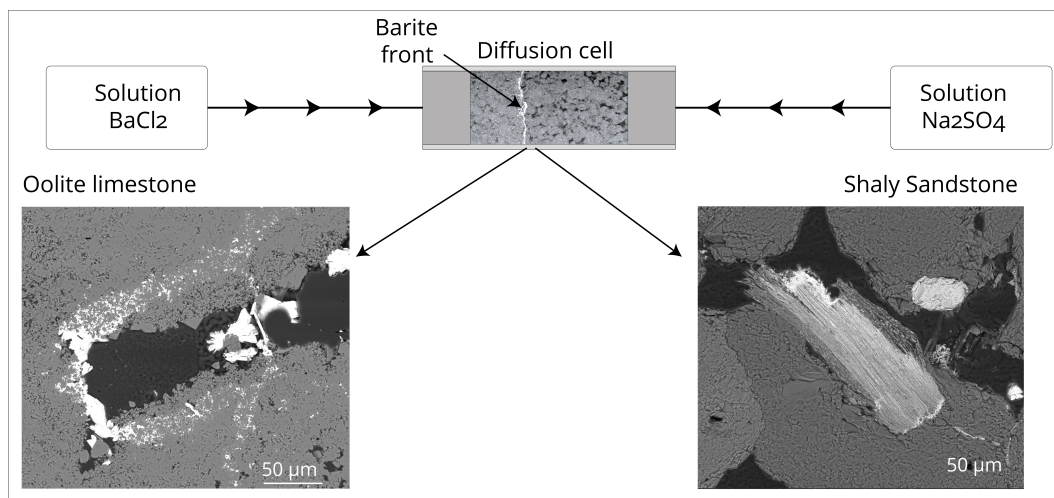


Figure 3.1: Graphical abstract.

3.1 Introduction

Barite precipitation has been extensively studied to improve the understanding of crystal homogeneous nucleation (Prieto, 2014; Putnis and Fernandez-Diaz, 1990; Putnis, Prieto, and Fernandez-Diaz, 1995), to explore growth rate and ontogeny of crystals of the barite group in porous media (Godinho and Stack, 2015; Prieto et al., 1992; Putnis, Prieto, and Fernandez-Diaz, 1995) and to propose inhibition solutions for barite clogging in porous reservoirs during seawater injection. More recently, with the problem of durability of long-term storage of nuclear waste in a deep geological repository, concerns arise on the interaction between the cementitious materials and the formation water from the surrounding clay host rock (Fukatsu et al., 2017; Melkior et al., 2009; Poonoosamy et al., 2016; Poonoosamy et al., 2020, 2015). More recently, (Rajyaguru et al., 2019) studied a set of two diffusion-driven reaction experiments focusing on precipitation of barite and gypsum in low permeability chalk. In parallel, numerous studies point out that crystallisation pressure may cause deformation in geological settings (Merino, Canals, and Fletcher, 2006; Noiriél et al., 2010; Wallace and Hood, 2018; Wiltschko and Morse, 2001). In this context, the occurrence of fibrous barite veins is documented (Cobbold et al., 2013) with a growing assumption that fibrous veins are caused by crystallisation (Bons, Elburg, and Gomez-Rivas, 2012; Hilgers and Urai, 2005; Ukar et al., 2017; Wiltschko and Morse, 2001) and that the ions are transported to the growing fibers by diffusion (Elburg et al., 2002). Therefore, we choose to precipitate barite in porous sedimentary rocks by adapting the contra diffusive experiment originally performed in silica gel (Prieto, 2014; Putnis and Fernandez-Diaz, 1990; Putnis, Prieto, and Fernandez-Diaz, 1995). We expected to obtain crystallisation pressure-induced damage during barite precipitation because barite could reach high supersaturation (Putnis, Prieto, and Fernandez-Diaz, 1995) a key term in the equation of crystallisation pressure (Correns, 1949; Steiger, 2005a).

3.2 Materials and methods

3.2.1 Materials

Two porous media are chosen to precipitate a barite front: a Lavoux limestone, a calcite pure porous medium with a pore fraction equal to 19.2%. The choice for the Lavoux is motivated by the well defined double porosity peaked at 317 nm and 20.7 μm and the calcite purity close to 98%. The sandstone is an Adamswiller sandstone (otherly termed Vosges), a reddish sandstone composed of Quartz, K-feldspar and a clay fraction with a porosity equal to 20.5% sampled in the Rauscher quarry (Bas-Rhin, France). The sandstone is chosen to test the influence of the clay fraction on barite precipitation. The porous rocks and barite are extensively described in section 2.1 of chapter 2.

3.2.2 Experimental protocol

The contra-diffusive experiment is set up with two reservoirs containing the same volume of solution connected with a valve to the diffusion cell, as depicted in figure 3.2. The diffusion cell consists of a porous rock sample, beforehand washed with deionised water then fully dried, clamped between two stainless steel inlets and confined with a sticky heat shrinkable covering. The distance between the sample and the reservoirs

are set at 8 cm. The dimensions of each rock sample are given in table 3.1. Two experiments are reported with two different porous medium. The contra diffusive test with Lavoux oolite limestone is designated with BF_L for barite front Lavoux. The test with Adamswiller sandstone is entitled BF_V for barite front Vosges. With this experiment we aim to precipitate a barite, $BaSO_4$, front in the porous rocks by contradiffusion of the Ba^{+2} rich $BaCl_2$ dissolved solution and the SO_4^{2-} rich Na_2SO_4 dissolved solution.

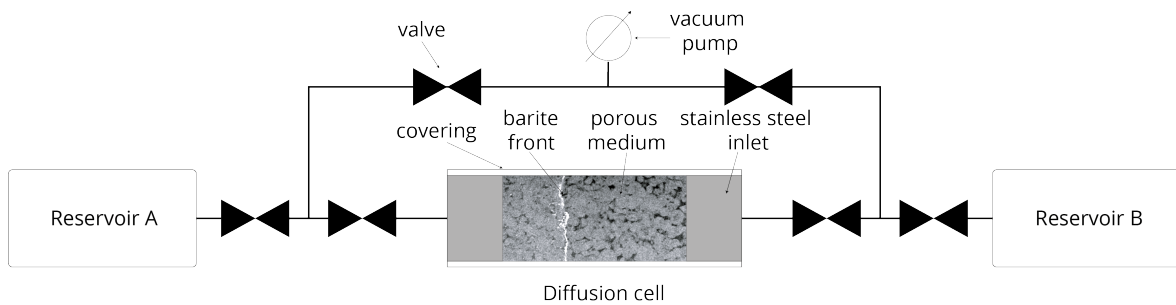


Figure 3.2: Experimental set-up. The core sample assembled with stainless steel inlet at both sides is tightened in a sticky heat shrinkable covering. The cell is located at an equal distance between the reservoir containing the solutions and tightly connected with PFA tubing of 1 inch and valves (Swagelok). A vacuum pump, PK 4 D57 712 (Pfeiffer vacuum) is connected to remove air from the circuit before saturating the circuit with the solutions.

The diffusion cell is prepared by fully saturating the cell and the sample inside with deionised water following the European Norm EN 1936: 1) the diffusion cell is placed vertically in a vacuum bell jar connected to a vacuum pump for at least 2 hours at 2 kPa to fully empty the sample. 2) Pure water (Milli- Ω from Millipore, 18 M Ω cm at 20°C) is slowly added until the top of the cell is covered. 2 kPa needs to be maintained for 15 min after adding the water. 3) The diffusion cell is kept at atmospheric pressure for at least 24 hours. The diffusion cell is connected to both reservoirs and the vacuum pump by means of tubing of equal length separated by valve. Before opening the reservoir valves, the tubing in between the reservoir valve and the cell valve is emptied for a couple of minutes, then the valves are open and saturate the tubing until the diffusion cell valves. The valves on the tubing connecting the now disconnected vacuum pump are used to equalize to the atmospheric pressure the pressure in the tubing and the reservoirs. The absence of air bubbles is controlled. Finally, the two diffusion cell valves are opened simultaneously.

The duration of each experiment is set according to simulations computed on Phreeqc (Parkhurst and Appelo, 2013) ensuring that the simulated saturation in the sample reached the experimentally measured supersaturation threshold obtained with similar starting concentrations in silica gel (Putnis, Prieto, and Fernandez-Diaz, 1995). The simulated pH in the cell at the barite precipitation site does not exceed 7.3. To

Table 3.1: Experimental conditions

Exp. reference	Rock type	Dimension (D(mm)xL(mm))	Duration (day)
BF_L	Lavoux limestone	25 x 38	66
BF_V	Adamswiller sandstone	6.9 x 25	75

minimize transport in a rotational flow induced by convection based on density difference between electrolytes (Poupeleer, 2007), the concentration in reservoir B is fixed at 0.5 molal of Na_2SO_4 while the concentration in reservoir A is 0.34 molal of $BaCl_2$. The density of solution in reservoir A is 1.043 by adding 7.1 gram of Na_2SO_4 to a volume of 100 ml of pure water and the density in reservoir B is 1.06 by adding 8.32 gram of $BaCl_2 \cdot 2H_2O$ to a volume of 98.7 ml of pure water. The sample is removed and characterized using the techniques described in the next section.

3.2.3 Characterization methods

3.2.3.1 X-Ray micro tomography

A Bruker Skyscan 1172 (UMS 3360 DMEX, UPPA) is employed to acquire X-ray microtomography scans of the rock samples to investigate the precipitated barite front and the microstructure of the porous medium in 3D. One post-mortem scan of the barite front precipitated in Lavoux is taken at a resolution of $9.95 \mu\text{m}$ and one post mortem scan of the barite front in the Adamswiller sandstone is taken at a resolution of $3.27 \mu\text{m}$. Scans are acquired at an energy of 100 keV, 2000 projections are taken over 360° , from which the 3D volume is reconstructed using a classical back-projection algorithm. The grey values in the reconstructed images reflect how strongly X-rays are attenuated by the components of the sample. The attenuation by a mineral or fluid is a function of its atomic number and its density, the heavier, the more it will attenuate. Low grey values (dark voxels) correspond to low attenuation and thus light elements, whereas high grey values (bright voxels) reflect higher attenuation and thus heavier elements. Therefore, in our images, pores appear dark while the skeleton of the porous medium appears greyish. Barium has the highest atomic number, and therefore barite minerals will appear as the brightest phase in the image. More pieces of information about the application of the methods of X-ray microtomography to barite rich sedimentary sandstone are given in section 2.2 of chapter 2.

3.2.3.2 SEM-EDS and QEMSCAN

An SEM-FEG Quanta 650 FEI (TOTAL CSTJF lab.) coupled with microanalysis EDS (Bruker X-Flash) is used to investigate the post-mortem chemical and micro structural changes in the porous media. Measurements are undertaken using a Back-Scattered Electrons (BSE) detector in vacuum mode at an accelerating voltage of 15 kV and a working distance of 13 mm. Since heavier atoms return more backscattered electrons they appear brighter. This explains the phase contrast between barite and the other minerals constituting the porous medium.

3.2.3.3 Thin section and polished section

Thin Section Lab (Toul, France) prepared the thin sections of the original rock samples with the following protocol: impregnation with epoxy resin, sawing and polishing with pure water. For the preparation of polished samples of the rocks after the contra diffusion experiment, which we further refer to as reacted samples, the dried-out samples are first impregnated with epoxy before sawing with mineral oil. A second impregnation with epoxy preceded the polishing. Thin section Lab prepared the polished section of reacted Lavoux limestone and the thin section of reacted Adamswiller sandstone is prepared at the LFCR laboratory (UMR 5150, UPPA).

3.3 Results

3.3.1 Barite front precipitation in Lavoux limestone

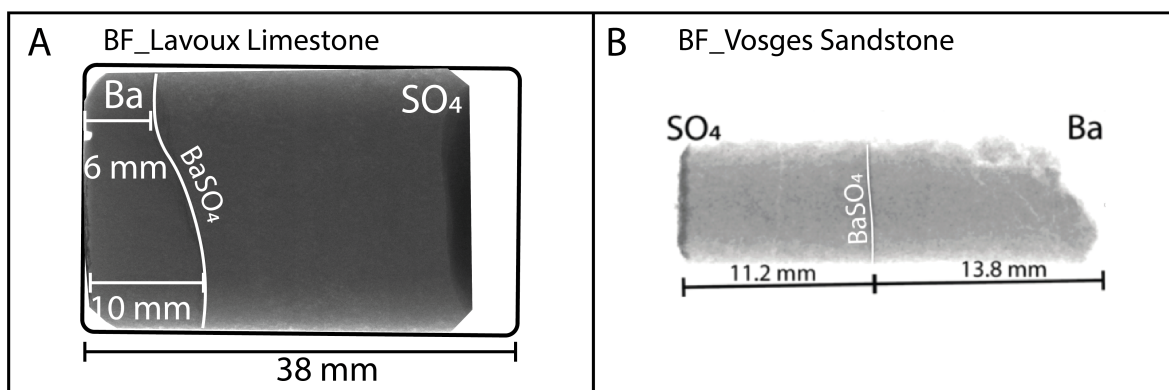


Figure 3.3: Bruker Skyscan 1172 X-ray post-mortem radiography A) BF_L at a $9.95 \mu m$ resolution, B) BF_V at a $3.27 \mu m$ resolution. The sandstone sample is fractured (thin white lines and the Ba side) during the removal of the stainless steel inlet.

The front is located 6 to 10 mm far from the barium source side (Lavoux sample length is 38 mm), as shown in figure 3.3A. It is the thin, 10-20 μm , white slightly bent continuous line separating the sample. Figure 3.4a presents a cross-section of the 3D reconstructed volume.

The dotted line delimits a zone where barite crystallites precipitate. We remark that the pores located on the barium source side are brighter than on the sulfate side because they are saturated with barium rich solution, which attenuates the X-rays more strongly than the sulfate solution. A 3D visualization (figure 3.4b), of the front segmented in ImageJ (Schindelin et al., 2012), confirms the previous observation. The front shape is a bumpy surface and the barite front frayed in the direction of the barium source side. No cracking following the barite front precipitation is reported after the X-ray microtomography examination. Based on [Scanning Electron Microscopy \(SEM\)](#) and [EDS](#) analysis, barite is identified as a light path (figure 3.5a), and as isolated crystals precipitated inside large pores on the barium source side (figure 3.5b). Large pores across the barite front path contain larger crystals (figure 3.5c). Xenomorphic barite precipitated preferentially in contact with micrite constituting the oolite along the barite front (figure 3.5d). A focus on an inter oolitic pore in which small crystallites precipitated shows that the nucleation happens preferentially on micrite, rather than on the sparite or pseudomorphic calcite (figure 3.5b).

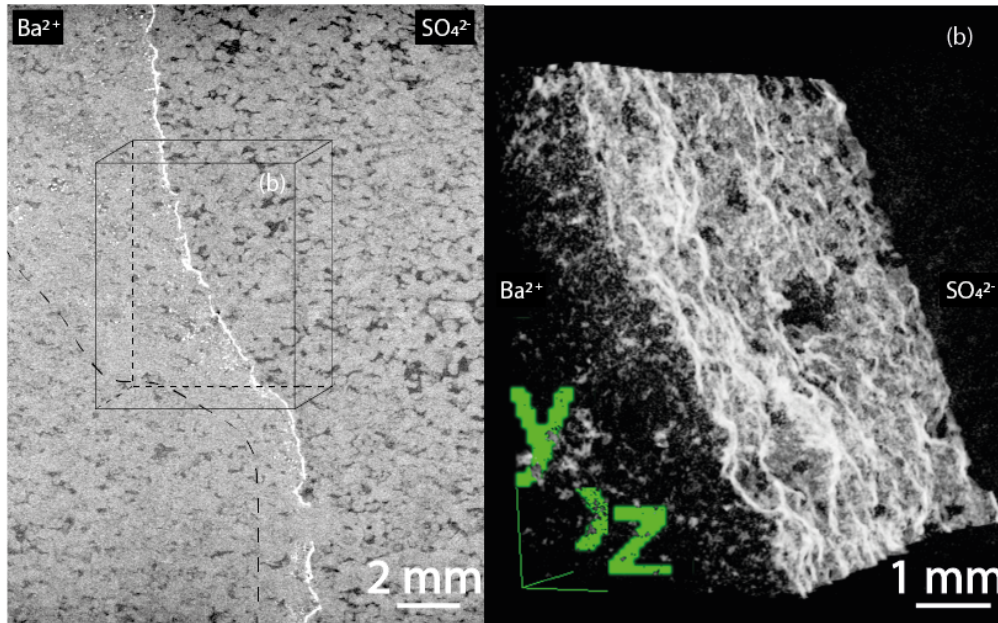


Figure 3.4: X-ray tomography analysis of sample BFL (a) 2D frontal cross-section centered on the barite front (white) precipitated in the porosity (dark grey). Isolated barite crystal are encountered on the left of the principal barite front.(b) 3D visualization of the segmented barite front.

In the upper part of the polished section, the front separates into two paths; the primary or more direct path crosses a large pore where large crystals are oriented perpendicularly to the pore wall (figure 3.5e and f). The secondary path contains crystallites precipitating in contact with micrite and does not cross inter-oolite pores (figure 3.5e and f). Despite the perpendicular orientation to the pore wall taken by the crystallite precipitated along the primary path in the large pore, similar to the crystal precipitated in the fibrous veins, no evidence of crack initiation is reported in Lavoux limestone after SEM-BSE observation.

3.3.2 Barite front precipitation in Adamswiller sandstone

A half millimeter-thick barite vertical front is precipitated, after 75 days contra-diffusion of the two solutions, at 13.8 mm of the barium source side (Adamswiller sample length is 25 mm) (figure 3.3B). On a vertical cross-section from X-ray tomography datasets centered on the barite front, depicted in figure 3.6top, the front is discontinuous, the barite crystallite fills the intergrain porosity between the quartz, the K-feldspar and the clay grains (light grey level). Diffused ions in solution contribute to the absorption of X-rays and thus the barium chloride side appears lighter than the sodium sulfate side due to the higher attenuation by barium compared to the other ions in solution. This is revealed by the horizontal normalized mean grey value calculated with ImageJ (bottom image in figure 3.6). No cracks are reported after X-ray microtomography observations.

SEM-BSE data are acquired on the polished section to enhance the understanding of the barite precipitation. An SEM-BSE overview of the polished section combined with EDS microanalysis allows distinguishing three cases of precipitation. Firstly, the barite will precipitate as micrometric crystals in the larger pores. Secondly, barite precipitates in contact with clay and especially the chlorite — smectite complex. Thirdly, small

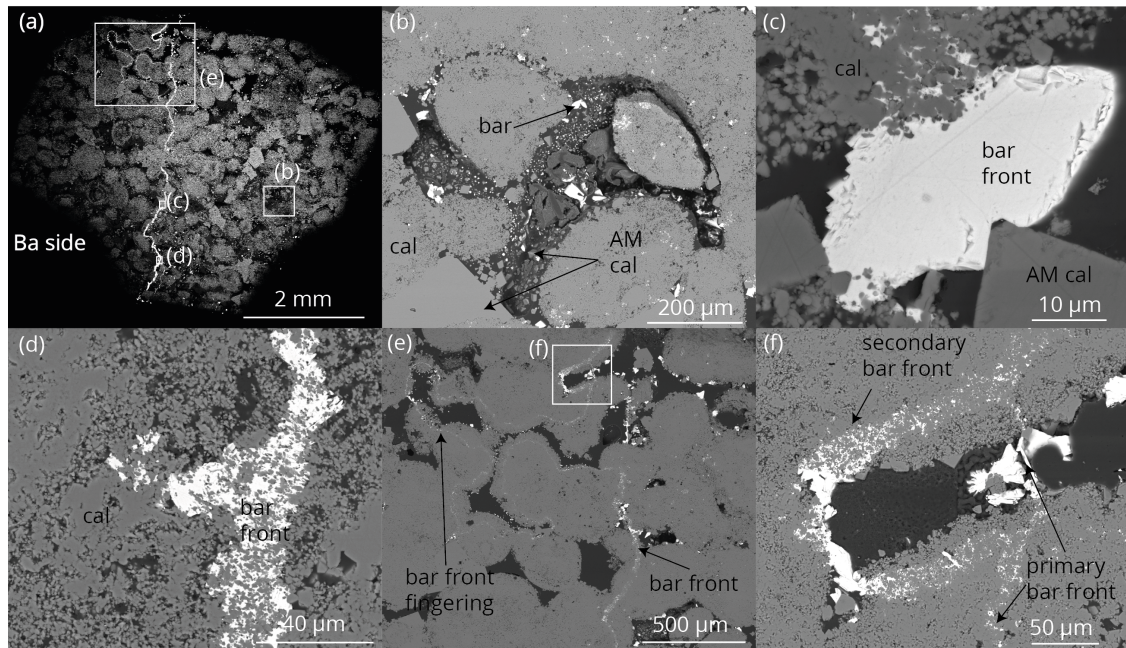


Figure 3.5: SEM-BSE observations on BF_L a) barite front highlighted; barite front separation in the top of the sample, barite crystals precipitated in the porosity on the Ba side (b) large pore localized away from the front in the barium side with barite crystals seeded on micrite, (c) large barite crystal on the barite front clamped between automorphic calcite (AM calcite) and micrite of oolite grains. The crystal is smoothed on the right and faceted on the left. (d) barite front precipitated in contact with micrite constituting oolite grains (e) barite front fingering (f) primary and secondary barite front in the fingering area; large barite in the large pore oriented perpendicularly to the pore wall.

barite crystallites are found in contact with dickite like kaolinite, as illustrated in figure 3.7, top. Zoom in the barite precipitated in contact with clay revealed that nanometric barite precipitated in the voids between the layers of the chlorite — smectite complex (figure 3.7, bottom). Barite, ferric oxide interlayered in the chlorite — smectite complex are identified with EDS microanalysis on a 1-3 μm volume of material (Bruker X-Flash) (figure 3.8).

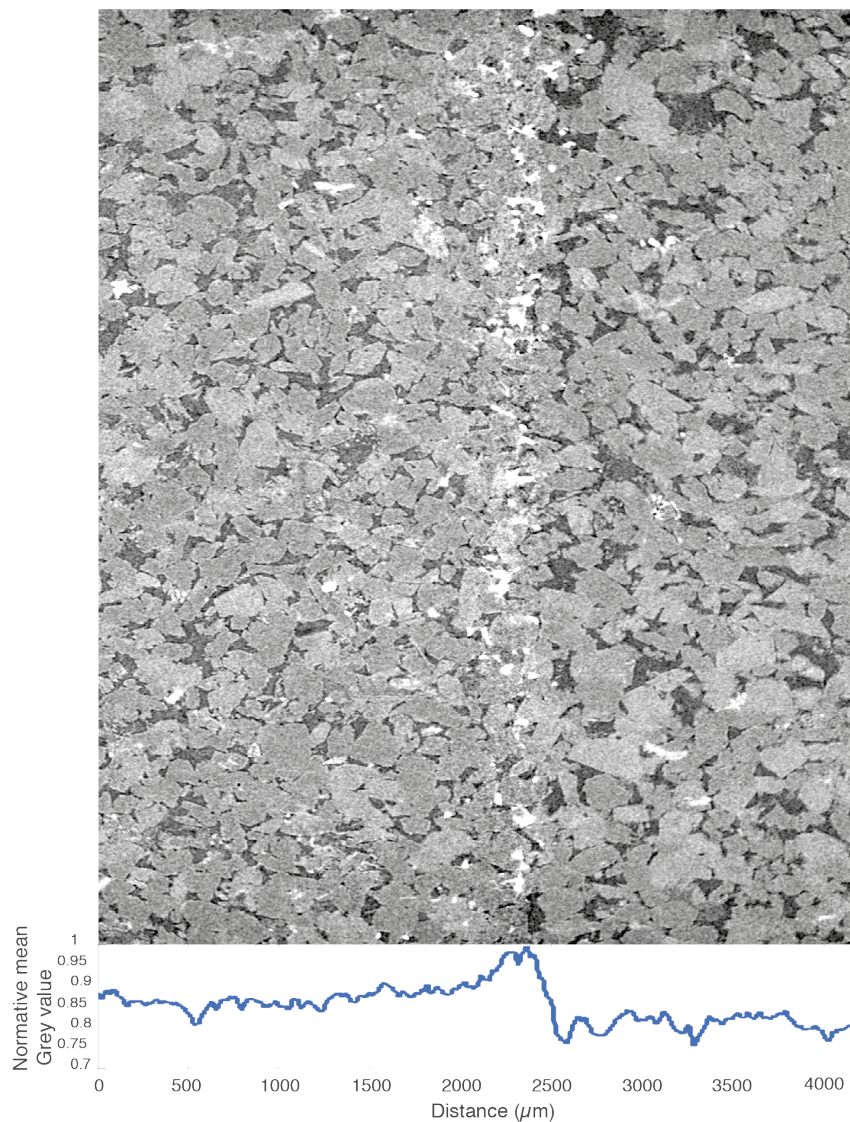


Figure 3.6: (Top) X-ray tomography vertical cross-section of sample BF_V processed with ImageJ 2D frontal cross-section centered on the barite front (white) precipitated in the porosity (dark grey) between feldspar, clay and quartz grains (light grey). (Bottom) Normalized mean grey values are obtained versus the horizontal axis by summation of the cross-section image pixel along the vertical axis.

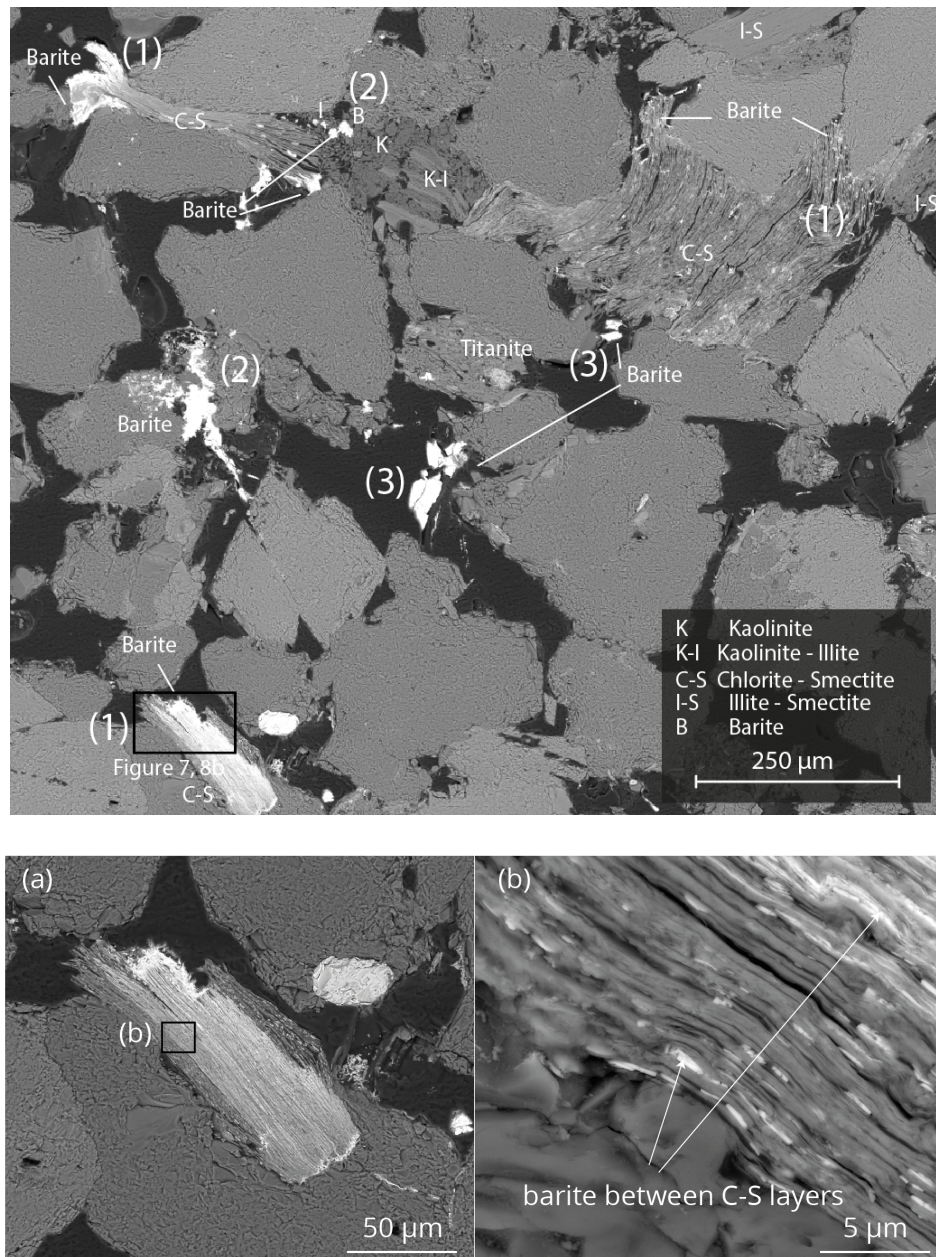


Figure 3.7: SEM-BSE observations on BF_V . Top, barite occurrences observed and interpreted with SEM BSE acquired on the BF_V sample polished section. Barite precipitate predominantly in contact with chlorite -smectite complex (1). Small barite crystallites precipitate in contact with dickite like kaolinite (2) and large barite crystals are observed in the larger pores with no clear contact with the clay complex (3). Bottom (a), cross sectional overview of a C-S complex with barite precipitated in contact. Bottom (b), thin barite layer precipitated between C-S layer.

3.4 Discussion

3.4.1 Preliminary discussion on minerals of barite group precipitation in sedimentary porous rock

In a preamble to the discussion, we recall the latest advances in classical and non-classical nucleation theory of crystals and celestine ($SrSO_4$, mineral of the barite group with similar properties) precipitation experiments in a clay-rich artificial porous medium. By applying them to our experiments, together with the concept of crystallisation pressure, they bring new perspectives for the understanding of crystallisation in saturated porous media.

3.4.1.1 High supersaturation reached during barite nucleation in silica gel

A contra diffusive experiment in a silica gel, used as artificial porous medium, with one solution rich in sulfate and another solution rich in barium, led to the precipitation of barite crystals (Prieto, 2014; Putnis and Fernandez-Diaz, 1990; Putnis, Prieto, and Fernandez-Diaz, 1995). Interestingly, because the mass transfer is strictly diffusive, the nucleation is homogeneous. Depending on the initial concentration of the electrolytes, high supersaturation is calculated by measuring the concentration every 100 hours at the location where the first crystallites are observed under a x500 magnification (Putnis and Fernandez-Diaz, 1990; Putnis, Prieto, and Fernandez-Diaz, 1995). With this method, they calculated a supersaturation as high as 10620 (Putnis, Prieto, and Fernandez-Diaz, 1995) with an initial concentration of 0.5 mol.l^{-1} of Ba^{+2} , and 0.3 mol.l^{-1} of SO_4^{2-} . This supersaturation is denominated “the supersaturation threshold” because when the saturation reached this level, the barite appeared in the solution and the saturation started to drop.

3.4.1.2 Amorphous barite nucleation before barite crystallisation

In the frame of the classical nucleation theory, in Putnis, Prieto, and Fernandez-Diaz (1995), they assume that barite is precipitated at an high supersaturation level by homogeneous nucleation. However, the discovering of prenucleation cluster of barite shows that the precipitation of amorphous barite would decrease the supersaturation of the solution. The detection of prenucleation clusters during crystallisation of calcium carbonate and calcium phosphate opened new perspectives via the PNC pathway (Gebauer and Cölfen, 2011; Gebauer et al., 2014) to understand the precipitation from supersaturated solutions in a porous medium. More recently, an amorphous barite precursor is also detected during a titration leading to barite nucleation and crystallisation (Ruiz-Agudo et al., 2020). Amorphous barite aggregates nucleate at the maximum IAP corresponding to the CNT supersaturation threshold. Solution IAP tends to an IAP’s

Table 3.2: Measured Supersaturation (S) when barite or amorphous barite nucleate and associated potential crystallisation pressure (CP)

	S	CP (MPa)
Barite nucleation (Putnis, Prieto, and Fernandez-Diaz, 1995)	10620	433.7
Amorphous barite onset IAP,(Ruiz-Agudo et al., 2020)	169.8	240.2
IAP’s First plateau,(Ruiz-Agudo et al., 2020)	30.6	160

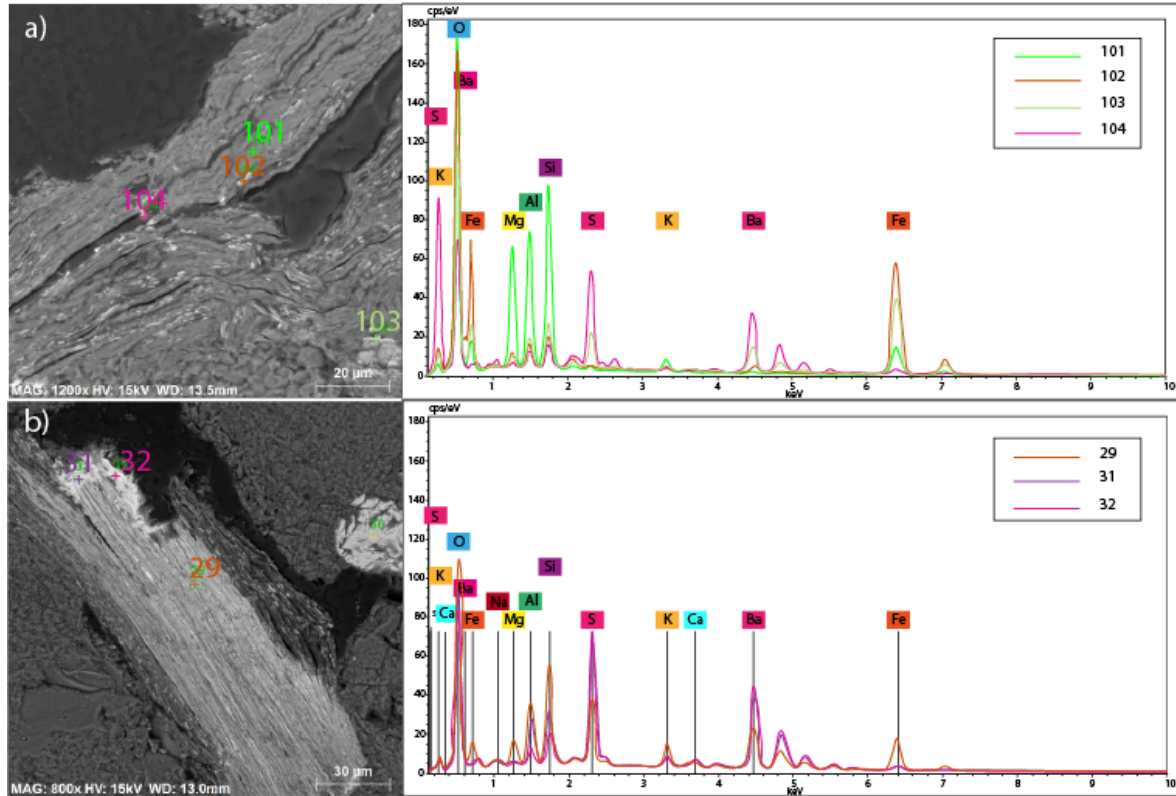


Figure 3.8: SEM BSE images of BF_V and EDS microanalysis (a) Cross sectional overview of a C-S complex (101) with barite (104) and ferric oxide (102) precipitated in contact (b) thin barite (32 and 31) and ferric oxide (29) precipitated between C-S layer.

first plateau and after approximately an hour amorphous aggregate redissolves and barite forms. Barite keeps precipitating until the solution IAP gets to the IAP's second plateau closely equal to the solubility product of barite (Ruiz-Agudo et al., 2020), figure 2.3, bottom. The introduction of a barite precursor implies that barite will not precipitate where and when the maximum IAP or supersaturation threshold happens but when the IAP's first plateau is reached and surely at a more favorable nucleation site than in the bulk solution. In table 3.2, we summarize measured supersaturation reported in (Putnis, Prieto, and Fernandez-Diaz, 1995; Ruiz-Agudo et al., 2020). The corresponding crystallisation pressure is calculated using equation 3.1. \bar{V}_m is the molar volume, T, the temperature and R, the gas constant (Correns, 1949; Steiger, 2005a)

$$PC = \frac{R * T}{\bar{V}_m} * \ln S \quad (3.1)$$

In our experiment, no cracks are observed in the region of the barite front, even though all crystallisation pressure values calculated are sufficient to exceed the tensile strength of the stone estimated via a splitting tensile strength test on intact dry core samples¹ in the LFCR laboratory (Adamswiller sandstone 4.9 MPa, Lavoux limestone 8.6 MPa). Perhaps, nucleation and crystallisation of barite consumed the ions in solution faster than the saturation is increasing. Thus, as the barite crystal reached the pore wall the poral solution is at a near equilibrium with the crystal and no sufficient pressure could be exerted (Naillon, Joseph, and Prat, 2018).

¹norm ASTM D3967-16

3.4.1.3 Restriction of anion diffusion caused by celestite crystallisation and electronegativity of TOT layer and accelerated cation diffusion in compacted bentonite.

In Chagneau et al. (2015a) and Fukatsu et al. (2017), diffusion coefficients of cationic $22Na^+$, anionic $36Cl$ and HTO are measured in compacted illite with and without a precipitation front of celestine ($SrSO_4$), a mineral of the barite group. Celestine is precipitated by diffusion for three months with a solution of similar ionic strength than ours. The anionic diffusion coefficient is very low without precipitate and completely restricted by the front. On the other side, cationic and HTO diffusion is higher without celestine and reduced with the precipitate. The authors proposed a model comprising an anion exclusion effect due to the electric double layer on the surface of TOT layers (Chagneau et al., 2015a,b; Fukatsu et al., 2017). Water is expelled from where the $SrSO_4$ precipitate according to neutron radiography. Interestingly, the $SrSO_4$ studied by X-ray diffraction analysis showed that it is microcrystalline and preferentially oriented in individual clusters (Loon et al., 2016). In Melkior et al. (2009), the authors measured an unexpectedly high diffusion coefficient for sodium when the smectite's TOT layers are hydrated with three water molecules. Consequently, TOT layers effects on ions diffusion (reduced sulfate diffusion and increased barium diffusion) within clay-rich medium combined with the precipitation of barite may explain the position of the barite front closer to the sulfate source in the Adamswiller sample.

3.4.2 Discussion on barite crystallisation in sedimentary rock

3.4.2.1 Diffusion versus advective/convective transport

All experiments are conducted with care to ensure only diffusive transport conditions. However, in BF_L the bending of the barite front and barite fraying on the barium source side as much as the position of the barite front might belong to advective transport features. These features are not recognized in BF_V . Despite the care taken, there could have been a slight pressure difference in BF_L when the diffusion started and/or when the diffusion is stopped by operating the valve leading to a combination of diffusive and convective flow causing the bending of the barite precipitation front. A convective flow effect related to the slight difference in the solution density may also have happened Poupeleer (2007).

3.4.2.2 Model for barite nucleation in a bimodal pore network

The supersaturation threshold defined in the CNT may reach a high value as measured experimentally for barite (Putnis, Prieto, and Fernandez-Diaz, 1995). The PNC pathway (Gebauer and Cölfen, 2011; Gebauer et al., 2014; Ruiz-Agudo et al., 2020) introduces a time/spatial buffer corresponding to the existence of a barite precursor. As the medium tested is not inert like the silica gel used in Prieto (2014), Putnis and Fernandez-Diaz (1990), and Putnis, Prieto, and Fernandez-Diaz (1995), heterogeneous nucleation conditions are linked to the roughness of the calcite surface where barite nucleates and leads to different supersaturation thresholds depending on the. We assume that the barite supersaturation in the medium has a Gaussian shape. We deduce from the barite affinity to nucleate and precipitate in contact with micrite that the supersaturation threshold S_1 in small micritic pores ($0.1 - 1\mu m$) is lower than the supersaturation threshold, S_2 , in contact with sparitic or pseudomorphic calcite, which

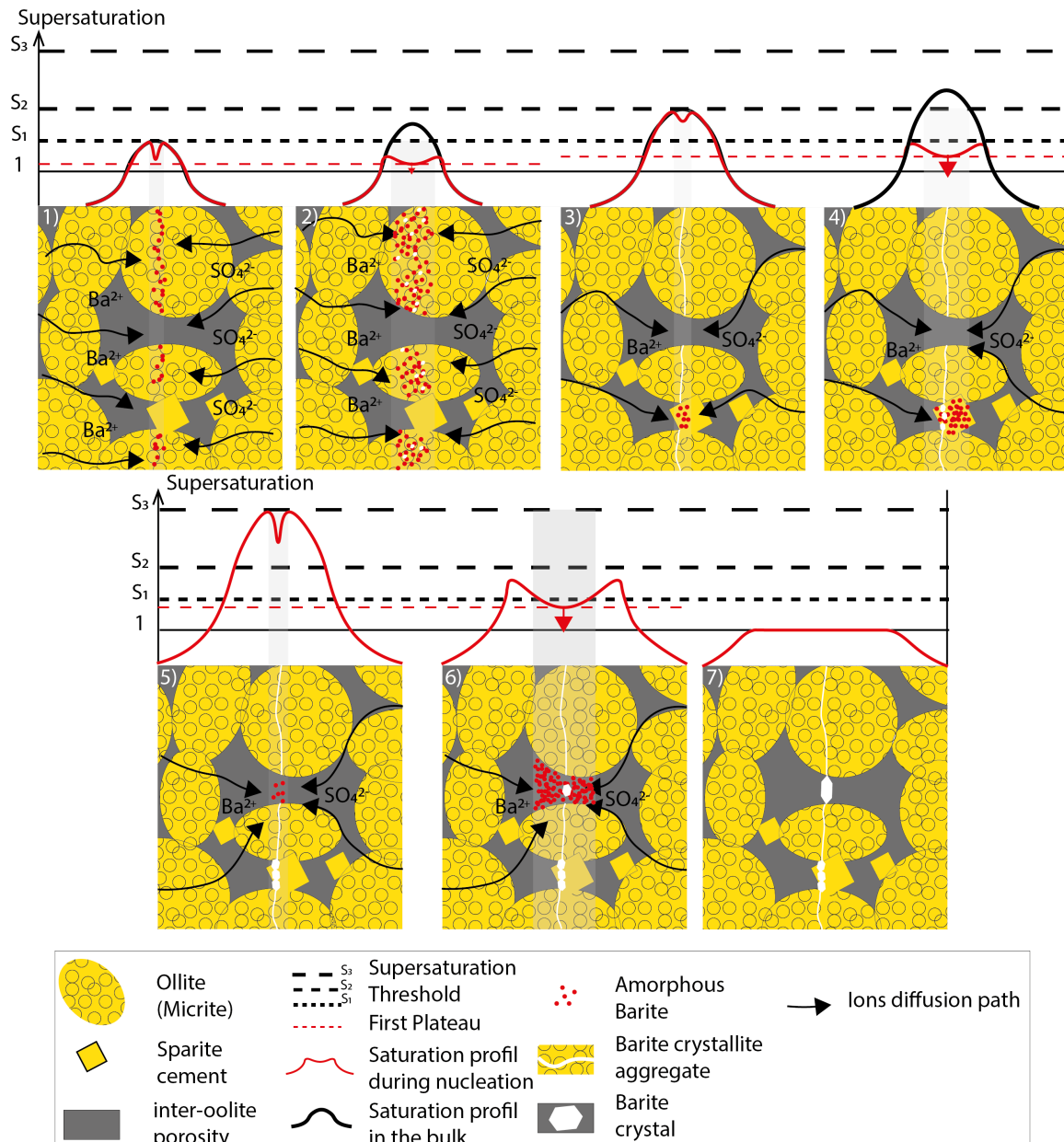


Figure 3.9: Conceptual model of barite precipitation in an oolitic limestone. 1) Amorphous barites nucleate in contact with micrite when S reaches S_1 . 2) Barite nucleates in contact with micrite while S decreases to the first plateau of saturation. 3) Amorphous barites nucleates in contact with sparite when S reaches S_2 4) Barite nucleates when S drops to the first plateau of saturation 5) Amorphous barites nucleate in the large pore (Bulk) when S attains S_3 6) Barite nucleates when S gets to the first plateau of saturation. 7) Connected barite front with reduced ion transport.

has a smoother surface that offers fewer nucleation sites. Finally, we can consider that the interoolitic pores are micro crystallisation bulk chambers with a higher supersaturation S_3 . A conceptual model is proposed to interpret the precipitation of barite in figure 3.9: according to the PNC pathway, in conditions of heterogeneous nucleation, nucleation of PNC occur when the effective saturation reaches the dedicated supersaturation threshold. In the majority of the cases, barite PNC will nucleate when the solution saturation reaches the supersaturation threshold. While forming, the PNC will consume the ions in solution and reduce the solution saturation. As observed in

Ruiz-Agudo et al. (2020) and modeled with calcite in Lassin et al. (2018), the barite will start to precipitate at a lower supersaturation. This two-step barite crystallisation mechanism may explain the “logic” behind the barite front. Indeed, barite must not precipitate at the site where the supersaturation threshold happens according to the CNT but will precipitate at a more adequate location. Some questions remain whether the barite front started from one or multiple seeding crystals, the duration of the front precipitation, whether the barite front after being connected kept increasing in thickness and at which speed or if the front acted like a permeability barrier like we propose in our conceptual model and observed in Chagneau et al. (2015a,b) and Fukatsu et al. (2017).

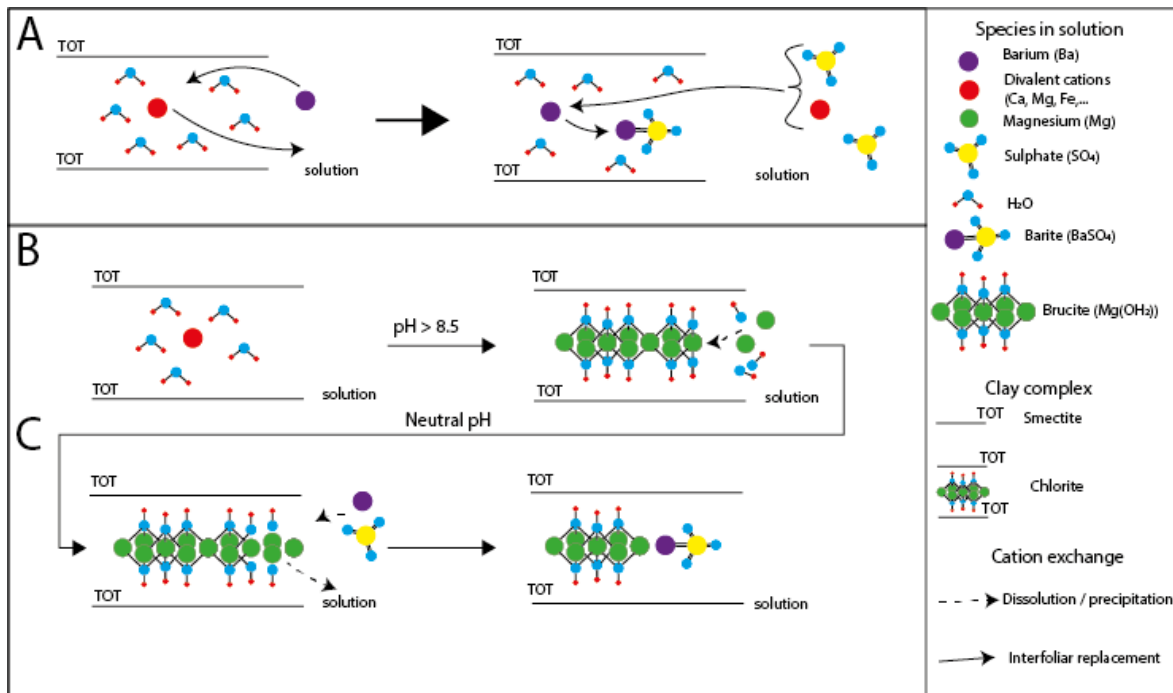


Figure 3.10: Conceptual model for barite precipitation in contact with smectite and chlorite-smectite complex: A) A divalent cation is desorbed as the concentration of barium in solution increase. Sulfate captures the barium sorbed and barite precipitates in the interlayer. B) Smectite transforms to chlorite by adjunction of a brucite layer and swells provided a sufficiently basic pH. As the pH is more acid during the experiment, brucite dissolves and barite precipitates in the interlayer.

3.4.2.3 Model for barite nucleation in clay-rich sandstone

Barite precipitate in Adamswiller sandstone as crystal in large pores, in the C-S complex void between layers and contact with dickite like kaolinite. On the one hand, crystallisation in large pore agrees with what is explained for barite precipitation in a near inert porous media like Lavoux limestone. On the other hand, the precipitation of barite in the interfoliar void in clay complex is a novelty and could be driven by cation exchange in clay sheets (Atun and Bascetin, 2003). In theory, illite interlayer sites are occupied by K^+ , the substitution of K^+ by a hydrated cation like Ba^{2+} , Na^+ , Mg^{2+} , Fe^{2+} distorts the structure and expands the illite basal spacing (Nakao et al., 2008). In the reacted Adamswiller sandstone, illite mineralisation is not expanded but in chlorite — smectite complex, the basal space is expanded and as such barium could come in replacement of divalent cations adsorbed between TOT smectite layers (figure

3.10A). The expansion of the basal space minimized the anion exclusion effect describe in Chagneau et al. (2015a,b) and Fukatsu et al. (2017) allowing sulfate to diffuse in the delaminated interlayer and capture the barium to precipitate barite in place. An alternative scenario is proposed in figure 3.10B suggested by the examination of not reacted Adamswiller sandstone thin section with peeled C-S complex and sometimes ferric oxide interlayered between the clay sheets figure 3.8: smectite to chlorite transformation takes place with the growth of a brucite layer between the smectite TOT provided that the pH is sufficiently basic (Pokrovsky and Schott, 2004). Then, smectite redissolve and rearrange to form chlorite. As stated in Bettison-Varga and Mackinnon (1997), both steps of the transformation go with a volume augmentation. The damage on the clay sheet and the interlayered ferric oxide may have originated from the transformation. During the experiment in Adamswiller sandstone, the pH is neutral. Therefore, the brucite layer can redissolve and barite precipitate in the interlayer alongside ferric oxides (figures 3.7 and 3.8).

3.5 Conclusion

We suggest that crystallisation of barite in sedimentary rock depends on pore distribution, pore rugosity and mineral of the porous medium skeleton. Combined with the presence of an amorphous barite precursor before barite nucleation, it explains the shape of the barite front in the Lavoux limestone. In the unreacted Adamswiller sandstone, chlorite — smectite complex are associated with ferric oxide precipitation probably linked to wedge expansion during smectite to chlorite transformation. During the experiment, barite precipitates in the C-S complex interlayers while the basal space is expanded by cation replacement and/or brucite dissolution. Wedge expansion cannot be related with any certainty to crystallisation pressure exerted in the thin film between barite and the pore surface.

Nevertheless, several clues show that the solution supersaturated with respect to barite at least in Lavoux and our model provides new ideas to deal with the crystallisation of aqueous species in confined rock. On the other side, the interaction between aqueous species crystallisation and the presence of clay fraction, once again raise the issue of high crystallisation pressure in a clay-rich environment. We believe that similar experiments should be redone over a longer diffusion time in shale or shaly sandstone with strain gages and acoustic emissions to measure if there are deformation across the barite front and potential damages during a prolonged experiment duration. The experimental crystallisation of barite front crystallisation in a porous sedimentary rock has not given the awaited proof of crystallisation induced damage in conditions mimicking diffusive transport in a geological reservoir. Consequently, there is no point to redo the experiment in confined reservoir conditions. The issue is to invent an experiment with an acceptable duration (from a day to a few month) that could induce damage in confined reservoir conditions.

*CHAPTER 3. UNCLASSICAL CRYSTALLISATION OF BARITE DURING
DIFFUSION DRIVEN BARITE PRECIPITATION IN SEDIMENTARY ROCK*

Chapter 4

Damage induced by mirabilite precipitation in confined reservoir conditions

Contents

4.1	Sample preparation	94
4.1.1	Introduction	94
4.1.2	Prerequisite	94
4.1.3	Thenardite dome precipitation protocol	96
4.1.4	Computation of salt saturation in the porous sample	96
4.1.5	Results and discussion	98
4.1.6	Conclusion	99
4.2	Acoustic monitoring of damage induced by mirabilite precipitation in confined shallow reservoir conditions	100
4.2.1	Introduction	100
4.2.2	Materials	100
4.2.3	Methods	101
4.2.4	Results	102
4.2.5	Discussion	111
4.2.6	Conclusion	115

Abstract

Crystallisation is suspected to induce damage in geological settings and reaction driven volume expansion is the major expression of crystallisation in these conditions. Sodium sulphate is an ideal crystal to provoke crystallisation damage in a porous media confined at a pressure equivalent to ~ 400 m burial. The transformation of thenardite to mirabilite is not a hydration reaction and thus rewetting of thenardite damages the porous medium only by mirabilite crystallisation. In this respect, the monitoring of the rewetting of thenardite precipitated in an Adamswiller sandstone emphasizes the role played by mirabilite crystallisation in the damage attributed to reaction driven volume expansion. A sample cylinder of Adamswiller sandstone impregnated with 5 grams sodium sulphate is reacted first without confining pressure and next with a 10 MPa isotropic confining pressure. It induces damage through mirabilite crystallisation that is recorded by the monitoring of [AE](#) and P-wave velocity evolution and unveiled by 3D X-ray microtomography scans and [BSE](#) analysis. A conceptual model is proposed to explain the damage induced at the pore scale. Besides the study of the propagation of the humidity and waterfront during the imbibition shows that the thenardite dome is originally a permeability barrier that is harmed by the dissolution of the thenardite and the precipitation of mirabilite.

4.1 Sample preparation

4.1.1 Introduction

The experimental precipitation of a barite front in sedimentary rocks shows that the solution probably reaches a certain level of supersaturation meanwhile, there is no damage induced by barite crystallisation. In parallel to these experiments, we have reproduced successfully, the experimental protocol of crystallisation described in Caruso, Wangler, and Flatt (2018), Espinosa-Marzal et al. (2011), and Espinosa Marzal and Scherer (2008) and also Noiriel et al. (2010) with a sodium sulphate rich solution (28.5 % (W/W)). Some of the results are published in the state of the art chapter 1 in section 1.2.1 next to the original experiment. We persisted to adapt one of the protocols to our experimental requisitions. This transition chapter aims to unveil the thinking behind the protocol adaptation to obtain damage induced by crystallisation after noticing the semi-failure with barite front precipitation. To begin, we recall the technical requisitions imposed by the use of a triaxial cell and monitoring techniques. Next, we discuss if literature protocols are achievable in a triaxial cell. The choice of chemical species and porous rocks is questioned as well. Then an experimental protocol is proposed. We analyse the prepared sample by means of 3D X-ray microtomography scans and interpret the acquired data with ImageJ.

4.1.2 Prerequisite

4.1.2.1 Technical requisitions

This work aims to do crystallisation pressure experiment in a confined triaxial cell, the 'Geodesign cell' (ENS Paris geological laboratory). A sample cylinder is clamped in a jacket between stainless steel inlet and outlet connected to a Quizix precision pump. The sample is height limited to 85 mm. Strain gauges and acoustic monitoring systems undertake the monitoring of the deformation. The internal cell temperature is not regulated. Previous experiments proved that limestone damages do not induce acoustic emissions (Fortin, 2007). Thus, out of the two porous rock described in section 2.1 of chapter 2, the Adamswiller sandstone is preferred for the experiment in the triaxial cell monitored with AE.

4.1.2.2 Discussion on merits of existing protocols

The choice of the right protocol depends on several characteristics inherent to the described experiments in the chapter 1:

1. Capillary uptake of a salt-rich solution: During pure water capillary uptake in porous rock, the height of the water front is higher than the dimension of the sample. Neglecting the evaporation effect, absent in the 'Geodesign cell', the calculation of the water front height in a pure quartz sandstone with the Jurin law, provided in equation 4.1, gives a height equal to 0.7 m:

$$h = \frac{2 * \gamma * \cos \theta}{r * \rho * g} \quad (4.1)$$

The value of Scherer (2004) is taken for γ , the surface tension of the solution (surface energy of the gas-liquid interface), 0.072 J/m^2 for pure water (the real

value for the solution is slightly different due to the dissolved salt). For r , the mean smaller pore diameter of an Adamswiller is taken, $18.5 \mu\text{m}$. The water contact angle is approximated to 26° according to the water-air contact angle with a glass surface (Erfani Gahrooei and Ghazanfari, 2017).

2. Cooling – heating cycle on a salt-rich solution: the “Geodesign” cell lacks a temperature control system (figure A.1) at low temperature.
3. Rewetting of thenardite impregnated porous rock: Pure water imbibing in a porous medium impregnated with thenardite would work in the ‘geodesign cell’, but the damages would be too widespread and thus too difficult to analyse. The second limit is that the protocol works with the sodium sulphate phases thenardite and mirabilite, below a confining pressure equal to 13.9 MPa at 20°C well below the required 30 MPa for geological reservoir conditions.

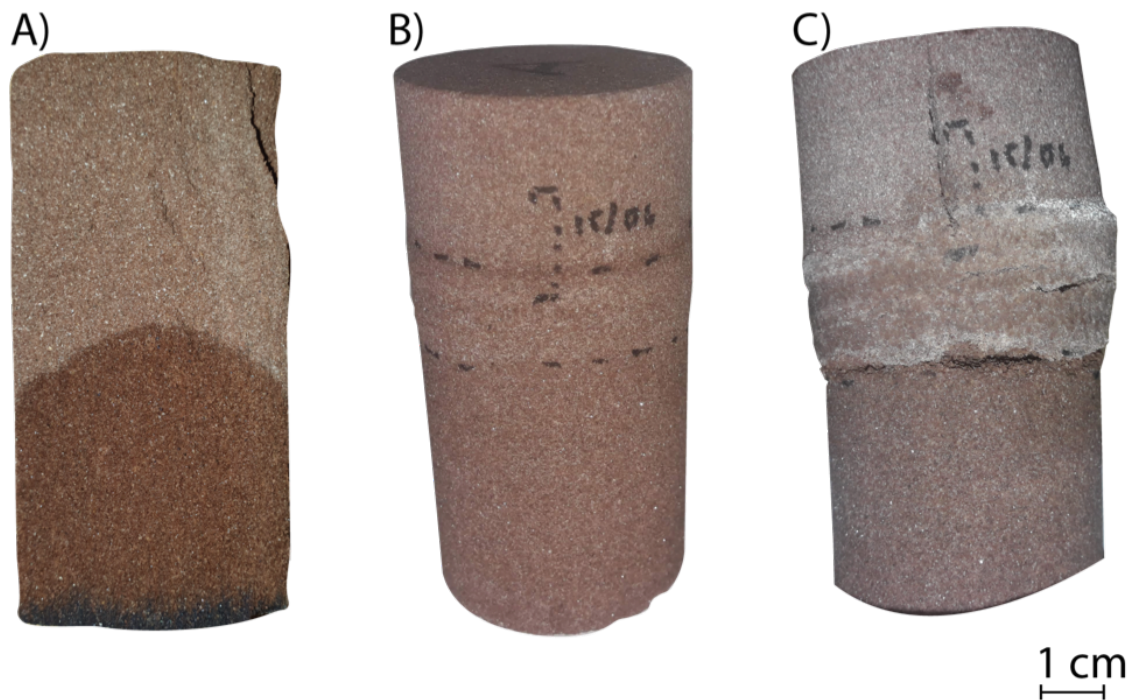


Figure 4.1: Photographies at different stages of the experimental protocol: A) Adamswiller sandstone sample cylinder split by Brazilian test immediately after the imbibition with a 28.5 % (W/W) sodium sulphate rich solution. The waterfront is a paraboloid surface. B) Adamswiller sample NRII (appendix A.4) containing 6.4 grams of Na_2SO_4 . Small swelling cracks propagate above the thenardite front. C) Adamswiller sample NRII after rewetting with pure water at laboratory temperature and pressure. The damage limits to the salt front and the propagation of swelling cracks above.

The final protocol, illustrated with figure 4.1, is a mix of the first and the third protocol to precipitate primarily an anhydrous salt dome in the middle of a porous sample (figure 4.1, A and B). Then, the idea is to provoke the rewetting with pure water of the salt impregnated sample to hydrate the anhydrous salt dome and induce damages (figure 4.1, C). Sodium sulphate is chosen due to the existence of several phases that can be easily precipitated with the help of a single oven. The protocols to prepare the sample with the the salt is written below.

4.1.3 Thenardite dome precipitation protocol

1. Sample of dimension 40 x 85 mm is cored, sored, rectified and weighted after drying following the current standards¹.
2. Half of the sample is covered with a heat-shrinkable sleeve terminated on a stainless-steel inlet.
3. The total porosity volume of the section covered with the heat shrinkable sleeve is calculated, 4.2.

$$V_{\phi} = \phi * V_{section} \quad (4.2)$$

By taking $\phi = 0.21$, $r = 20$ mm and $h = 40$ mm, we obtain $V_{\phi} = 10.5$ ml.

4. A volume of a solution concentrated with respect to the desired salt is injected by the stainless-steel inlet. After multiple attempts, it appears that a volume of approximately 4 ml is suitable for an Adamswiller sandstone and a porosity volume equal to V_{ϕ} . Above this value, the sample does not absorb entirely the injected volume. A plug is put on the inlet and the sample is weighted.
5. The sample is oven-dried at a temperature ensuring the precipitation of the anhydrous phase. During the drying, the solution will naturally migrate to the evaporation sleeve free part of the sample and salt will precipitate along a paraboloid surface (figure 4.2). For example for Na_2SO_4 , we will dry at a temperature higher than 33°C to precipitate thenardite according to the phase diagram provided in figure 2.6.
6. Daily, the sample is weighted to measure the volume of water evaporated. The volume of water evaporated is replaced by the same volume of the solution so that the salt precipitate from the solution along the same parabolic front.
7. When the desired quantity of salt is precipitated in the sample, the sample is dried following the current norm². The sample is stored in an oven or humidity control environment to hinder the transformation of the anhydrous to the hydrated phase.

In appendix A.4, a table describes samples impregnated with Na_2SO_4 .

4.1.4 Computation of salt saturation in the porous sample

X-ray microtomography datasets are acquired on impregnated sandstone samples with thenardite. The salt domes are targeted to be analysed. The pore salt saturation is estimated and strives to predict the thickness of the hydrated dome after damages induced by crystallisation:

1. Importation in Image J (Schindelin et al., 2012) of the microtomography datasets, brightness/contrast adjusting and scale definition.
2. X-ray μ tomography datasets vertically resliced.

¹ASTM D2216

²ASTM D2216

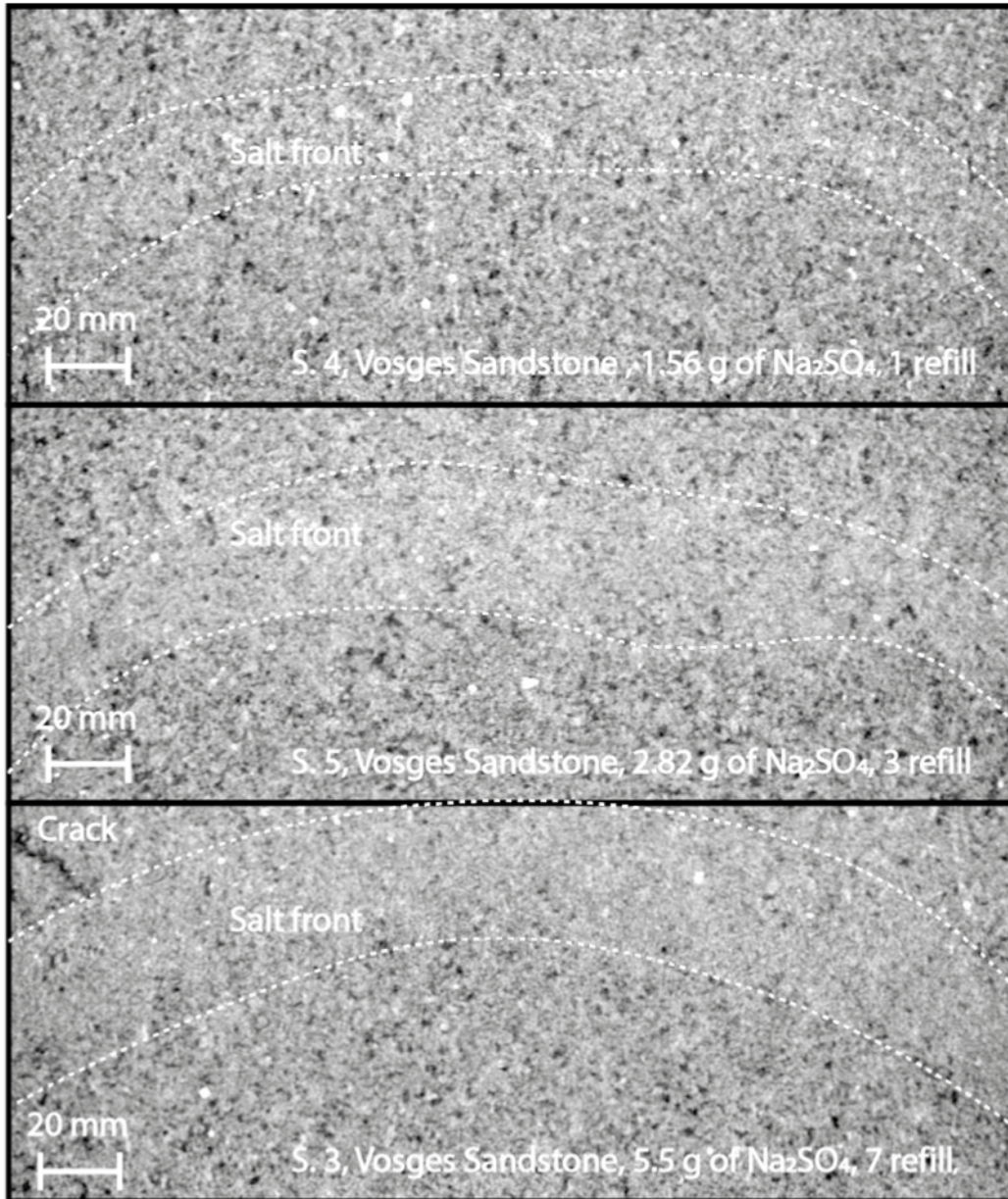


Figure 4.2: Vertical cross sections from 3D X-ray tomographic datasets. S.4 after 1 imbibition - drying cycles with 2.8 molal Na_2SO_4 solution, S.5 after 3 imbibition - drying cycles with 2.8 molal Na_2SO_4 solution, S.3 after 7 imbibition - drying cycles with 2.8 molal Na_2SO_4 solution. Extension crack appear at the top right.

3. Color segmentation (1: pore; 2: skeleton) and binarization of the segmented cross-section.
4. Profile plotting along the vertical axis.
5. Computation of the ratio pore/skeleton and the salt saturation in the pores by assuming a constant porosity in the initial rock with MATLAB (2010).
6. Computation of the salt mass in the precipitation dome based on the salt saturation computed previously and of the hydrated dome thickness assuming that 100% of the salt in the dome hydrate with MATLAB (2010).

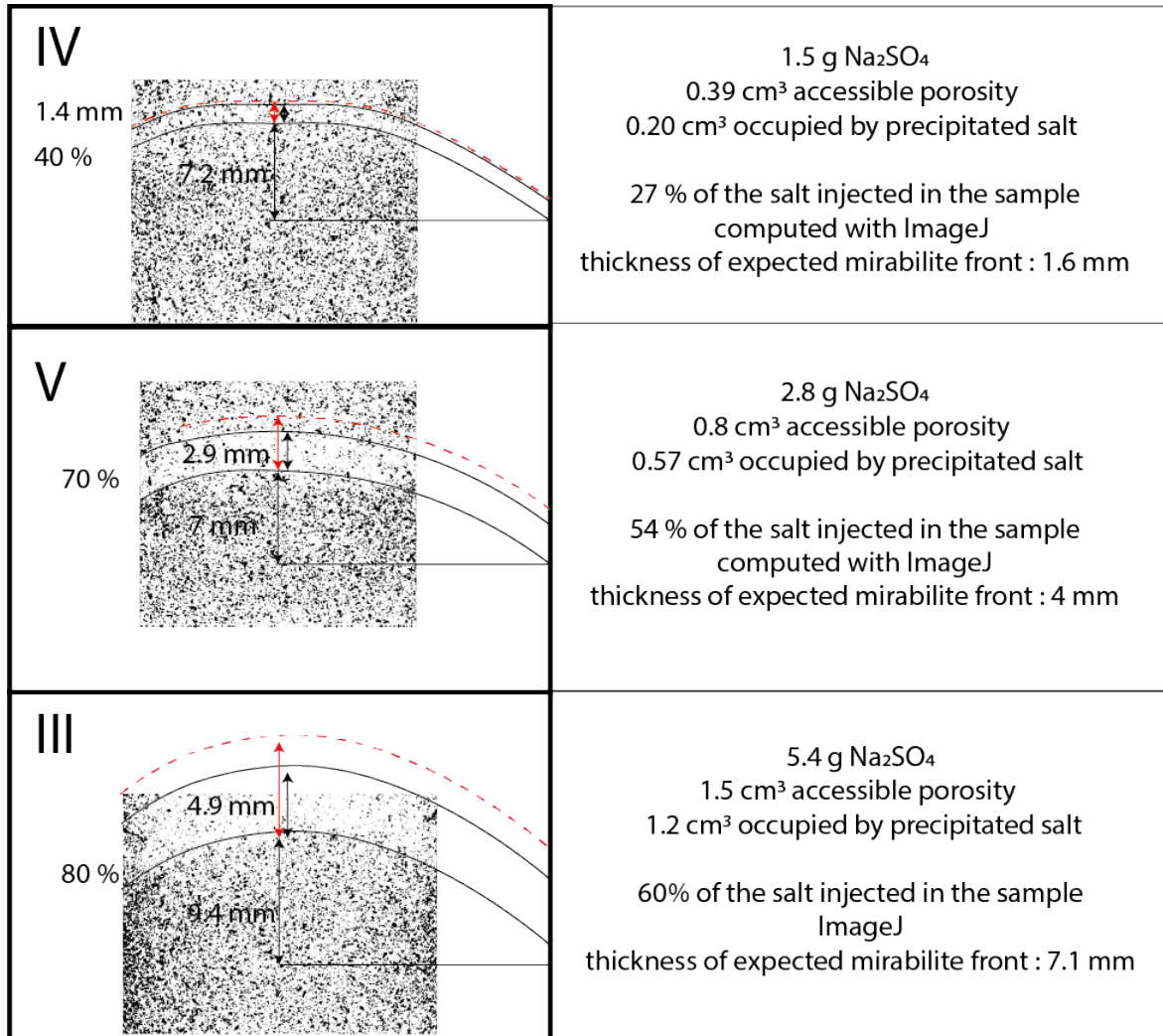


Figure 4.3: Properties of Na_2SO_4 domes precipitated at different concentration in Adamswiller sandstones: top, sample IV with 1.5 gram of Na_2SO_4 ($18 \times 19 \text{ mm}^2$), middle, sample V with 2.8 gram of Na_2SO_4 ($18 \times 18 \text{ mm}^2$) and bottom, sample III with 5.4 gram of Na_2SO_4 ($18 \times 20 \text{ mm}^2$).

4.1.5 Results and discussion

A cross-sectional view on the salt precipitated indicates that the volume impregnated is best described in the case of thenardite as a few millimeter-thick paraboloid dome. The width of the thenardite dome is equal to 1.4 mm in sample IV, 2.9 mm in sample V and 4.9 mm in sample III. Na_2SO_4 occupies approximately 40% of the accessible porosity in the dome of sample IV. This percentage is equal to 70% in sample V and 80% in sample III. It indicates that a fraction of the Na_2SO_4 injected precipitated out of the dome: 73% in sample IV, 46% in sample V and only 40% in sample III. Obviously, repeating the injection increase the thickness of the dome and its salt saturation. We computed an expected dome thickness after rewetting the dome with pure water by estimating the volume of mirabilite that corresponds to the volume of the thenardite precipitated in the dome. The predicted mirabilite dome thickness is equal to 1.6 mm for sample IV, 4 mm for sample V and 7.1 mm in sample III. A cross-section computed from sample III X-ray μ tomography scan datasets displays cracks branched on the salt dome (figure 4.2). Moreover, visual control proves that sample III bulges laterally (+0.5 mm) and in height (+0.3 mm). We can not validate the post-treatment methods

of the X-ray microtomography data-sets to calculate the salt saturation in the porous sandstone with the weighting of the sample. The weighting says that an higher volume of salt is precipitated in the sample than the volume calculated in the dome and we conclude that the undetected volume of salt might be found in the porous medium below the salt dome. To solve this question, we could scan the sample by targeting the salt precipitated dome and by choosing an energy level where the contrast between the thenardite and the mineral of the skeleton will let us segment the different phases (close to 1 keV according to the figure 2.18). Because this sample maintains a good mechanical cohesion and because no cracks are visible in the dome, the sample is kept for the experiment in confined reservoir conditions (figure 4.3).

4.1.6 Conclusion

Inspired by many examples of salt damaging experiments we have obtained a sample that can react in confined reservoir conditions to release stress by crystallisation pressure. Besides, the concentration of salt is computed for future modeling of the experiment. Unfortunately, samples prepared with more than ~ 5 grams of Na_2SO_4 are already damaged. The extent of the damage is difficult to evaluate at the resolution of $27.26 \mu m$ available with 3D X-ray microtomography on sample of these size (40 mm diameter) but as samples keep a good cohesion they are used in the following section 4.2.

4.2 Acoustic monitoring of damage induced by mirabilite precipitation in confined shallow reservoir conditions

4.2.1 Introduction

The literature mentioning crystallisation-induced damages in geological settings emphasizes the role played by hydration reaction. From the serpentinization of the oceanic crust at 300 bar and 300° C (Malvoisin, Brantut, and Kaczmarek, 2017) to the hydration of anhydrite to gypsum (Sass and Burbaum, 2010; Skarbek et al., 2018) in the subsurface. Additionally, published experimental hydration of lime (Wolterbeek, Noort, and Spiers, 2018) or periclase (Zheng et al., 2018) successfully proved that crystallisation damage exists in a confined environment. But, it lacks the proof of existence and the modus operandi of damages induced by crystals growing in porous confined rock.

For this purpose, we adapted the experimental protocol explained in Caruso, Wangler, and Flatt (2018) to a triaxial cell that applies a confining isotropic pressure during the rewetting of a sample impregnated with sodium sulphate. The objective is to measure the damage induced by mirabilite crystallisation.

4.2.2 Materials

4.2.2.1 Porous medium:

Two Adamswiller sandstone samples cylinder, I and III, 85x40mm (height x diameter) are impregnated with 5.4 g of thenardite according to the protocol described in section 4.1. The detail of their preparation is in appendix A.4. Adamswiller sandstone is a lower Triassic age sandstone sampled in the Rauscher quarry (Bas-Rhin, France). The porosity of the sandstone is equal to 20.5%. Its tensile strength is measured at 4.9 MPa \pm 0.5.

4.2.2.2 Hydrating salt:

Sodium sulphate is renowned to be one of the most damaging salts in civil engineering. Two main phases are responsible for these damages, the anhydrous phase, otherly named thenardite, and the decahydrate phase, the mirabilite. Thenardite may induce damage upon drying above \sim 32°C. Below 32°C, the damages are attributed to mirabilite upon drying (Scherer, 2004) and upon dissolution/reprecipitation of thenardite in mirabilite (Espinosa-Marzal et al., 2011; Flatt, 2002). A rapid and spontaneous mirabilite crystal growth comes alongside with high crystallisation pressure reported notably in Espinosa Marzal and Scherer (2008) and a volume increase equal to 180%. The hydrostatic pressure applied on the mirabilite is however limited up to 13.9 MPa imposed by the pressure solution limit of mirabilite at 20°C (Steiger, Kieckbusch, and Nicolai, 2008). This is why the maximum confining pressure applied by the triaxial press is limited to 10 MPa.

4.2.3 Methods

4.2.3.1 Experimental protocol

During the first test, the sample baths in ultrapure Milli-Q water without external confinement. Ice cubes are positioned around the container and aim to reduce the temperature regarding the lab temperature at 23°C. Temperature probes display that the temperatures change during the test from 13°C to 21°C in the air and from 9 to 20°C in the bath because ice cubes melt during the experiment and then the temperature increases. The first test lasts 325 min (\sim 5h30min).

The second test takes place in the ‘Geodesign’ triaxial cell between two stainless inlet/outlet connected to a Quizix precision pump (Borgomano, 2019; Fortin et al., 2006). Mineral oil is pumped in the triaxial cell chamber and pressurized at 10 MPa by the radial pump. No deviatoric stress is applied. After stabilisation of the strain gauge and the vanishing of acoustic emissions emit by micro-cracks closure (Fortin et al., 2006), 24 ml of ultra-pure milli-Q water is pumped at a constant rate of 25 $\mu\text{l}/\text{min}$. The temperature of the laboratory and the injecting water vary between 20 and 25 °C. The solubility of sodium sulphate is dependent on temperature and humidity. Ideally, the use of a climatic chamber is necessary, but in practice, the use of a confining apparatus is hardly compatible with a marketed climatic chamber. The confined test is 1400 min long (\sim 23h20min)

4.2.3.2 Monitoring

4.2.3.3 Acoustic monitoring:

The ‘Richter Mini-system’ described in Fortin (2007) of the laboratoire de Géologie of Ecole Normale Supérieure (UMR 8538) is used to record the acoustic emissions and monitor the sample with the pulse transmission method (figure 2.19). Eight PZTs, polarized to emit P-waves are positioned oppositely by pair on the sample at different heights: two pairs below the thenardite rich dome, one pair on the dome surface and one pair above the thenardite dome. The height of the sensors is reported in table 4.1. The PZT position is also given in figures 4.6 (\emptyset confining pressure) and 4.9 (10 MPa confining pressure). The trigger level is set at 60 mV and the acoustic monitoring system pulses every two minutes (unconfined test) and every 5 minutes (10 MPa confining pressure). In the experiment without confining pressure, the PZTs pair at the bottom is too noisy and thus not analyzed. In this study, the amplitudes and the velocities of the elastic P-waves are measured because they are sensitive to the moisture content, the fluid and salt saturation in the porous medium and the presence of cracks (David et al., 2017a,b; Fortin, 2007; Pimienta et al., 2019).

Table 4.1: Height distribution of piezoelectric transducer

\emptyset confining pressure		cpl.1-6	cpl.5-7	cpl.3-8
height (mm)		30	48.8	65
10 MPa confining pressure	cpl.4-8	cpl.2-6	cpl.3-7	cpl.1-5
height (mm)	13.7	24.7	44.7	64.7

4.2.3.4 Post-treatment

4.2.3.4.1 X-ray microtomography

After the experiment, the sample is immediately dried in an oven at 80°C to reprecipitate the thenardite to interrupt the damaging hydration reaction. A Bruker Skyscan 1172 (UMS 3360 DMEX, UPPA, Pau, France) was employed to acquire X-ray microtomography scans of the thenardite dome precipitated in the rock samples to investigate the evolution of the salt hydrate dome and the microstructure of the porous medium in 3D. Balancing the benefits to be taken by targeting lower energy level and the time cost, we choose to scan the reacted and unreacted sample at 100 keV and 100 A. 2000 projections were taken over 360°(scan duration \sim 15h), from which the 3D volume (pixel size: 27.26 μ m) was reconstructed using a classical back-projection algorithm.

4.2.3.4.2 Making of polish section:

After the X-ray μ tomography scans, polish sections of the samples are produced at the LFCR lab (UMR 5150, UPPA). The protocol is as follows: 1) Sample I are impregnated with epoxy resin before sawing with a diamond sawing machine cooled with mineral oil and better, sample III is sawed with an angle grinder equipped with a diamond grinding wheel because it needs no cooling fluid to cool down the sawing instrument. The cooling fluid may react with the salt precipitated that is why we try to avoid the use of it. 2) A second impregnation with epoxy resin precedes the polishing with alumina powder. 3) The polish surface is metalized for BSE analysis.

4.2.3.4.3 SEM-EDS

SEM-FEG Quanta 650 FEI (TOTAL CSTJF lab.) coupled with microanalysis EDS (Bruker X-Flash) is used to investigate the chemical and microstructural changes on the polish section. Measurements are undertaken using a BSE detector in vacuum mode at an accelerating voltage of 15 kV and a working distance of 13 mm. By using the phase contrast between the phase precipitated, the skeleton and the porosity, the BSE images are segmented to estimate the ratio of each phase. The same segmentation parameters are kept between the BSE images to reduce the variability of the results.

4.2.4 Results

4.2.4.1 Reference sample

The pure water capillary uptake in a reference Adamswiller sandstone cylinder without thenardite precipitated inside is monitored with a digital camera. It gives a reference for the mean sorption rate at different heights in the Adamswiller sandstone:

- between 0 and 30 mm: 1.37 *mm/min*,
- between 30 and 50 mm: 0.63 *mm/min*,
- between 50 and 70 mm: 0.38 *mm/min* .

Then, based on the methodology to get the P-wave velocities reported in tables 4.2 and figure 4.4 which consists of picking manually the first arrival on a waveform obtained by summation of five successive P-waves after propagation between pairs

of PZT. We place on an Admaswiler sandstone sample without salt precipitated, two pairs of PZT positioned oppositely at different heights. They provide a P-wave velocity reference in absence of confinement and at 10 MPa isotropic confining pressure in the dry Admaswiler sandstone. We recall the accuracy of the measurement that is $25\text{-}50\text{ m}\cdot\text{s}^{-1}$.

Table 4.2: P-wave velocities measured across a dry reference Admaswiler sample not confined and confined at 10 MPa

	No confinement P-wave velocity	Confinement 10 MPa P-wave velocity
$V_{P,Dry}(m\cdot s^{-1})$	2300	2950

4.2.4.2 Sample I rewetted without confining pressure

4.2.4.2.1 P-wave velocities and amplitudes description

The initial, dry sample P-wave velocities are manually picked on summed five successive shots transmitted between each pair of PZTs positioned on sample I and III at different confining pressure. They are averaged and reported in figure 4.4.

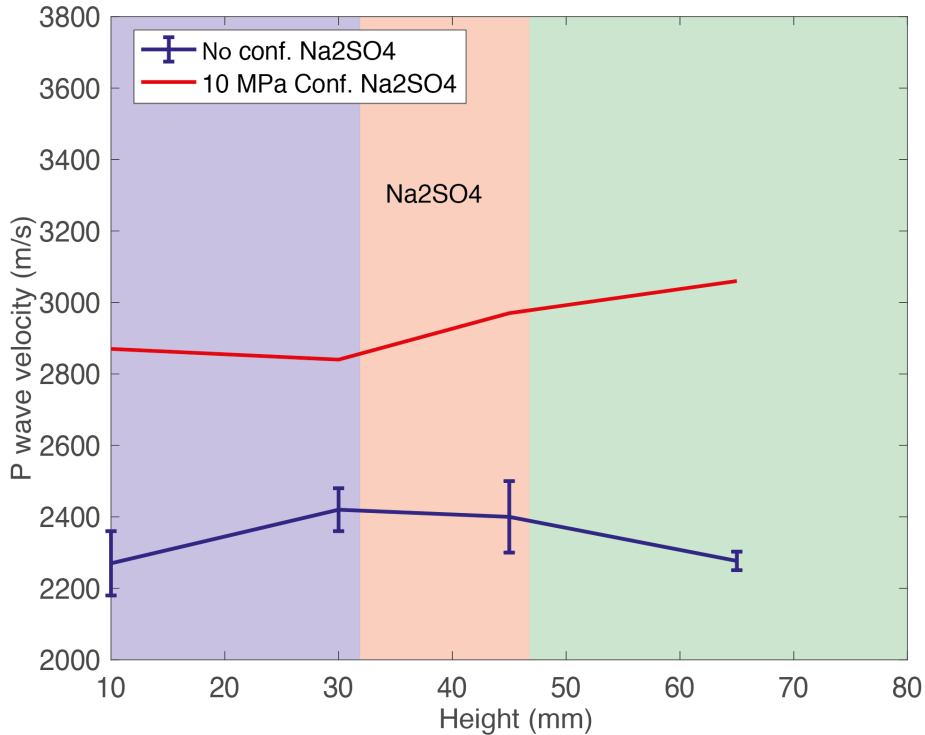


Figure 4.4: P-wave velocities measured across dry sample impregnated with ~ 5.4 gram of thenardite at 0 (blue curve) and 10 MPa (red curve) isotropic confining pressure (raw data in appendix A.3).

Comparison between the P-wave velocities measured in the reference Admaswiler sandstone and the sample without confining pressure and at 10 MPa confining pressure Without confining pressure, the P-wave velocity (blue

curve in figure 4.4 below the thenardite layer is similar to the reference value at 10 mm from the bottom but increase of about 100 m^{-1} at 30 mm right below the thenardite layer. This prove that there are a significant volume of thenardite precipitated below the thenardite layer of sample I and III. Through the salt rich layer, the P-wave velocity is significantly higher and above ther P-wave velocity is the velocity of the reference Adamswiller sandstone (table 4.2. When sample III is confined at 10 MPa (red curve in figure ??, the P-wave velocity increase generally. In the detail, Below the thenardite layer, the P-wave velocity is the lowest, the P-wave velocity across the thenardite rich layer is transient and above the P-wave velocity is the highest. The global P-wave velocity increase compared with the same measurement without confining pressure is attributed to the progressive cracks closure during the loading at 10 MPa (Fortin, 2007; Fortin et al., 2006).

P-waves properties profiles in sample I during the rewetting of the thenardite layer The normalized P-wave velocities profile is plotted to compare the evolution of the P-wave velocities in sample I at the different height during the water capillary uptake. The normalized velocity corresponds to : $V_{Normalized} = \frac{V(t)}{V(t_0)}$, with $V(t)$, the P-wave velocity at the instant t and $V(t_0)$, the P-wave velocity at the beginning. The normalized P-wave velocity aims to emphasize the evolution of the porous medium regarding the position of the PZTs with respect to the thenardite impregnated in the thick paraboloid dome. The normalized P-wave velocities picked on the spectrum in appendix A.3, and the maximum amplitudes of the P-waves are plotted in figure 4.5 as a function of the experimental time expressed in minutes. The diagram representing the number of acoustic emissions during five minutes is represented atop as a function of time.

Below the dome, at 30 mm, the normalized P-wave velocity rises and peaks at 1.13 (normalized P-wave velocity). At the same time, the micro-seismic activity is important. After, the velocity decreases constantly. At 48.8 mm, the P-wave velocity increases after one hour to 1.025 then diminishes constantly. A horizontal cross-section resliced from the X-ray microtomography datasets shows that the ultrasonic waves cross for one part equal to 60%, a porous medium deprived in thenardite and cross-cut by vertical swelling cracks, and for the other part equal to 40%, the porous medium filled at a pore fraction of 80% with thenardite according to the estimation in section 4.1. At 65 mm, shortly after one hour, the P-wave velocity, beforehand constant, starts decreasing to 0.975 then rises and reaches a plateau value at 1.1 (normalized P-wave velocity) higher than the initial normalized P-wave velocity.

According to David et al. (2017b), the starting point of P-wave velocity variation during the capillary uptake happens when the imbibition water front invades the porosity in the vicinity of the PZTs pair, which they call the Fresnel clearance zone. Consequently, the mean water sorption is calculated based on the timing of the first variation observed in the P-wave velocities profile:

- between 0 mm and 30 mm: $2.14 \text{ mm}/\text{min}$ ($\pm 0.9 \text{ mm}/\text{min}$),
- between 30 mm and 48.8 mm: $0.28 \text{ mm}/\text{min}$ ($\pm 0.02 \text{ mm}/\text{min}$),
- between 48.8 mm and 66 mm: $0.4 \text{ mm}/\text{min}$ ($\pm 0.05 \text{ mm}/\text{min}$).

The sorption rates below the salt dome and above the salt dome are in line with the reference sorption rate. Between 30 and 48.8 mm, the imbition front crosses the

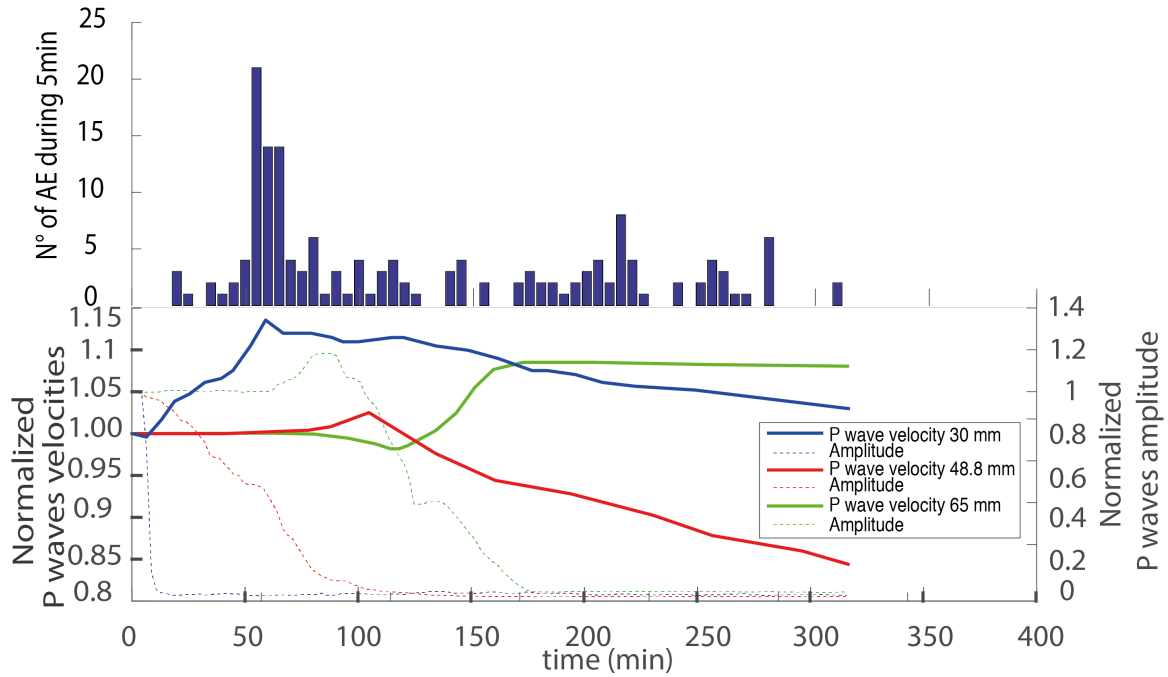


Figure 4.5: Top: diagram of number of cumulated acoustic emissions recorded every five minutes during the experiment without confining pressure, Bottom: normalized P-wave velocities and maximum amplitudes evolution of transmitted P-waves signals through sample I at different heights during the pure water capillary uptake without confining pressure applied on the rewetted sample.

salt dome and the sorption rate is three times lower than the reference one. To fulfill the analysis of the P-wave variation, the maximum amplitude is plotted to account for the moisture diffusion in sample I. According to David et al. (2017b), Pimienta et al. (2019), and Van Den Abeele (2002), the decrease in the P-wave amplitude precedes the variation of the P-wave velocity and marks the moistening of the pore. The moistening occurs early and rapidly between the pair of PZTs at 30 mm (below the salt dome). At 48.8 mm, the amplitude drop starts early but it is slow compared to the rapid drop measured below the salt dome at 30 mm. Finally, the amplitude variation between the pair of PZTs at 65 mm happens later, during the first bloom of acoustic emissions.

4.2.4.2.2 Acoustic emissions detected in sample I during the pure water capillary uptake

The first bloom of acoustic emissions peaks one hour after the beginning of the ultrasonic acquisition while water is invading the region below the salt dome. It fades shortly before 100 min when the waterfront is detected by the pair of PZTs positioned at 48.8 mm. Otherwise, AEs are detected until the end of the acquisition. In total, 170 events are detected during the experiment (figure 4.6).

The acoustic emission hypocenters and amplitudes are represented in figure 4.6, in a top and side view straddling on a vertical slice from a $27.26 \mu\text{m}$ resolution X-ray microtomography datasets acquired on sample I after the test. The time-lapse of the position of the hypocenter of AE reveals that at first, hypocenters of the AEs locate at the bottom of the dome and propagate upward.

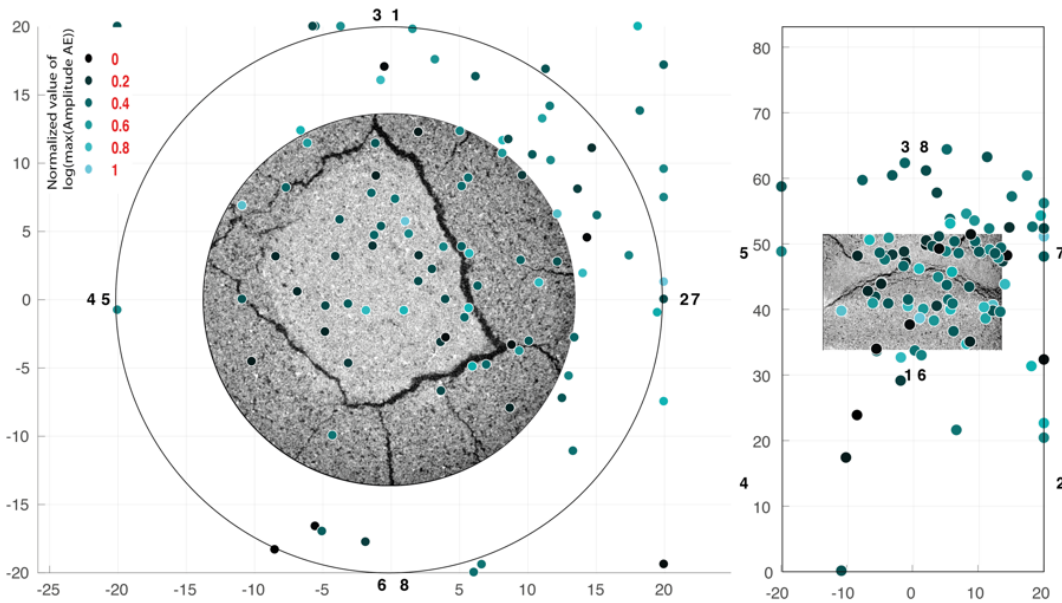


Figure 4.6: Acoustic emissions hypocenter represented on planar and vertical slice reconstructed from X-ray microtomography datasets acquired on sample I after the thenardite dome hydration. The X-ray planar slice reveals the medium crossed by the P-wave between pair of PZTs 5 - 7 at 48.8 mm. NB: The X-ray slice have a 27.26 mm diameter imposed by the acquisition in the XRay MicroCT Skyscan 1172. The hypocenter of the acoustic emission are calculated with a constant and isotropic P-wave velocity field. It explains the error in the positioning of the acoustic emission since the real P-wave velocity field is anisotropic and change during the experiment with the water saturation, the thenardite saturation and hydration in mirabilite and the presence of cracks.

4.2.4.2.3 BSE and X-ray microtomography analysis of reacted sample I polished section

On the X-ray vertical slice, a damaged zone is observed at the bottom of the salt dome with thin cracks parallel to the paraboloid dome. In the salt dome, the X-ray acquisition resolution is too low to detect intra-granular damages induced by crystallisation reported in Noiriel et al. (2010). Above the dome, the swelling cracks, that are already visible in the initial sample I impregnated with thenardite, expand. The BSE images acquired on the polished section are positioned relative to the X-ray microtomography vertical slice of sample I. The thenardite dome is delimited by the solid red line. The cracks are highlighted with dashed red lines on BSE images and the X-ray slice (figure 4.7). It is worth recalling that thenardite is reprecipitated from mirabilite when the sample is dried at 80°C after the experiment. Consequently, the volume of thenardite reprecipitated is at least 32% of the dried mirabilite if, during drying, the transport of dissolved sodium sulphate in poral solution is not taken into account. The ratios of the phases segmented are displayed on each BSE image with a pie chart (figure 4.7).

The pie charts are detailed in table 4.3. The ratio between the pores and the skeleton in the undamaged sandstone (above the dome) is 35%, while it should be 20.5%. This bias credits to the fraction of clay present in the original sandstone, that confuses during the BSE acquisition with thenardite, and by the quality of the segmentation tool. Meanwhile, these percentages of surface occupation are interesting because they show the evolution of the thenardite fraction and the pore volume creation during the

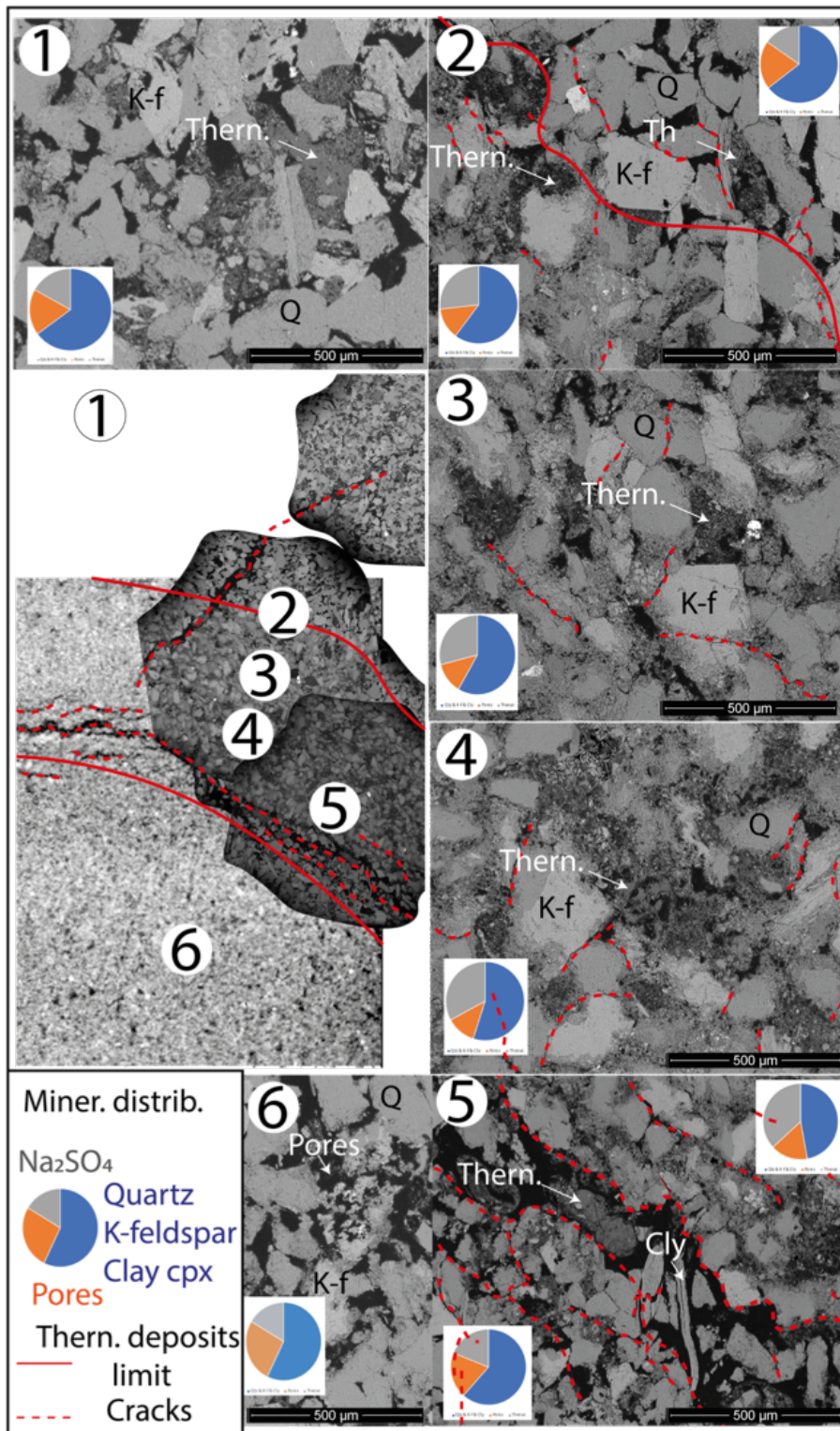


Figure 4.7: X-ray vertical slice of the damaged zone obtained from X-ray microtomography datasets at a resolution of $27.26 \mu\text{m}$ and BSE images of sample I polished sections. Mineral of the matrix, pores and Na_2SO_4 are segmented using the color segmentation tool provided with ImageJ. NB: the sodium sulphate phase observed is an anhydrous phase since we had to dry the sample to stop the rewetting reaction and preserve the sample in the same state. As such there is not information on the mirabilite habitus and nucleation site.

experiment.

Table 4.3: P-wave velocities measured across sample I at the beginning and at the end of the test

N° BSE image	thenardite %	pores %	skeleton %
1 (above the dome)	17	18	65
2 (above the dome)	15	20	65
2 (inside the dome)	27	13	60
3 (inside the dome)	29	13	58
4 (inside the dome)	33	12	55
5 (inside the dome)	37	13	50
5 (below the dome)	19	20	62
6 (below the dome)	16	26	57

It comes out of the ratios that thenardite is precipitated in all BSE images in varying proportions. Remarkably, in the dome, from figure 4.7.2 to figure 4.7.5, by going through the dome from the top to its bottom, the skeleton proportions decreases from 60% to 50% while outside of the dome, the skeleton proportion is $\sim 60\%$. The fraction of pores filled with thenardite or empty increases regarding the skeleton fraction. The fraction of thenardite increases as well compared to the empty pore fraction. Below and above the dome, the fraction of thenardite is lower (15% to 19%) than in the dome (27% to 37%) conversely with the empty pore fraction (18% to 26%) that is higher than in the dome ($\sim 13\%$) and close to 20%.

The damages in the salt dome are contrasted: at the bottom, large cracks parallel to the salt dome are recognized. Thenardite patch hundred of micrometer wide are even precipitated inside the crack opening. In the dome, the matrix is shattered by intragranular cracks and crushed grains and the damage in the dome seems to decrease with a growing height. Outside the dome, no intra-granular damage is reported, except the swelling cracks already observed on the X-ray vertical cross-section before the experiment.

4.2.4.3 Sample III rewetted at a 10 MPa confining pressure

4.2.4.3.1 P waves velocities and amplitudes description

Comparison between the initial and final P-wave velocities in confined sample III Finally, the P-wave velocities are measured at the end of the pure water injection. The difference with the dry confined sample III is minor in the medium at 64.7 mm. By contrast, at 44.7 mm, the P-wave velocity is $410m.s^{-1}$ higher than the P-wave velocity in the dry confined sample given in table 4.2.

P-wave properties profiles in confined sample III during the pure water injection in sample III The normalized P-wave velocities and maximum amplitudes, picked on the figure provided in appendix A.3 are plotted in figure A.3 as a function of the experimental time. Atop, the cumulated number of acoustic emissions recorded during five minutes is represented as a function of time. A pore pressure gauge evaluated the injection pressure during the test and is represented at the bottom. At 13.7 mm and 24.7 mm, the normalized P-wave velocity grows to a plateau at 1.035

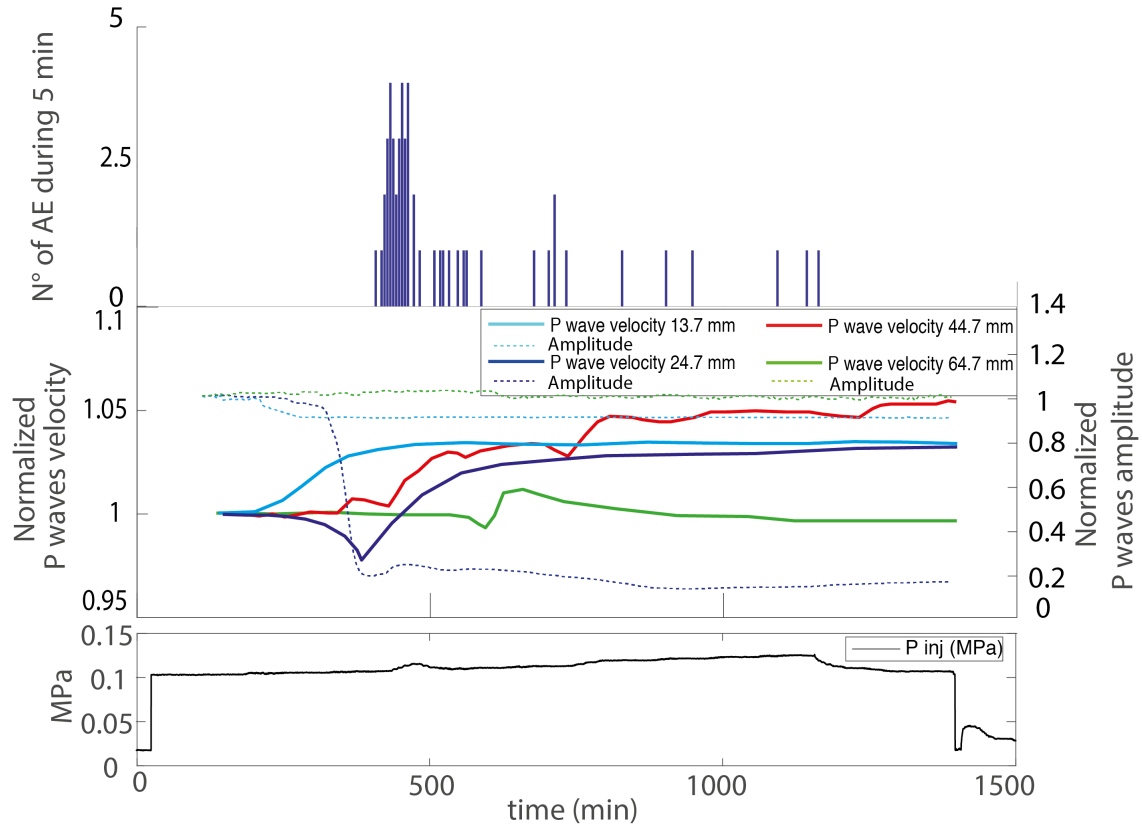


Figure 4.8: top: diagram of cumulated acoustic emissions recorded every five minutes during the experiment, Center: normalized P-wave velocities and maximum amplitudes profiles measured on the transmitted P-waves at different height through the sample confined at 10 MPa during the pure water injection, Bottom: Injection pressure measured in the tubing connecting the bottom of the sample and the Quizik pump.

(after a short decline for the P-wave propagating at the height of 24.7 mm). At 44.7 mm, the normalized P-wave velocity augments continuously to 1.05 until the end of the shots acquisition. Finally, at 64.7 mm, the normalized velocity slightly drops to 0.99 increases to 1.01 and tends toward 1.

According to David et al. (2017b), the imbibition front progression rate is calculated based on the P-wave velocity dip in the profile:

- between 0 mm and 13.7 mm: $0.29\text{mm}/\text{min}(\pm 0.03)$,
- between 13.7 mm and 24.7 mm: $0.2\text{mm}/\text{min}(\pm 0.02)$,
- between 24.7 mm and 44.7 mm: $0.33\text{mm}/\text{min}(\pm 0.03)$,
- between 44.7 mm and 64.7 mm: $0.09\text{mm}/\text{min}(\pm 0.002)$.

The imbibition front progression rates are in a closed range between 0 and 44.7 mm. Between 44.7 mm and 64.7 mm, the imbibition rate is divided by about according to the reference capillary uptake rate. It is worth noting that the injection pressure gauge records a bump simultaneously with the inflection displayed on the P-wave velocity across sample III at 44.7 mm shortly before 500 min.

Concerning the maximum amplitude of the P-wave transmitted through sample III, the signal between the pair of PZTs 3-7 was noisy and thus not represented. Otherwise, the

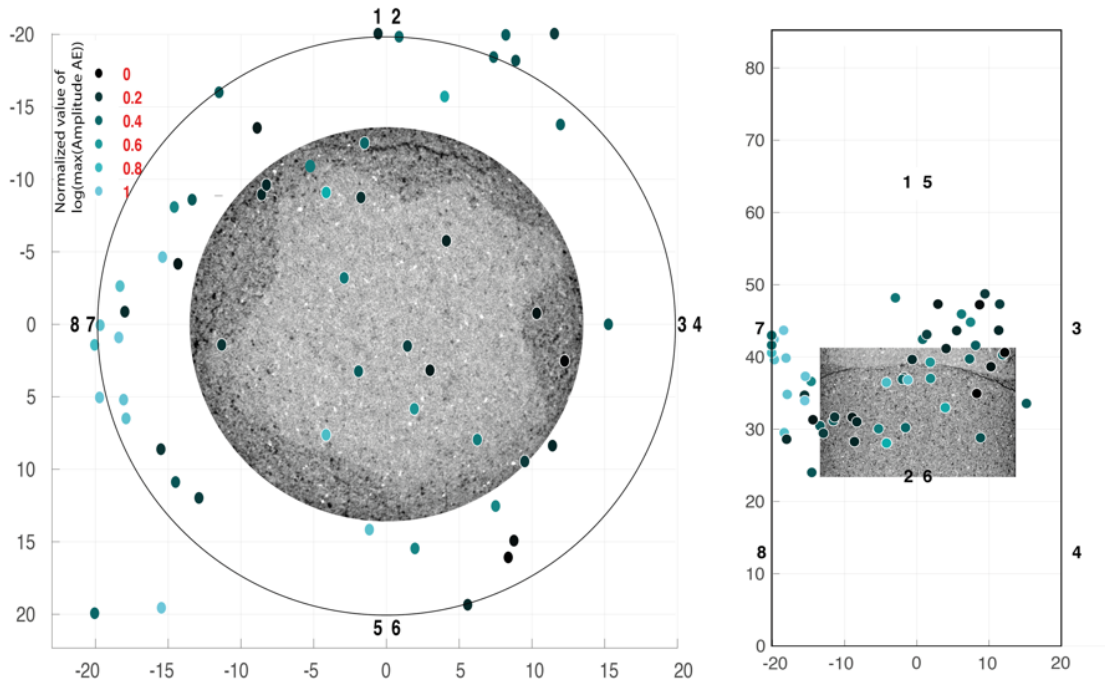


Figure 4.9: Acoustic emissions hypocenter represented on planar and vertical slice reconstructed from X-ray microtomography acquired on sample III after the rewetting of the sample initially impregnated with 5.4 g of thenardite and confined at 10 MPa.

maximum amplitudes of the P-wave across the sample precedes the velocity drop by 25 minutes at 13.7 mm and tends to 0.14. At 24.7 mm, it comes 60 minutes before the velocity variation and achieved a limit at 0.83. Surprisingly the drop in the maximum amplitude is simultaneous with the velocity dip at 64.7 mm and tends to only 0.95.

4.2.4.3.2 Acoustic emissions detected in confined sample III during the pure water capillary uptake

Regarding the detected acoustic emissions, 54 events are located during the test. The major shot of acoustic emissions happens during the growth of the P-wave velocities propagating at 24.7 mm and 44.7 mm and fades before the wetting of the region at 64.7 mm. Sparse events are detected until the end of the test (figure 4.8). The hypocenters and amplitudes of the acoustic emissions are represented in figure 4.9 on X-ray microtomography horizontal and vertical slice. The hypocenters are distributed in the region of the paraboloid salt dome mostly at the periphery of sample III than in its center.

4.2.4.3.3 X-ray microtomography analysis of reacted confined at 10 MPa sample III

On the vertical cross-section resliced from the X-ray microtomography datasets acquired on the dry reacted sample, thin slits cut across the porous medium at the base of the thenardite dome. The cracks thicken on the side of the vertical cross-section. Swelling cracks inherited from the thenardite impregnation are observed as well on the top right and left of the cross-section. On the side of the thenardite dome, the greyish pore filling is attenuated. Besides X-ray artifacts, it may reveal dissolution paths through the salt dome. No damages are observed in the center of the volume

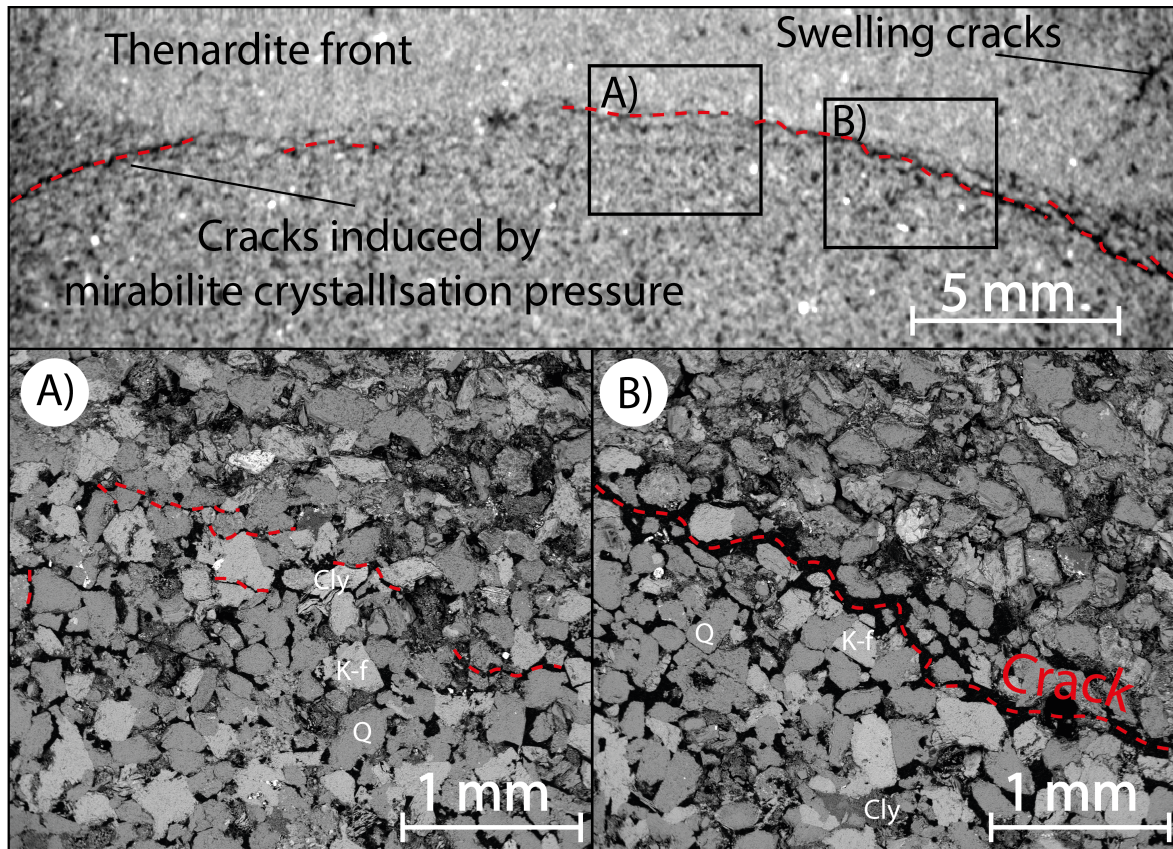


Figure 4.10: Vertical cross-sections from 3D X-ray tomographic datasets acquired after the experiment on sample III at a resolution of $27.26 \mu\text{m}$. A) and B) BSE images of sample III polished sections centered on the hydrated dome.

occupied by the precipitated salt, maybe because the scan resolution is over the crack size range (figure 4.10, top). BSE image A) in figure 4.10 illustrates the damages at the bottom of the hydrated dome in the middle of the sample. BSE image B) in figure 4.10 depicts similar view on the sample side. As described on the X-ray vertical slice, the cracks at the base of the salt dome are wider on the sample side. Above the crack, the polished surface is rougher than below the dome where the grains are firmly cemented. The rough surface is explained by the weakening of the skeleton after the thenardite dome precipitation described in section 4.1 and the rewetting of the thenardite dome.

4.2.5 Discussion

4.2.5.1 Acoustic signature of water saturating the porosity

We interpret the effect of the water capillary front progression on P-wave during spontaneous imbibition like in David et al. (2017a,b) and Pimienta et al. (2019). The softening effect of moisture adsorption in the pore is well observed below the salt dome by the P-wave amplitude drop in sample I and confined sample III. The salt fraction precipitated across the sample stops the moisture transport upward. It explains the delayed P-wave amplitude drop at 65 mm in sample I and the absence of drop at 64.7 mm on confined sample III.

Concerning the P-wave velocity, the picked profile shows that on part of the sample deprived of thenardite precipitated in the pore network, a short drop precedes the velocity increase to a plateau. According to the recap figure 1.24, the drop is the

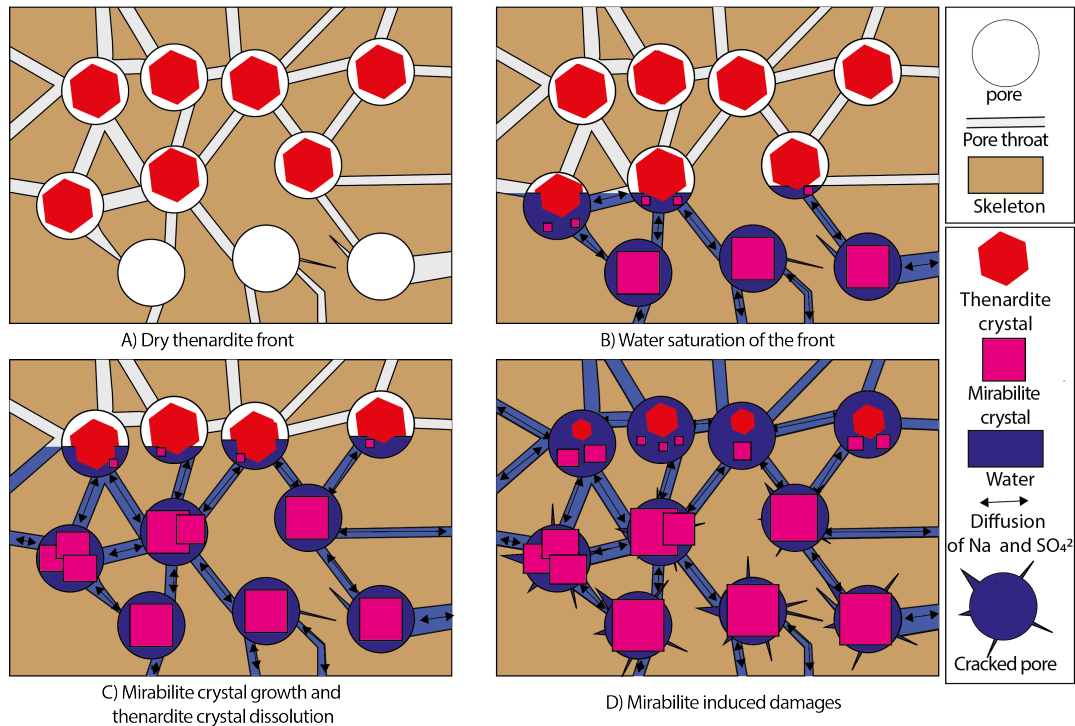


Figure 4.11: Conceptual model for damages induced by mirabilite crystallisation during rewetting of a dry porous medium impregnated with a thenardite fraction. NB: the thenardite dissolve and the solution become supersaturated with regards to mirabilite which will ultimately nucleates and precipitates.

expression of wave-induced flow while the sample is partially saturated. The increase and final plateau are the expressions of the Gassmann effect when the sandstone is fully saturated. Where the sandstone is enriched with thenardite, the P-wave velocity profile does not record the velocity drop. There, the fluid dissolves thenardite crystals that are consumed to precipitate mirabilite. Moreover, the solution is supersaturated with respect to mirabilite and consequently, it is more viscous than pure water. Because wave-induced flow in the pores depends on the fluid viscosity and the fluid saturation in the pore network, it may explain the originality of the velocity profile picked on the P-wave propagating through the salt dome.

4.2.5.2 Acoustic signature of thenardite/mirabilite phase transformation

At a 10 MPa isotropic confining pressure, at the height of 44.7 mm, a large excess in velocity is reported at the end of the acquisition. The PZTs at 44.7 mm are covering an area close to the thenardite dome. In the other part of the sample monitored, the variation is only a ten of $m.s^{-1}$. We attribute this excess in P-wave velocity to the progressive 'hydration' of the thenardite dome: the transformation of thenardite into mirabilite comes with a 180 % volume increase (Espinosa Marzal and Scherer, 2008). In the beginning, we estimate that 80% of the pore volume is filled by thenardite in the thenardite dome (figure 4.11 A). Consequently, mirabilite crystals grow in the pore space emptied by thenardite dissolution and may occupy up to 100% of the available porosity and contribute to the stiffening of the porous medium (figure 4.11 B and C).

As stated in the next section, the recording of acoustic emissions is related to cracks generation in the paraboloid dome. In the unconfined experiment, the P-wave velocity continuously decreases at the height of 48.8 mm in sample I and it goes with the acoustic emissions bloom attributed to crack generation induced by mirabilite crystallisation. According to Schubnel and Guéguen (2003) acoustic wave propagating in a cracked porous rock is lowered by a frequency-dependent dispersion attributed to squirt fluid flow or viscous fluid flow through the cracks (figure 4.11 D). This effect on P-wave velocity is highlighted in sample I at 30 mm and 48.8 mm, but in sample III, the crack generation does not seem to affect the P-wave velocity at 44.7 mm, maybe because the salt hydration stiffening effect balance the softening effect related to fluid flow through the newly grown cracks.

4.2.5.3 Mirabilite crystallisation induced damages

The interpretation of the P-wave velocity in the preceding section 4.2.5.2 shows the water flooding in the porous medium below the dome followed by dissolution of thenardite and precipitation of mirabilite that induces damages. The damage on the porous rock are also evidenced by the 170 acoustic emissions recorded in absence of confining pressure (figure 4.6) and the 54 events at a 10 MPa confining pressure (figure 4.9). It is interesting to see that bloom of AE happen during the saturation of the level below the dome. It means that the mirabilite supersaturation conditions are quickly reached to damage the sample. The hypocenters of the events locate first in the lower part of the dome. They are emitted by the crack spread at the bottom of the dome induced by the phase transformation that we observe on the X-ray vertical slice and the BSE images (figures 4.7 and 4.10). Then, the AEs prove that damage is induced during the experiments on a sample confined to a 10 MPa pressure. The cracks induced by mirabilite crystallisation are incontestably lower when the confining pressure is higher. The crystallisation pressure and the supersaturation index are estimated in next section for both experiments to explain this difference.

4.2.5.4 Microscopic estimation of crystallisation pressure and solution supersaturation with respect to mirabilite

The crystallisation pressure necessary to deform and damage the Adamswiller sandstone is approximated with Adamswiller sandstone uniaxial tensile strength (4.9 MPa) to which we add the confining pressure equal to 10 MPa in the second experiment. We use equation 4.3 (Steiger, 2005a) that gives the supersaturation necessary to get a crystallisation pressure that may deform and damage the sample in the condition of the two experiments. The results are written in table 4.4.

$$S = \exp \frac{PC * V_m}{R * T} \quad (4.3)$$

Taking $R=8.32 \text{ m}^3.Pa.K^{-1}.mol^{-1}$, and $\bar{V}_m=219.8 \text{ cm}^3.mol^{-1}$ for mirabilite, the results are reported in table 4.4.

A quick modeling with Phreeqc (Parkhurst and Appelo, 2013) and database Pitzer.dat of the maximum supersaturation predicted when thenardite is set at the equilibrium phase in an aqueous solution at 20°C, gives a saturation of the solution with respect to mirabilite, equal to 3.47 and thus a crystallisation pressure induced by mirabilite equal to 13.8 MPa. In the confined experiment at 23°C, the modeled supersaturation is equal to 2.57 and the corresponding mirabilite crystallisation pressure is 10.6 MPa.

Table 4.4: Estimate of the lowest supersaturation bound to damage sample I and III by mirabilite crystallisation

	Sample I 20°C No confinement	Sample III 23°C 10 MPa confinement
Mirabilite	1.56	3.8

Without confining pressure, the Phreeqc-modeled crystallisation pressure bound match with the requisition regarding the tensile strength of the Adamswiller sandstone. At a 10 MPa confining pressure, the Phreeqc-modeled crystallisation pressure is 10.5 MPa. It is below the requisition regarding the confinement and the tensile strength of the porous medium, 14.9 MPa. According to our macroscopic assumptions no cracks should be generated during the hydration reaction, nevertheless, AEs are recorded. It means that locally the strength of the material must be lower because the recording of AEs sign the onset of tensile failure. The pressure exerted in the fluid film between the mirabilite crystal and the pore wall may have deformed the pore until failure.

The effect of the confining pressure is sensible on the damage differences between the two tests. As calculated in table 4.4, with the confining pressure at 10 MPa, cracks generation requires a higher solution supersaturation with respect to mirabilite. Thus the time necessary to build the saturation is longer at a higher confining pressure. Also, more thenardite has to dissolve to generate the supersaturation and more pore volume is available for mirabilite reprecipitation. The second reason is linked to the transport of the chemical species in the connected porosity because a concentration gradient exists between the supersaturated solution in the salt dome and the solution saturating the pores in the remaining rock. An extended duration to reach the sufficient supersaturation results in the transport of more sodium and sulphate ions in the rest of the saturated sample. Finally, to counterbalance a higher confining pressure, a higher supersaturation with respect to mirabilite must be overtaken and it results in more empty pore volume and more materials transported. In the end, it explains the low damage obtained during the confined experiment.

4.2.5.5 Thenardite dome control on water transport

During both tests, the progressions of the moistening and the water imbibition front are delayed by the thenardite dome according to the reference sorption rate. The moisture is probably captured in the thenardite dome. More striking, the P-wave amplitude variation above the dome comes after the record of the first bloom of AE. We think it means that cracks propagate in the dome according to the acoustic emissions recorded and the P-wave velocity reduction. These cracks become the preferential path for moisture transport in the upper part of the sample. Concerning the waterfront progression, differences exist in the transport between the two experiments related to the modus operandi: free uptake in the unconfined test and the constant injection rate in the confined one. Apart from this, delays in the waterfront arrival are evidenced beside the injection pressure bump in the confined experiment which significate that the thenardite dome acted like a permeability barrier. Cracks create paths for water and moisture transport across the dome permeability barrier. Besides, during the experiment with a 10 MPa confining pressure, the dome sides seem to be dissolved. Then the fluid may ahev crossed the front there.

4.2.6 Conclusion

The acoustic monitoring of pure water capillary uptake in an Adamswiller sandstone impregnated with ~ 5.4 grams of thenardite dome, successfully detects the water saturation of the porous medium and the transition between thenardite and mirabilite. The acoustic monitoring emphasizes the damages induced by mirabilite crystallisation via the recording of acoustic emissions and the P-wave velocity drops measured on the wave-path across the thenardite dome. The damages induced by mirabilite precipitation on the porous rock in the second experiment validate the assumption of crystallisation induced damages in confined conditions at least to a burial of several hundred meters (~ 400 m). To prove the validity of crystallisation induced damage in reservoir conditions (to a pressure level close to 30 MPa), we need to move on to another salt because the hydration reaction of thenardite cannot exert a sufficient crystallisation pressure according to Steiger (2005a) and Steiger, Kiekbusch, and Nicolai (2008). This is the objective of the next chapter 5, which presents a series of rewetting experiments with Adamswiller sandstone samples impregnated with magnesium sulphate. To our knowledge, the modeling of such a hydration reaction leading to the porous medium stiffening and cracks generation provoked by precipitation of mirabilite or any other hydrated mineral is not addressed yet in the literature. Nevertheless, it would bring valuable information to study geological applications concerned with ongoing salt dissolution/crystallisation in the porous reservoir.

Chapter 5

Damage induced by epsomite precipitation in confined reservoir conditions

Contents

5.1	Sample preparation	120
5.1.1	Introduction	120
5.1.2	Kieserite dome precipitation protocol	120
5.1.3	Conclusion	121
5.2	Damage induced during rewetting of an Adamswiller sandstone impregnated with kieserite	122
5.2.1	Introduction	122
5.2.2	Experimental protocol	122
5.2.3	Results	122
5.2.4	Discussion	124
5.2.5	Conclusion	126
5.3	Damage induced by epsomite crystallisation in a uni-axially confined sample at 10 MPa	127
5.3.1	Introduction	127
5.3.2	Methods	127
5.3.3	Results	129
5.3.4	Discussion	132
5.3.5	Conclusion	133
5.4	Mechanical stiffening driven by crystallisation of epsomite in confined reservoir conditions	134
5.4.1	Introduction	134
5.4.2	Methods	134
5.4.3	Results	135
5.4.4	Discussion	138
5.4.5	Conclusion	142
5.5	General conclusion	143

Abstract

In the preceding work, the damages induced by the phase transition thenardite to mirabilite in a porous Adamswiller sandstone at different confining pressure (0 and 10 MPa) are monitored. It validates the onset of mirabilite crystallisation induced damage at 10 MPa. In the quest to prove damages induced by crystallisation in deeper geological settings (~ 30 MPa), a similar experiment must be conducted at this level of confining pressure. Magnesium sulphate is chosen because, like sodium sulphate, it has several hydrate phases stable in a temperature range accessible with an oven and the phases are keen to induce a higher crystallisation pressure than mirabilite. The rewetting of kieserite previously impregnated in a porous rock leads to epsomite crystallisation and induces internal damages described in Balboni et al. (2011), Lindström et al. (2016), Ruiz-Agudo et al. (2007), and Steiger et al. (2011). In this chapter, we exploit the phase change between kieserite and epsomite at a temperature close to 20°C in an Adamswiller sandstone. We describe four experiments of pure water capillary uptake in an Adamswiller sandstone impregnated with kieserite: first in absence of confinement, second and third at 0 and 27 MPa isotropic confining pressures and fourth at 10 MPa uniaxial pressure. The second and third experiments are monitored with the Richter mini system and the sample is clamped in the 'Geodesign' triaxial cell of the laboratoire de Géologie of Ecole Normale Supérieure of Paris. The fourth experiment is monitored with the Mistras acoustic monitoring set-up. Before and after the rewetting, 3D X-ray microtomography scans are acquired on the samples to describe the distribution of kieserite and epsomite precipitated in the porous sample and the damage. Without confining pressure, after around 10 days, we see damage on the surface of a rewetted sample prepared with $MgSO_4$. When we had a confining pressure, no damage are recorded with acoustic emission and observed on the X-ray microtomography datasets acquired post-mortem. Nevertheless, at the micro to nano-scale, some deformation related to the hydration of kieserite are reported.

5.1 Sample preparation

5.1.1 Introduction

The protocol written at the beginning of chapter 4 section 4.1 to prepare a thenardite dome in an Adamswiller sandstone needs to be adjusted to suit the specific properties of the magnesium sulphate.

5.1.2 Kieserite dome precipitation protocol

First of all, we had to modify the drying temperature during the drying sequence of the sample. Indeed, at the drying temperature used for thenardite precipitation, hydrated phases as $MgSO_4 \cdot 2H_2O$, $MgSO_4 \cdot 1.25H_2O$ or $MgSO_4 \cdot 4H_2O$ are likely to persist in the porous medium. An additional drying step above 115°C (Haynes, 2005) during is required to dehydrate all phases in kieserite. However Pr. Michael Steiger advertised us that Kirsten Linnow obtained mixtures containing the five fourth hydrates unless drying the sample at 200°C during at least 3 weeks (Steiger et al., 2008). Secondly, Espinosa-Marzal et al. (2011) pointed out that for a similar concentration with dissolved sodium sulphate, the solution with magnesium sulphate is more viscous which slow down the fluid transport. To work around the problems, firstly we choose to use a less concentrated solution to reduce the viscosity effect. Secondly, the precipitation of the kieserite dome is done in two steps:

1. The first step is the precipitation of a hydrated magnesium sulphate mix by drying the sample between 50°C and 60°C . 4-4.5 ml of $MgSO_4$ rich solution is injected and the sample is weighted to control the rate of evaporation.
2. The next step starts when all the free water is evaporated. The covering is removed and the oven temperature is set above 120°C during one week to dehydrate the hydrated magnesium sulphate into kieserite (Haynes, 2005) or most probably a mixture of the five fourth hydrates (Steiger et al., 2008). The sample is weighted daily to control the rate of dehydration. One may wonder why step one is not bypassed. In fact, the adhesive on the heat-shrinkable covering used does not resist at a temperature above 80°C .
3. the cycle is repeated to increase the concentration of kieserite in the dome.

In appendix A.4, a table summarizes the properties of samples impregnated with $MgSO_4 \cdot H_2O$.

5.1.2.1 Results and discussion

Contrary to samples prepared with thenardite where a unique dome is detected, kieserite precipitates are more widespread and several kieserite impregnated layers are described in the prepared sample. We summarize their properties in figure 5.1. X-ray scans are taken on sample IX, XI and XII. Sample IX is impregnated with 7.8 g of kieserite revealing 3.6 mm and 2.9 mm thick kieserite bands saturated both at 65%. It represents 35% of the total amount of kieserite precipitated. Horizontal slits are visible on the sample surface. Sample XI is impregnated with 7.59 g of kieserite revealing a 6 mm thick kieserite band saturated at 70%. It represents 36% of the salt injected. Sample XII charged with 7.11 g has two bands with a computed porosity saturation

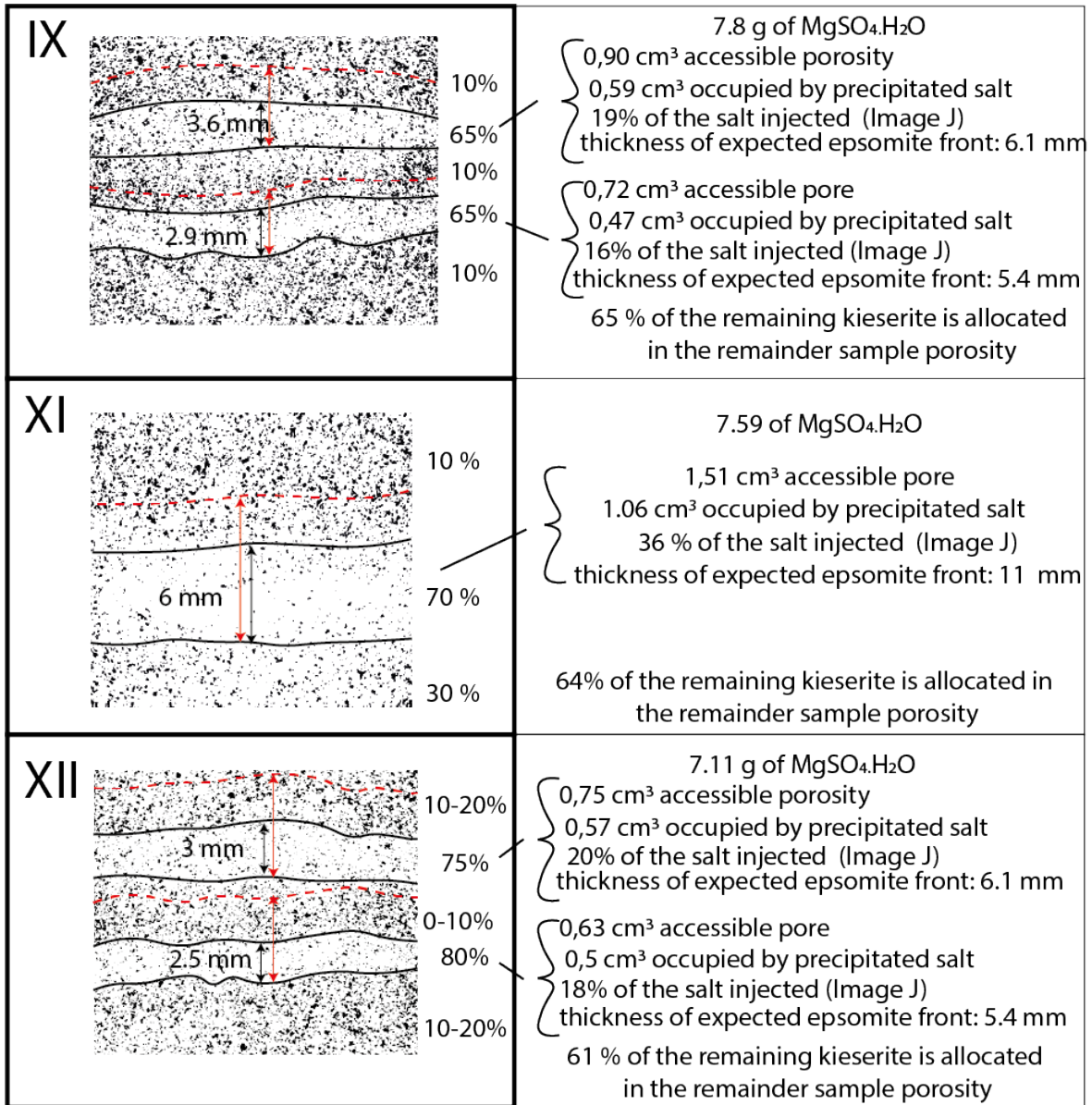


Figure 5.1: Properties of $MgSO_4 \cdot H_2O$ precipitated in Adamswiller: top, sample IX, 7.8 gram of $MgSO_4 \cdot H_2O$ ($19 \times 18 \text{ mm}^2$), middle sample XI, 7.6 gram of $MgSO_4 \cdot H_2O$ ($18 \times 17 \text{ mm}^2$) and bottom, sample XII, 7.11 gram of $MgSO_4 \cdot H_2O$ ($18 \times 18 \text{ mm}^2$).

at 75% and 80% with kieserite. The bandwidths are 3 mm and 2.5 mm. A calculation shows that for an original rock with a porosity equal to 0.205, the salt content in the band is only 29%. Sample XI is impregnated with 7.59 g of kieserite revealing a 6 mm thick kieserite band saturated at 70%. It represents 36% of the salt injected. To conclude, about a third of the kieserite precipitates is in the band according to the computation (figure 5.1). The two-other third are precipitated in the remaining porosity covered by the heat shrinkable sleeve.

5.1.3 Conclusion

Inspired by many examples of salt damaging experiments we have obtained a sample that can react in confined reservoir conditions to release stress by epsomite crystallisation pressure. Unfortunately, samples prepared with more than ~ 7.5 grams of

$MgSO_4 \cdot H_2O$ are already damaged. The extent of the damage is difficult to evaluate at the resolution available with X-ray microtomography but as samples keep a good cohesion they are used thereafter.

5.2 Damage induced during rewetting of an Adamswiller sandstone impregnated with kieserite

5.2.1 Introduction

The transition phase between kieserite and epsomite is renowned to induce internal damages in porous rock (Balboni et al., 2011; Ruiz-Agudo et al., 2007). As a preparation for future tests with monitoring, we want to evaluate the time necessary to observe damages in the sample and to have an idea of the damaging mechanism. The sample is not confined and kept at a varying laboratory temperature $\sim 25^\circ\text{C}$.

5.2.2 Experimental protocol

Sample X is an Adamswiller sandstone cylinder ($80.4 \times 40 \text{ mm}^2$) containing 9.5 g of kieserite precipitated according to the protocol for magnesium sulphate presented in section 5.1. The sample is stored at 120°C to ensure that only kieserite crystals precipitated. Before the experiment, the sample is first cooled down to the laboratory temperature, $\sim 25^\circ\text{C}$. Then, sample X is bathed, by its salt-free side, in a white plastic dish containing 45 ml of pure water (Milli-Q from Millipore, $18 \text{ M}\Omega\text{cm}$ at 25°C). The bath is isolated from the laboratory air by a layer of parafilm taped on the sample and the plastic dish. Pictures are taken with the same sample orientation and show the evolution of the sample after 15, 18 and 28 days (figure 5.2). At the end of the test, after the remaining water in the sample evaporates, the sample is impregnated with epoxy. An X-ray microtomography scan at a $27.26 \mu\text{m}$ resolution is taken targeting the cracked region and processed with ImageJ (Schindelin et al., 2012) to extract vertical cross-sections of the damaged zone (figure 5.3).

5.2.3 Results

5.2.3.1 Epsomite needles growth

The kieserite impregnated sample X surface is crossed by thin cracks marked in red on figure 5.2, D.0. After 15 days, needles of salt, one millimeter thick, grow perpendicular to the main cracks. The salt is probably epsomite which is the stable magnesium phase at the laboratory temperature. A thin crack, drawn in red, propagates above the fibrous crack (figure 5.2, D.+15). On the 18th day, the main crack opens up and the needles of epsomite deform to follow the opening or broke up. In that case, the shattered fibers turn whitish because they dehydrate in a less hydrated form probably hexahydrate. Above the main fibrous crack, the horizontal crack, marked in red, expands and vertical swelling cracks develop perpendicularly (figure 5.2, D.+18). On the 28th day, the grown magnesium sulfate needles still attached to the top of the main crack surface are disconnected from the bottom surface. Above, the vertical cracks are filled with epsomite needles (figure 5.2, D.+28).

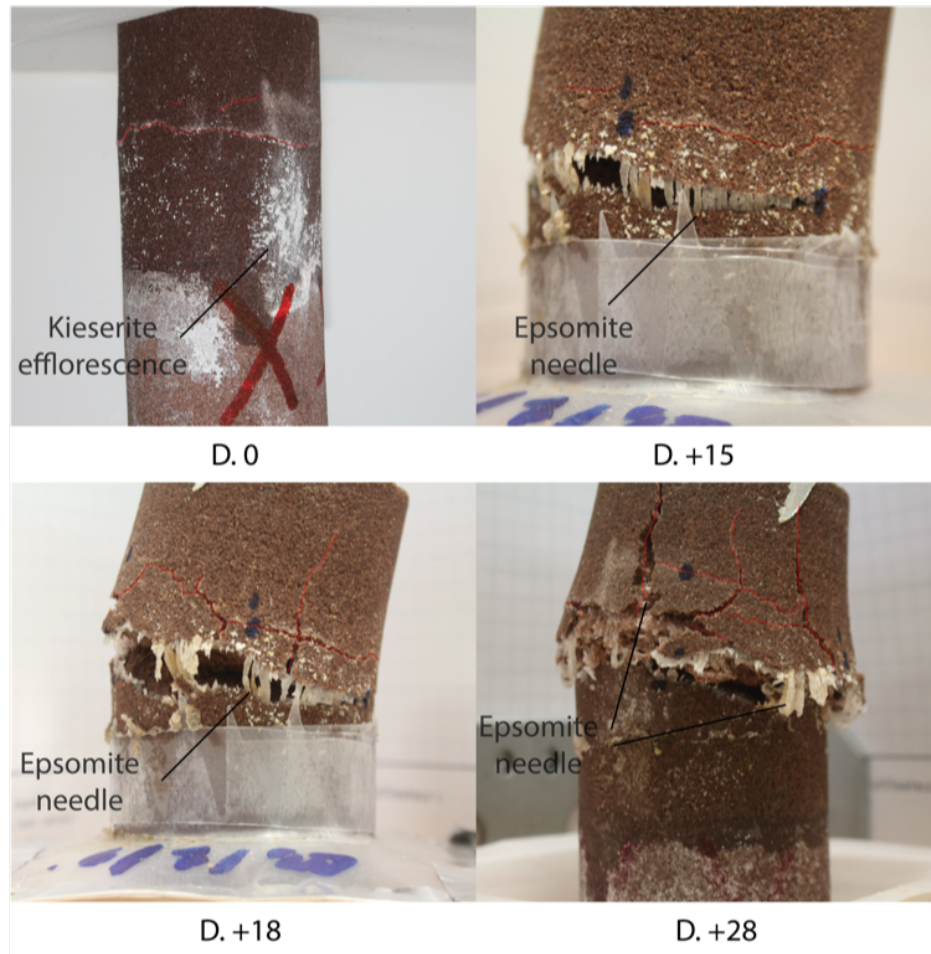


Figure 5.2: Photo gallery of the pure water capillary uptake in sample X, an Adamswiller sandstone impregnated with 9.5 g of kieserite/monohydrate mix.

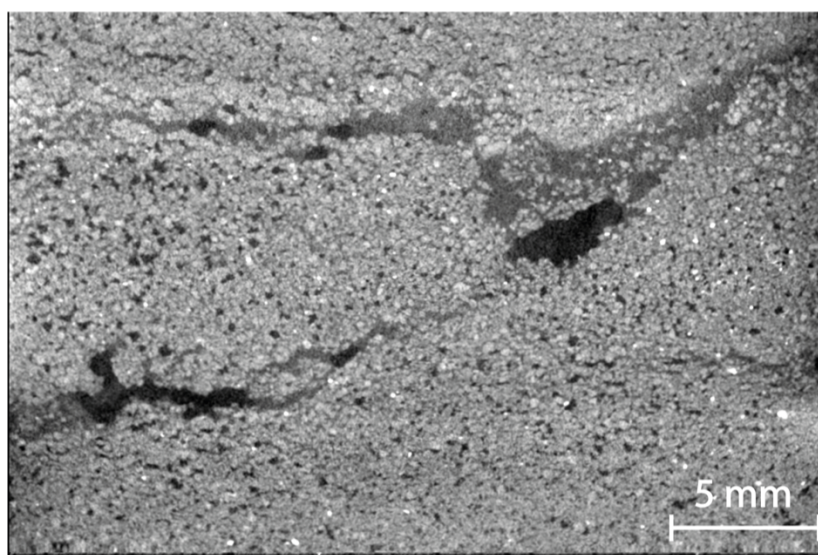


Figure 5.3: vertical cross section resliced with ImageJ from 3D X-ray tomography datasets, targeting the damaged zone in kieserite rich sample X after one month in a pure water bath.

5.2.3.2 Internal damage induce by magnesium sulphate precipitation

The vertical cross-section processed with ImageJ (Schindelin et al., 2012) displays the internal damages induced by magnesium sulphate crystallisation on sample X (figure 5.3). The cross-section displays two millimeter thick veins filled with a greyish mineral paste. As explained in the chapter 2, section 2.2, magnesium sulphate attenuation is lower than the attenuation of quartz and K-feldspar. The greyish filling is identified as the epoxy resin with traces of Magnesium and Sulphate after EDS microanalysis. The dark pixels are empty pores. About the cracks, the lower cracks divide to the right in thinner horizontal slits ($\approx 100\mu\text{m}$). The upper crack left termination also prolongs in thin slits. Thin diagonal slits connect the two veins. Millimetric voids are observed in the top and bottom veins. Between the veins, the pore network is composed of large empty pores and smaller greyish pores that could be filled by epoxy or magnesium (figure 5.4).

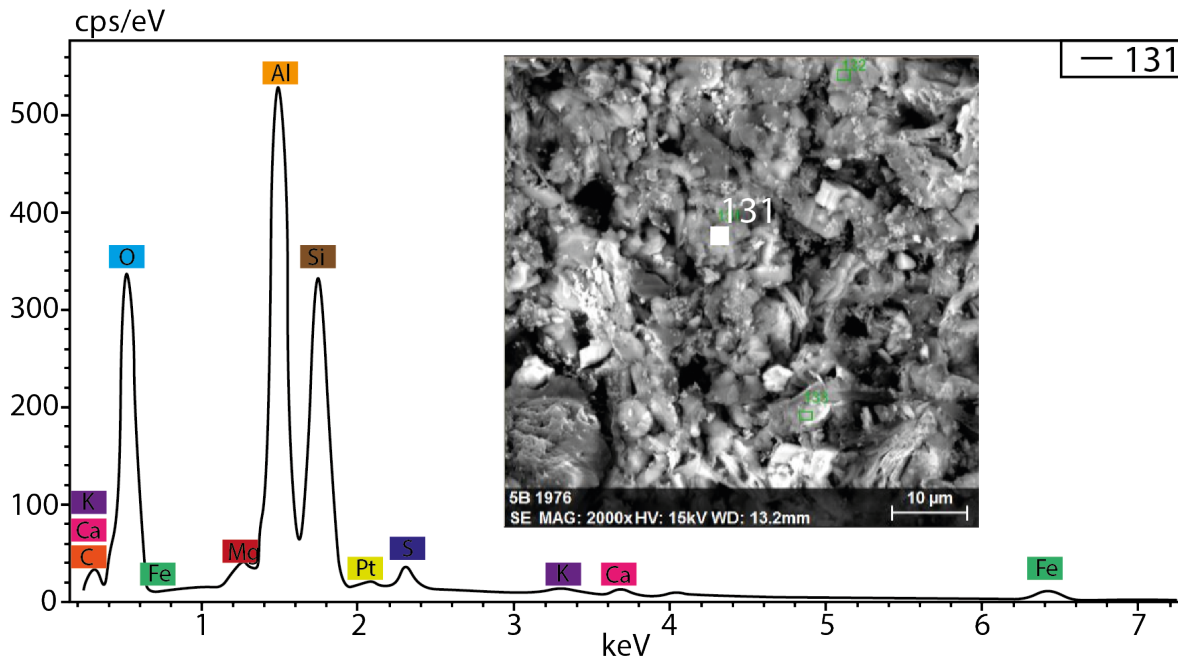


Figure 5.4: SEM BSE image focus on sample X damaged area microanalysed with EDS. The surface is crosscuts by thin slits between the grains. Traces of $MgSO_4$ are evidenced after point 131 EDS microanalysis. The high aluminium peak corresponds to alumina's particle used to polish the section.

5.2.4 Discussion

5.2.4.1 Epsomite crystallisation pressure

The pure water capillary uptake in sample X leads to the transition of kieserite in epsomite, which we will loosely designate as a hydration reaction. Undoubtedly the hydration of kieserite results in important damages on sample X induced by epsomite crystallisation. The level of pressure is predicted with Phreeqc using the Pitzer (high salinity) database (Parkhurst and Appelo, 2013): the temperature is set at 25°C and kieserite is set in excess as equilibrium phase in the aqueous solution (10 mole in the assemblage at the beginning). Phreeqc simulates that the saturation index of epsomite is 0.67, 0.54 for hexahydrate, 0.41 for pentahydrate and 0.17 for starkeyite

(leonhardite). The corresponding crystallisation pressure potentially exerted by epsomite is equal to 11.3 MPa, 10.2 MPa for hexahydrate, 9.2 MPa for pentahydrate and 4.4 MPa for starkeyite (source <http://webmineral.com/> for hexahydrate and starkeyite molar volume). Consequently, it confirms the work of Balboni et al. (2011) and Ruiz-Agudo et al. (2007), who show that rewetting of kieserite provokes high crystallisation pressure and epsomite crystallisation induced damage.

5.2.4.2 Comparison with thenardite dome hydration

The described experiment is a capillary uptake in a sandstone sample impregnated with magnesium sulphate like in the experiment described in chapter 4 with sodium sulphate. Several differences are reported: with magnesium sulphate, the damages happens after several days, at least two horizontal millimeter veins formed and epsomite needles grow athwart the horizontal and vertical cracks. With sodium sulphate, the cracks occur rapidly after the waterfront reaches the salt dome and thinner veins ($\approx 100\mu m$ formed at the bottom of a thenardite dome. To explain the delay in the damage, Balboni et al. (2011) and Ruiz-Agudo et al. (2007) propose a hindered epsomite nucleation and a slower solution capillary uptake imposed by a higher viscosity in the magnesium sulphate dissolved solution. Additionally, we can mention the lower crystal growth and dissolution rate of epsomite compared to mirabilite: the growth rate of mirabilite and epsomite plotted in chapter 2.1, section 2.1, shows that at similar laboratory temperature, the epsomite dissolution/growth rate is about four times lower than the mirabilite dissolution/growth rate. Then at an equal pore dimension, a single epsomite takes four more time to reach a damaging size than a thenardite single crystal at the same temperature and saturation.

5.2.4.3 Mechanism of damages

The conceptual model in chapter 4 proposes that the phase transition of thenardite in mirabilite happens in-situ or in the immediate vicinity porosity. These experiments detailed in chapter 4 last less than two days, that is why we do not see the effect of mirabilite remobilisation. Several signs indicate that kieserite hydrates in situ and is remobilized: the width of the cracks filled with epoxy and the growth of the needles prove that some material is transported through the connected pore network to the site of crystallisation where it precipitates in thickening epsomite veins and fibrous needles. Moreover, because the cracks are epoxy filled, it emphasizes that the epsomite veins are redissolved and reprecipitated to form thickening epsomite veins upward (figure 5.3). In a preceding paragraph, we calculated with Phreeqc the higher limit for epsomite crystallisation pressure in sample X. The value is high enough to induce damages in an Adamswiller sandstone. The veins are necessarily cracked and thicken by epsomite crystallisation since it is the only active damaging process. A conceptual model is proposed in figure 5.5. The main points are the thin slits induced by epsomite crystallisation that thicken driven by the accumulation of magnesium sulphate transported to the veins. At the same time, the water imbibing front progress upward through the kieserite impregnated porosity by kieserite dissolution and stretching induced cracking induced by epsomite crystallisation and the global swelling of the porous medium below. Newly formed thin slits expand in thick veins while the epsomite veins below are dissolved and the ions Mg^{2+} and SO_4^{2-} are transported upward. The discussion is illustrated with figure 5.5. Elburg et al. (2002) remarks the relation between stylolitisation and fibrous veins related to crystallisation like in Merino, Canals, and Fletcher (2006)

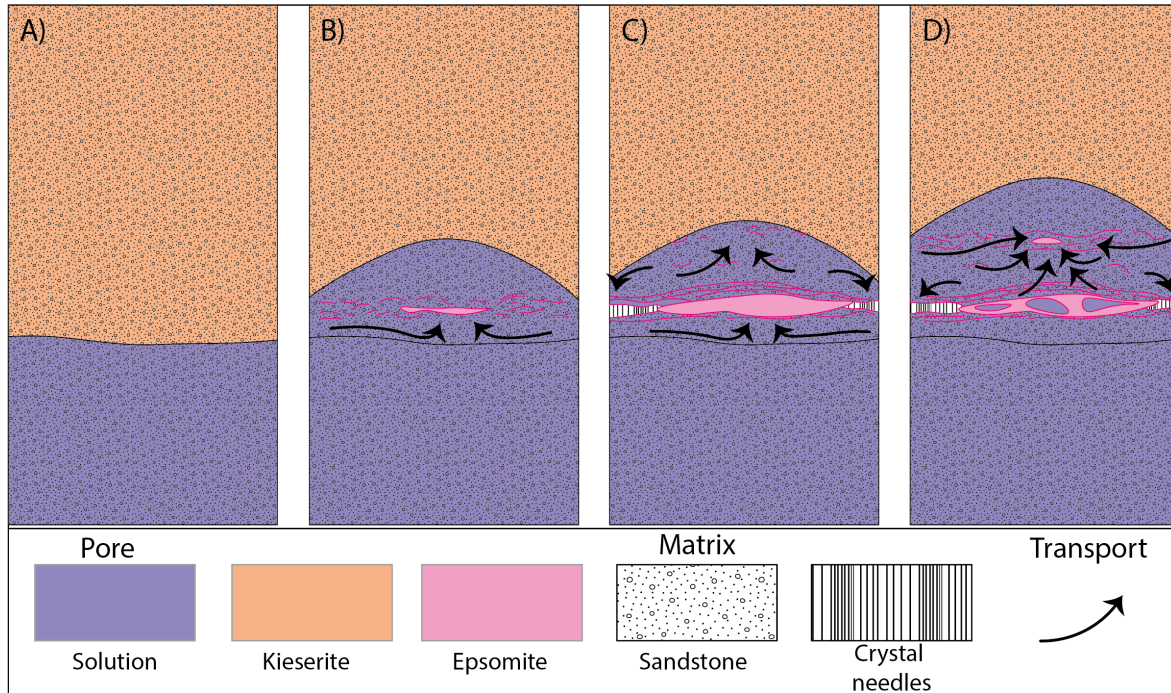


Figure 5.5: Conceptual model to illustrate the damage related to salt remobilisation during pure water capillary uptake in a sandstone impregnated with magnesium sulphate: A) the pure water imbibition front reach the kieserite rich porosity. B) kieserite dissolve in the aqueous solution supersaturated with respect to epsomite. Epsomite crystallisation induced thin cracks that begin to localize a primary damage front. This step is explained in figure 4.11 C) Epsomite vein precipitate, and fracture the porous medium. Epsomite needles follow the fracture spreading. Upward, thin cracks start to localise a secondary damaged zone D) Dissolution of the primary epsomite vein, ions transport and recrystallisation in the secondary damaged zone.

for zebra textures. They conclude that the fibrous material precipitated comes from the stylolite dissolved material. This experiment validates to a certain extent their intuition of material dissolution that leads to crystallisation damages in the vicinity.

5.2.5 Conclusion

Pure water capillary uptake in an Adamswiller sandstone impregnated with 9.5 mg of kieserite results in important internal damages induced by epsomite crystallisation. The kieserite hydration occurs for an extended time regarding the hydration of the thenardite studied in chapter 4. Then it leads to more materials transported through the connected porosity of the saturated porous rock and epsomite veins widening by material accumulation. Also, we calculate that the maximum predicted crystallisation pressure is of the order of the effective pressure encountered in a geological reservoir. Consequently, we will re-edit this test under confined conditions with an acoustic set-up to monitor the potential damages, which should be important. In the next section, an Adamswiller sample impregnated with kieserite and confined uni-axially is rewetted in a thermoregulated chamber for 20 days. An acoustic monitoring system logs continuously the absolute acoustic energy in the sample and the acoustic emissions.

5.3 Damage induced by epsomite crystallisation in a uni-axially confined sample at 10 MPa

5.3.1 Introduction

To validate the rewetting protocol in confined conditions, a rewetting experiment of an Adamswiller sandstone impregnated with kieserite is conducted while the sample is uni-axially confined at 10 MPa. Besides, we test a thermoregulated chamber and another acoustic monitoring system. In the future, they will be employed for crystallisation pressure experiments in the LFCR laboratory.

5.3.2 Methods

5.3.2.1 Experimental protocol

Sample IX is an Adamswiller sandstone cylinder ($80.4 * 40mm^2$) impregnated with 7.8 g of kieserite. Thin horizontal cracks are optically recognized on the sample surface before the pure water capillary uptake test. Before the test, a 3D X-ray microtomography scan ($27.26 \mu m$ resolution) is acquired on the sample and focus on the precipitated kieserite. Resliced vertical slice displays 3.6 and 2.9 mm thick kieserite rich layers but no internal cracks. An insulated chamber adapted to the Zwick HB 250 kN controls the temperature. It maintains a temperature between 25 °C and 15 °C around the sample. A cold bath regulates between 15 °C and 20 °C the imbibing water poured in a plastic dish.

Sample monitoring consists of the logging of the piston displacement and an acoustic monitoring system, the MISTRAS system. Two polystyrene foam base plates help to position the six PZTs on the sample surface with rubber bands. A layer of vacuum grease ensures a good coupling between PZTs and the sample surface. The sample is oriented with the salt-free side at the bottom and placed under the piston in a plastic dish. 10 MPa are progressively applied by the piston and later 40 ml of pure Milli-Q water (Milli- Ω from Millipore, 18 M Ω cm at 20 °C) is poured into the plastic dish.

5.3.2.2 MISTRAS high-frequency acoustic monitoring system

5.3.2.2.1 Description

The system available at the laboratory of complex fluid (UMR 5150) has been already used experimentally to study crack propagation in concrete and size effect on the fracture process zone (Grégoire et al., 2015; Jacqueline Saliba, 2012; Lefort, Pijaudier-Cabot, and Grégoire, 2015; Saliba et al., 2016). The mechanical oscillation is acquired by six acoustic transducers with resonant frequency at 150 kHz, diameter 10 mm and sensible to P wave, R15 α a PZT manufactured by Mistras¹. The PZT are allocated on the sample surface around the damage zone. A thin layer of silicon grease is laid at the interface with the sample to act as a couplant and improve the strain transmission to the PZT and thus the detection of AE. In preliminary tests with the MISTRAS system, the PZT are attached with duct tape (figure 5.6). For this experiment, two polystyrene baseplates kept the PZT sensors in position with rubber bands.

¹<https://mistrasgroup.co.uk/products-and-systems/ae-systems/>



Figure 5.6: Photography illustrating a free capillary uptake in a sample prepared with Sodium Sulphate monitored with six PZTs attached with duct tape and communicating with Mistras acoustic system.

5.3.2.2.2 Calibration, data visualisation and post-processing

AEwin™ is the program for real-time “simultaneous” AE feature and waveform processing, display, fast storage, and replay. It is used for true, real-time operation and control with the MISTRAS AE Systems. The good communication between the sensors is checked with Auto Sensor Test (AST) which pulse alternatively all sensors, record, and analyze the response on the others. Bad communication can be improved by adding couplant between the sensors and the PZT surface or by changing the disposition of the sensor. Before launching an experiment, the system is validated following the European standard ²: the tip of a graphite pencil is broken at various locations on the sample surface to induce an AE localized by the system. A good coupling is accepted when the AE is localized with an accuracy of 4 mm by adjusting the material velocity in AEwin. It is worth noting that the evolution of the sample properties would require a perfect velocity model to locate precisely the AE. Meanwhile, the timing of the AE is well defined at the time-scale used and indicates when the sample is damaged. During the experiment, we store 'Hit' and 'Event' and visualize them in the AEwin interface. Also, Mistras calculate the absolute energy on every channel at 1 Hz. After the experiment, the data are exported in a text file, read and plotted in MATLAB (2010).

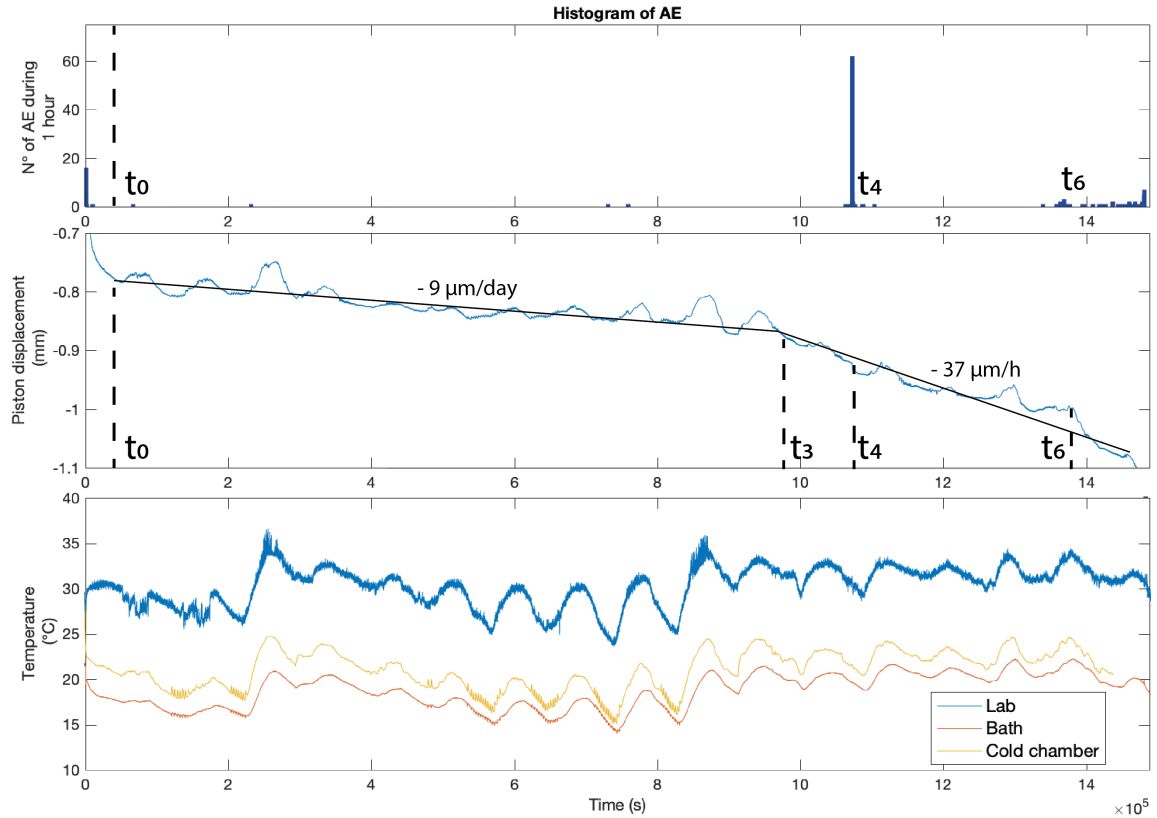


Figure 5.7: Top plot: Acoustic emission distribution. Medium plot: piston displacement in mm and the linear regression lines. Bottom plot: Measured laboratory, pure water bath and cold chamber temperature curves.

5.3.3 Results

5.3.3.1 Loading to 10 MPa axial pressure

Consequently to the sample loading, the piston measured a negative displacement equal to 0.8 mm (figure 5.7), medium plot. 46 acoustic emissions are recorded during the axial loading in figure 5.7, top plot. They relate to perpendicular or sub-perpendicular cracks closure like the cracks induced during the sample preparation.

5.3.3.2 Damage induced during the free imbibition

The piston displacement is a decreasing sinusoid (figure 5.7) medium plot. The peaks of the piston displacement sinusoid correspond to the temperature sinusoid peaks (figure 5.7 medium and bottom plot). However, a global trend emerges from the sinusoid fluctuation and is approximated by two linear regression lines describing the evolution of the sample stiffness during the experiment. Between t_0 and t_3 , the slope is equal to $-9 \mu\text{m}\cdot\text{day}^{-1}$. Only nine events are located (figures 5.7, top plot and 5.8, second plot). After t_3 and before the sample failure, the slope is $-37 \mu\text{m}\cdot\text{day}^{-1}$: the sample retracts four times faster than before. A close look at the piston displacement during the second phase reveals that the piston dropped suddenly of $13 \mu\text{m}$ at t_4 . About sixty acoustic emissions are located in the salty region during the first failure (figure 5.8, fourth plot). Between t_4 and t_6 more acoustic emissions happen in the

²NF EN 1330

sample. They are located above the shot at t_4 . The piston finally smashes the sample and the white plastic dish after 17-day and 2 hours, t_7 . In total 292 acoustic emissions are located and 245 represented after removal of the events positioned remotely.

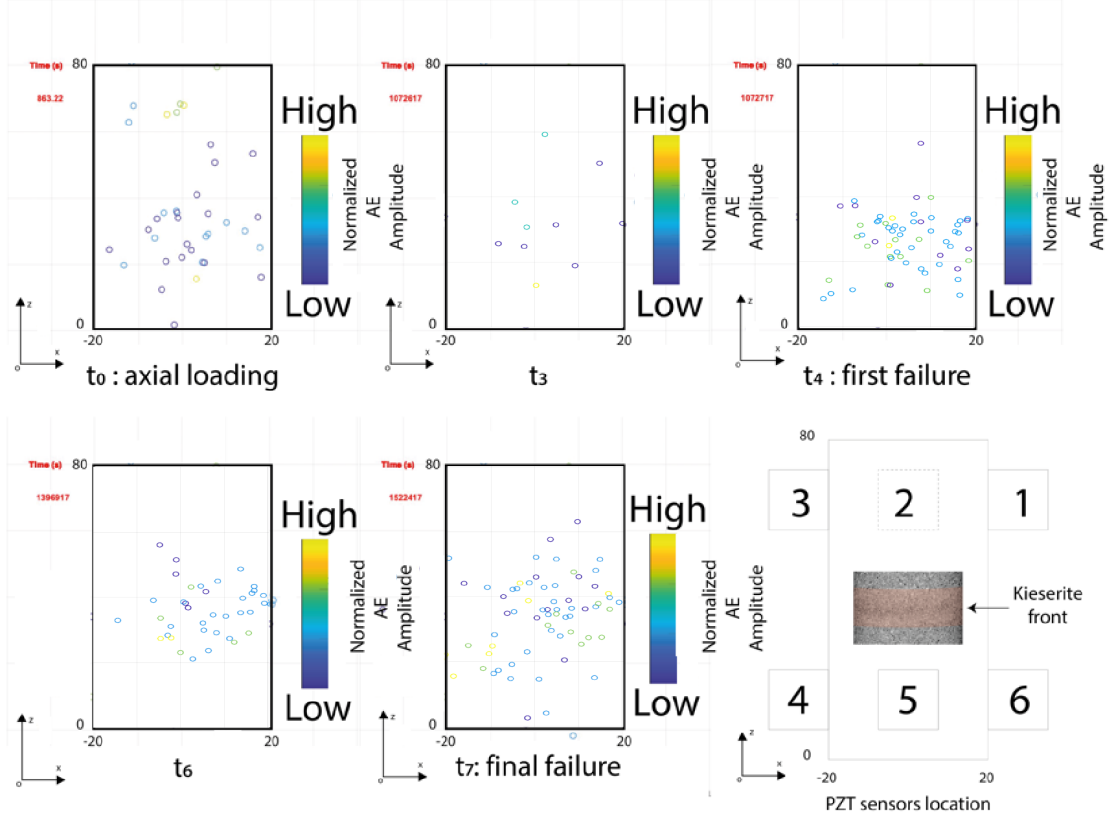


Figure 5.8: first plots: AE hypocenters distribution projected on the (x,z) plane during the different phases of the capillary uptake in sample IX uniaxially loaded at 10 MPa. The last plot is the geometry of the acoustic monitoring set up drawn with a vertical slice reconstructed from the 3D X-ray microtomography datasets of the initial sample.

5.3.3.2.1 Continuous monitoring of absolute energy

The continuous monitoring of absolute energy is an analysis of the background noise on each channel. The absolute energies inflections match with the piston displacement changes, thus it looks like their evolutions are meaning full for the experiment monitoring. In the following, the inflection in the normalized absolute energy curves is described. The point of inflexion time are designated as t_0, t_1, \dots, t_7 . Before t_0 while the sample accommodates the axial loading and Milli-Q water is poured in the white plastic dish, the absolute energies on channels 2 and 3 (above the kieserite hydration front) increase. On channel 4 and 5 (below the kieserite hydration front), the absolute energies stay constant.

We summarize on each channel the absolute energy evolution during the pure water capillary uptake in sample IX:

- channel 2 (65 mm): From t_0 to t_1 the profile increases. Between t_1 and t_3 , the absolute energy reached a plateau. At t_3 , the absolute energy drops exponentially. At t_4 , a sudden drop is recorded and the profile slowly decreases,

- channel 3 (65 mm): Same trend than Channel 2 between t_0 and t_4 . After t_4 , the profile increases again and decreases after t_6 ,
- channel 4 (15 mm): The profile is constant between t_0 and t_1 . Channel four grows slowly between t_1 and t_4 , reach a plateau between t_4 and t_5 and drop slowly after t_5 ,
- channel 5 (15 mm): Constant profile between t_0 and t_1 . Rapid rise between t_1 and t_2 . Plateau between t_2 and t_3 . It falls with a stair shape at t_3 , t_4 and t_5 . Rapid growth at t_6 then slowly reducing to the end.

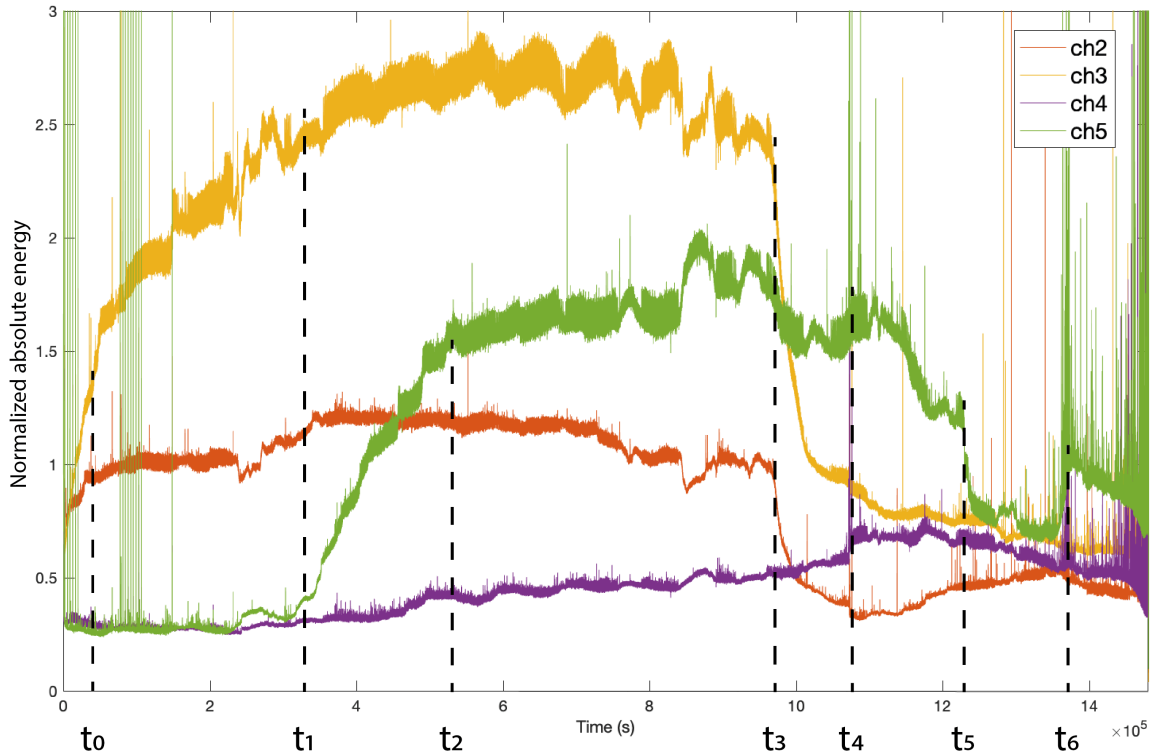


Figure 5.9: Absolute energy continuous monitoring of rewetting sample IX at a 10 MPa uniaxial confining pressure: channel 2, 3 at 65 mm height and 4,5 at 15 mm height. Time: t_1) 3 day 2h, t_2) 6 day 3h, t_3) 11 day 5h, t_4) 12 day 1h, t_5) 14 day 5h, t_6) 15 day 2h.

5.3.3.2.2 Hit distribution and amplitude

Hits provide an enhanced picture of the acoustic emissions that are not detected or located. The hits are represented on a graphic (Time (s) versus amplitude (dB)) by an asterisk sign. The different colors depend on the channel (figure 5.10). Channel 1 and 6 are not represented because too noisy. Globally, the distribution of the hits follows the trend displayed by the distribution of the event. In addition, hits are detected between t_1 and t_3 . After t_3 , hits increase in density and amplitude before the first failure at t_4 . An important cluster is detected and is in majority constituted by hit detected by channel 5. After the failure, the hit amplitudes decrease but the hit density is higher than before. At t_6 , another cluster is detected. Between t_6 and the final failure, the hit density and amplitude increase again. In total, 636 hits are detected by channel 2, 1330 hits by channel 3, 1278 hits by channel 4 and 1832 hits by channel 5.

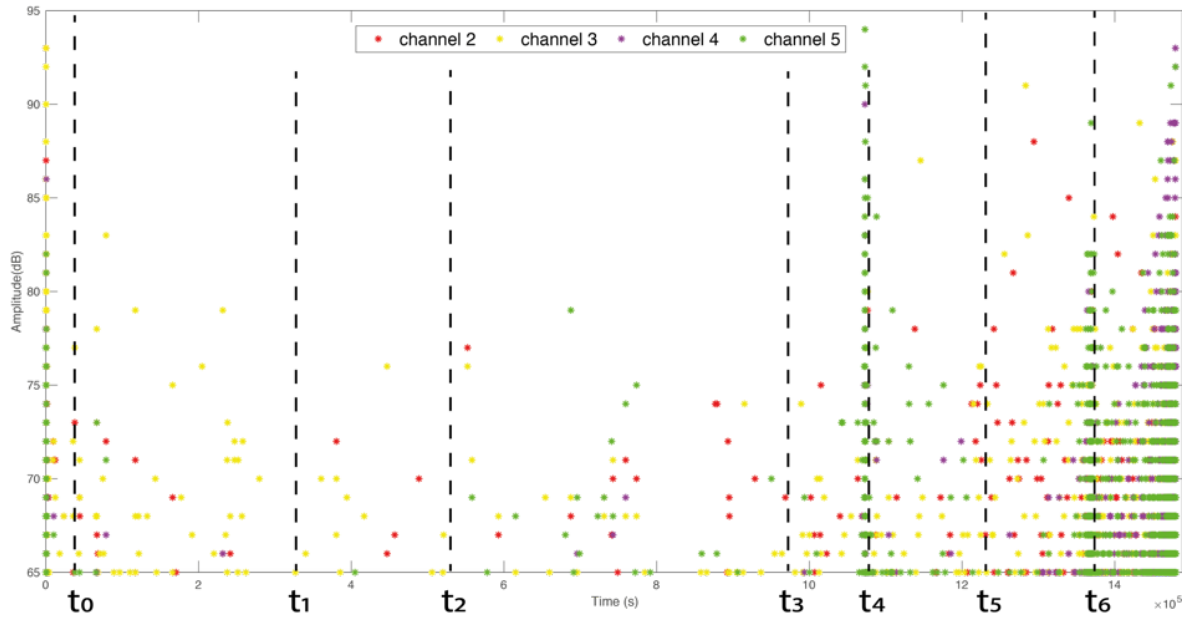


Figure 5.10: Hits amplitude represented in function of experimental time (s) for channel 2,3,4,5.

5.3.4 Discussion

5.3.4.1 Damages induced after kieserite hydration

During the water capillary uptake, 205 acoustics emissions locate in the part of the Adamswiller sandstone cylinder initially impregnated with kieserite (figures 5.8 and 5.7). Their positions in the middle of the sample show that these AE are related to the rewetting of kieserite precipitated since the kieserite rich volume start in the middle of the sample and by definition, they show that epsomite crystallisation cracks the sample. The upward progression of the hypocenters (t_4 to t_7 attests a progression of the hydration front during the test. The hydration of the kieserite consists of the dissolution of kieserite followed by the precipitation of epsomite. In the next section, we will detail the evolution of the monitored values during both steps.

5.3.4.2 Kieserite dissolution

The sample linear contraction at a rate of $9 \mu m.day^{-1}$ between t_0 and t_3 is close to $11.52 \mu m.day^{-1}$, the measured linear axial contraction in the confined rewetting test described in section 5.4. This contraction is attributed to kieserite dissolution, in the discussion 5.4.4.4. Only very few acoustic emissions and hits are recorded during the kieserite dissolution episode, consequently the damages induced on the skeleton are negligible. It is worth noting that the absolute energy measured by the upper PZTs increases during the kieserite dissolution.

5.3.4.3 Epsomite crystallisation

At the temperature of the pure imbibing water and the insulated chamber, the aqueous solution is highly supersaturated with respect to epsomite consequently to the dissolution of kieserite. Previous experimental observations prove that an epsomite paraboloid dome precipitate and damaged the porous medium by epsomite crystallisation within ten days. At t_4 , t_6 and at the sample failure, three blooms of acoustic

emissions are recorded (figure 5.8) and visually, the positions of the hypocenters of the acoustic emissions in the bloom at t_4 are below the bloom at $t_6 \sim 3.5$ days later. These steps correspond to the conceptual model of salt remobilisation and precipitation upward in figure 5.5. Nevertheless, the sample sags instead of swelling. At t_3 , ~ 5 hour before the AE bloom (t_4), the contraction of the sample cylinder accelerates at $-37 \mu\text{m}/\text{day}$, the absolute energies drop on the upper channels and the hit activity increases. Then, this combination of hits, absolute energy and sparse AE activities ceases at t_3 and it coincides with the acceleration of the sample contraction without bloom of AE. To us, it means that epsomite crystallisation starts to sap the skeleton at t_3 . At t_4 this sample skeleton undermining leads to an important failure at t_4 related to the continuation of epsomite crystallisation and maybe the fast propagation of larger cracks. If the hypothesis is confirmed, the skeleton undermining is quasi-aseismic. It is likely since aseismic rupture is assessed in marble (Fortin, 2007) or plaster (personal communication from Dr. Olivier Nouailletas). Aseismic rupture is attributed to intragranular plastic deformation.

5.3.5 Conclusion

The 10 MPa uniaxial loading and rewetting of an impregnated Adamswiller sandstone cylinder leads up to epsomite crystallisation induced damage of the sample. It is finally the first step to try again the same experiment in a triaxial cell during an extended time. Open questions remain, like the origin of the background noise and the reason behind the contrasted absolute energies evolution recorded on each channel. It alights the possible aseismicity of the first step of crystallisation induced damage that consists in skeleton weakening and preparation of major seismic failure. In the next section, two Adamswiller sample impregnated with kieserite are rewetted in the 'Geodesign' triaxial cell. An acoustic monitoring system logs the AE, the P-wave propagated through the sample and the deformation of the sample surface.

5.4 Mechanical stiffening driven by crystallisation of epsomite in confined reservoir conditions

5.4.1 Introduction

In this section, we will describe the pure capillary uptake in two Adamswiller sandstone impregnated with magnesium sulphate first without confining pressure and secondly with the sample confined at 27 MPa isotropic pressure. The tests are monitored with acoustic emissions to measure P-wave velocities and amplitudes and strain gauges to measure the sample deformation on the surface. 3D X-ray microtomography scans are acquired on the samples before and after the capillary uptake to describe the distribution of magnesium sulphate in the porous sample and the damage.

5.4.2 Methods

5.4.2.1 Experimental protocol

The different testing conditions applied on the Adamswiller sandstone are listed below: The ‘geodesign’ triaxial cell is equipped with strain gauges and the Richter Mini System (read section 2.2 chapter 2.2’) to relocate the AE and measure the properties of elastic waves across the porous medium.

Sample XII is an Adamswiller sandstone cylinder ($86.3 \times 39.8 \text{ mm}^2$) containing 7.58 g of a kieserite and $MgSO_4 \cdot 1.25H_2O$ mix precipitated according to the magnesium sulphate impregnation protocol. Before the experiment, a 3D X-ray microtomography scan at a $27.26 \mu\text{m}$ resolution is taken targeting the salt-rich region of the sample which starts at 45 mm. The resliced vertical cross-sections relate to no damages. The sample is prepared with eight P-PZTs. Their elevations are given in table 5.11. Three strain gauges (radial strain gauges at 15 mm, axial and radial strain gauges at 45 mm) equipped the sample. Finally, sample XII bottom is immersed in 45 ml pure water (Milli-Q from Millipore, $18 \text{ M } \Omega\text{cm}$ at $20 \text{ }^\circ\text{C}$). The sample is oriented so that the salt-free part is at the bottom. After 21 hours, the sample is removed from the bath and rolled up in parafilm foil. Sample XII is conserved at $20 \text{ }^\circ\text{C}$ for 3 months. After this time, a 3D X-ray microtomography is taken of the sample.

Sample XI is an Adamswiller sandstone cylinder ($85.2 \times 39.8 \text{ mm}^2$) impregnated with 7.1 grams of a mix kieserite and $MgSO_4 \cdot 1.25H_2O$. A 3D X-ray tomography dataset is taken of the sample targeting the salt-rich region which starts at about 50 mm. In the laboratory of geologie of Ecole Normale Supérieure of Paris, 6 P-PZTs (1,2,3,5,6,7) that are positioned on the sample surface. Four strain gauges (two axial and two radial) are positioned at 20 mm and 57 mm on the sample. The sample is placed in the ‘geodesign’ cell between a stainless steel inlet and an outlet. The sample is oriented so that the salt-free side is at the bottom. 27 MPa isotropic confinement is applied and maintained during the experiment around the sample. To realize the imbibition, a tube connects the inlet with the Quizix QX Precision Pump and the pressure regulation is fixed at 0.13 MPa so that the porous rock capillary suction only controls the rate of imbibition. In total, 15.670 ml of pure water is pumped and 12 ml fill the sample porosity. During the test, the axial and radial strain gauges at 20 mm ceased functioning after 5000 min. At 57 mm, a contact failure between the axial and radial gauges connections results in the recording of the axial strain solely.

5.4.2.1.1 Duration

The first experiments, in sections 5.2 and 5.3 involving an Adamswiller sandstone impregnated with magnesium sulphate proved that a long time (<10-15 days) is necessary to damage the sample. However, because of our limited-time access to the confining apparatus and monitoring system, the experiments were shortened. In absence of confinement, the capillary uptake in sample XII lasts about 21 hours while it lasts 6 days and 14 hours in sample XI confined at 27 MPa.

5.4.3 Results

5.4.3.1 Rewetting of kieserite impregnated in sample XII without confining pressure

5.4.3.1.1 Description of P-wave velocities measured in dry sample XII

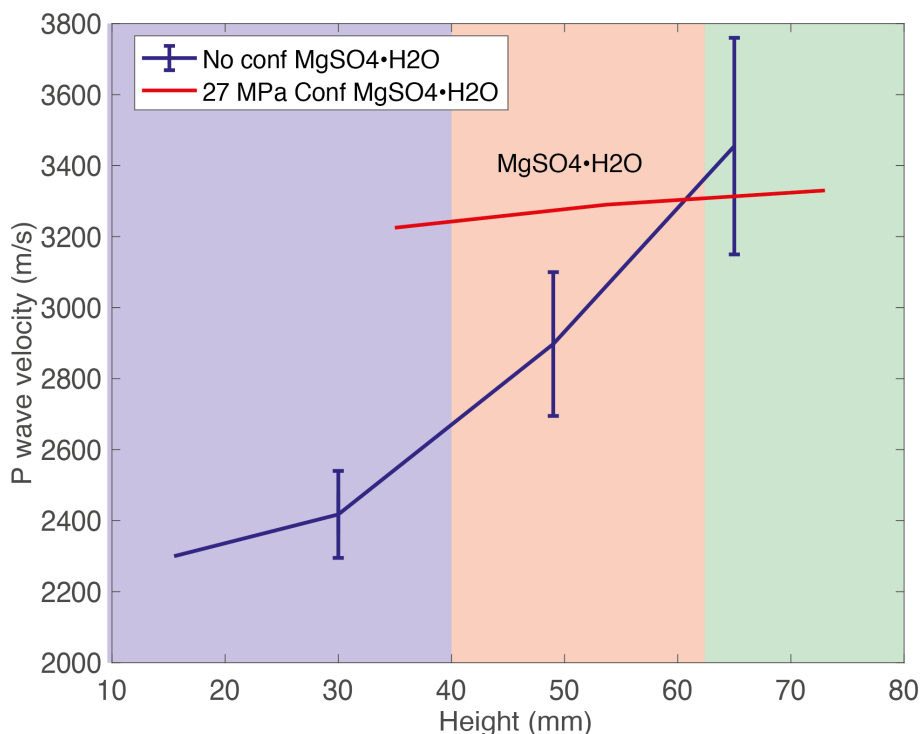


Figure 5.11: P-wave velocities measured across dry sample impregnated with ~ 7 gram of kieserite at 0 (blue curve) and 27 MPa (red curve) isotropic confining pressure (raw data in appendix A.3).

The reference radial P-wave velocity measured on a dry Adamswiller sandstone is 2300 m.s^{-1} . We report in figure 5.11 the initial P-wave velocities in the sample to assess the effect of kieserite impregnation in the sample. Below the kieserite rich mid-part of the sample, the P-wave velocity measured corresponds to the value of an intact Adamswiller sandstone. Across the mid-part impregnated with kieserite, the P-wave velocity exceeds of 500 to 1000 m.s^{-1} the velocity in the intact sandstone. Confined at 27 MPa, the P-wave velocity across the bottom part increase ($+ \sim 900 \text{ m.s}^{-1}$) due to the crack closure Fortin et al. (2006). Across the kieserite rich region, the P-wave velocity increase (0 to $\sim 400 \text{ m.s}^{-1}$). This difference is linked to the precipitation of kieserite that probably fills the cracks and thus hinder their closure.

5.4.3.1.2 Normalized P-wave velocities and amplitudes profiles during the water capillary uptake in sample XII

The P-wave velocity measured by the pair of PZT at 15.5 mm increases and reaches, a few minutes after the beginning of the rewetting, a plateau value. At the height of 31.5 mm, the P-wave velocity drops first then slowly augments during the experiment. The normalized P-wave velocity evolution measured at the height of 50 mm decreases first, then grows to 1.1. Above, at 66 mm, the normalized velocity is unchanged. The normalized P-waves amplitudes measured at 15.5 mm and 31.5 mm drop successively to a value close to 0.05 shortly after the beginning of the capillary uptake. At 50 mm, the normalized amplitude slowly decreases during 100 min then drops suddenly to 0.05 conversely with the P-wave velocity augmentation at the same height. At 66 mm, the P-wave velocity amplitude is unchanged.

Like in David et al. (2017b), the imbibition front progression rate is calculated based on the P-wave velocities evolution's between 31.5 mm and 50 mm: $0.24 \text{ mm} \cdot \text{min}^{-1}$. The wetting front rate is 2.6 times slower than the reference value at a similar height.

5.4.3.1.3 Strain gauges evolution

The axial strain gauge at 15 mm measures a contraction equal to $-5000 \mu\text{m} \cdot \text{m}^{-1}$ as the pure water imbibing front invades the pores, then it grows and tends to a limit at $1000 \mu\text{m} \cdot \text{m}^{-1}$. At 45 mm, the radial strain gauge contracts to $-2500 \mu\text{m} \cdot \text{m}^{-1}$ then augments to $-1000 \mu\text{m} \cdot \text{m}^{-1}$. On the contrary, the axial strain gauge at 45 mm reports an extension ($0.2 \mu\text{m} \cdot \text{m}^{-1} \cdot \text{s}^{-1}$) beginning at 200 min. It keeps extending more slowly ($0.5 \mu\text{m} \cdot \text{m}^{-1} \cdot \text{min}^{-1}$) until the end of the experiment.

5.4.3.1.4 3D X-ray microtomography scan description

After 3 months at 20°C , a vertical cross-section resliced from a 3D X-ray microtomography datasets reveals a crack with a half-dome shape that crosscuts the reacted sample XII and is overlapped by a 3-4 mm thick, greyish halo (figure 5.13). The crack is thicker at the top and divides into thinner slits in the bottom left of the cross-section. Below the cracks, the pore network is preserved. The porosity in the greyish halo capping the salt dome is not distinguishable which means that the pores are filled with magnesium sulphate.

5.4.3.2 Rewetting of kieserite impregnated in sample XI at 27 MPa confining pressure

5.4.3.2.1 Normalized P-wave velocities and amplitude profile during the water capillary uptake in sample XI

The P-wave velocities have a contrasted progression measured at different height through sample XI during the rewetting. At 35 mm, the velocity drops suddenly then augments slowly after 1000 min to $3269 \text{ m} \cdot \text{s}^{-1}$ at the end of the test. At 53.7 mm, the velocity rises continuously to reach $3584 \text{ m} \cdot \text{s}^{-1}$ at the end of the experiment, $\sim 300 \text{ m} \cdot \text{s}^{-1}$. At 73 mm, the P-wave signal is sometimes noisy thus difficult to be interpreted in terms of velocity and amplitude. However, we manage to pick a constant velocity close to $3333 \text{ m} \cdot \text{s}^{-1}$ (figure 5.14 and table 5.15).

The P-waves amplitudes are analysed only at 35 and 53.7 mm, because the P-wave is noisy at 65 mm. In both cases, the amplitudes drop a few minutes after the beginning of

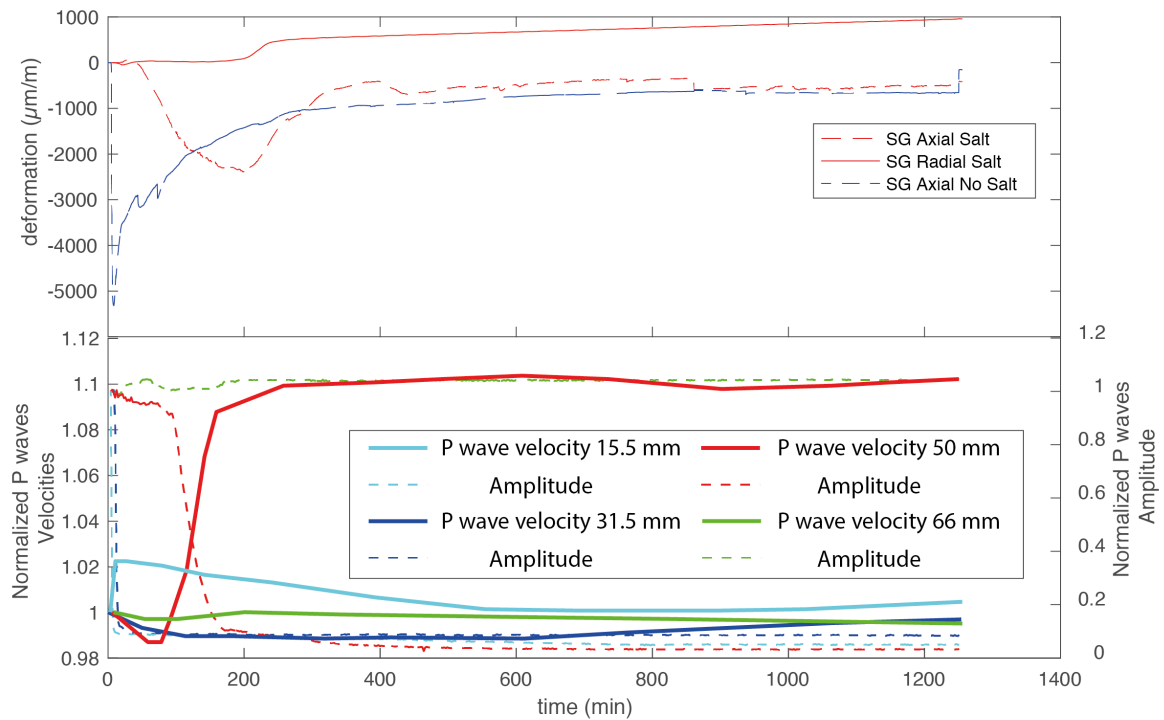


Figure 5.12: Top: Evolution of one axial (45 mm) and two radial strain gauges (15 mm and 45 mm) measuring the sample surface deformation in the salt deprived volume and near the salt rich region of sample XII. Bottom: normalized P-wave velocities and amplitudes profiles through sample XII at the heights of 15.5 mm, 31.5 mm, 50 mm and 66 mm during the pure water capillary uptake (appendix A.3).

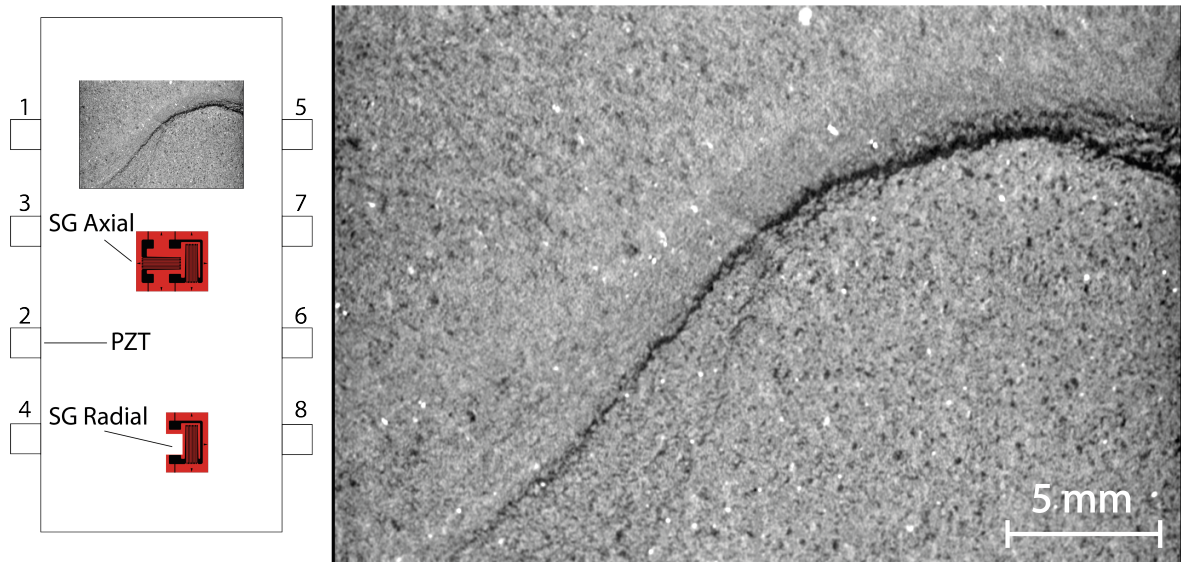


Figure 5.13: X-ray tomography vertical cross section processed with ImageJ (Schindelin et al., 2012), targeting the salt dome in sample XII after the pure water capillary uptake during 21 hours and three months at 20°C. 1,5,3,7 gives the height of the PZTs.

sample XI imbibition. Like in David et al. (2017b), the water imbibing front progression rates are calculated and match with the reference values given in chapter 4:

- between 0 mm and 35 mm: 0.9 mm.min^{-1} ,

- between 35 mm and 53.7 mm: 0.6 mm.min^{-1} .

5.4.3.2.2 Strain gauges

The radial strain gauge and the axial strain gauge at 20 mm contracts to respectively $-135 \mu\text{m.m}^{-1}$ and $517 \mu\text{m.m}^{-1}$ when the porosity is water-filled. After, the axial gauge grows and tends to a limit at $106 \mu\text{m.m}^{-1}$. At 57 mm, the axial strain gauge extends to $123 \mu\text{m.m}^{-1}$ then contracts to $127 \mu\text{m.m}^{-1}$ and keeps retracting during the rest of the test at a mean rate of $-0.1 \mu\text{m.m}^{-1}.\text{min}^{-1}$

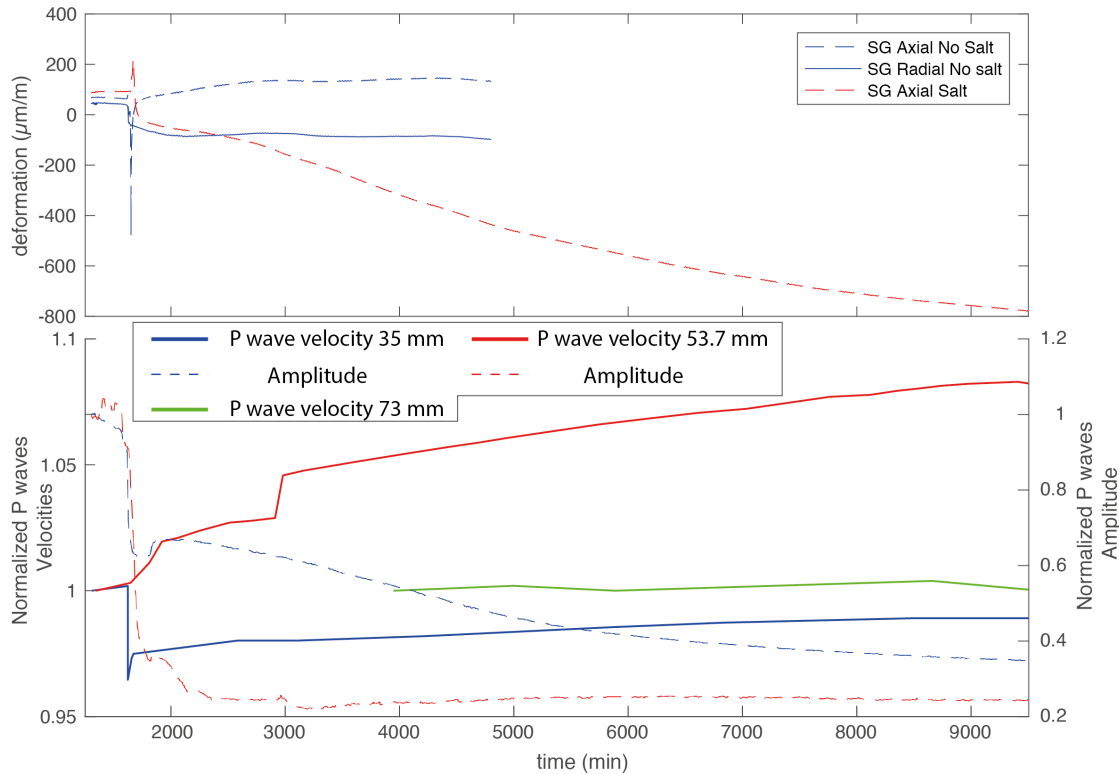


Figure 5.14: Top: Evolution of two axial (20 mm and 57 mm) and one radial strain gauges (20 mm) measuring the sample surface deformation in the salt deprived volume and near the salt rich region. Bottom: Evolution of the normalized P-wave velocities and amplitude through sample XI at 35 mm, 53.7 mm and 73 mm (appendix A.3).

5.4.3.2.3 3D X-ray microtomography scan description

A 3-4 mm thick greyish parabolic zone stands out from the rest of the porous medium depicted in the vertical slice resliced from the X-ray microtomography scan acquired on dried sample XI. No damages are distinguishable (figure 5.15).

5.4.4 Discussion

5.4.4.1 Pressure dependence of Magnesium Sulphate hydrated phases

Similarly to the graphic in Steiger and Asmussen (2008) that provides the sodium sulphate phases solubility dependence with respect to solution pressure, the solubility dependence of magnesium sulphate hydrated phases regarding the hydrostatic pressure is modeled with Phreeqc using the Pitzer database (Parkhurst and Appelo, 2013). The

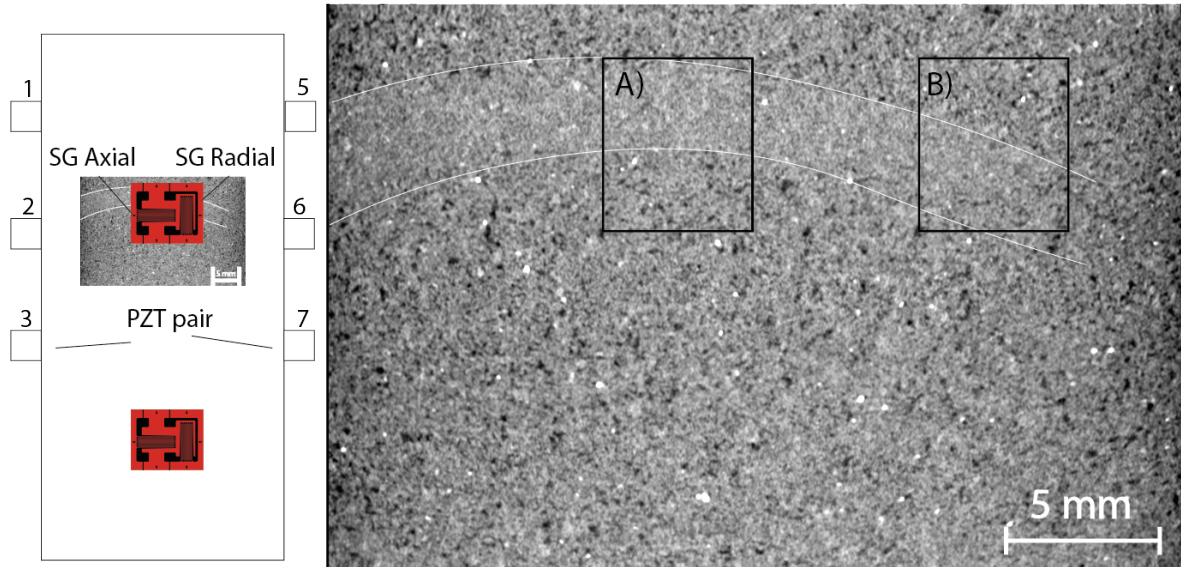


Figure 5.15: X-ray tomography vertical cross section processed with ImageJ (Schindelin et al., 2012), targeting the salt dome after rewetting of sample XI loaded at 27 MPa. 1,2,3,5,6,7 give the height of the PZT pair.

results are plotted in figure 5.16: the maximum pressure potentially exerted by epsomite at 20°C is estimated at 33 MPa, which should be sufficient for epsomite crystallisation to induce damages in an Adamswiller sandstone confined at 27 MPa.

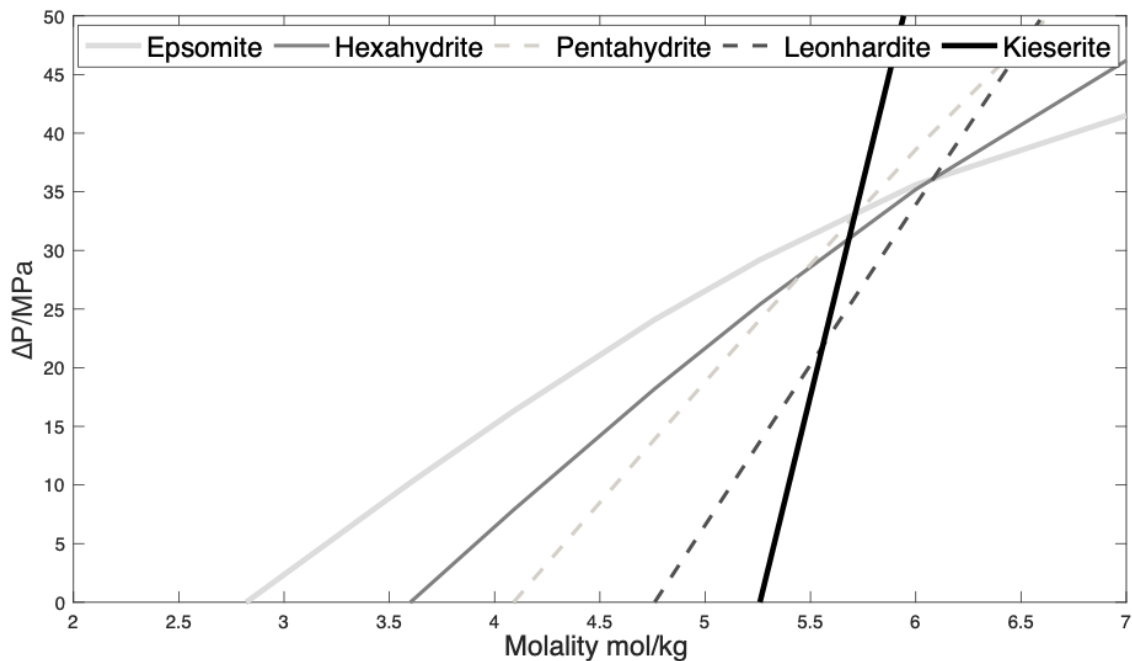


Figure 5.16: Crystallisation pressure at 293.15 K of: Epsomite ($MgSO_4 \cdot 7H_2O$), Hexahydrate ($MgSO_4 \cdot 6H_2O$), Pentahydrate ($MgSO_4 \cdot 5H_2O$), Leonhardite ($MgSO_4 \cdot 4H_2O$) and Kieserite ($MgSO_4 \cdot H_2O$) (Database Pitzer, Phreeqc). The maximum crystallisation pressure for epsomite is 33 MPa where epsomite and kieserite exhibit the same solubility.

5.4.4.2 Porous medium stiffening induced by magnesium sulphate crystallisation

The P-wave velocities measured through dry not confined and not reacted sample XI and XII proves that kieserite impregnation greatly increases the stiffness of the Adamswiller sandstone. After confining the sample XI at 27 MPa, the P-wave velocity in the pores impregnated with kieserite increases by only 5-10 % while at the bottom is the salt deprived volume, the increase is equal to 20%. As the P-wave velocities increase during loading is mainly attributed to cracks and pores closure (Fortin et al., 2006), then it means that fewer cracks and pores closure happens in the kieserite rich volume than in the kieserite deprived volume. Kieserite impregnation stiffens the dry porous medium rich in precipitated salt.

At 31.5 mm and 35 mm in both experiments, the medium softens as the imbibing waterfront fills the pores according to the P-wave velocity evolution. The interpretation of the velocity drop according to Mayr and Burkhardt (2006), Müller, Gurevich, and Lebedev (2010), and Pimienta et al. (2019) is a partial pore saturation and a softening attributed to wave-induced flow. As the water imbibing front invades the porosity at the bottom of the kieserite rich region, the pair of PZT at 50 mm on sample XII and at 53.7 mm on sample XI detect a stiffening of the kieserite rich porous medium. A potential Gassmann stiffening effect does not explain solely the P-wave velocities augmentations: for example sample XII gains $\sim 250 \text{ m.s}^{-1}$ whereas the Gassmann stiffening effect should account to $\sim 100 \text{ m.s}^{-1}$ maximum in a kieserite deprived Adamswiller sandstone, in absence of confining pressure. Then, kieserite dissolution replaced by epsomite crystallisation is involved in the stiffening effect alongside the Gassmann stiffening effect.

The sample confined at 27 MPa keeps stiffening during the next six days upon the continuation of kieserite dissolution and reprecipitation in epsomite. No AE is emitted though. In absence of confining pressure, the P-wave velocity measured on the P-wave transmitted across the zone hydrating at 50 mm is nearly constant furthermore no AE is recorded, but the test is not monitored long enough.

5.4.4.3 Magnesium sulphate remobilisation

In section 5.2, pieces of evidence of salt remobilisation are emphasized. In these experiments, well-defined parabolic domes are displayed in resliced vertical cross-section after the capillary uptake (figures 5.13 and 5.15), whereas the kieserite is more widespread and the domes are not visualized in figure 6.3 the original sample vertical cross-sections. This confirms that the ascending imbibing water front dissolves kieserite, transports the dissolved kieserite and precipitates epsomite upward.

5.4.4.4 Effect of confining pressure on sample deformation

Without confining pressure, the profile of the axial strain gauge stuck on the sample below the kieserite rich volume depicts the sample deformation when water saturates the pores. The salt strain gauges profiles display an attenuated pore saturation evolution and radial swelling that is probably linked to kieserite's hydration. On the sample confined at 27 MPa, the axial strain gauge pasted on the salt-free sample surface records the partial pore saturation but by contrast, the axial strain gauge pastes on the salt-rich zone record a continuous axial contraction. This could seem contradictory with the P-wave velocity profile measured at the height of PZTs 2 and 6 that is interpreted

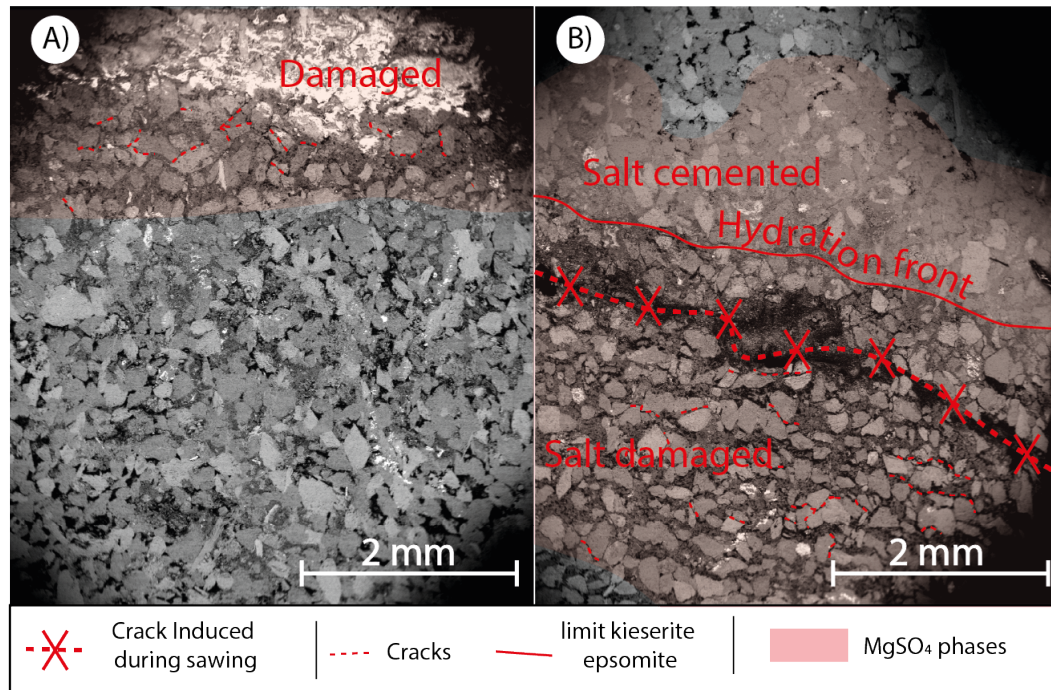


Figure 5.17: BSE images of sample III polished sections centered on the $MgSO_4$ dome: A) Atop a damaged zone where the grains are disjunct and surrounded by a mixture of skeleton fragments and magnesium sulphate crystals bathing in epoxy resin. Below, the damaged zone, the porosity is preserved. The whitish grains atop are BSE acquisition artifacts. B) Above the magnesium sulphate rich region, the sample porosity is preserved. In the middle of the image, there is a region where the pores are cemented and below, separated by a fracture that happens during sawing, the porosity is fragmented: the grains are disjunct and divided by a greyish paste.

as porous medium stiffening. But, if one considers that the first step of the equation is the dissolution of kieserite that stiffens the porous medium and previously prevents it to shrink during the loading to 27 MPa. During the imbibition, the dissolution of kieserite may account for the contraction measured by the axial strain gauge. After, epsomite will precipitate and increase the P-wave velocity across the rewetted sample. The modeling in chapter ?? of the first experiment in chapter 4 describes well the competing mechanism between the dissolution of the anhydrous salt and the precipitation of the hydrated salt.

5.4.4.5 Damages induced by epsomite crystallisation

Neither acoustic emissions are recorded during the monitoring of the two experiments. On the contrary, the samples stiffen between the PZT pair positioned nearby the hydration front in both experiments meaning that epsomite is precipitating. As discussed in the previously described test 5.3, there is a 10 days latency between the saturation of the kieserite rich region and the visualisation of the damage induced by epsomite crystallisation. A hindered nucleation of epsomite crystals was evoked to explain this delay but in fact, the stiffening of the porous medium emphasizes that epsomite probably starts to crystallise shortly after the saturation of the pores. We propose that it is a reduced epsomite crystal growth rate combined with enhanced ions exchanges in the connected pore network that are the major end members to explain the delay in the onset of epsomite crystallisation induced damage. About the lack of

AE, the polish section obtained from the sample reacted at a 27 MPa, shows that the magnesium sulphate rich zone is partly damaged, partly tightly cemented (figure 5.17). We deduce from the P-wave velocities analysis, that epsomite precipitates during the experiment but we are not sure whether the damage is induced during the capillary uptake experiment or after the test during drying in the oven. If it is the first option, it means that the cracks disjointing the grains are not recorded by the acoustic monitoring system. The second case means that during drying at 80°C in absence of confining pressure, a magnesium sulphate phase, with a higher density than epsomite that is stable at a lower temperature, precipitates from the solution remaining in the pores and disjoints the grains. Both hypotheses are likely to occur.

5.4.5 Conclusion

We listen to no damage induced by epsomite crystallisation in the Adamswiller sandstone during the experimental time. Kieserite dissolution supersaturates the aqueous solution with respect to epsomite and the crystallisation of the heptahydrated magnesium sulphate phase is monitored. Damages are recognized afterward on sample XII, conserved at a similar temperature during 3 months. These experiments confirm the delayed damages relatively to the rewetted thernadite impregnated sample described by Balboni et al. (2011) and Ruiz-Agudo et al. (2007). It is probably linked to the hindered epsomite nucleation, the lower crystallisation growth rate of epsomite and more ions transports in the connected porosity. At 27 MPa, it is difficult to attribute without doubt the intergranular cracks in the hydrated epsomite dome to crystallisation pressure since no acoustic activity is recorded. Meanwhile this result is promising and require additional test in geological reservoir settings. Beside, the long duration to establish favorable conditions of epsomite crystallisation pressure lets study step by step the hydration reaction in the porous rock.

5.5 General conclusion

The rewetting of Adamswiller sandstone impregnated with a fraction of kieserite-induced damages by epsomite precipitation first in absence of confinement and at a 10 MPa confining pressure on the sample. In absence of acoustic emissions recorded during the rewetting of the sample impregnated with kieserite at confinement equivalent to geological reservoir conditions (27 MPa), we are not certain if epsomite crystallisation induced damage despite the intergranular cracks visible on the polish section: these cracks could be formed during the deconfinement of the sample. Meanwhile, because we see a cracked zone in the polish section of the reacted sample and we record a continuous acoustic activity during the uniaxial confined test at 10 MPa, we suppose an aseismic weakening of the skeleton of the sample that precedes crack propagation both induced by epsomite crystallisation.

Chapter 6

Effective modeling of crystallisation in a porous sandstone

Contents

6.1	Introduction	148
6.2	Material	148
6.2.1	Idealized Adamswiller sandstone	148
6.2.2	Inclusions properties	148
6.3	Modeling of water capillary uptake in the thenardite rich Adamswiller sandstone	149
6.3.1	Description of the impregnated sample I	149
6.3.2	Effective P-wave's velocity of an idealized Adamswiller sandstone modeled in the dry and wet case	150
6.3.3	Effective velocity of an idealized Adamswiller modelled in the case of impregnation with a thenardite fraction	151
6.3.4	Effective velocity modeling of an idealized Adamswiller sandstone containing a thenardite fraction hydrating in mirabilite	153
6.4	General conclusion	156

Abstract

Experiments of rewetting of thenardite impregnated samples in chapter 4 point that the material is stiffening via thenardite filling of the pore, water saturation of the remaining empty volume and the dissolution of thenardite and the precipitation of mirabilite. The rewetted material softens when the material starts to crack. It is provoked by mirabilite crystallisation, when the crystallisation pressure exerted in a thin liquid film between the pore wall and the mirabilite crystal overpasses the tensile strength of the pore. Easy modeling of the effects describes above is possible with the homogenisation method that let's model the elastic properties of an isotropic homogeneous material composed of a skeleton and inclusions. The modeling based on autoconsistent schema reproduces the experiment without confining pressure described in chapter 4. Like in the experiment, the modeled P-wave velocity increases with the thenardite pore fraction and the transformation of thenardite into mirabilite that happens during the rewetting of an Adamswiller sandstone impregnated with 80% of thenardite. Three types of cracks induced by mirabilite crystallisation are described via X-ray microtomography datasets of the reacted sample and BSE images of a polished section. A P-wave velocity reduction is recognized but not the extent measured during the experiment.

6.1 Introduction

The water capillary uptake described in chapter 4 and 5 provide indications on the poro-mechanical's mechanism during the thenardite and kieserite dome rewetting in an Adamswiller sandstone. In this section, we attempt to model the first rewetting experiment described in chapter 4. We will expose the stiffening mechanism of thenardite impregnation in the porous rock, then the competing mechanisms during the hydration of the thenardite dome precipitated in the Adamswiller sandstone. To do so, we used effective medium schema described briefly in the state of the art chapter 1 and more extensively in Fortin et al. (2011), Fortin (2007), Huynh (2007), and Schubnel and Guéguen (2003).

6.2 Material

The sandstone is considered as a homogeneous medium with spherical pores. The sandstone porosity content is a mixture of salts (anhydrous and hydrate phase) and fluid phase (air and water).

6.2.1 Idealized Adamswiller sandstone

We will consider an isotropic homogeneous porous medium based on the mean mechanical properties calculated for the Adamswiller sandstone and with a porosity equal to 20.5%. The bulk and shear moduli of the skeleton are recalled in table 2.6 in chapter 2, section 2.1. The Adamswiller sandstone has a unimodal pore distribution (table 2.16), it is assumed that the pore filling is homogeneous in the salt dome described in the next paragraphs.

6.2.2 Inclusions properties

Like the effective porous medium, the inclusion materials are supposed to be homogeneous isotropic materials (Huynh, 2007). In the case of gaseous or fluid phases like air and water, this assumption is correct and it is assumed that the salt inclusions are also homogeneous isotropic. The properties of the different inclusions phases are gathered in table 6.1. Thenardite and mirabilite elastic moduli are taken from Brand (2009) and Jain et al. (2013). The elastic moduli of the sample are given in the chapter 2 as well as the effective properties of the skeleton calculated thanks to the auto coherent schema.

Table 6.1: Description of the materials composing the inclusions

height	Bulk moduli (GPa)	Shear moduli (GPa)	Density (kg/m ³)
Air	$101 * 10^{-6}$	0	1.204
Water	2.2	0	1000
Thenardite (Jain et al., 2013)	43.4	22.3	2664
Mirabilite (Brand, 2009)	21.5	11	1464

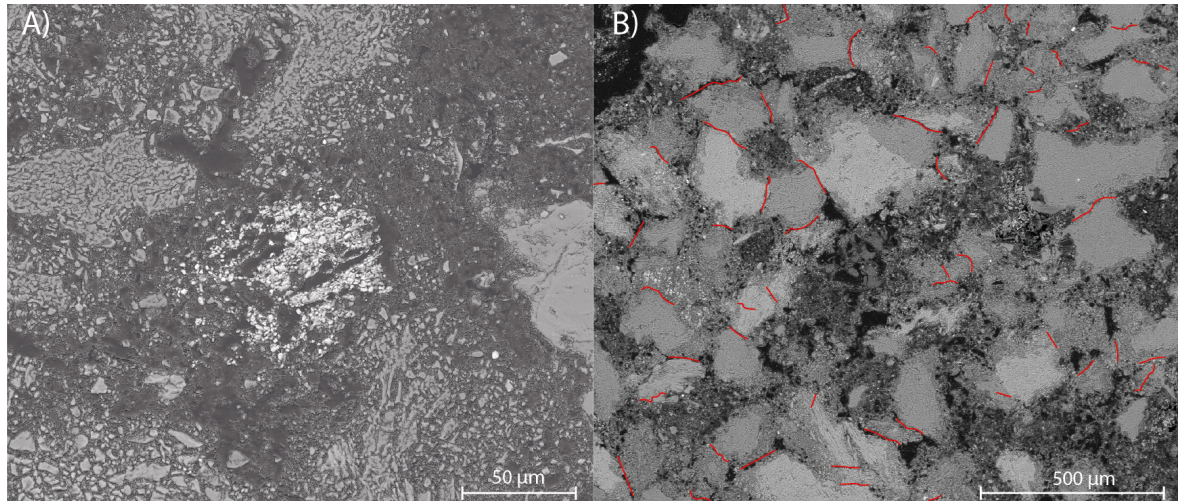


Figure 6.1: SEM BSE images acquired on sample I polish section in the region cracked after thenardite hydration. A) Micro metric crack induced by grain crushing. B) Medium size inter granular cracks.

6.3 Modeling of water capillary uptake in the thenardite rich Adamswiller sandstone

6.3.1 Description of the impregnated sample I

6.3.1.1 Salt content

The initial Adamswiller sandstone is impregnated with a certain amount of thenardite as described in chapter 4. The interpretation of X-ray datasets gives a concentration of salt equal to 80% in the paraboloid thenardite dome. The remaining 40% of thenardite are precipitated below the dome. If it is assumed a homogeneous distribution of salt below the thenardite dome, the thenardite fills 7.8% ($\pm 0.1\%$) of the pore volume.

6.3.1.2 Crack patterns

Three types of crack patterns weaken the sandstone's skeleton embedding the porosity filled with a salt phase. They are recognized on the image displayed in figure 6.1, drawn and analyzed with ImageJ (Schindelin et al., 2012). Their description is given in table 6.2:

- small cracks are induced by grain crushing. They are randomly distributed,
- medium cracks correspond to the intergranular cracks displayed on the BSE acquisition all over the dome. These cracks are randomly distributed. The origin of the small and medium cracks is debated: This cracking sequence is probably initiated during the thenardite dome precipitation as proposed in chapter 4 and initiates the propagation of the tensile swelling cracks above the dome,
- large cracks at the bottom of the dome are undoubtedly linked to the mirabilite crystallisation. The vectors normal to the cracks are parallel to the paraboloid salt dome. To simplify the modeling, we assume they are horizontal.

To estimate the crack dimensions, we used imageJ to trace the width and diameter of the cracks. The measures are summarized to get an average crack dimension. The cracks are then counted manually. To estimate the crack density coefficient, we take for the REA, the recognizable cracked area visible on the image, for the number of cracks N , the crack counts and for c_i , the averaged large crack radius. For the small crack, the bad quality of the polished section coupled with the low resolution of the BSE images prevents giving an accurate description of the crack. Then we assume a crack aspect ratio equal to 10^{-3} . The crack radius is approximated to $1 \mu\text{m}$ and the crack density coefficient is approximated to 0.1. To count the cracks, we segmented the cracks on the image displayed in figure 6.1 A). The segmented image is skeletonized and analyzed with ImageJ (Schindelin et al., 2012). The number of segments with an average branch length in the range of 2μ is used to calculate the crack density coefficient ρ_{small} of the small cracks. The squirt flow cut off frequency is also calculated for each class of cracks described above and reported in table 6.2 For the medium and large crack pattern, the squirt flow cut-off frequency is above 1 MHz and consequently, the cracked hydrated porous rock is in the frame of the relaxed regime. The small cracks are in the frame of the unrelaxed regime which means less dispersion due to the inertial effect of the fluid trapped in the crack.

Table 6.2: Cracks characteristics

	c (μm)	w (μm)	ρ	Cut-off frequency (MHz)
Small cracks	2	0.002	0.1	0.4
Medium cracks	85	2	0.06	88
Large cracks	711	114	0.4	1700

6.3.1.3 Initial P-wave velocity in the dry sample I

The P-wave velocity in the dry sample I are described in chapter 4. Pair of PZT 5-7 reports a velocity deviation with the dry idealized sandstone velocity, which is equal to $\sim 180\text{m.s}^{-1}$. This positive deviation is attributed to the precipitation of thenardite in the porosity crossed by the ultrasonic waves between PZT 5 and 7. Indeed, according to the planar cross-section provided in chapter 4 (figure 4.6), the PZT pair 5-7 is covering a region at 60% deprived in thenardite but cross-cut by tensile swelling cracks and filled at 40% with thenardite (80% pore volume).

6.3.2 Effective P-wave's velocity of an idealized Adamswiller sandstone modeled in the dry and wet case

6.3.2.1 Hypothesis and modeling

The idealized isotropic and homogeneous Adamswiller sandstone contains 20.5% of spherical pores primarily saturated with 100% of air (dry case) and secondarily 100% of water (Wet case). The effective elastic properties and P-wave velocities are calculated with the autocohherent schema and reported in table 6.3.

Table 6.3: Effective elastic moduli and P-wave velocity of the dry or water saturated idealized Adamswiller sandstone calculated with Autocoherent (AC) schemas

height	Eff. Bulk moduli (GPa)	Eff. Shear moduli (GPa)	Density ($kg.m^{-3}$)	Eff. P-wave velocity ($m * s^{-1}$)
AC Dry A.S.	4.87	4.22	1974	2306
AC Wet A.S.	6.14	4.28	2179	2323

6.3.2.2 Results, comparison and discussion

The effective P-wave velocity calculated with the autocohesent schema is equal to experimental P-wave velocity measured in the dry Adamswiller sandstone. By contrast, in the wet case, the effective velocity calculated with the autocohesent schema rises by about $20 m.s^{-1}$ between the dry and wet porous medium state. Similar experimental situations, give a rise of about 30 to $80 m.s^{-1}$, slightly higher than the gain modeled with the autocohesent schema.

6.3.3 Effective velocity of an idealized Adamswiller modelled in the case of impregnation with a thenardite fraction

6.3.3.1 Hypothesis

The idealized Adamswiller sandstone corresponds to the porous medium described in section 6.2.1. The spherical inclusions are filled with an effective mixture composed of a thenardite crystals fraction and fluid or gaseous phase (air in the dry case or water in the wet case).

6.3.3.2 Modeling

The modeling of a thenardite fraction precipitated in the Adamswiller sandstone porosity consist in:

1. Calculation of the pore mixture effective elastic properties with the autocohesent schema that is adapted to poly-crystal material. The effective P-wave's velocity in figure 6.2, left) represents the effective velocity of the pore mixture at different thenardite pore fraction (from 40% to 100%).
2. Homogenisation of the pore mixture spherical inclusions with the idealized Adamswiller sandstone. We model the effective elastic properties with the autocohesent schema from which we calculate and represent the effective P-wave's velocity in figure 6.2, right).

6.3.3.3 Results

The autocohesent schema solves real positive solutions to the equations system for the effective mixture elastic properties only when the thenardite pore volume fraction represents more than 40% of the mix. About the mix air-thenardite, below 50% of thenardite, the effective velocity of the modeled mixture tends toward 0. In the mix water-thenardite, the effective P-wave modeled tends toward the velocity of P-wave in water.

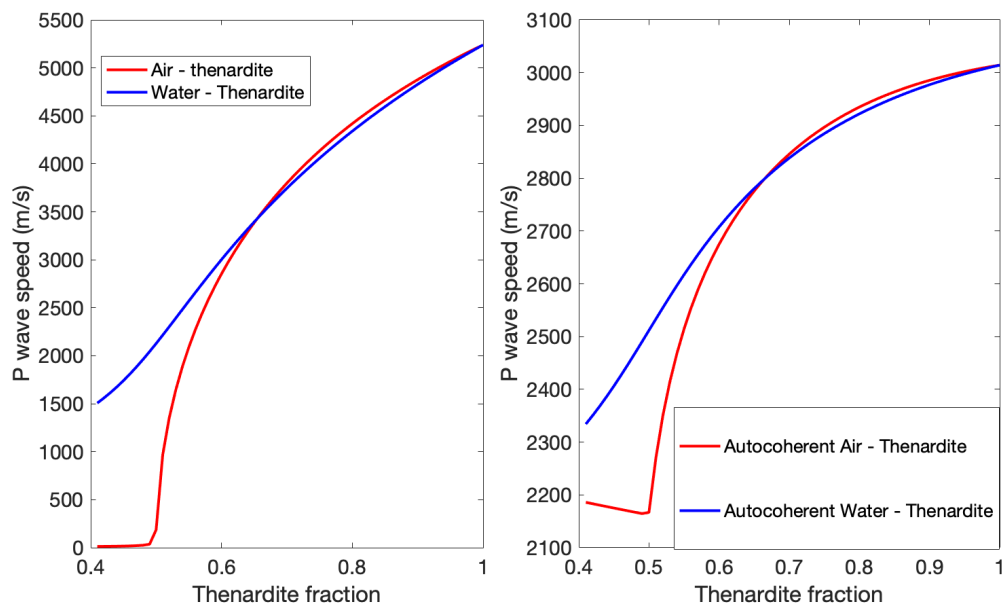


Figure 6.2: Left graphic: Effective velocity of two mixture homogenized with the Auto-coherent schema: Thenardite and Air & Thenardite and Water at different thenardite pore fraction, Right graphic: Effective velocity of homogenized with the autocoherent schema of an idealized porous Adamswiller sandstone containing left graphic mixture inclusions at different thenardite pore fraction.

After the homogenisation of the sandstone skeleton with the effective mixtures, the effective velocities of the homogenised medium are represented in figure 6.2, right. The effective P-wave’s velocities augment with the thenardite fraction in the mixture air or water and thenardite constituting the inclusion. An exception, below 50% of thenardite in the mix air-thenardite, the effective P-wave’s velocity decrease, this is due to the concomitant increase of the material density and the stagnation of the effective elastic properties of the air-thenardite mixture.

At 80% of thenardite fraction in the mix air-thenardite, that corresponds to the thenardite concentration found in the thenardite dome (chapter 4.1), both schemas predict an effective velocity in the range of 2900 m.s^{-1} . At 100% of thenardite pore fraction which is equivalent to homogenising the Adamswiller with spherical inclusions of thenardite, the P-wave effective velocity tends to 3040 m.s^{-1} .

6.3.3.4 Discussion

First of all, we do not have experimental data on the elastic properties of the sandstone sample during the impregnation with thenardite. Previously, we estimated that the thenardite phase fills 80% of a pore volume forming a thenardite dome in the porous rock. We have an estimation of the velocity through the salt dome thanks to the P-wave propagation before the beginning of the experiment: the PZT pair 5-7 are positioned to monitor the evolution of elastic properties in the thenardite dome (NB: 2480 m.s^{-1} in the dry dome). If we neglect the effect of random cracks probably induced during the sample impregnation, we calculate the P-wave’s velocity of the dry sample between PZT pair 5-7 according to the P-wave effective velocity modeling of the thenardite dome and the reference P-wave’s velocity through the Adamswiller

sandstone, equation 6.1

$$0.4 * V_{P,dry80\%thenardite} + 0.6 * V_{P,dry} = 2553m.s^{-1} \quad (6.1)$$

The P-wave's velocity modeled is evaluated at $2553 m.s^{-1}$, $\approx 70 m.s^{-1}$ above the experimental value, The excess velocity may be attributed to the random cracks displayed in figure 6.1 that we choose not to include in the modeling yet.

6.3.3.5 Conclusion

The cementing effect of thenardite precipitated in the pore is quite well-rendered with the help of homogenisation method to model the inclusion contents and the material with the inclusion.

6.3.4 Effective velocity modeling of an idealized Adamswiller sandstone containing a thenardite fraction hydrating in mirabilite

6.3.4.1 Hypothesis

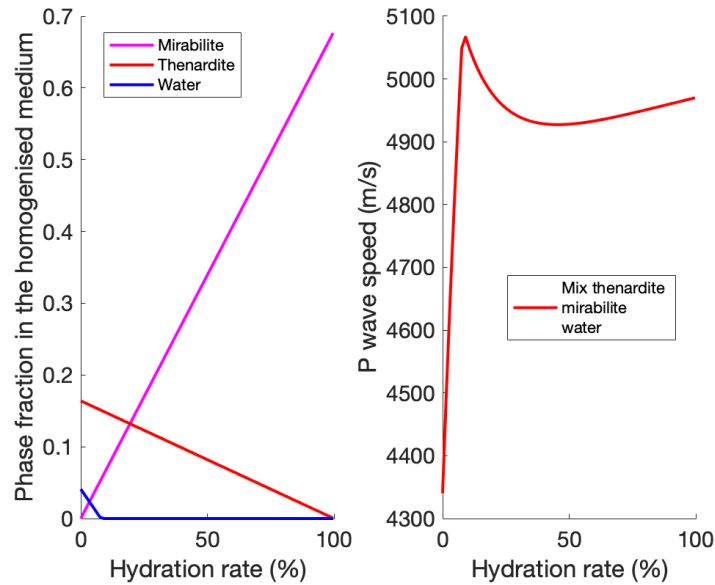
As depicted in the conceptual model discussed in chapter 4, the remaining free porosity is saturated as the water imbibition front reaches the porosity filled by crystallized thenardite. In contact with water, thenardite dissolves and reprecipitates in mirabilite. In the modeling, it is assumed that the remaining porosity is fully water-saturated despite the progressive integration of water molecules in the mirabilite lattice. The initial homogenised material is a medium containing inclusions concentrated at 80% with thenardite as estimated in chapter 4.1. The phase transformation from thenardite to mirabilite is accompanied by high solution supersaturation with respect to mirabilite. When there is a thin film of fluid between the crystal and the pore wall, it may result in a crystallisation pressure sufficient to deform and damage the porous sample (figure 6.1).

6.3.4.2 Model

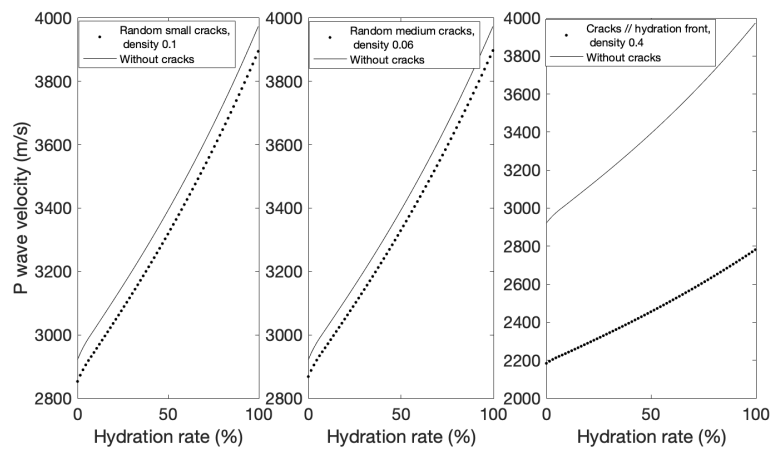
The effective properties of the mixture occupying the pore are modeled with an auto-coherent schema in two steps. The first step consists of modeling with an auto-coherent schema the effective properties of a mixture of thenardite transforming in mirabilite and the second step, to fill the remaining void with water. The auto-coherent schema let homogenise the skeleton of the adamswiller sandstone with the spherical inclusion and takes into account that the volume fraction of inclusions increases in the mix skeleton-inclusions. The effective P-wave's velocity evolution in the thenardite filled porosity during the phase transition from thenardite to mirabilite is obtained with the auto-coherent schemas by homogenising spherical inclusions of the mixture calculated previously with the skeleton.

6.3.4.3 Results

For a given volume of thenardite dissolving, a volume of mirabilite equal to $V_{mirabilite} = \frac{\bar{V}_{mirabilite}}{\bar{V}_{thenardite}} * V_{thenardite}$ crystallize (figure 6.3a, left graphic). At 100% hydration of thenardite in mirabilite, the mixture is composed with mirabilite and the inclusion



(a) Evolution of the polycrystalline mixture made of thenardite, mirabilite and water fraction in the homogenised model during phase transformation from thenardite to mirabilite, left graphic. Evolution of the autoconsistent effective P-wave's velocity in the hydrating sodium sulphate mixture, right graphic.



(b) P-wave effective velocity in the homogenised medium constituted by the Adamswiller sandstone skeleton and the hydrating mixture inclusions without and with cracks. Left graphic, small randomly oriented cracks with a crack density coefficient equal to 0.1. Middle graphic, medium randomly oriented cracks with a crack density coefficient equal to 0.06. Right graphic, large cracks, parallel to the hydrating front with a crack density coefficient equal to 0.4.

Figure 6.3: Evolution of the phases fraction and the P-wave effective velocity in a cracked homogenised Adamswiller sandstone

concentration in the homogenised medium is equal to 68% instead of 20% at the beginning.

The effective P-wave's velocity calculated in the inclusion displays two trends: from 0% to 9% the effective P-wave's velocity increase from $\approx 4350 \text{ m.s}^{-1}$ to $\approx 5050 \text{ m.s}^{-1}$. The sharp increase depicts the progressive integration of water in the mirabilite lattice and the quasi complete disappearance of the water in the mixture. Above 9% of thenardite hydration, the effective P-wave's velocity in the mixture regress because the thenardite crystals are progressively transformed into mirabilite crystals and the mirabilite elastic properties are half the values of the thenardite elastic properties (figure 6.3a, right graphic). At 100% of thenardite hydration, the effective P-wave's velocity corresponds to the theoretical P-wave's velocity in pure mirabilite, 4970 m.s^{-1}

The effective P-wave's velocity of the homogenised medium constituted of the skeleton and the spherical inclusions increase with the hydration rate. The addition of the small cracks randomly distributed reduces the effective P-wave's velocity of about $\approx 75 \text{ m.s}^{-1}$, the addition of the random distribution of medium cracks reduce the effective P-wave of $\approx 65 \text{ m.s}^{-1}$ and the addition of the large cracks parallel to the hydration front reduce the P-wave effective velocity of about $\approx 950 \text{ m.s}^{-1}$.

6.3.4.4 Discussion

The phase transition of the thenardite phase contained in the pore in mirabilite during the free imbibition has competing effects: medium stiffening observed by the P-wave's velocity increased due to the progressive filling of the quasi totality of the pore space with the crystal of mirabilite and the medium weakening via the damages induced by mirabilite crystallisation. In the water capillary uptake experiment realized on sample I without confining pressure described in chapter 4, we see that the P-wave's velocity at 48.8 mm increases slightly ($\approx 50 \text{ m.s}^{-1}$) when the imbibition waterfront reaches the porosity filled with thenardite. However, it is not clear if the increase is induced by the stiffening effect of water saturation ($\approx 80 \text{ m.s}^{-1}$) of the remaining free porosity or by the growth of the mirabilite crystal. Fortunately, the P-wave's velocity measured during a similar experiment realized with a confining pressure of 10 MPa on sample III shows that the increase on the P-wave's velocity relates well the additional effect of mirabilite crystallisation: the P-wave's velocity at 44.7 mm through the salt dome increases continuously ($\approx 200 \text{ m.s}^{-1}$) and exceed the stiffening effect induced by the water saturation visible at 13.7 and 24.7 mm ($\approx 90 \text{ m.s}^{-1}$).

The volume expansion comes with damages on the skeleton by mirabilite crystallisation that is described by three classes of cracks (table 6.2). According to the modeling, the large cracks account for the most reduction on P-wave velocity (figure 6.3b). In 4, figure 4.5, the picked P-wave velocity between PZT 5 and 7 is 1700 m.s^{-1} well below, 2200 m.s^{-1} the modeled value with the large cracks at 0% of hydration of thenardite. Meanwhile, at the height of PZT 5 and 7, the P-wave crosscuts swelling-induced cracks that we do not take into account. It may explain the divergence between the experimental and modeled velocity.

6.3.4.5 Conclusion

The coupled effect of thenardite hydration, namely the stiffening and cracking of the material containing the hydrating salt, is rendered by the homogenisation of the inclusions containing the hydrating mixture with the skeleton and the cracks analyzed on the BSE and 3D X-ray images.

6.4 General conclusion

Homogenisation methods are implemented to reproduce analytically the P-wave's velocity measured during the capillary uptake experiment in the Adamswiller sandstone sample prepared with a fraction of thenardite. The model succeeds to give a P-wave's velocities evolution that agrees with the experimental data: the cementation effect provoked by the precipitation of a foreign salt phase in the porosity in absence of damages. The hydration of the salt phase is accompanied by a competing effect between the global increase of the inclusions elastic properties and the cracks induced by the crystallisation of mirabilite.

The modeling of the effective elastic properties of an Adamswiller sandstone impregnated with kieserite during rewetting has not been achieved due to the ignorance of Kieserite elastic properties. Only epsomite properties are reported in (Brand, 2009; Brand et al., 2010). Using an iterative inverse homogenisation method, we could measure the elastic properties of the inclusion if we know the elastic properties of a sample homogeneously filled with kieserite or epsomite and the elastic properties of the skeleton. By means of standard mechanical tests, we can measure the Poisson ratio and the Young modulus. We can also use the P and S-wave propagation through the impregnated sample. This analytical study is a first draft to try to quantify the damages induced by salt crystallisation with the help of acoustic monitoring techniques. The methods employed may help to quantify the effect of salt crystallisation in a natural context like for example the problem posed by the hydration of shallowly buried anhydrite formation and the costly damaged resulting (Ramon and Alonso, 2018; Sass and Burbaum, 2010).

Conclusion and perspectives

Contents

6.5	Conclusion	158
6.6	Perspectives	159

6.5 Conclusion

To provide an experimental proof of damage induced by crystallisation in confined reservoir conditions, several aqueous sulphate species, barium sulphate, sodium sulphate and magnesium sulphate have been precipitated and rehydrated in two sedimentary rock: a Lavoux limestone (only for barite) and an Adamswiller sandstone at various confining pressure. The experiments are monitored with ultrasonic measurement, strain gauges and the recording of acoustic emissions to survey in the porous rock the crystallisation of the aqueous species and the damage induced on the porous rock. The in situ monitoring was completed by microstructure observations of the damaged zone via the acquisition of 3D X-ray microtomography scans, SEM/BSE and EDS microanalysis of the polished sections. The major result obtained is the experimental proof of crystallisation induced damages to a confining pressure simulating several hundred meters of burial. Secondary promising results and technical benefits are spotlighted:

1. Experimental crystallisation of barite in sedimentary porous rock with a contradiffusive set-up provoked the onset of solution supersaturation in the Lavoux limestone leading to a barite front crystallisation. It ensued an advanced model for aqueous species crystallisation from a supersaturated solution filling a porous rock. This model is based on the nucleation of amorphous barite. The amorphous phase interacts with the porous medium skeleton before the crystallisation of the stable barite crystal. This model may extent to many other aqueous species precipitating in porous rock since the nucleation of amorphous barite seems to be the case for many more aqueous species. Additionally, unclassical barite crystallisation has been emphasized in contact with clay fraction. Barium adsorbs between smectite or chlorite interlayer and replaces other cations. It ensues the precipitation of barite between the expanded wedge.
2. The ultrasonic P-wave velocity monitoring of an Adamswiller sandstone impregnated with thenardite and kieserite shows before all, a stiffening effect induced by salt crystallisation in the open porosity emphasized by higher P-wave velocities through the salt-rich region of the sandstone. During the water imbibition, the Adamswiller sandstone stiffens via the Gassmann effect when water saturates the porosity. If an anhydrous salt is precipitated in the porosity, an additional stiffening effect happens by hydration of the salt and compete with the damage of the material induced by the hydrate salt crystallisation. The competing effect depends on the confining pressure that favors material transport and reduces the damage induced by crystallisation. Finally, the monitoring of the elastic properties of a medium submitted to salt crystallisation and hydration can be used to monitor the fraction of salt precipitated, the hydration rate and the presence of cracks.
3. After the precursory work of Menéndez and David (2013) that first measures acoustic emissions emitted by damages during gypsum weathering, we managed to locate cracks induced by mirabilite and epsomite crystallisation. Nevertheless, we suspect that some damages are nearly aseismic and can be listened to only by the continuous recording of the acoustic activity.

6.6 Perspectives

In short-terms, we can prospect in two directions:

1. In the conclusion of chapter ??, we proposed a method to determine the elastic properties of a known amount of the kieserite precipitated homogeneously in a known porous rock. This method could be generalized to the homogeneous impregnation of a porous rock with thenardite. We may then control the validity of our results. To do that, we would privilege non-damaging methods like P and S-waves monitoring through the sample.
2. Obviously, the experiment realized with the sample prepared with 7 grams kieserite does not last long enough. It would be wise to redo it in the same conditions but for at least 15 days. I would advise using P and S- waves to compute the elastic moduli variation of the material and estimate the properties of the cracks generated like in Fortin et al. (2011).

In longer terms, we propose two other perspectives:

1. The serpentinization of ultramafic rock is a key hydration reaction proposed as a geological example in the chapter 1. It happens at a pressure of 30 MPa and 30 °C. As the reactive surface generation mechanism is debated, it would be wise to apply the acoustic monitoring techniques employed in this thesis onto an ultramafic rock during serpentinization. There are some technical issues to solve: the resistance of the piezoelectric transducers in the experimental conditions of temperature and pressure. Moreover, if like the literature Malvoisin, Brantut, and Kaczmarek (2017) and Plümper et al. (2012) and passive seismicity observation in the Mauleon basin (to be published by Dr. Eric C. Gaucher and Dr. Sylvain Calassou) such a reaction may induce damages and seismicity, the monitoring of the seismicity would bring useful pieces of information about the reactivity of the ultramafic rock and the potential native hydrogen production.
2. Diagenetic replacement revealed in Maliva and Siever (1988a) and phase change driven by stress from volume expansion during hydration of granulite in amphibolite (Centrella, 2019; Centrella, Austrheim, and Putnis, 2015) raise the question of a role played by the pressure solution exerted by the replacement phase or hydrating phase on the host phase. It is another point of view on crystallisation pressure. Instead of cracking the porous medium, the crystallisation of a foreign phase may dissolve the host phase. As such a reaction is supposed to happen during dolomitization (Maliva and Siever, 1988a; Merino, Canals, and Fletcher, 2006), it would be wise to propose a test to solve this question. To us, the rewetting of a limestone sample impregnated with magnesium sulphate may work by following this sequence: 1) a limestone sample impregnated with kieserite is rewetted at an isotropic confining pressure sufficiently high (>33 MPa) to prevent epsomite crystallisation-induced damages. 2) Nevertheless, the crystallisation pressure exerted by epsomite (≈ 33 MPa) increases the solubility limit of calcite: calcite may dissolve. If our hypothesis is correct, the calcium and carbonate ions could combine with magnesium cations in solution and reprecipitate as dolomite.

Appendix A

A.1 Geodesign triaxial cell

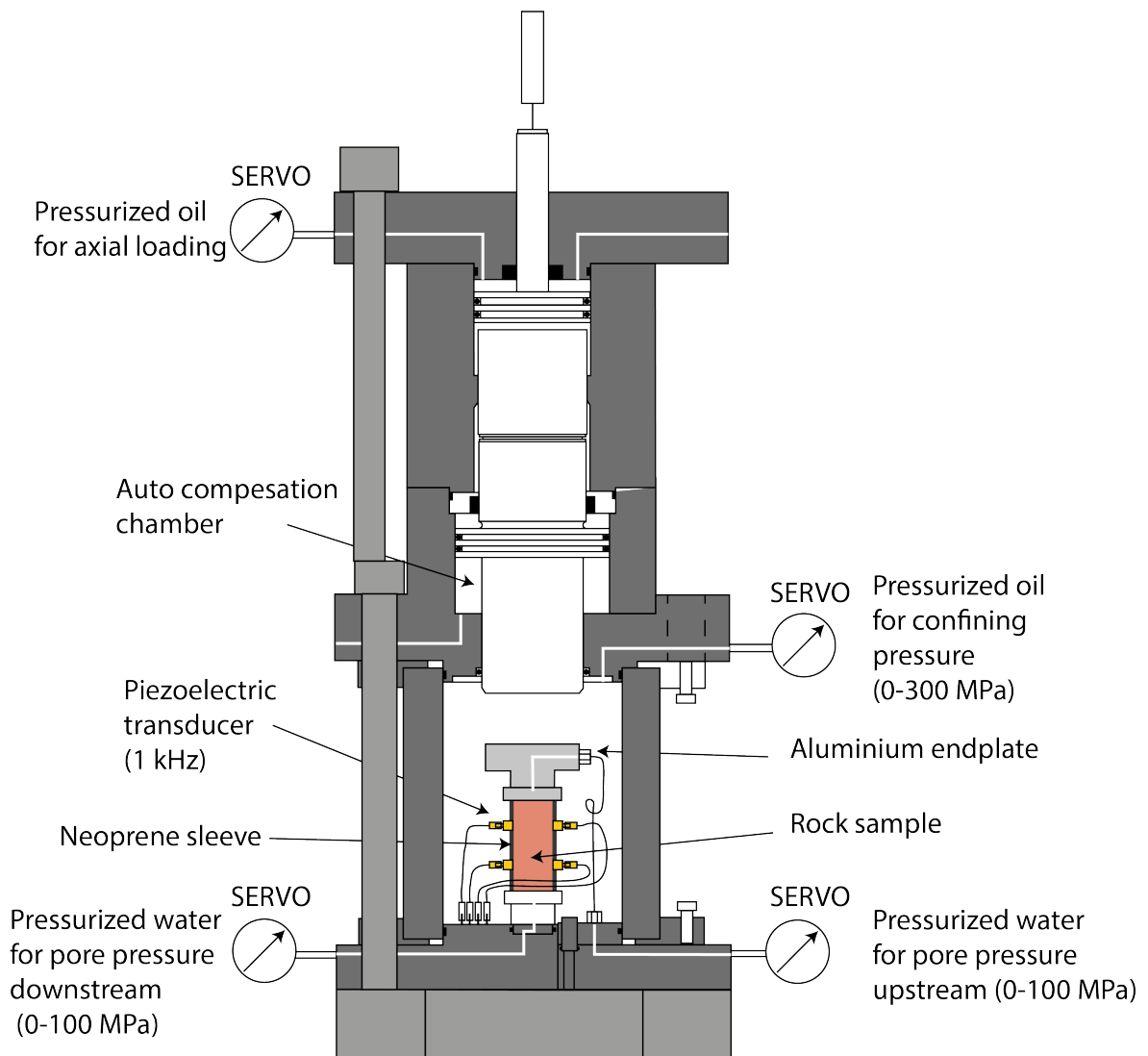


Figure A.1: Schematic representation of the Geodesign triaxial cell adapted from (Borgo-
mano, 2019)

A.2 Shots picking methods

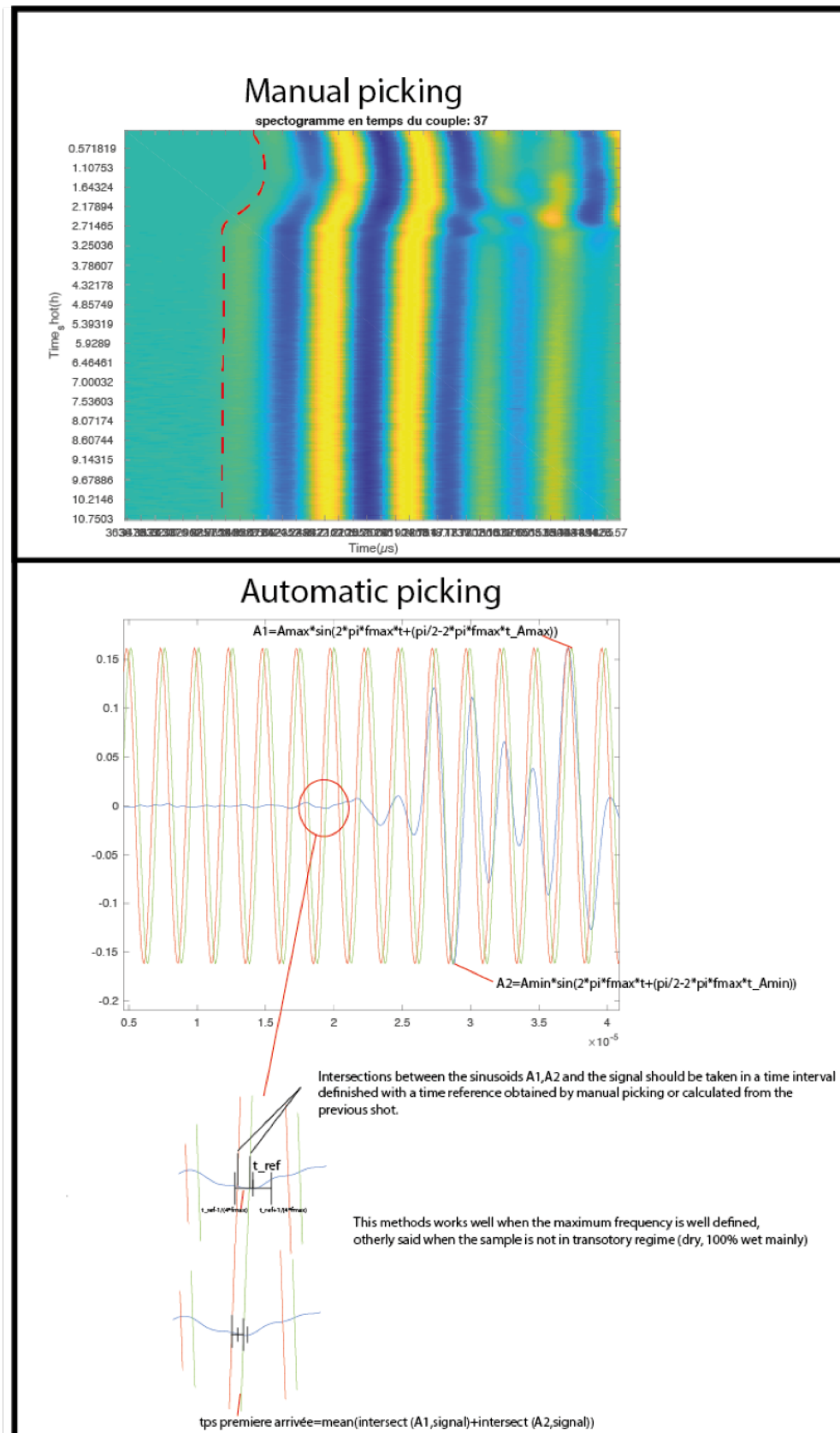
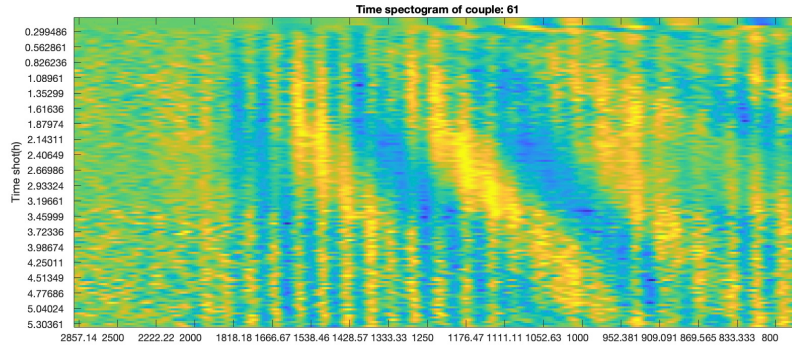
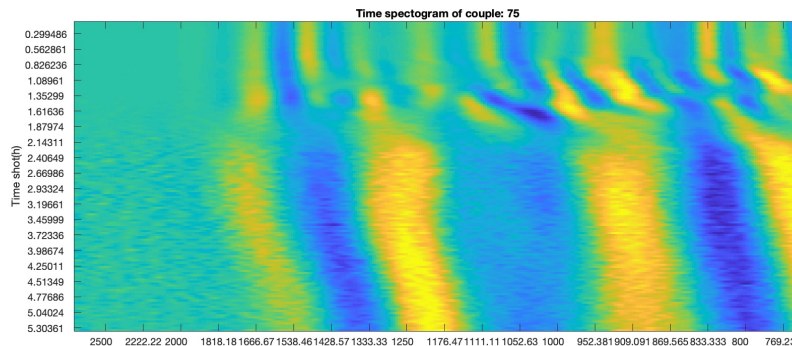


Figure A.2: First arrival picking methods

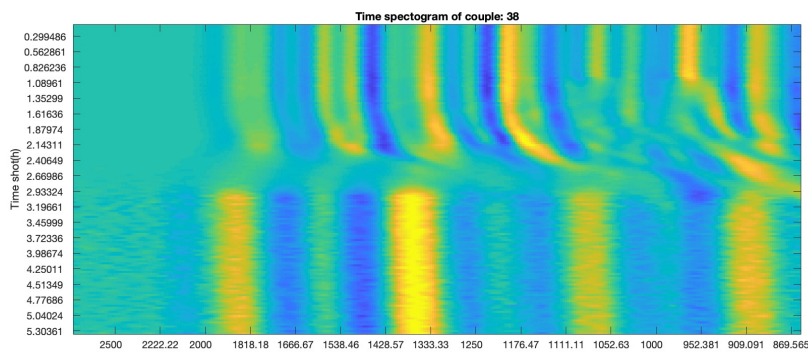
A.3 P-wave propagation spectrogram in ENS experiments



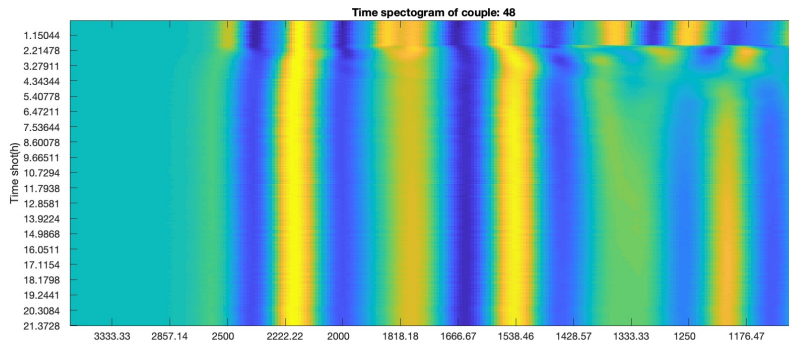
(a) Unconfined sample I, Trace of PZT pair 1-6



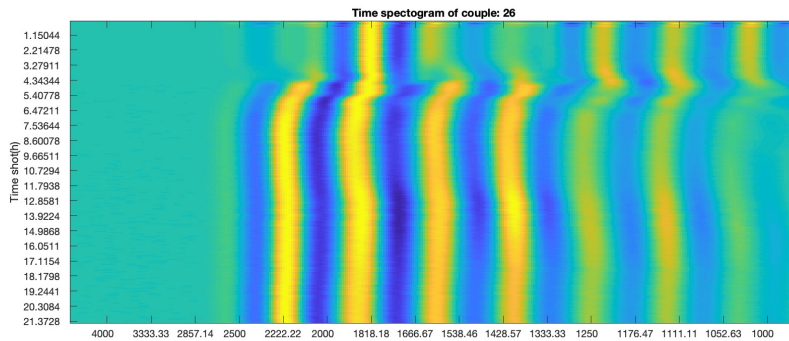
(b) Unconfined sample I, Trace of PZT pair 5-7



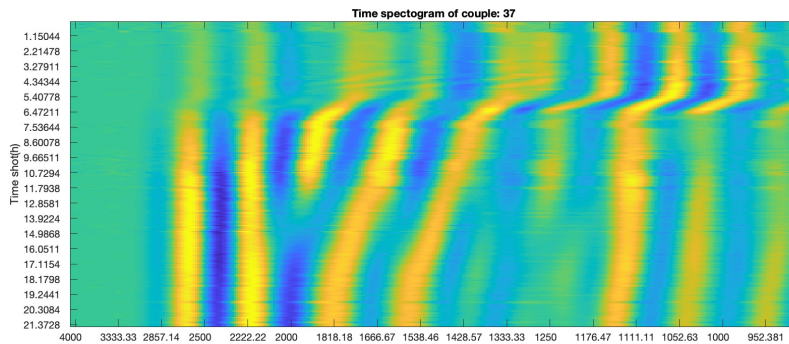
(c) Unconfined sample I, Trace of PZT pair 3-8



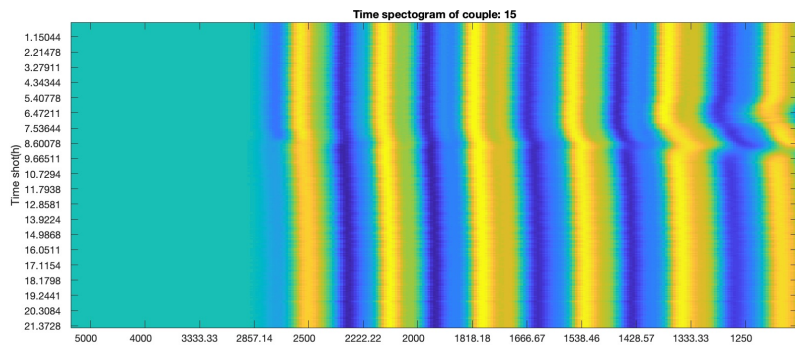
(a) Confined 10 MPa sample III, Trace of PZT pair 4-8



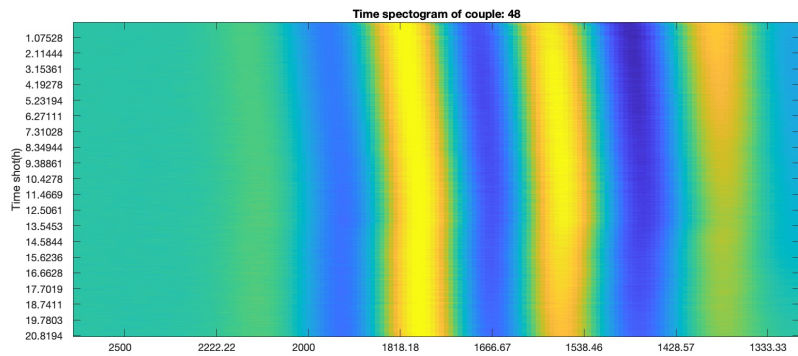
(b) Confined 10 MPa sample III, Trace of PZT pair 2-6



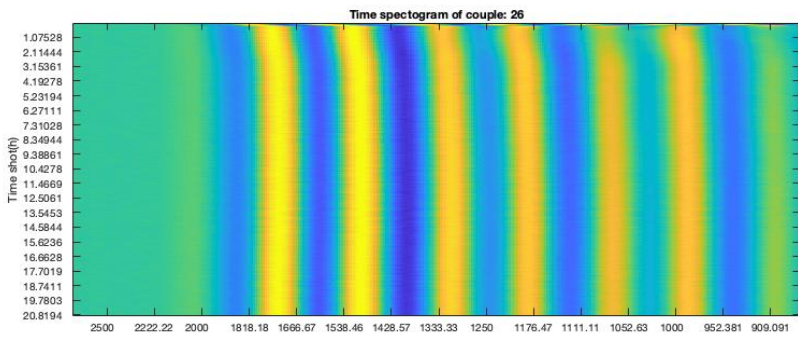
(c) Confined 10 MPa sample III, Trace of PZT pair 3-7



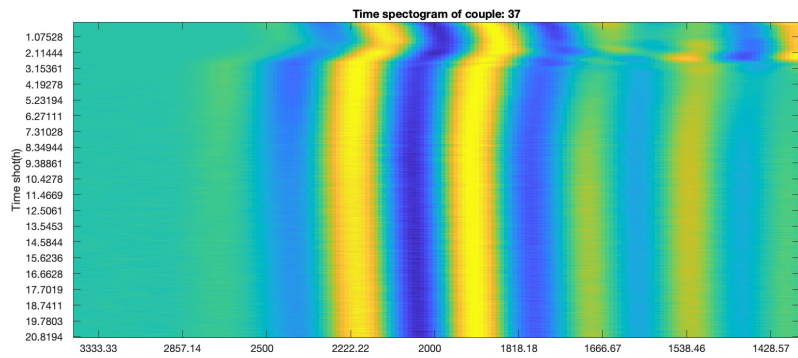
(d) Confined 10 MPa sample III, Trace of PZT pair 1-5



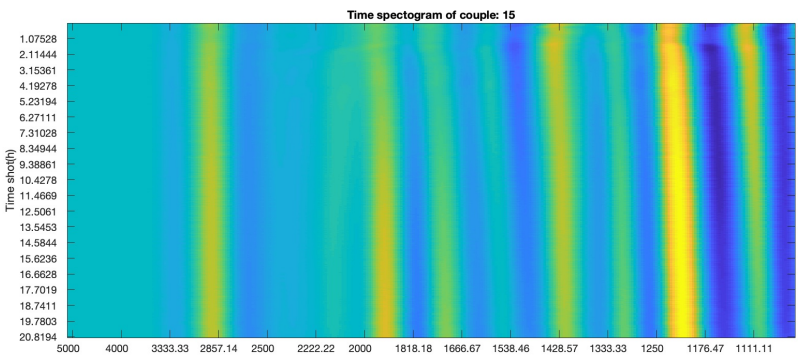
(a) Unconfined sample XII, Trace of PZT pair 4-8



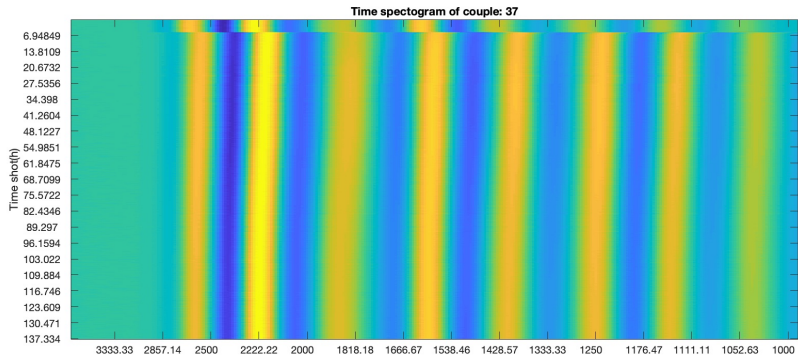
(b) Unconfined sample XII, Trace of PZT pair 2-6



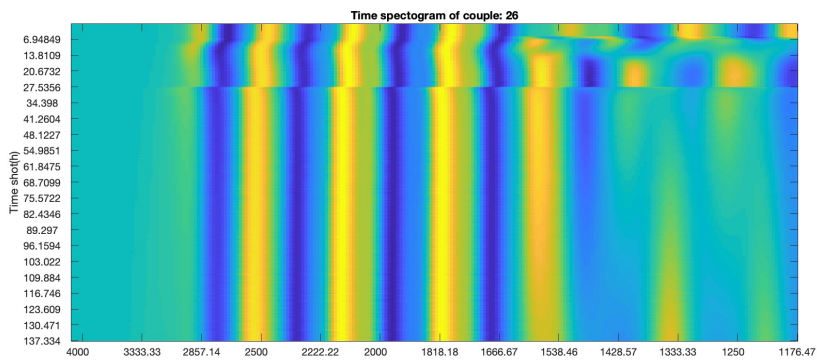
(c) Unconfined sample XII, Trace of PZT pair 3-7



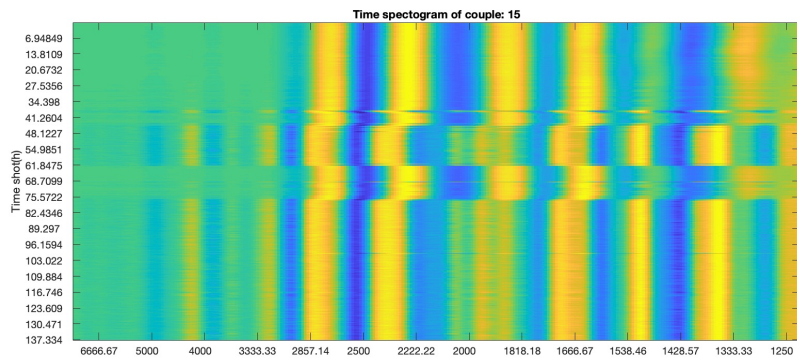
(d) Unconfined sample XII, Trace of PZT pair 1-5



(a) Confined sample XI at 27 MPa, Trace of PZT pair 3-7



(b) Confined sample XI at 27 MPa, Trace of PZT pair 2-6



(c) Confined sample XI at 27 MPa, Trace of PZT pair 1-5

A.4 Adamswiller sample description

N°	Rock type	Salt	Mass impregnated (g)	Salt pore sat.	N° inj.	Cycle 120°C	Initial hght. (mm)	Initial diam. (mm)	Final hght. (mm)	Final diam. (mm)
NR11	Vosges	Na_2SO_4	6.4		7	0	79	40.3		
I	Vosges	Na_2SO_4	5.26	80%	7	0	84.25	39.9	84.6	40.9
III	Vosges	Na_2SO_4	5.38	80%	7	0	85.71	39.7	86	40.9
IX	Vosges	$MgSO_4$	7.82	65-65%	5	2	80.44	40		
X	Vosges	$MgSO_4$	9.47		5	3	80.4	40		
XI	Vosges	$MgSO_4$	7.59	70%	4	3	86.3	39.8		
XII	Vosges	$MgSO_4$	7.11	75-80%	3	3	85.2	39.8		

A.5 Supplementary material

Supplementary material can be found on-line at
<https://nuage.univ-pau.fr/s/JjJdGMdq9ZGbymn>

Appendix B

Glossary

ABS Amorphous Barite Precursor. [52](#)

AC Autocoherent. [41](#)

AE Acoustic emission. [68](#), [69](#), [71](#), [93](#), [94](#), [105](#), [113](#), [114](#), [127](#), [128](#), [130](#), [132–134](#), [140](#), [142](#)

BSE Back-Scattered Electrons. [78](#), [93](#), [102](#), [106](#), [108](#), [111](#), [141](#), [147](#)

CNT Classical Nucleation Theory. [10](#), [84](#), [86](#), [88](#)

CP Crystallisation Pressure. [9](#)

EDS Energy Dispersive X-ray Spectroscopy. [62](#), [78](#), [79](#), [102](#), [124](#)

FFT Fast Fourier Transform. [37](#), [70](#)

IAP Ion Activity Product. [8](#), [20](#), [51](#)

pH Hydrogen Potential. [13](#)

PNC Pre-nucleation Cluster. [10](#), [84](#), [86](#), [87](#)

PZT lead-zirconate piezoceramic transducers. [38](#), [68–70](#), [101](#), [103–106](#), [109](#), [112](#), [127](#), [128](#), [132](#), [134](#), [136](#), [137](#), [139–141](#), [150](#), [155](#)

REA Representative Elementary Area. [42](#), [150](#)

REV Representative Elementary Volume. [36](#), [42](#)

RH Relative Humidity. [38](#), [47](#), [54](#), [55](#), [58](#)

S Saturation. [8](#), [13](#), [16](#), [18–20](#)

SEM Scanning Electron Microscopy. [79](#)

SI Saturation index. [8](#)

Bibliography

- Al-Jibbouri, Sattar, Christine Strege, and Joachim Ulrich (2002). “Crystallization kinetics of epsomite influenced by pH-value and impurities”. In: *Journal of Crystal Growth* 236.1-3, pp. 400–406. ISSN: 00220248. DOI: [10.1016/S0022-0248\(01\)02172-8](https://doi.org/10.1016/S0022-0248(01)02172-8).
- Atun, G. and E. Bascetin (2003). “Adsorption of barium on kaolinite, illite and montmorillonite at various ionic strengths”. In: *Radiochimica Acta* 91.4, pp. 223–228. ISSN: 00338230. DOI: [10.1524/ract.91.4.223.19964](https://doi.org/10.1524/ract.91.4.223.19964).
- Aubry, J., F. X. Passelègue, D. Deldicque, F. Girault, S. Marty, A. Lahfid, H. S. Bhat, J. Escartin, and A. Schubnel (2018). “Frictional Heating Processes and Energy Budget During Laboratory Earthquakes”. In: *Geophysical Research Letters* 45.22, pp. 12,274–12,282. ISSN: 19448007. DOI: [10.1029/2018GL079263](https://doi.org/10.1029/2018GL079263).
- Balboni, Enrica, Rosa M. Espinosa-Marzal, Eric Doehne, and George W. Scherer (2011). “Can drying and re-wetting of magnesium sulfate salts lead to damage of stone?” In: *Environmental Earth Sciences* 63.7, pp. 1463–1473. ISSN: 18666280. DOI: [10.1007/s12665-010-0774-1](https://doi.org/10.1007/s12665-010-0774-1).
- Barrière, Julien (2011). “Atténuation et dispersion des ondes P en milieu poreux partiellement saturé : approche expérimentale”. PhD thesis. URL: <https://tel.archives-ouvertes.fr/tel-00734463>.
- Barrière, Julien, Clarisse Bordes, Daniel Brito, Pascale Sénéchal, and Hervé Perroud (2012). “Laboratory monitoring of P waves in partially saturated sand”. In: *Geophysical Journal International* 191.3, pp. 1152–1170. ISSN: 0956540X. DOI: [10.1111/j.1365-246X.2012.05691.x](https://doi.org/10.1111/j.1365-246X.2012.05691.x).
- Bettison-Varga, Lori and Ian D R Mackinnon (1997). “The Role of Randomly Mixed-Layered Chlorite/Smectite in the Transformation of Smectite to Chlorite”. In: *Clays and Clay Minerals* 45.4, pp. 506–516. ISSN: 1552-8367. DOI: [10.1346/CCMN.1997.0450403](https://doi.org/10.1346/CCMN.1997.0450403). URL: <https://doi.org/10.1346/CCMN.1997.0450403>.
- Biot, M. A. (1956a). “Theory of Propagation of Elastic Waves in a Fluid-Saturated Porous Solid. I. Low-Frequency Range”. In: *Journal of the Acoustical Society of America* 28.2, pp. 168–178. ISSN: NA. DOI: [10.1121/1.1908239](https://doi.org/10.1121/1.1908239).
- (1956b). “Theory of Propagation of Elastic Waves in a Fluid-Saturated Porous Solid II. Higher Frequency Range”. In: *Journal of the Acoustical Society of America* 28.2, pp. 179–191. ISSN: NA. DOI: [10.1121/1.1908241](https://doi.org/10.1121/1.1908241).
- Blaise, Thomas, Norbert Clauer, Michel Cathelineau, Marie Christine Boiron, Isabelle Techer, and Philippe Boulvais (2016). “Reconstructing fluid-flow events in Lower-Triassic sandstones of the eastern Paris Basin by elemental tracing and isotopic dating of nanometric illite crystals”. In: *Geochimica et Cosmochimica Acta* 176, pp. 157–184. ISSN: 00167037. DOI: [10.1016/j.gca.2015.12.018](https://doi.org/10.1016/j.gca.2015.12.018). URL: <http://dx.doi.org/10.1016/j.gca.2015.12.018>.

- Bons, Paul D., Marlina A. Elburg, and Enrique Gomez-Rivas (2012). “A review of the formation of tectonic veins and their microstructures”. In: *Journal of Structural Geology* 43, pp. 33–62. ISSN: 01918141. DOI: [10.1016/j.jsg.2012.07.005](https://doi.org/10.1016/j.jsg.2012.07.005).
- Bons, Paul D. and Mark W. Jessell (1997). “Experimental simulation of the formation of fibrous veins by localised dissolution-precipitation creep”. In: *Mineralogical Magazine* 61.404, pp. 53–63. ISSN: 0026-461X. DOI: [10.1180/minmag.1997.061.404.06](https://doi.org/10.1180/minmag.1997.061.404.06).
- Bons, Paul D. and Michael Montenari (2005). “The formation of antitaxial calcite veins with well-developed fibres, Oppaminda Creek, South Australia”. In: *Journal of Structural Geology* 27.2, pp. 231–248. ISSN: 01918141. DOI: [10.1016/j.jsg.2004.08.009](https://doi.org/10.1016/j.jsg.2004.08.009).
- Borgomano, Jan (2019). “Dispersion des modules élastiques de carbonates saturés : étude expérimentale et modélisation”. PhD thesis.
- Brand, H. (2009). “Thermoelastic properties of salt hydrates and implications for geological structures”. PhD thesis. URL: <http://eprints.ucl.ac.uk/18903/>.
- Brand, Helen E.A., A. Dominic Fortes, Ian G. Wood, and Lidunka Vočadlo (2010). “Equation of state and pressure-induced structural changes in mirabilite (Na₂SO₄·10H₂O) determined from ab initio density functional theory calculations”. In: *Physics and Chemistry of Minerals* 37.5, pp. 265–282. ISSN: 03421791. DOI: [10.1007/s00269-009-0331-1](https://doi.org/10.1007/s00269-009-0331-1).
- Brandt, Felix, Thorsten Schäfer, Francis Claret, and Dirk Bosbach (2012). “Heterogeneous formation of ferric oxide nanoparticles on chlorite surfaces studied by x-ray absorption spectromicroscopy (STXM)”. In: *Chemical Geology* 329, pp. 42–52. ISSN: 00092541. DOI: [10.1016/j.chemgeo.2011.08.016](https://doi.org/10.1016/j.chemgeo.2011.08.016). URL: <http://dx.doi.org/10.1016/j.chemgeo.2011.08.016>.
- Caruso, Francesco, Timothy Wangler, and Robert J. Flatt (2018). “Easy Illustration of Salt Damage in Stone”. In: *Journal of Chemical Education* 95.9, pp. 1615–1620. ISSN: 19381328. DOI: [10.1021/acs.jchemed.7b00815](https://doi.org/10.1021/acs.jchemed.7b00815).
- Castellini, D. Grace, Gerald R. Dickens, Glen T. Snyder, and Carolyn D. Ruppel (2006). “Barium cycling in shallow sediment above active mud volcanoes in the Gulf of Mexico”. In: *Chemical Geology* 226.1-2, pp. 1–30. ISSN: 00092541. DOI: [10.1016/j.chemgeo.2005.08.008](https://doi.org/10.1016/j.chemgeo.2005.08.008).
- Centrella, Stephen (2019). “The Granulite- to Eclogite- and Amphibolite-Facies transition: A volume and mass transfer study in the Lindås Nappe, Bergen arcs, west Norway”. In: *Geological Society Special Publication* 478.1, pp. 241–263. ISSN: 03058719. DOI: [10.1144/SP478.9](https://doi.org/10.1144/SP478.9).
- Centrella, Stephen, Håkon Austrheim, and Andrew Putnis (2015). “Coupled mass transfer through a fluid phase and volume preservation during the hydration of granulite: An example from the Bergen Arcs, Norway”. In: *Lithos* 236-237, pp. 245–255. ISSN: 18726143. DOI: [10.1016/j.lithos.2015.09.010](https://doi.org/10.1016/j.lithos.2015.09.010). URL: <http://dx.doi.org/10.1016/j.lithos.2015.09.010>.
- Chagneau, Aurélie, Francis Claret, Frieder Enzmann, Michael Kersten, Stephanie Heck, Benoît Madé, and Thorsten Schäfer (2015a). “Mineral precipitation-induced porosity reduction and its effect on transport parameters in diffusion-controlled porous media”. In: *Geochemical Transactions* 16.1, p. 13. ISSN: 14674866. DOI: [10.1186/s12932-015-0027-z](https://doi.org/10.1186/s12932-015-0027-z). URL: <http://www.geochemicaltransactions.com/content/16/1/13>.
- Chagneau, Aurélie, Christophe Tournassat, Carl I. Steefel, Ian C. Bourg, Stéphane Gaboriau, Imène Esteve, Tomas Kupcik, Francis Claret, and Thorsten Schäfer (2015b). “Complete restriction of ³⁶Cl- diffusion by celestite precipitation in densely com-

- pacted illite". In: *Environmental Science and Technology Letters* 2.5, pp. 139–143. ISSN: 23288930. DOI: [10.1021/acs.estlett.5b00080](https://doi.org/10.1021/acs.estlett.5b00080).
- Cobbold, Peter R., Alain Zanella, Nuno Rodrigues, and Helge Løseth (2013). "Bedding-parallel fibrous veins (beef and cone-in-cone): Worldwide occurrence and possible significance in terms of fluid overpressure, hydrocarbon generation and mineralization". In: *Marine and Petroleum Geology* 43, pp. 1–20. ISSN: 02648172. DOI: [10.1016/j.marpetgeo.2013.01.010](https://doi.org/10.1016/j.marpetgeo.2013.01.010). URL: <http://dx.doi.org/10.1016/j.marpetgeo.2013.01.010>.
- Collins, Ian (2005). "Predicting the Location of Barium Sulfate Scale Formation in Production Systems". In: *SPE International Symposium on Oilfield Scale* 1, pp. 1–6. DOI: [10.2523/94366-ms](https://doi.org/10.2523/94366-ms). URL: <http://www.onepetro.org/mslib/servlet/onepetroreview?id=SPE-94366-MS>.
- Corre, Benjamin, Yves Lagabrielle, Pierre Labaume, Serge Fourcade, Camille Clerc, and Michel Ballèvre (2016). "Deformation associated with mantle exhumation in a distal, hot passive margin environment: New constraints from the Sarailé Massif (Châinons Béarnais, North-Pyrenean Zone)". In: *Comptes Rendus - Geoscience* 348.3-4, pp. 279–289. ISSN: 16310713. DOI: [10.1016/j.crte.2015.11.007](https://doi.org/10.1016/j.crte.2015.11.007). URL: <http://dx.doi.org/10.1016/j.crte.2015.11.007>.
- Correns, Carl W. (1949). "Growth and dissolution of crystals under linear pressure". In: 5, pp. 267–271. ISSN: 03669033. DOI: [10.1039/DF9490500267](https://doi.org/10.1039/DF9490500267).
- Coussy, Olivier (2006). "Deformation and stress from in-pore drying-induced crystallization of salt". In: *Journal of the Mechanics and Physics of Solids* 54.8, pp. 1517–1547. ISSN: 00225096. DOI: [10.1016/j.jmps.2006.03.002](https://doi.org/10.1016/j.jmps.2006.03.002).
- Cox, S. F. and M. A. Etheridge (1983). "Crack-seal fibre growth mechanisms and their significance in the development of oriented layer silicate microstructures". In: *Tectonophysics* 92.1-3, pp. 147–170. ISSN: 00401951. DOI: [10.1016/0040-1951\(83\)90088-4](https://doi.org/10.1016/0040-1951(83)90088-4).
- David, Christian, Christophe Barnes, Mathilde Desrues, Lucas Pimienta, Joël Sarout, and Jérémie Dautriat (2017a). "Ultrasonic monitoring of spontaneous imbibition experiments: Acoustic signature of fluid migration". In: *Journal of Geophysical Research: Solid Earth* 122.7, pp. 4931–4947. ISSN: 21699356. DOI: [10.1002/2016JB013804](https://doi.org/10.1002/2016JB013804).
- David, Christian, Joël Sarout, Jérémie Dautriat, Lucas Pimienta, Marie Michée, Mathilde Desrues, and Christophe Barnes (2017b). "Ultrasonic monitoring of spontaneous imbibition experiments: Precursory moisture diffusion effects ahead of water front". In: *Journal of Geophysical Research: Solid Earth* 122.7, pp. 4948–4962. ISSN: 21699356. DOI: [10.1002/2017JB014193](https://doi.org/10.1002/2017JB014193).
- Derluyn, Hannelore (2012). "Salt transport and crystallization in porous limestone Neutron-X-ray imaging and poromechanical modeling". PhD thesis. ISBN: 9783033046412. DOI: [10.3929/ETHZ-B-000225616](https://doi.org/10.3929/ETHZ-B-000225616). URL: <http://scholar.google.com/scholar?hl=en&btnG=Search&q=intitle:Photogrammetric+scanners+-+survey,+technological+developments+and+requirements{#\#}0>.
- Derluyn, Hannelore, Jan Dewanckele, Matthieu N. Boone, Veerle Cnudde, Dominique Derome, and Jan Carmeliet (2014). "Crystallization of hydrated and anhydrous salts in porous limestone resolved by synchrotron X-ray microtomography". In: *Nuclear Instruments and Methods in Physics Research, Section B: Beam Interactions with Materials and Atoms* 324, pp. 102–112. ISSN: 0168583X. DOI: [10.1016/j.nimb.2013.08.065](https://doi.org/10.1016/j.nimb.2013.08.065). URL: <http://dx.doi.org/10.1016/j.nimb.2013.08.065>.
- Derluyn, Hannelore, Tamerlan A. Saidov, Rosa M. Espinosa-Marzal, Leo Pel, and George W. Scherer (2011). "Sodium sulfate heptahydrate I: The growth of sin-

- gle crystals". In: *Journal of Crystal Growth* 329.1, pp. 44–51. ISSN: 00220248. DOI: [10.1016/j.jcryspro.2011.06.024](https://doi.org/10.1016/j.jcryspro.2011.06.024). URL: <http://dx.doi.org/10.1016/j.jcryspro.2011.06.024>.
- Desarnaud, J., D. Bonn, and N. Shahidzadeh (2016). "The Pressure induced by salt crystallization in confinement". In: *Scientific Reports* 6.1, p. 30856. ISSN: 20452322. DOI: [10.1038/srep30856](https://doi.org/10.1038/srep30856). URL: <http://www.nature.com/articles/srep30856>.
- Desarnaud, J. and N. Shahidzadeh-Bonn (2011). "Salt crystal purification by deliquescence/crystallization cycling". In: *Epl* 95.4. ISSN: 02955075. DOI: [10.1209/0295-5075/95/48002](https://doi.org/10.1209/0295-5075/95/48002).
- Elburg, Marlina A., Paul D. Bons, John Foden, and Cees W. Passchier (2002). "The origin of fibrous veins: Constraints from geochemistry". In: *Geological Society Special Publication* 200.1, pp. 103–118. ISSN: 03058719. DOI: [10.1144/GSL.SP.2001.200.01.07](https://doi.org/10.1144/GSL.SP.2001.200.01.07). URL: <http://sp.lyellcollection.org/content/specpubgsl/200/1/103.full.pdf%0Ahttp://sp.lyellcollection.org/lookup/doi/10.1144/GSL.SP.2001.200.01.07>.
- Erfani Gahrooei, Hamid Reza and Mohammad Hossein Ghazanfari (2017). "Toward a hydrocarbon-based chemical for wettability alteration of reservoir rocks to gas wetting condition: Implications to gas condensate reservoirs". In: *Journal of Molecular Liquids* 248. June 2019, pp. 100–111. ISSN: 01677322. DOI: [10.1016/j.molliq.2017.10.043](https://doi.org/10.1016/j.molliq.2017.10.043). URL: <http://dx.doi.org/10.1016/j.molliq.2017.10.043>.
- Espinosa-Marzal, Rosa M., Andrea Hamilton, Megan McNall, Kathryn Whitaker, and George W. Scherer (2011). "The chemomechanics of crystallization during rewetting of limestone impregnated with sodium sulfate". In: *Journal of Materials Research* 26.12, pp. 1472–1481. ISSN: 08842914. DOI: [10.1557/jmr.2011.137](https://doi.org/10.1557/jmr.2011.137).
- Espinosa Marzal, Rosa M. and George W. Scherer (2008). "Crystallization of sodium sulfate salts in limestone". In: *Environmental Geology* 56.3-4, pp. 605–621. ISSN: 09430105. DOI: [10.1007/s00254-008-1441-7](https://doi.org/10.1007/s00254-008-1441-7).
- Espinosa-Marzal, Rosa M. and George W. Scherer (2010). "Advances in understanding damage by salt crystallization". In: *Accounts of Chemical Research* 43.6, pp. 897–905. ISSN: 00014842. DOI: [10.1021/ar9002224](https://doi.org/10.1021/ar9002224).
- Evans, Bernard W., Keiko Hattori, and Alain Baronnet (2013). "Serpentinite: What, why, where?" In: *Elements* 9.2, pp. 99–106. ISSN: 18115209. DOI: [10.2113/gselements.9.2.99](https://doi.org/10.2113/gselements.9.2.99).
- Filho, F. F. Mendonça, H. Morillas, H. Derluyn, M. Maguregui, and D. Grégoire (2019). "In-situ versus laboratory characterization of historical site in marine environment using X-ray fluorescence and Raman spectroscopy". In: *Microchemical Journal* 147, pp. 905–913. ISSN: 0026265X. DOI: [10.1016/j.microc.2019.02.014](https://doi.org/10.1016/j.microc.2019.02.014).
- Flatt, Robert J. (2002). "Salt damage in porous materials: How high supersaturations are generated". In: *Journal of Crystal Growth* 242.3-4, pp. 435–454. ISSN: 00220248. DOI: [10.1016/S0022-0248\(02\)01429-X](https://doi.org/10.1016/S0022-0248(02)01429-X).
- Flatt, Robert J., Francesco Caruso, Asel Maria Aguilar Sanchez, and George W. Scherer (2014). "Chemo-mechanics of salt damage in stone". In: *Nature Communications* 5, pp. 1–5. ISSN: 20411723. DOI: [10.1038/ncomms5823](https://doi.org/10.1038/ncomms5823).
- Fortin, J., S. Stanchits, S. Vinciguerra, and Y. Guéguen (2011). "Influence of thermal and mechanical cracks on permeability and elastic wave velocities in a basalt from Mt. Etna volcano subjected to elevated pressure". In: *Tectonophysics* 503.1-2, pp. 60–74. ISSN: 00401951. DOI: [10.1016/j.tecto.2010.09.028](https://doi.org/10.1016/j.tecto.2010.09.028). URL: <http://dx.doi.org/10.1016/j.tecto.2010.09.028>.

- Fortin, Jerome (2007). “Compaction homogène et compaction localisée des roches poreuses . Etude expérimentale et théorique To cite this version : HAL Id : tel-00180388 Compaction homogène et compaction localisée des roches poreuses”. PhD thesis.
- Fortin, Jérôme, Sergei Stanchits, Georg Dresen, and Yves Guéguen (2006). “Acoustic emission and velocities associated with the formation of compaction bands in sandstone”. In: *Journal of Geophysical Research: Solid Earth* 111.10, pp. 1–16. ISSN: 21699356. DOI: [10.1029/2005JB003854](https://doi.org/10.1029/2005JB003854).
- Fortin, Jerome, Sergei Stanchits, Georg Dresen, and Yves Gueguen (2009). “Acoustic emissions monitoring during inelastic deformation of porous sandstone: Comparison of three modes of deformation”. In: *Pure and Applied Geophysics* 166.5-7, pp. 823–841. ISSN: 14209136. DOI: [10.1007/s00024-009-0479-0](https://doi.org/10.1007/s00024-009-0479-0).
- Fukatsu, Yuta, Luc R. Van Loon, Amir Shafizadeh, Daniel Grolimund, Yasuhisa Ikeda, and Takehiko Tsukahara (2017). “Effect of Celestite Precipitation in Compacted Illite on the Diffusion of HTO, $^{36}\text{Cl}^-$, and $^{22}\text{Na}^+$ ”. In: *Energy Procedia* 131, pp. 133–139. ISSN: 18766102. DOI: [10.1016/j.egypro.2017.09.450](https://doi.org/10.1016/j.egypro.2017.09.450). URL: <https://doi.org/10.1016/j.egypro.2017.09.450>.
- Gaucher, Eric C. (2020). “New perspectives in the industrial exploration for native hydrogen”. In: *Elements* 16.1, pp. 8–9. ISSN: 18115217. DOI: [10.2138/gselements.16.1.8](https://doi.org/10.2138/gselements.16.1.8).
- Gebauer, Denis and Helmut Cölfen (2011). “Prenucleation clusters and non-classical nucleation”. In: *Nano Today* 6.6, pp. 564–584. ISSN: 17480132. DOI: [10.1016/j.nantod.2011.10.005](https://doi.org/10.1016/j.nantod.2011.10.005). URL: <http://dx.doi.org/10.1016/j.nantod.2011.10.005>.
- Gebauer, Denis, Matthias Kellermeier, Julian D. Gale, Lennart Bergström, and Helmut Cölfen (2014). “Pre-nucleation clusters as solute precursors in crystallisation”. In: *Chemical Society Reviews* 43.7, pp. 2348–2371. ISSN: 14604744. DOI: [10.1039/c3cs60451a](https://doi.org/10.1039/c3cs60451a).
- Gebauer, Denis, Paolo Raiteri, Julian D. Gale, and Helmut Cölfen (2018). “On classical and non-classical views on nucleation”. In: *American Journal of Science* 318.9, pp. 969–988. ISSN: 00029599. DOI: [10.2475/09.2018.05](https://doi.org/10.2475/09.2018.05).
- Godinho, Jose R.A., Kirill M. Gerke, Andrew G. Stack, and Peter D. Lee (2016). “The dynamic nature of crystal growth in pores”. In: *Scientific Reports* 6.1, p. 33086. ISSN: 20452322. DOI: [10.1038/srep33086](https://doi.org/10.1038/srep33086). URL: <http://www.nature.com/articles/srep33086>.
- Godinho, Jose R.A. and Andrew G. Stack (2015). “Growth kinetics and morphology of barite crystals derived from face-specific growth rates”. In: *Crystal Growth and Design* 15.5, pp. 2064–2071. ISSN: 15287505. DOI: [10.1021/cg501507p](https://doi.org/10.1021/cg501507p).
- Gratier, Jean Pierre, Emanuelle Frery, Pierre Deschamps, Anja Røyne, François Renard, Dag Dysthe, Nadine Ellouz-Zimmerman, and Bruno Hamelin (2012). “How travertine veins grow from top to bottom and lift the rocks above them: The effect of crystallization force”. In: *Geology* 40.11, pp. 1015–1018. ISSN: 00917613. DOI: [10.1130/G33286.1](https://doi.org/10.1130/G33286.1).
- Grégoire, David, Laura Verdon, Vincent Lefort, Peter Grassl, Jacqueline Saliba, Jean-Pierre Regoin, Ahmed Loukili, and Gilles Pijaudier-Cabot (2015). “Mesoscale analysis of failure in quasi-brittle materials: comparison between lattice model and acoustic emission data”. In: *International Journal for Numerical and Analytical Methods in Geomechanics* 39, pp. 1639–1664. DOI: [10.1002/nag](https://doi.org/10.1002/nag). URL: [http :](http://)

- <https://onlinelibrary.wiley.com/doi/10.1002/nag.527/abstract>{\%}5Cnhttps://web.natur.cuni.cz/uhigug/masin/download/MTVC{_}IJNAMG06-pp.pdf.
- Guillot, Stéphane, Stéphane Schwartz, Bruno Reynard, Philippe Agard, and Cécile Prigent (2015). “Tectonic significance of serpentinites”. In: *Tectonophysics* 646. February, pp. 1–19. ISSN: 00401951. DOI: [10.1016/j.tecto.2015.01.020](https://doi.org/10.1016/j.tecto.2015.01.020). URL: <http://dx.doi.org/10.1016/j.tecto.2015.01.020>.
- Hamilton, Andrea, Christopher Hall, and Leo Pel (Nov. 2008). “Sodium sulfate heptahydrate: Direct observation of crystallization in a porous material”. In: *J. Phys. D: Appl. Phys* 41, pp. 212002–5. DOI: [10.1088/0022-3727/41/21/212002](https://doi.org/10.1088/0022-3727/41/21/212002).
- Haynes, Harvey (2005). “ASTM C 88 test on soundness of aggregate using sodium sulfate or magnesium sulfate: A study of the mechanisms of damage”. In: *Journal of ASTM International* 2.1. ISSN: 1546962X. DOI: [10.1520/jai12517](https://doi.org/10.1520/jai12517).
- Hilgers, Christoph and Janos L. Urai (2005). “On the arrangement of solid inclusions in fibrous veins and the role of the crack-seal mechanism”. In: *Journal of Structural Geology* 27.3, pp. 481–494. ISSN: 01918141. DOI: [10.1016/j.jsg.2004.10.012](https://doi.org/10.1016/j.jsg.2004.10.012).
- Hirth, Greg and Stéphane Guillot (2013). “Rheology and tectonic significance of serpentinite”. In: *Elements* 9.2, pp. 107–113. ISSN: 18115209. DOI: [10.2113/gselements.9.2.107](https://doi.org/10.2113/gselements.9.2.107).
- Hoareau, Guilhem (2009). “Relations sulfates-carbonates pendant la diagenèse des sédiments marins : étude sédimentologique du delta éocène du Sobrarbe (Espagne) et modélisation thermodynamique des données ODP/IODP”. Thèse de doctorat dirigée par Odonne, Francis et Monnin, Christophe Sédimentologie. Géochimie Toulouse 3 2009. PhD thesis, 1 vol. (304 p.) URL: <http://www.theses.fr/2009TOU30252>.
- Hosgörmez, Hakan (2007). “Origin of the natural gas seep of Çirali (Chimera), Turkey: Site of the first Olympic fire”. In: *Journal of Asian Earth Sciences* 30.1, pp. 131–141. ISSN: 13679120. DOI: [10.1016/j.jseaes.2006.08.002](https://doi.org/10.1016/j.jseaes.2006.08.002).
- Huynh, Quoc Vu (2007). “Estimation des propriétés poromécaniques effectives des argilites: apport des méthodes d’homogénéisation”. PhD thesis.
- Incel, Sarah et al. (2019). “Reaction-induced embrittlement of the lower continental crust”. In: *Geology* 47.3, pp. 235–238. ISSN: 19432682. DOI: [10.1130/G45527.1](https://doi.org/10.1130/G45527.1).
- Iyer, K., B. Jamtveit, J. Mathiesen, A. Malthe-Sørensen, and J. Feder (2008). “Reaction-assisted hierarchical fracturing during serpentinitization”. In: *Earth and Planetary Science Letters* 267.3–4, pp. 503–516. ISSN: 0012821X. DOI: [10.1016/j.epsl.2007.11.060](https://doi.org/10.1016/j.epsl.2007.11.060).
- Jacqueline Saliba (2012). “Apport De L’Émission Acoustique Dans La Compréhension Et La Modélisation Du Couplage Fluage-Endommagement Du Béton”. PhD thesis, p. 171.
- Jain, Anubhav et al. (2013). “The Materials Project: A materials genome approach to accelerating materials innovation”. In: *APL Materials* 1.1, p. 011002. ISSN: 2166532X. DOI: [10.1063/1.4812323](https://doi.org/10.1063/1.4812323). URL: <http://link.aip.org/link/AMPADS/v1/i1/p011002/s1&Agg=doi>.
- Jamtveit, Bjørn, Christine V. Putnis, and Anders Malthe-Sørensen (2009). “Reaction induced fracturing during replacement processes”. In: *Contributions to Mineralogy and Petrology* 157.1, pp. 127–133. ISSN: 00107999. DOI: [10.1007/s00410-008-0324-y](https://doi.org/10.1007/s00410-008-0324-y).
- Jourdon, Anthony, Laetitia Le Pourhiet, Frédéric Mouthereau, and Emanuel Masini (2019). “Role of rift maturity on the architecture and shortening distribution in mountain belts”. In: *Earth and Planetary Science Letters* 512. February, pp. 89–99.

- ISSN: 0012821X. DOI: [10.1016/j.epsl.2019.01.057](https://doi.org/10.1016/j.epsl.2019.01.057). URL: <https://doi.org/10.1016/j.epsl.2019.01.057>.
- Kalo, K., D. Grgic, C. Auvray, A. Giraud, B. Drach, and I. Sevostianov (2017). “Effective elastic moduli of a heterogeneous oolitic rock containing 3-D irregularly shaped pores”. In: *International Journal of Rock Mechanics and Mining Sciences* 98, June, pp. 20–32. ISSN: 13651609. DOI: [10.1016/j.ijrmms.2017.07.009](https://doi.org/10.1016/j.ijrmms.2017.07.009). URL: <http://dx.doi.org/10.1016/j.ijrmms.2017.07.009>.
- Kelemen, P. B. et al. (2018). “In situ carbon mineralization in ultramafic rocks: Natural processes and possible engineered methods”. In: *Energy Procedia* 146, pp. 92–102. ISSN: 18766102. DOI: [10.1016/j.egypro.2018.07.013](https://doi.org/10.1016/j.egypro.2018.07.013). URL: <https://doi.org/10.1016/j.egypro.2018.07.013>.
- Kelemen, Peter B. and Greg Hirth (2012). “Reaction-driven cracking during retrograde metamorphism: Olivine hydration and carbonation”. In: *Earth and Planetary Science Letters* 345–348, pp. 81–89. ISSN: 0012821X. DOI: [10.1016/j.epsl.2012.06.018](https://doi.org/10.1016/j.epsl.2012.06.018). URL: <http://dx.doi.org/10.1016/j.epsl.2012.06.018>.
- Kelka, Ulrich, Manolis Veveakis, Daniel Koehn, and Nicolas Beaudoin (2017). “Zebra rocks: Compaction waves create ore deposits”. In: *Scientific Reports* 7.1, pp. 1–9. ISSN: 20452322. DOI: [10.1038/s41598-017-14541-3](https://doi.org/10.1038/s41598-017-14541-3). URL: <http://dx.doi.org/10.1038/s41598-017-14541-3>.
- Keulen, N T, S W J Den Brok, and C J Spiers (2001). “Force of crystallisation of gypsum during of hydration of synthetic anhydrite rock .” In: *Earth* 26, pp. 2001–2001.
- Lafay, Romain, German Montes-Hernandez, François Renard, and Pierre Vonlanthen (2018). “Intracrystalline reaction-induced cracking in olivine evidenced by hydration and carbonation experiments”. In: *Minerals* 8.9. ISSN: 2075163X. DOI: [10.3390/min8090412](https://doi.org/10.3390/min8090412).
- Lassin, Arnault, Laurent André, Nicolas Devau, Adeline Lach, Thomas Beuvier, Alain Gibaud, Stéphane Gaboreau, and Mohamed Azaroual (2018). “Dynamics of calcium carbonate formation: Geochemical modeling of a two-step mechanism”. In: *Geochimica et Cosmochimica Acta* 240, pp. 236–254. ISSN: 00167037. DOI: [10.1016/j.gca.2018.08.033](https://doi.org/10.1016/j.gca.2018.08.033).
- Laurent, Dimitri (2015). “Marqueurs de la dynamique des fluides associée à l’enfouissement des bassins sédimentaires : Exemples du Bassin Permien de Lodève (France) et du North Viking Graben (Mer du Nord)”. PhD thesis, p. 626.
- Lefort, Vincent, Gilles Pijaudier-Cabot, and David Grégoire (2015). “Analysis by Ripley’s function of the correlations involved during failure in quasi-brittle materials: Experimental and numerical investigations at the mesoscale”. In: *Engineering Fracture Mechanics* 147, pp. 449–467. ISSN: 0013-7944. DOI: <https://doi.org/10.1016/j.engfracmech.2015.07.046>. URL: <http://www.sciencedirect.com/science/article/pii/S0013794415004221>.
- Li, Lei, Felix Kohler, Anja Røyne, and Dag Kristian Dysthe (2017). “Growth of calcite in confinement”. In: *Crystals* 7.12. ISSN: 20734352. DOI: [10.3390/cryst7120361](https://doi.org/10.3390/cryst7120361).
- Lindström, Nadine, Tanya Talreja, Kirsten Linnow, Amelie Stahlbuhk, and Michael Steiger (2016). “Crystallization behavior of Na₂SO₄-MgSO₄ salt mixtures in sandstone and comparison to single salt behavior”. In: *Applied Geochemistry* 69, pp. 50–70. ISSN: 18729134. DOI: [10.1016/j.apgeochem.2016.04.005](https://doi.org/10.1016/j.apgeochem.2016.04.005).
- Loon, L.R. Van, M.A. Glaus, S. Frick, P. Bunic, Y. Chen, C. Wigger, Y. Fukatsu, Y. Zhao, and 5.1 (2016). *DIFFUSION PROCESSES*. Tech. rep. Laboratory for Waste

- Management. URL: <https://www1.nyc.gov/html/onenyc/downloads/pdf/publications/OneNYC-2016-Progress-Report.pdf>.
- MATLAB (2010). *version 7.10.0 (R2010a)*. Natick, Massachusetts: The MathWorks Inc.
- Maliva, R. G. and R. Siever (1988a). “Diagenetic replacement controlled by force of crystallization”. In: *Geology* 16.8, pp. 688–691. ISSN: 00917613. DOI: [10.1130/0091-7613\(1988\)016<0688:DRCBFO>2.3.CO;2](https://doi.org/10.1130/0091-7613(1988)016<0688:DRCBFO>2.3.CO;2).
- (1988b). “Diagenetic replacement controlled by force of crystallization”. In: *Geology* 16.8, pp. 688–691. ISSN: 00917613. DOI: [10.1130/0091-7613\(1988\)016<0688:DRCBFO>2.3.CO;2](https://doi.org/10.1130/0091-7613(1988)016<0688:DRCBFO>2.3.CO;2).
- Malvoisin, Benjamin, Nicolas Brantut, and Mary Alix Kaczmarek (2017). “Control of serpentinisation rate by reaction-induced cracking”. In: *Earth and Planetary Science Letters* 476, pp. 143–152. ISSN: 0012821X. DOI: [10.1016/j.epsl.2017.07.042](https://doi.org/10.1016/j.epsl.2017.07.042). URL: <http://dx.doi.org/10.1016/j.epsl.2017.07.042>.
- Marcaillou, Clement (2011). “Serpentinisation et production d ’ hydrogene en contexte de dorsale lente : approche experimentale et numerique”. PhD thesis. Université de Grenoble.
- Marty, S., F. X. Passelègue, J. Aubry, H. S. Bhat, A. Schubnel, and R. Madariaga (2019). “Origin of High-Frequency Radiation During Laboratory Earthquakes”. In: *Geophysical Research Letters* 46.7, pp. 3755–3763. ISSN: 19448007. DOI: [10.1029/2018GL080519](https://doi.org/10.1029/2018GL080519).
- Mayr, Sibylle I. and Hans Burkhardt (2006). “Ultrasonic properties of sedimentary rocks: Effect of pressure, saturation, frequency and microcracks”. In: *Geophysical Journal International* 164.1, pp. 246–258. ISSN: 0956540X. DOI: [10.1111/j.1365-246X.2005.02826.x](https://doi.org/10.1111/j.1365-246X.2005.02826.x).
- McCollom, Thomas M. and Christopher Donaldson (2016). “Generation of Hydrogen and Methane during Experimental Low-Temperature Reaction of Ultramafic Rocks with Water”. In: *Astrobiology* 16.6, pp. 389–406. ISSN: 15311074. DOI: [10.1089/ast.2015.1382](https://doi.org/10.1089/ast.2015.1382). URL: <http://online.liebertpub.com/doi/10.1089/ast.2015.1382>.
- Means, W D and T Li (2001). “A laboratory simulation of R brous veins : some R rst observations”. In: *Most* 23, pp. 857–863.
- Melkior, T., E. C. Gaucher, C. Brouard, S. Yahiaoui, D. Thoby, Ch Clinard, E. Ferrage, D. Guyonnet, C. Tournassat, and D. Coelho (2009). “Na⁺ and HTO diffusion in compacted bentonite: Effect of surface chemistry and related texture”. In: *Journal of Hydrology* 370.1-4, pp. 9–20. ISSN: 00221694. DOI: [10.1016/j.jhydrol.2009.02.035](https://doi.org/10.1016/j.jhydrol.2009.02.035). URL: <http://dx.doi.org/10.1016/j.jhydrol.2009.02.035>.
- Menéndez, Beatriz and Christian David (2013). “The influence of environmental conditions on weathering of porous rocks by gypsum: A non-destructive study using acoustic emissions”. In: *Environmental Earth Sciences* 68.6, pp. 1691–1706. ISSN: 18666280. DOI: [10.1007/s12665-012-1861-2](https://doi.org/10.1007/s12665-012-1861-2).
- Merino, E., Angels Canals, and R. C. Fletcher (2006). “Genesis of self-organized zebra textures in burial dolomites: Displacive veins, induced stress, and dolomitization”. In: *Geologica Acta* 4.3, pp. 383–393. ISSN: 16956133. DOI: [10.1344/105.000000352](https://doi.org/10.1344/105.000000352).
- Miri, Rohaldin and Helge Hellevang (2016). “Salt precipitation during CO₂ storage-A review”. In: *International Journal of Greenhouse Gas Control* 51, pp. 136–147. ISSN: 17505836. DOI: [10.1016/j.ijggc.2016.05.015](https://doi.org/10.1016/j.ijggc.2016.05.015). URL: <http://dx.doi.org/10.1016/j.ijggc.2016.05.015>.

- Mohamad-Hussein, Assef and Qinglai Ni (2018). “Numerical modeling of onset and rate of sand production in perforated wells”. In: *Journal of Petroleum Exploration and Production Technology* 8.4, pp. 1255–1271. ISSN: 21900566. DOI: [10.1007/s13202-018-0443-6](https://doi.org/10.1007/s13202-018-0443-6). URL: <https://doi.org/10.1007/s13202-018-0443-6>.
- Mourgues, Regis (2004). “Surpressions de fluide et d’ecollements. Modelisations analogique et numerique”. PhD thesis. ISBN: 12401498\r2914375247.
- Müller, Tobias M., Boris Gurevich, and Maxim Lebedev (2010). “Seismic wave attenuation and dispersion resulting from wave-induced flow in porous rocks - A review”. In: *Geophysics* 75.5. ISSN: 00168033. DOI: [10.1190/1.3463417](https://doi.org/10.1190/1.3463417).
- Mullin, J.W. (2001). In: *Crystallization (Fourth Edition)*. Ed. by J.W. Mullin. Fourth Edition. Oxford: Butterworth-Heinemann, pp. 1–594. ISBN: 978-0-7506-4833-2. DOI: <https://doi.org/10.1016/B978-075064833-2/50003-6>. URL: <http://www.sciencedirect.com/science/article/pii/B9780750648332500036>.
- Naillon, A., P. Joseph, and M. Prat (2018). “Ion Transport and Precipitation Kinetics as Key Aspects of Stress Generation on Pore Walls Induced by Salt Crystallization”. In: *Physical Review Letters* 120.3, pp. 1–8. ISSN: 10797114. DOI: [10.1103/PhysRevLett.120.034502](https://doi.org/10.1103/PhysRevLett.120.034502).
- Nakao, Atsushi, Yves Thiry, Shinya Funakawa, and Takashi Kosaki (2008). “Characterization of the frayed edge site of micaceous minerals in soil clays influenced by different pedogenetic conditions in Japan and northern Thailand”. In: *Soil Science and Plant Nutrition* 54.4, pp. 479–489. ISSN: 00380768. DOI: [10.1111/j.1747-0765.2008.00262.x](https://doi.org/10.1111/j.1747-0765.2008.00262.x).
- Noiriel, Catherine, François Renard, Mai Linh Doan, and Jean Pierre Gratier (2010). “Intense fracturing and fracture sealing induced by mineral growth in porous rocks”. In: *Chemical Geology* 269.3-4, pp. 197–209. ISSN: 00092541. DOI: [10.1016/j.chemgeo.2009.09.018](https://doi.org/10.1016/j.chemgeo.2009.09.018). URL: <http://dx.doi.org/10.1016/j.chemgeo.2009.09.018>.
- Okhrimenko, Larysa Mikolaivna (2018). “Stockage d’énergie thermique par un composite zéolite/MgSO₄-H₂O : étude thermocinétique du système MgSO₄ – H₂O et étude expérimentale des composites”. PhD thesis.
- Olson, Jon E., Stephen E. Laubach, and Robert H. Lander (2007). “Combining diagenesis and mechanics to quantify fracture aperture distributions and fracture pattern permeability”. In: *Geological Society Special Publication* 270.1, pp. 101–116. ISSN: 03058719. DOI: [10.1144/GSL.SP.2007.270.01.08](https://doi.org/10.1144/GSL.SP.2007.270.01.08).
- Parkhurst, David L. and C. A. J. Appelo (2013). *Description of Input and Examples for PHREEQC Version 3 — A Computer Program for Speciation, Batch-Reaction, One-Dimensional Transport, and Inverse Geochemical Calculations*. English. Tech. rep. Reston, VA, 6–43A. DOI: [10.1016/0029-6554\(94\)90020-5](https://doi.org/10.1016/0029-6554(94)90020-5). URL: <http://pubs.er.usgs.gov/publication/tm6A43>.
- Peterson, R.C., W. Nelson, B. Madu, and Herbert Shurvell (Oct. 2007). “Meridianiite: A new mineral species observed on Earth and predicted to exist on Mars”. In: *American Mineralogist - AMER MINERAL* 92, pp. 1756–1759. DOI: [10.2138/am.2007.2668](https://doi.org/10.2138/am.2007.2668).
- Peuble, Steve, Muriel Andreani, Philippe Gouze, Marion Pollet-Villard, Bruno Reynard, and Bertrand Van de Moortele (2018). “Multi-scale characterization of the incipient carbonation of peridotite”. In: *Chemical Geology* 476. February 2018, pp. 150–160. ISSN: 00092541. DOI: [10.1016/j.chemgeo.2017.11.013](https://doi.org/10.1016/j.chemgeo.2017.11.013). URL: <https://doi.org/10.1016/j.chemgeo.2017.11.013>.

- Peysson, Y., B. Bazin, C. Magnier, E. Kohler, and S. Youssef (2011). “Permeability alteration due to salt precipitation driven by drying in the context of CO₂ injection”. In: *Energy Procedia* 4, pp. 4387–4394. ISSN: 18766102. DOI: [10.1016/j.egypro.2011.02.391](https://doi.org/10.1016/j.egypro.2011.02.391). URL: <http://dx.doi.org/10.1016/j.egypro.2011.02.391>.
- Pimienta, L., C. David, J. Sarout, X. Perrot, J. Dautriat, and C. Barnes (2019). “Evolution in Seismic Properties During Low and Intermediate Water Saturation: Competing Mechanisms During Water Imbibition?” In: *Geophysical Research Letters* 46.9, pp. 4581–4590. ISSN: 19448007. DOI: [10.1029/2019GL082419](https://doi.org/10.1029/2019GL082419).
- Plümper, Oliver, Anja Røyne, Anna Magrasó, and Bjørn Jamtveit (2012). “The interface-scale mechanism of reaction-induced fracturing during serpentinization”. In: *Geology* 40.12, pp. 1103–1106. ISSN: 00917613. DOI: [10.1130/G33390.1](https://doi.org/10.1130/G33390.1).
- Pokrovsky, Oleg S. and Jacques Schott (2004). “Experimental study of brucite dissolution and precipitation in aqueous solutions: Surface speciation and chemical affinity control”. In: *Geochimica et Cosmochimica Acta* 68.1, pp. 31–45. ISSN: 00167037. DOI: [10.1016/S0016-7037\(03\)00238-2](https://doi.org/10.1016/S0016-7037(03)00238-2).
- Poonoosamy, J., E. Curti, G. Kosakowski, D. Grolimund, L. R. Van Loon, and U. Mäder (2016). “Barite precipitation following celestite dissolution in a porous medium: A SEM/BSE and μ -XRD/XRF study”. In: *Geochimica et Cosmochimica Acta* 182.April, pp. 131–144. ISSN: 00167037. DOI: [10.1016/j.gca.2016.03.011](https://doi.org/10.1016/j.gca.2016.03.011). URL: <http://dx.doi.org/10.1016/j.gca.2016.03.011>.
- Poonoosamy, Jenna, Martina Klinkenberg, Guido Deissmann, Felix Brandt, Dirk Bosbach, Urs Mäder, and Georg Kosakowski (2020). “Effects of solution supersaturation on barite precipitation in porous media and consequences on permeability: Experiments and modelling”. In: *Geochimica et Cosmochimica Acta* 270, pp. 43–60. ISSN: 00167037. DOI: [10.1016/j.gca.2019.11.018](https://doi.org/10.1016/j.gca.2019.11.018).
- Poonoosamy, Jenna, Georg Kosakowski, Luc R. Van Loon, and Urs Mäder (2015). “Dissolution-precipitation processes in tank experiments for testing numerical models for reactive transport calculations: Experiments and modelling”. In: *Journal of Contaminant Hydrology* 177-178, pp. 1–17. ISSN: 18736009. DOI: [10.1016/j.jconhyd.2015.02.007](https://doi.org/10.1016/j.jconhyd.2015.02.007).
- Pouit, G. and J.-P. Bois (1986). “Arrens Zn (Pb), Ba Devonian deposit, Pyrénées, France: an exhalative-sedimentary-type deposit similar to Meggen”. In: *Mineralium Deposita* 21.3, pp. 181–189. ISSN: 0026-4598. DOI: [10.1007/bf00199798](https://doi.org/10.1007/bf00199798).
- Poupeleer, Anne-Severine (2007). “Transport and crystallization of dissolved salts in cracked porous building materials. Ph.D Thesis”. PhD thesis, p. 323. ISBN: 9789056827977.
- Prieto, M. (2014). “Nucleation and supersaturation in porous media (revisited)”. In: *Mineralogical Magazine* 78.6, pp. 1437–1447. ISSN: 0026-461X. DOI: [10.1180/minmag.2014.078.6.11](https://doi.org/10.1180/minmag.2014.078.6.11). URL: <http://openurl.ingenta.com/content/xref?genre=article{\&}issn=0026-461X{\&}volume=78{\&}issue=6{\&}page=1437>.
- Prieto, Manuel, Andrew Putnis, Jose Arribas, and Lurdes Fernandez-Diaz (1992). “Ontogeny of baryte crystals grown in a porous medium”. In: *Mineralogical Magazine* 56.385, pp. 587–598. ISSN: 0026-461X. DOI: [10.1180/minmag.1992.056.385.15](https://doi.org/10.1180/minmag.1992.056.385.15).
- Prieto, Manuel, Andrew Putnis, and Lurdes Fernandez-Diaz (1993). “Crystallization of solid solutions from aqueous solutions in a porous medium: Zoning in (Ba, Sr)SO₄”. In: *Geological Magazine* 130.3, pp. 289–299. ISSN: 14695081. DOI: [10.1017/S0016756800019981](https://doi.org/10.1017/S0016756800019981). URL: http://www.journals.cambridge.org/abstract{_}S0016756800019981.

- Prinzhofer, Alain, Cheick Sidy Tahara Cissé, and Aliou Boubacar Diallo (2018). “Discovery of a large accumulation of natural hydrogen in Bourakebougou (Mali)”. In: *International Journal of Hydrogen Energy* 43.42, pp. 19315–19326. ISSN: 03603199. DOI: [10.1016/j.ijhydene.2018.08.193](https://doi.org/10.1016/j.ijhydene.2018.08.193).
- Putnis, A. and G. Mauthe (2001). “The effect of pore size on cementation in porous rocks”. In: 1.1, pp. 37–41. ISSN: 14688115. DOI: [10.1046/j.1468-8123.2001.11001.x](https://doi.org/10.1046/j.1468-8123.2001.11001.x). URL: <file:///Users/workstation/Documents/Sente/2001PutnisTheeffectofpores.pdf><http://www.scopus.com/scopus/inward/record.url?eid=2-s2.0-0002007562&partnerID=40&rel=R8.0.0><file:///localhost/Users/workstation/Docume>.
- Putnis, Andrew and Lurdes Fernandez-Diaz (1990). “Factors controlling the kinetics of crystallization: Supersaturation evolution in a porous medium. Application to barite crystallization”. In: *Geological Magazine* 127.6, pp. 485–495. ISSN: 14695081. DOI: [10.1017/S0016756800015417](https://doi.org/10.1017/S0016756800015417).
- Putnis, Andrew, Manuel Prieto, and Lurdes Fernandez-Diaz (1995). “Fluid supersaturation and crystallization in porous media”. In: *Geological Magazine* 132.1, pp. 1–13. ISSN: 14695081. DOI: [10.1017/S0016756800011389](https://doi.org/10.1017/S0016756800011389). URL: http://www.journals.cambridge.org/abstract/_S0016756800011389.
- Putnis, Andrew and Christine V. Putnis (2007). “The mechanism of reequilibration of solids in the presence of a fluid phase”. In: *Journal of Solid State Chemistry* 180.5, pp. 1783–1786. ISSN: 00224596. DOI: [10.1016/j.jssc.2007.03.023](https://doi.org/10.1016/j.jssc.2007.03.023).
- Radilla, G., M. Kacem, J. M. Lombard, and M. Fourar (2010). “Transport properties of lavoux limestone at various stages of CO₂-like acid-rock alteration”. In: *Oil and Gas Science and Technology* 65.4, pp. 557–563. ISSN: 12944475. DOI: [10.2516/ogst/2009081](https://doi.org/10.2516/ogst/2009081).
- Rajyaguru, A., E. L’Hôpital, S. Savoye, C. Wittebroodt, O. Bildstein, P. Arnoux, V. Dettleux, I. Fatnassi, P. Gouze, and V. Lagneau (2019). “Experimental characterization of coupled diffusion reaction mechanisms in low permeability chalk”. In: *Chemical Geology* 503, pp. 29–39. ISSN: 0009-2541. DOI: <https://doi.org/10.1016/j.chemgeo.2018.10.016>. URL: <https://www.sciencedirect.com/science/article/pii/S0009254118305199>.
- Ramon, Anna and Eduardo E. Alonso (2018). “Heave of a Building Induced by Swelling of an Anhydritic Triassic Claystone”. In: *Rock Mechanics and Rock Engineering* 51.9, pp. 2881–2894. ISSN: 07232632. DOI: [10.1007/s00603-018-1503-4](https://doi.org/10.1007/s00603-018-1503-4). URL: <http://dx.doi.org/10.1007/s00603-018-1503-4>.
- Ramsay, John G. (1980). “The crack-seal mechanism of rock deformation”. In: *Nature* 284.5752, pp. 135–139. ISSN: 00280836. DOI: [10.1038/284135a0](https://doi.org/10.1038/284135a0).
- Regenspurg, Simona, Elvira Feldbusch, James Byrne, Fiorenza Deon, Dejene Legesse Driba, Jan Henninges, Andreas Kappler, Rudolf Naumann, Thomas Reinsch, and Christine Schubert (2015). “Mineral precipitation during production of geothermal fluid from a Permian Rotliegend reservoir”. In: *Geothermics* 54, pp. 122–135. ISSN: 0375-6505. DOI: <https://doi.org/10.1016/j.geothermics.2015.01.003>. URL: <http://www.sciencedirect.com/science/article/pii/S0375650515000073>.
- Rijniers, LA, H. Huinink, Leo Pel, and Klaas Kopinga (Mar. 2005). “Experimental Evidence of Crystallization Pressure inside Porous Media”. In: *Physical review letters* 94, p. 075503. DOI: [10.1103/PhysRevLett.94.075503](https://doi.org/10.1103/PhysRevLett.94.075503).
- Rimmelé, G., V. Barlet-Gouédard, and F. Renard (2010). “Evolution of the petrophysical and mineralogical properties of two reservoir rocks under thermodynamic con-

- ditions relevant for CO₂ geological storage at 3 km depth”. In: *Oil and Gas Science and Technology* 65.4, pp. 565–580. ISSN: 12944475. DOI: [10.2516/ogst/2009071](https://doi.org/10.2516/ogst/2009071).
- Rudge, John F., Peter B. Kelemen, and Marc Spiegelman (2010). “A simple model of reaction-induced cracking applied to serpentinization and carbonation of peridotite”. In: *Earth and Planetary Science Letters* 291.1-4, pp. 215–227. ISSN: 0012821X. DOI: [10.1016/j.epsl.2010.01.016](https://doi.org/10.1016/j.epsl.2010.01.016). URL: <http://dx.doi.org/10.1016/j.epsl.2010.01.016>.
- Ruiz-Agudo, Cristina, Jonathan Thomas Avaro, David Joshua Schupp, David McDonogh, and Denis Gebauer (2020). “Capturing an amorphous BaSO₄ intermediate precursor to barite”. In: *CrystEngComm* 22.8, pp. 1310–1313. ISSN: 14668033. DOI: [10.1039/c9ce01555h](https://doi.org/10.1039/c9ce01555h).
- Ruiz-Agudo, Cristina, Christine V. Putnis, Encarnación Ruiz-Agudo, and Andrew Putnis (2015). “The influence of pH on barite nucleation and growth”. In: *Chemical Geology* 391, pp. 7–18. ISSN: 00092541. DOI: [10.1016/j.chemgeo.2014.10.023](https://doi.org/10.1016/j.chemgeo.2014.10.023).
- Ruiz-Agudo, Encarnación, S. McCabe, B. J. Smith, and P. A. Warke (2007). “Preliminary observations on the impact of complex stress histories on sandstone response to salt weathering: Laboratory simulations of process combinations”. In: *Environmental Geology* 52.2, pp. 269–276. ISSN: 09430105. DOI: [10.1007/s00254-006-0476-x](https://doi.org/10.1007/s00254-006-0476-x).
- Saliba, J., M. Matallah, A. Loukili, J.P. Regoin, D. Grégoire, L. Verdon, and G. Pijaudier-Cabot (2016). “Experimental and numerical analysis of crack evolution in concrete through acoustic emission technique and mesoscale modelling”. In: *Engineering Fracture Mechanics* 167. SI:CRACK PATHS 2015, pp. 123–137. ISSN: 0013-7944. DOI: <https://doi.org/10.1016/j.engfracmech.2016.03.044>. URL: <http://www.sciencedirect.com/science/article/pii/S0013794416301515>.
- Sarout, Joël (2012). “Impact of pore space topology on permeability, cut-off frequencies and validity of wave propagation theories”. In: *Geophysical Journal International* 189.1, pp. 481–492. ISSN: 0956540X. DOI: [10.1111/j.1365-246X.2011.05329.x](https://doi.org/10.1111/j.1365-246X.2011.05329.x).
- Sass, Ingo and Ulrich Burbaum (2010). “Damage to the historic town of staufen(Germany) caused by geothermal drillings through anhydrite-bearing formations”. In: *Acta Carolologica* 39.2, pp. 233–245. ISSN: 15802612. DOI: [10.3986/ac.v39i2.96](https://doi.org/10.3986/ac.v39i2.96).
- Sayers, C M and M Kachanov (1995). “Microcrack-induced elastic wave anisotropy of brittle rocks”. In: *Journal of Geophysical Research* 100.B3, pp. 4149–4156. ISSN: 01480227. DOI: [10.1029/94JB03134](https://doi.org/10.1029/94JB03134).
- Scherer, George W. (1999). “Crystallization in pores”. In: *Cement and Concrete Research* 29.8, pp. 1347–1358. ISSN: 00088846. DOI: [10.1016/S0008-8846\(99\)00002-2](https://doi.org/10.1016/S0008-8846(99)00002-2).
- (2004). “Stress from crystallization of salt”. In: *Cement and Concrete Research* 34.9, pp. 1613–1624. ISSN: 00088846. DOI: [10.1016/j.cemconres.2003.12.034](https://doi.org/10.1016/j.cemconres.2003.12.034).
- Schindelin, Johannes et al. (2012). “Fiji: an open-source platform for biological-image analysis”. In: *Nature Methods* 9.7, pp. 676–682. ISSN: 1548-7105. DOI: [10.1038/nmeth.2019](https://doi.org/10.1038/nmeth.2019). URL: <https://doi.org/10.1038/nmeth.2019>.
- Schubnel, Alexandre and Yves Guéguen (2003). “Dispersion and anisotropy of elastic waves in cracked rocks”. In: *Journal of Geophysical Research: Solid Earth* 108.B2, pp. 1–15. ISSN: 21699356. DOI: [10.1029/2002jb001824](https://doi.org/10.1029/2002jb001824).
- Schubnel, Alexandre and Yves Guéguen (2003). “Dispersion and anisotropy of elastic waves in cracked rocks”. In: *Journal of Geophysical Research: Solid Earth* 108.B2. DOI: [10.1029/2002JB001824](https://doi.org/10.1029/2002JB001824). eprint: <https://agupubs.onlinelibrary.wiley.com/doi/pdf/10.1029/2002JB001824>. URL: <https://agupubs.onlinelibrary.wiley.com/doi/abs/10.1029/2002JB001824>.

- Shahidzadeh-Bonn, Noushine, Julie Desarnaud, François Bertrand, Xavier Chateau, and Daniel Bonn (2010). “Damage in porous media due to salt crystallization”. In: *Physical Review E - Statistical, Nonlinear, and Soft Matter Physics* 81.6. ISSN: 15393755. DOI: [10.1103/PhysRevE.81.066110](https://doi.org/10.1103/PhysRevE.81.066110).
- Skarbek, Rob M., Heather M. Savage, Peter B. Kelemen, and Demetra Yancopoulos (2018). “Competition Between Crystallization-Induced Expansion and Creep Compaction During Gypsum Formation, and Implications for Serpentinization”. In: *Journal of Geophysical Research: Solid Earth* 123.7, pp. 5372–5393. ISSN: 21699356. DOI: [10.1029/2017JB015369](https://doi.org/10.1029/2017JB015369).
- Steiger, Michael (2005a). “Crystal growth in porous materials - I: The crystallization pressure of large crystals”. In: *Journal of Crystal Growth* 282.3-4, pp. 455–469. ISSN: 00220248. DOI: [10.1016/j.jcrysgr.2005.05.007](https://doi.org/10.1016/j.jcrysgr.2005.05.007).
- (2005b). “Crystal growth in porous materials - II: Influence of crystal size on the crystallization pressure”. In: *Journal of Crystal Growth* 282.3-4, pp. 470–481. ISSN: 00220248. DOI: [10.1016/j.jcrysgr.2005.05.008](https://doi.org/10.1016/j.jcrysgr.2005.05.008).
- Steiger, Michael and Sönke Asmussen (2008). “Crystallization of sodium sulfate phases in porous materials: The phase diagram Na₂SO₄-H₂O and the generation of stress”. In: *Geochimica et Cosmochimica Acta* 72.17, pp. 4291–4306. ISSN: 00167037. DOI: [10.1016/j.gca.2008.05.053](https://doi.org/10.1016/j.gca.2008.05.053).
- Steiger, Michael, Jana Kiekbusch, and Andreas Nicolai (2008). “An improved model incorporating Pitzer’s equations for calculation of thermodynamic properties of pore solutions implemented into an efficient program code”. In: *Construction and Building Materials* 22.8, pp. 1841–1850. ISSN: 09500618. DOI: [10.1016/j.conbuildmat.2007.04.020](https://doi.org/10.1016/j.conbuildmat.2007.04.020).
- Steiger, Michael, Kirsten Linnow, Dorothee Ehrhardt, and Mandy Rohde (2011). “Decomposition reactions of magnesium sulfate hydrates and phase equilibria in the MgSO₄-H₂O and Na⁺-Mg²⁺-Cl⁻-SO₄²⁻-H₂O systems with implications for Mars”. In: *Geochimica et Cosmochimica Acta* 75.12, pp. 3600–3626. ISSN: 00167037. DOI: [10.1016/j.gca.2011.03.038](https://doi.org/10.1016/j.gca.2011.03.038). URL: <http://dx.doi.org/10.1016/j.gca.2011.03.038>.
- Steiger, Michael, Kirsten Linnow, Herbert Juling, Gerd Gülker, Akram El Jarad, Stefan Brüggerhoff, and Dirk Kirchner (2008). “Hydration of MgSO₄ · H₂O and generation of stress in porous materials”. In: *Crystal Growth and Design* 8.1, pp. 336–343. ISSN: 15287483. DOI: [10.1021/cg060688c](https://doi.org/10.1021/cg060688c).
- Taber, S. (1916). “The growth of crystals under external pressure”. In: s4-41.246, pp. 532–556. ISSN: 0002-9599. DOI: [10.2475/ajs.s4-41.246.532](https://doi.org/10.2475/ajs.s4-41.246.532).
- Tada, Ryuji, Robert Maliva, and Raymond Siever (1987). “A new mechanism for pressure solution in porous quartzose sandstone”. In: *Geochimica et Cosmochimica Acta* 51.9, pp. 2295–2301. ISSN: 00167037. DOI: [10.1016/0016-7037\(87\)90282-1](https://doi.org/10.1016/0016-7037(87)90282-1).
- To, Thanh and Chandong Chang (2019). “Comparison of Different Permeability Models for Production-induced Compaction in Sandstone Reservoirs”. In: 29.4, pp. 367–381.
- Torres, M. E., H. J. Brumsack, G. Bohrmann, and K. C. Emeis (1996). “Barite fronts in continental margin sediments: A new look at barium remobilization in the zone of sulfate reduction and formation of heavy barites in diagenetic fronts”. In: *Chemical Geology* 127.1-3, pp. 125–139. ISSN: 00092541. DOI: [10.1016/0009-2541\(95\)00090-9](https://doi.org/10.1016/0009-2541(95)00090-9).
- Ukar, Estibalitz, Ramiro G. Lopez, Julia F.W. Gale, Stephen E. Laubach, and Rene Manceda (2017). “New type of kinematic indicator in bed-parallel veins, Late Jurassic–Early Cretaceous Vaca Muerta Formation, Argentina: E-W shortening during

- Late Cretaceous vein opening". In: *Journal of Structural Geology* 104.October, pp. 31–47. ISSN: 01918141. DOI: [10.1016/j.jsg.2017.09.014](https://doi.org/10.1016/j.jsg.2017.09.014). URL: <https://doi.org/10.1016/j.jsg.2017.09.014>.
- Vacquand, Christèle, Eric Deville, Valérie Beaumont, François Guyot, Olivier Sissmann, Daniel Pillot, Carlo Arcilla, and Alain Prinzhofer (2018). "Reduced gas seepages in ophiolitic complexes: Evidences for multiple origins of the H₂-CH₄-N₂ gas mixtures". In: *Geochimica et Cosmochimica Acta* 223.January, pp. 437–461. ISSN: 00167037. DOI: [10.1016/j.gca.2017.12.018](https://doi.org/10.1016/j.gca.2017.12.018).
- Van Den Abeele, K. E.-A. (2002). "Influence of water saturation on the nonlinear elastic mesoscopic response in Earth materials and the implications to the mechanism of nonlinearity". In: *Journal of Geophysical Research* 107.B6, pp. 1–11. ISSN: 0148-0227. DOI: [10.1029/2001jb000368](https://doi.org/10.1029/2001jb000368).
- Wallace, Malcolm W. and Ashleigh v.S. Hood (2018). "Zebra textures in carbonate rocks: Fractures produced by the force of crystallization during mineral replacement". In: *Sedimentary Geology* 368, pp. 58–67. ISSN: 00370738. DOI: [10.1016/j.sedgeo.2018.03.009](https://doi.org/10.1016/j.sedgeo.2018.03.009). URL: <http://linkinghub.elsevier.com/retrieve/pii/S0037073818300496>.
- Wiltschko, David V. and John W. Morse (2001). "Crystallization pressure versus crack seal as the mechanism for banded veins". In: *Geology* 29.1, pp. 79–82. ISSN: 00917613. DOI: [10.1130/0091-7613\(2001\)029<0079:CPVCSA>2.0.CO;2](https://doi.org/10.1130/0091-7613(2001)029<0079:CPVCSA>2.0.CO;2).
- Wolterbeek, Timotheus K.T., Reinier van Noort, and Christopher J. Spiers (2018). "Reaction-driven casing expansion: potential for wellbore leakage mitigation". In: *Acta Geotechnica* 13.2, pp. 341–366. ISSN: 18611133. DOI: [10.1007/s11440-017-0533-5](https://doi.org/10.1007/s11440-017-0533-5).
- Xing, Tiange, Wenlu Zhu, Florian Fuisseis, and Harrison Lisabeth (2018). "Generating porosity during olivine carbonation via dissolution channels and expansion cracks". In: *Solid Earth* 9.4, pp. 879–896. ISSN: 18699529. DOI: [10.5194/se-9-879-2018](https://doi.org/10.5194/se-9-879-2018).
- Yuan, Yujie and Reza Rezaee (2019). "Comparative porosity and pore structure assessment in shales: Measurement techniques, influencing factors and implications for reservoir characterization". In: *Energies* 12.11. ISSN: 19961073. DOI: [10.3390/en12112094](https://doi.org/10.3390/en12112094).
- Zanella, A., P. R. Cobbold, and T. Boassen (2015). "Natural hydraulic fractures in the Wessex Basin, SW England: Widespread distribution, composition and history". In: *Marine and Petroleum Geology* 68, pp. 438–448. ISSN: 02648172. DOI: [10.1016/j.marpetgeo.2015.09.005](https://doi.org/10.1016/j.marpetgeo.2015.09.005). URL: <http://dx.doi.org/10.1016/j.marpetgeo.2015.09.005>.
- Zheng, Xiaojiao, Benoît Cordonnier, Jessica McBeck, Elodie Boller, Bjørn Jamtveit, Wenlu Zhu, and François Renard (2019). "Mixed-Mode Strain Localization Generated by Hydration Reaction at Crustal Conditions". In: *Journal of Geophysical Research: Solid Earth* 124.5, pp. 4507–4522. ISSN: 21699356. DOI: [10.1029/2018JB017008](https://doi.org/10.1029/2018JB017008).
- Zheng, Xiaojiao, Benoît Cordonnier, Wenlu Zhu, François Renard, and Bjørn Jamtveit (2018). "Effects of Confinement on Reaction-Induced Fracturing During Hydration of Periclase". In: *Geochemistry, Geophysics, Geosystems* 19.8, pp. 2661–2672. ISSN: 15252027. DOI: [10.1029/2017GC007322](https://doi.org/10.1029/2017GC007322).
- Zhu, Wenlu, Florian Fuisseis, Harrison Lisabeth, Tiange Xing, Xianghui Xiao, Vincent De Andrade, and Shun Ichiro Karato (2016). "Experimental evidence of reaction-induced fracturing during olivine carbonation". In: *Geophysical Research Letters* 43.18, pp. 9535–9543. ISSN: 19448007. DOI: [10.1002/2016GL070834](https://doi.org/10.1002/2016GL070834).

BIBLIOGRAPHY

Zotz-Wilson, Reuben, Lisanne A.N.R. Douma, Joel Sarout, Jeremie Dautriat, David Dewhurst, and Auke Barnhoorn (2020). “Ultrasonic Imaging of the Onset and Growth of Fractures Within Partially Saturated Whitby Mudstone Using Coda Wave Decorrelation Inversion”. In: *Journal of Geophysical Research: Solid Earth* 125.7. ISSN: 21699356. DOI: [10.1029/2020JB020042](https://doi.org/10.1029/2020JB020042).